CONTROL OF COMPLEX STRUCTURAL GEOMETRY IN OPTICAL FIBRE DRAWING

A thesis submitted for the degree of
Doctor of Philosophy

by

KATJA JOHANNA LYYTIKÄINEN

School of Physics
and
Optical Fibre Technology Centre
University of Sydney

2004

Preface

This thesis contains no material which has been presented for a degree at this or any other university and, to the best of my knowledge and belief, contains no copy or paraphrase of work published by another person, except where duly acknowledged.

Katja Lyytikäinen
Sydney, 28th March 2004

TABLE OF CONTENTS

ACKNOWLEDGEMENTS

I would like to thank my supervisors Pam McNamara, Simon Fleming and Adrian Carter for all the help they have provided during the course of this study. Special thanks are due to John Canning for his support and time in helping to solve the numerous challenges in the silica PCF project. I would also like to acknowledge the OFTC fibre fabrication team for their help. The preforms were made by Justin Digweed, Ron Bailey, Peter Henry, Tom Ryan and Barry Reed. Special thanks are due to Justin Digweed for setting up the pressurisation system, help in fibre drawing, measurements and stacking of the PCF preforms.

I also wish to acknowledge Shane Huntington of the University of Melbourne for making the etching and AFM measurements and Peter Pace for providing data on fibre etching. I thank the staff of the Australian Key Centre for Microscopy and Microanalysis, University of Sydney: Adam Sikorski for preparing the TEM samples, Shaun Bulcock for operating the STEM and Ian Kaplin for his help with the SEM. I would also like to acknowledge Yucheng Zhao of the OFTC who developed the tomographic software and Jarek Abramczyk of Nufern Ltd for fibre refractive index profile measurements.

Appreciation must also go to the following members of OFTC for their help: Elizabeth Buckley for measurements on PCFs, Joseph Zagari for stacking PCF preforms and Leon Poladian for doing the dispersion simulations. I also thank the following people: Geoff Barton (University of Sydney), Karl-Friedrich Klein (FH Giessen-Friedberg) and Gerhard Schötz (Heraeus-Tenevo) for useful discussions and Heraeus-Tenevo for preform samples; Juha Ruokolainen and Peter Råback from CSC-Scientific Computing for developing the ELMER-program; Bernard Pailthorpe and Ben Simmons of Vislab at the University of Sydney for computing help. I would also like to acknowledge Australian Government, DEST, the University of Sydney and the Australian Photonics Cooperative Research Centre for funding.

Finally I would like to express my deepest gratitude and love for my fiancé Justin for his dedication in helping me in every way possible during my candidature.

ABSTRACT

Drawing of standard telecommunication-type optical fibres has been optimised in terms of optical and physical properties. Specialty fibres, however, typically have more complex dopant profiles. Designs with high dopant concentrations and multidoping are common, making control of the fabrication process particularly important. In photonic crystal fibres (PCF) the inclusion of air-structures imposes a new challenge for the drawing process.

The aim of this study is to gain profound insight into the behaviour of complex optical fibre structures during the final fabrication step, fibre drawing. Two types of optical fibre, namely conventional silica fibres and PCFs, were studied. Germanium and fluorine diffusion during drawing was studied experimentally and a numerical analysis was performed of the effects of drawing parameters on diffusion. An experimental study of geometry control of PCFs during drawing was conducted with emphasis given to the control of hole size. The effects of the various drawing parameters and their suitability for controlling the air-structure was studied. The effect of air-structures on heat transfer in PCFs was studied using computational fluid dynamics techniques.

Both germanium and fluorine were found to diffuse at high temperature and low draw speed. A diffusion coefficent for germanium was determined and simulations showed that most diffusion occurred in the neck-down region. Draw temperature and preform feed rate had a comparable effect on diffusion. The hole size in PCFs was shown to depend on the draw temperature, preform feed rate and the preform internal pressure. Pressure was shown to be the most promising parameter for on-line control of the hole size. Heat transfer simulations showed that the air-structure had a significant effect on the temperature profile of the structure. It was also shown that the preform heating time was either increased or reduced compared to a solid structure and depended on the air-fraction.

PUBLICATIONS

The majority of the work presented in this thesis has been published in the following publications [A1-A9]. During the course of the study a large number of papers were published which resulted indirectly from the findings in this thesis and where the research done in this thesis was essential to the published studies. These co-authored papers are listed below in [A10-A41] and include studies in the area of FBG in PCFs [A20, A22, A29, A39], Fresnel fibres [A18, A19, A23, A26, A27, A38], cleaving of PCFs [A16, A30, A31], tapering of PCFs [A21], microfluidics [A11, A34-A37] and preform and fibre measurement techniques [A10, A13, A14, A28, A32, A33].

First author journal papers

A1. Lyytikäinen, K., Huntington, S. T., Carter, A. L. G., McNamara, P., Fleming, S., Abramczyk, J., et al., "Dopant diffusion during optical fibre drawing," Optics Express, Vol. 12, No.6, pp. 972-977, 2004.

A2. Lyytikäinen, K., Zagari, J., Barton, G., and Canning, J., "Heat transfer within a microstructured polymer optical fibre," Modelling and Simulation in Materials Science and Engineering, Vol. 12, pp. S255-S265, 2004.

First author conference papers

A3. Lyytikäinen, K., Råback, P., and Ruokolainen, J., "Numerical simulation of a specialty optical fibre drawing process," Proceedings of 4th International ASME/JSME/KSME Symposium on Computational Technologies for Fluid/ Thermal/ Chemical/ Stress Systems with Industrial Applications, Vancouver, BC, Canada, S. Kawano and V. V. Kudriavtsev, Vol. PVP448-2, American Society of Mechanical Engineers, pp. 267-275, 2002. (full reviewed paper)

A4. Lyytikäinen, K., Canning, J., Digweed, J., and Zagari, J., "Geometry control of air-silica structured optical fibres using pressurisation," Proceedings of International Microwave and Optoelectronics Conference, Parana, Brazil, Sept 20-23, Vol. 2, pp. 1001-1005, 2003.

A5. Lyytikäinen, K., Huntington, S. T., Carter, A., Fleming, S., and McNamara, P., "Germanium diffusion during optical fibre drawing," Proceedings of Conference on the Optical Internet & Australian Conference on Optical Fibre Technology, Melbourne, Australia, July 13-16, pp. 357-360, 2003.

A6. Lyytikäinen, K., Canning, J., Digweed, J., and Zagari, J., "Geometry control of air-silica structured optical fibres," Proceedings of Conference on the Optical Internet & Australian Conference on Optical Fibre Technology, Melbourne, Australia, July 13-16, pp. 137-140, 2003.

A7. Lyytikäinen, K. and Huntington, S. T., "Characterising submicron changes in optical fibres due to the drawing process using atomic force microscopy,"

Presented at The Fourth Australian Scanning Probe Microscopy Conference, Melbourne, Australia, July 9-11, 2003.

A8. Lyytikäinen, K., "Numerical simulation of a specialty optical fibre drawing process," Proceedings of 27th Australian Conference on Optical Fibre Technology, Sydney, Australia, Photonics Institute Pty Ltd, The Institute of Engineers Australia, pp. 134-136, 2002.

A9. Lyytikäinen, K., Zagari, J., Barton, G., and Canning, J., "Heat transfer in a microstructured optical fibre preform," Proceedings of 11th International Plastic Optical Fibers Conference, Tokyo, Japan, Sept 18-20, pp. 53-56, 2002.

Co-authored journal papers

A10. Zhao, Y., Fleming, S., Lyytikäinen, K., and Poladian, L., "Nondestructive measurement for arbitrary RIP distribution of optical fiber preforms," Journal of Lightwave Technology, Vol. 22, No.2, pp. 478-486, 2004.

A11. Canning, J., Buckley, E., and Lyytikainen, K., "Electrokinetic air-silica structured multi-microchannel capillary batteries," Electronic Letters, Vol. 40, No.5, pp. 298-299, 2004.

A12. Town, G. E., Funaba, T., Ryan, T., and Lyytikainen, K., "Optical supercontinuum generation from nanosecond pump pulses in an irregularly microstructured air-silica optical fiber," Journal of Applied Physics B - Lasers and Optics, Vol. 77, No.2-3, pp. 235-238, 2003.

A13. Pace, P., Huntington, S. T., Lyytikäinen, K., Roberts, A. and Love, J. D., "Refractive index profiles of Ge-doped optical fibers with nanometer spatial resolution using atomic force microscopy," Optics Express, Vol. 12, No.7, pp. 1452-1457, 2004.

A14. Zhao, Y., Lyytikainen, K., van Eijkelenborg, M., and Fleming, S., "Nondestructive measurement of refractive index profile for holey fiber preforms," Optics Express, Vol. 11, No.20, pp. 2474-2479, 2003.

A15. McNamara, P., Lyytikäinen, K., Ryan, T., Kaplin, I. J., and Ringer, S. P., "Germanium-rich "starburst" cores in silica-based optical fibres fabricated by modified chemical vapour deposition," Optics Communications, Vol. 230, No.1-3, pp. 45-53, 2003.

A16. Huntington, S. T., Lyytikainen, K., and Canning, J., "Analysis and removal of fracture damage during and subsequent to holey fiber cleaving," Optics Express, Vol. 11, No.6, pp. 535-540, 2003.

A17. Canning, J., Buckley, E., and Lyytikäinen, K., "Multiple source generation using air-structured optical waveguides for optical field shaping and transformation within and beyond the waveguide," Optics Express, Vol. 11, No.4, pp. 347-358, 2003.

A18. Canning, J., Buckley, E., and Lyytikäinen, K., "Propagation in air by field superposition of scattered light within a Fresnel fibre," Optics Letters, Vol. 28, No.4, pp. 230-232, 2003.

A19. Canning, J., Buckley, E., and Lyytikäinen, K., "All-fibre phase-aperture zone plates," Electronic Letters, Vol. 39, No.3, pp. 311-312, 2003.

A20. Groothoff, N., Canning, J., Buckley, E., Lyytikäinen, K., and Zagari, J., "Bragg gratings in air silica structured fibers," Optics Letters, Vol. 28, No.4, pp. 233-235, 2003.

A21. Huntington, S. T., Katsifolis, J., Gibson, B. C., Canning, J., Lyytikäinen, K., Zagari, J., et al., "Retaining and characterising nano-structure within tapered air-silica structured fibers," Optics Express, Vol. 11, No.2, pp. 98-104, 2003.

A22. Canning, J., Groothoff, N., Buckley, E., Ryan, T., Lyytikainen, K., and Digweed, J., "All-fibre photonic crystal distributed Bragg reflector (PC-DBR) fibre laser," Optics Express, Vol. 11, No.17, pp. 1995-2000, 2003.

A23. Canning, J., Buckley, E., Lyytikäinen, K., and Ryan, T., "Wavelength dependent leakage in a Fresnel-based air-silica structured optical fibre," Optics Communications, Vol. 205, No.1-3, pp. 95-99, 2002.

A24. Canning, J., van Eijkelenborg, M., Ryan, T., Kristensen, M., and Lyytikäinen, K., "Complex mode coupling with in-air silica structured optical fibres and applications," Optics Communications, Vol. 185, No.4-6, pp. 321-324, 2000.

A25. van Eijkelenborg, M. A., Canning, J., Ryan, T., and Lyytikäinen, K., "Bending-induced colouring in a photonic crystal fibre," Optics Express, Vol. 7, No.2, pp. 88-94, 2000.

Co-authored conference papers

A26. Canning, J., Buckley, E., and Lyytikäinen, K., "Propagation in air by field superposition of scattered light within a Fresnel fibre," Proceedings of Optical Fiber Communication Conference, Atlanta, Georgia, USA, Optical Society of America, Vol. 1, MF2, pp. 2, 2003.

A27. Canning, J., Buckley, E., Lyytikainen, K., and Huntington, S. T., "Optical fibre Fresnel lenses and zone plates," Proceedings of International Microwave and Optoelectronics Conference, Parana, Brazil, Sept 20-23, Vol. 2, pp. 633-636, 2003.

A28. Zhao, Y., Fleming, S., Lyytikäinen, K., and Poladian, L., "Nondestructive measurement of two dimensional refractive index profile of non-circularly symmetric optical fibre preform," Proceedings of Conference on the Optical Internet & Australian Conference on Optical Fibre Technology, Melbourne, Australia, July 13-16, pp. 323-326, 2003.

A29. Groothoff, N., Canning, J., Ryan, T., Lyytikäinen, K., and Digweed, J., "Distributed Bragg Reflector (DBR) Er3+ doped air-silica structured fibre laser," Proceedings of Conference on the Optical Internet & Australian Conference on Optical Fibre Technology, Melbourne, Australia, post-deadline paper, 2003.

A30. Huntington, S. T., Lyytikäinen, K., and Canning, J., "Crack generation and removal in cleaved air-silica structured optical fibres," Proceedings of International Microwave and Optoelectronics Conference, Parana, Brazil, Sept 20-23, Vol. 2, pp. 997-1000, 2003.

A31. Huntington, S. T., Lyytikäinen, K., and Canning, J., "Analysis and removal of fracture damage from holey fibres," Proceedings of Conference on the Optical Internet & Australian Conference on Optical Fibre Technology, Melbourne, Australia, July 13-16, pp. 149-152, 2003.

A32. Pace, P., Lyytikainen, K., Huntington, S. T., Roberts, A., and Love, J. D., "Characterisation of single dopant core fibres," Proceedings of Conference on the Optical Internet & Australian Conference on Optical Fibre Technology, Melbourne, Australia, July 13-16, pp. 330-333, 2003.

A33. Pace, P., Lyytikainen, K., Huntington, S. T., Roberts, A., and Love, J. D., "Characterisation of germanium doped core fibres," Proceedings of Australasian Conference on Optics, Lasers, & Spectroscopy, Melbourne, Australia, 1-4 December 2003, 2003.

A34. Rodd, L. E., Huntington, S. T., Lyytikainen, K., Boger, D. V., and Cooper-White, J. J., "The effect of surface character on flows in microchannels," Proceedings of SPIE's International Symposium on Microelectronics, MEMS, and Nanotechnology, Perth, Australia, December, 2003.

A35. Rodd, L. E., Huntington, S. T., Lyytikainen, K., Boger, D. V., and Cooper-White, J. J., "Velocity profiles in circular microchannels with hydrophobic and hydrophilic surfaces," Presented at The Annual Society of Rheology Meeting, Pittsburgh, Pennsylvania, US, October, 2003.

A36. Rodd, L. E., Huntington, S. T., Lyytikainen, K., Boger, D. V., and Cooper-White, J. J., "Quantifying surface effects on Newtonian laminar flows in cylindrical microchannels," Presented at The Korean and Australian Society of Rheology Meeting, Geongju, Korea, September, 2003.

A37. Rodd, L. E., Huntington, S. T., Lyytikainen, K., Boger, D. V., and Cooper-White, J. J., "Quantifying surface effects on Newtonian laminar flows in circular microchannels," Presented at The 7th International Conference on Micro Total Analysis Systems, Lake Tahoe, California, US, October 5-9, 2003.

A38. Canning, J., Buckley, E., Lyytikäinen, K., and Ryan, T., "Wavelength dependent leakage in a Fresnel-based air silica structured optical fibre," Proceedings of 27th Australian Conference on Optical Fibre Technology, Sydney, Australia, Photonics Institute Pty Ltd, The Institution of Engineers Australia, pp. 32-34, 2002.

A39. Groothoff, N., Canning, J., Buckley, E., Lyytikäinen, K., and Zagari, J., "Gratings in Air-Silica Structured Fibres," Proceedings of 27th Australian Conference on Optical Fibre Technology, Sydney, Australia, Photonics Institute Pty Ltd, The Institution of Engineers Australia, pp. 84-85, 2002.

A40. Town, G., Funaba, T., Ryan, T., and Lyytikäinen, K., "Optical continuum generation with nanosecond pump pulse in an irregularly microstructured optical," Proceedings of 27th Australian Conference on Optical Fibre Technology, Sydney, Australia, Photonics Institute Pty Ltd, The Institution of Engineers Australia, pp. 84-85, 2002.

A41. Ryan, T., Canning, J., Kristensen, M., and Lyytikäinen, K., "Multiple-core air-silica structure optical fibre," Proceedings of Optoelectronics and Communications Conference OECC'2000, Chiba, Japan, 2000.

ACRONYMS

AFM	atomic force microscopy
ASOF	application specific optical fibres
BHF	buffered HF
BSE	back-scattered electron
CRN	continuous random network
CT	computer tomography
DCF	dispersion-compensating fibre
EDFA	erbium-doped fibre amplifier
EDS	energy dispersive spectrometry
EELS	electron energy loss spectroscopy
EMU	Electron Microscope Unit
EPMA	electron probe microanalyser
ESI	equivalent step-index
FBG	fibre Bragg gratings
FEG	field emission guns
FFP	far-field profile
FIB	focused ion beam
FIC	flow indicator and controller
ID	inner diameter
MCVD	modified chemical vapour deposition
MFD	mode-field diameter
MM	multimode
MPOF	microstructured polymer optical fibre
NA	numerical aperture
NFP	near-field profile
NZ-DSF	nonzero-dispersion-shifted fibres
OD	outer diameter
OFTC	Optical Fibre Technology Centre, University of Sydney
OVD	outside vapour deposition
PBG	photonic band gap
PCF	photonic crystal fibre
PCS	plastic-clad silica

PCVD	plasma chemical vapour deposition
PIC	pressure indicator and controller
PID	proportional-integral and derivative
PIPS	precision ion polishing system
PMD	polarisation mode dispersion
PMMA	polymethylmethacrylate
POF	polymer optical fibre
RI	refractive index
RIP	refractive index profile
RNF	refracted near-field
SD	standard deviation
SE	secondary electron
SEM	scanning electron microscopy
SIMS	secondary ion mass spectrometry
SM	single-mode
STEM	scanning transmission electron microscope
TEC	thermally expanded core
TEM	transmission electron microscopy
TIR	total internal reflection
VAD	vapour-phase axial deposition
WDM	wavelength division multiplexing
WDS	wavelength dispersive spectrometer
ZDF	zero-dispersion-shifted fibres

NOMENCLATURE

A	Area, m^2
C	Concentration, mol%
C_i	Concentration of species i, mol%
D	Diameter, m or diffusion coefficient, m^2/s
D_0	Pre-exponential diffusion term, m^2/s
E	Activation energy, J/mol or emissivity matrix (AIII)
F	Force, N or view factor matrix (AIII)
G	Gebhardt factor
H	Internal heat generation, J/m^3s or visibility function (AIII)
J	Diffusion flux, mol/m^2s
K	Equilibrium constant
L	Length, m
N	Number of layers
M	Total amount of substance, mol
R	Gas constant, J/molK
S	Surface area, m^2 or sensitivity factor
T	Temperature, K or °C
V	Normalized frequency (Ch1) or velocity, m/s
a	Scaling factor
a_i	Constant (AIII), i=1-4
b	Constant (AIII)
c	Concentration, mol/m^3 or constant (AIII)
c_p	Specific heat capacity, J/kgK
d	Diameter, m
f	Function
g	Acceleration of gravity, m/s^2
h	Heat transfer coefficient W/m^2K, or thickness (S4.1.2), m
k	Heat conductivity, W/mK
k_j	Reaction rate constant, j=reaction number
n	Normal to the surface or refractive index or reaction order
p	Pressure, Pa

p_0	Pressure difference between hole and atmosphere, Pa
q	Heat flux, W/m^2
r	Radial coordinate, radius, m
r_{etch}	Etching reaction rate, mol/m^2s
r_{ID}	Initial tube inner radius, m
t	Time, s or thickness, m
v	Velocity, m/s
x	Spatial coordinate, m
y	Spatial coordinate, m
z	Axial coordinate, m or length, m

Greek symbols

Δ	Relative index difference
Λ	Pitch, m
α	Absorption coefficient, m^{-1}
β	Angle
ε	Emissivity
ε'	Constant involving emissivity (S5.1)
ϕ_c	Critical angle
η	Kinematic viscosity, m^2/s
λ	Wavelength, m
μ	Dynamic viscosity, Pas
θ	Angle
ρ	Density, kg/m^3
σ	Stefan-Boltzmann constant
ξ	Surface tension, N/m

Subscripts

0	Initial
1	Inner (S.5.1)
2	Outer (S5.1)
a	Ambient
c	Conduction

e	External fluid
ext	External
f	Fibre or fictive (S4.1.1)
g	Gravity or glass transition (S4.1.1)
I	Inertia
i	Surface participating in radiation
k	Surface participating in radiation
p	Preform
r	Radiation
T	Tension
ξ	Surface tension

CHAPTER 1 INTRODUCTION

1.1 Optical fibres in telecommunications

Optical fibres were proposed for telecommunication transmission nearly four decades ago by Kao and Hockham [1]. Although glass fibres had been used for other purposes as early as the 19th century, it was not until the 1970s when optical fibre with loss less than 20dB/km was demonstrated [2] that intensive research began in the development of silica optical fibres in various research laboratories around the world. The adoption of chemical vapour deposition techniques, used in the semiconductor industry, for optical fibre manufacturing further reduced the transmission losses and significant improvements in fibre strength were achieved. Research was driven by the demand for increased long-distance capacity in telecommunications. The move to use single-mode fibre and the shift to a longer operating wavelength (1550nm) in the 1980s made greater bandwidth, longer system spans available and enabled significantly higher bit-rates. The first transatlantic cable system using optical fibres, TAT-8, was deployed in 1988 [3, 4].

The invention of the erbium-doped fibre amplifier (EDFA) in 1987 [5] facilitated a significant advancement in optical fibre communication systems. EDFAs enabled considerably longer repeater spacing and overcame the bit-rate limitation of electronic regeneration. These advantages ensured the rapid incorporation of EDFAs into operating systems in just three years [4]. The 1990s saw an ever-increasing market demand for bandwidth driven by the introduction of the internet and applications such as digital television, streaming video and multi-media on-demand products. Progress in photonic components such as EDFAs and fibre Bragg gratings (FBG) made possible the launch of wavelength division multiplexing (WDM) technology that uses many high-speed channels carried by different wavelengths and enabled a dramatic increase in fibre capacity and even larger amplifier spacing. These advances have resulted in optical fibre becoming the main information transmission medium for large bandwidth applications.

1.2 Application specific optical fibres

Erbium-doped fibre is a prime example of how functionality can be added to optical fibres. In addition to optically active ions in silica glass, functionality can be added by varying the constituents and dopant concentrations to create complex and/or asymmetric refractive index profiles and stress structures. These fibres that are modified for specific applications from the simple structure used in standard long-haul fibres are called Application Specific Optical Fibres (ASOF) or simply, specialty fibres. Specialty fibres have played an important role in the advances in telecommunication technologies. As longer transmission lengths and higher powers were used, non-linear effects became an issue and fibres with modified dispersion properties had to be developed. To realise the use of WDM systems, sophisticated components that used, for example FBGs, were required involving special photosensitive fibres. Speciality fibres are also used in couplers, lasers, filters and in pigtailing.

Over the last decade the focus of development and innovation has shifted largely to ASOF for fibre devices. Specialty fibres have found their way not only into telecommunications applications but also in various other fields such as medical, military and industrial processing (including gyroscopes and lasers). Specialty fibres are used for example in temperature, stress and strain sensors as well as in imaging systems. New designs of optical fibres are constantly developed to improve the existing fibres or to develop fibres for novel applications. The past seven years have seen intense research into a new type of optical fibre called Photonic Crystal Fibre (PCF) where the optical fibre structure is greatly modified by the introduction of arrays of holes. Optical properties that are impossible to obtain with conventional specialty fibres can be achieved with these structures and there is potential even to surpass the attenuation limits of standard telecommunications fibre.

1.3 Optical fibre fabrication

The intense research into optical fibres resulted in well-established fabrication methods for standard telecommunication fibres that met the stringent low-loss and high strength requirements. The subsequent research has mainly been towards reducing fabrication costs by producing larger preforms, removing the OH peak and controlling dispersion and PMD (polarisation mode dispersion). In fibre drawing the quest has been to increase the draw speeds without compromising the fibre quality.

Although the specialty fibres are fabricated using similar techniques to those used to manufacture standard telecommunication fibres, an added complexity in the fabrication is created irrespective of the means by which the structure of the fibre has been altered. In addition, in most cases the fibre properties require the structures to be produced to great precision. In order to manufacture these specialty fibres to their tight specifications in a repeatable manner, and in order to realise some of the more complex designs yet to be manufactured, it is of utmost importance to understand the phenomena by which the fabrication steps affect the final optical fibre structures.

1.4 Motivation for the study

This thesis looks at some of the changes produced in optical fibres during the fibre drawing process. Fibre drawing is the final stage in the optical fibre fabrication process. Although post processing such as testing, cabling and packaging are frequently applied, the fibre does not typically experience significant changes in its properties as a result. Fibre drawing is the most important stage after the preform fabrication stage where the optical and geometrical properties of the fibre are determined. As mentioned earlier, fibre drawing for standard telecommunication-type fibres has been optimised in terms of optical properties such as attenuation and physical properties such as geometric control and strength. Specialty fibres are however drawn under very different drawing conditions mainly due to the considerably shorter length requirements and the limitations imposed by the complex fibre structures. Although some fibre properties can be related to the same optimal drawing conditions as standard telecommunication fibre, by no means can it be expected that the optimal drawing conditions are exactly the same for fibres with different structures, dopants and geometry.

Due to high temperatures in the fibre formation process changes in fibre structure and geometry are possible during drawing. Changes in dopant distribution can occur via diffusion or viscous flow. This results in change of the fibre refractive index profile that determines the optical properties of the fibre. In standard telecommunication fibres the dopant concentrations are small and cross-sectional profiles are symmetric making the minimisation of profile changes relatively easy. In specialty fibres however, some fibre designs have non-circular cross-sectional symmetry. Many specialty fibre designs also have very high dopant concentrations and multiple dopants are frequently used. These

structures are more vulnerable to dopant distribution changes during the fibre drawing process.

There are very few studies published on dopant diffusion during drawing. Although germanium was qualitatively reported to diffuse during drawing by Hersener *et al* in 1984 [6] a more recent study by Pugh *et al* in 1993 [7-9] specifically concluded that no such diffusion was observed. Germanium diffusion induced in optical fibres by various heat treatments has been measured in a number of studies but considerable scatter in the results was found in a literature survey (see Chapter 4, Section 4.1.3.1, p88). As germanium is the most common dopant used in specialty fibres for increasing the refractive index of silica it was chosen in this thesis as the focus of study in dopant diffusion during drawing. Another dopant, namely fluorine, was also considered in this study. Fluorine is frequently used in optical fibres to reduce the refractive index of silica. Unlike the results for germanium, the literature is relatively consistent with regard to the reported diffusion coefficient of fluorine (see Chapter 4, Section 4.1.3.3, p92). However no studies of fluorine diffusion during fibre drawing were found in the literature. This thesis presents a qualitative study of fluorine diffusion during fibre drawing.

It is surprising how few studies can be found on the fabrication of photonic crystal fibres. This can perhaps partly be accounted for by the secrecy characteristic of the optical fibre fabrication industry. In addition to this a trial and error type approach is common when novel structures are fabricated for the first time and it is likely that not all aspects of the fabrication of PCFs have yet been looked at in detail. The inclusion of air structures in silica imposes a new challenge for the drawing process and entails an additional control target, namely the numerous internal air-silica interfaces absent in solid fibres. Numerous studies of PCFs which report on the fascinating optical properties of these fibres imply that the fibre drawing step is crucial for obtaining a suitable geometry and some important draw parameters are listed but no further elaboration on the fabrication aspects are given. A theoretical study has been published by Fitt *et al* [10, 11] on draw parameter effects on fibre capillaries and some experimental results are given for a simple structure with one hole. A purely theoretical study on PCF drawing has also been published by Deflandre [12] who does take into account the complex geometry of the fibre, however no supporting experimental results

are given. The objective of the present study is to look at the geometry control of PCFs during the fibre drawing stage including some aspects relating to preform fabrication. An experimental approach is chosen and the effects of all draw variables are studied with specific focus on control of the PCF hole structure.

Both the dopant diffusion study and the study of geometry control of PCFs during drawing require detailed knowledge on the physical aspects of the fibre drawing process. Elaborate heat and mass transfer studies have been conducted to optimise the standard telecommunication fibre drawing process. Some of the studies date back to the early days of optical fibre research in the late 1960s and 1970s [13-16]. The latest studies have taken full advantage of the computing power available today and all the aspects of heat and mass transfer have been incorporated into these studies [17-21]. These sophisticated models however tend to assume a simple structure for the preform and fibre, an assumption which is valid for standard telecommunications fibres. Specialty fibres however, often have structures with high dopant concentration modifying the thermal properties of the glass and asymmetric and complex internal geometries. More drastic changes are expected for heat transfer in PCFs arising from the effects of the hole structure. In addition to solid fibre drawing the effects of air structures are studied in this thesis using numerical methods.

The aim of the research project is to gain profound insight into the behaviour of complex fibre structures during the final fibre fabrication step, fibre drawing. Germanium and fluorine diffusion during drawing has been studied experimentally and a numerical analysis of the effects of various draw parameters on diffusion has been performed. Specific questions addressed include whether dopant diffusion can be induced during drawing, at what stage of the drawing the diffusion occurs and what are the effects of the various drawing parameters on diffusion. A detailed experimental study of geometry control of photonic crystal fibres during drawing has been conducted with particular emphasis given to the control of hole size. The effects of the various drawing parameters and their suitability for controlling the air-structure have been studied. The effect of air structures on the heat transfer in PCF structures is looked at using computational fluid dynamics techniques. Special attention is given to providing results that are reliable and applicable for a wide range of fibres and draw conditions and in some cases not limited to silica fibres.

1.5 Outline of the thesis

The structure of this thesis is shown in the diagram in Figure 1-1. Chapter 2 provides a background relating to optical fibres and their fabrication. Chapter 3 describes the methods used in the experimental studies, including fibre designs used and their fabrication and describes the various techniques used for preform and fibre measurements. Chapters 4 to 6 present the results. Experimental dopant diffusion results are given in Chapter 4. Chapter 5 presents the experimental results of geometry control of photonic crystal fibres. Heat and mass transfer simulations are presented in Chapter 6 including dopant diffusion during drawing and the effect of air structures in PCF structures. Conclusions are presented in Chapter 7.

Due to the complex nature of this study the various chapters are interdependent. Significant improvements in the analysis techniques were implemented during the course of the diffusion study. Consequently some repetition is necessary to give a clear and logical flow of thought in the text. Some of the diffusion results are repeated in the methods chapter, Chapter 3, and some of the methods are discussed in Chapter 4 when diffusion results are presented. As both experimental and theoretical studies have been conducted, some of the experimental results are discussed in Chapter 6, where theoretical heat and mass transfer computations are presented. The same applies to the experimental results of PCF fabrication. Great effort was taken to cohesively present these studies together, however due to the very different nature of the phenomena characterising the fabrication issues this was sometimes found very challenging. To improve readability a detailed background and literature review are provided at the beginning of each of chapters 4, 5 and 6.

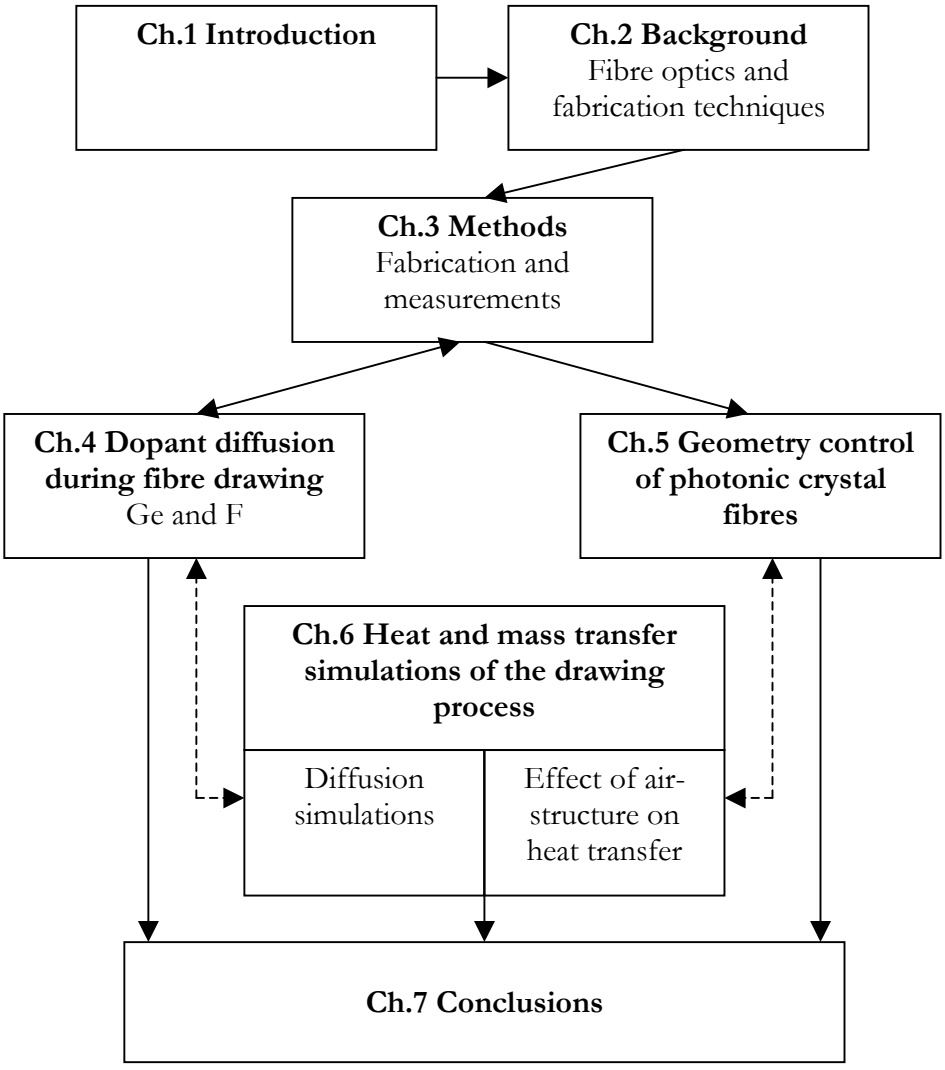

Figure 1-1. Diagram of the structure of the thesis.

CHAPTER 2 BACKGROUND

2.1 Principles of fibre optics

In its simplest form optical fibre structure consists of a core and a cladding as shown in Figure 2-1. The light propagates in the core when the core material has higher refractive index (n_{core}) than that of the cladding ($n_{cladding}$). When light travelling in a higher refractive index impinges on the interface with a lower refractive index medium at an angle greater than a critical angle it is totally reflected. This is called total internal reflection (TIR). The critical angle ϕ_c is defined as $\sin\phi_c = n_{cladding} / n_{core}$.

A light wave has certain paths it can follow down an optical fibre, which are called modes. More specifically, modes are permitted solutions to Maxwell's equations. Depending on its refractive index profile (RIP), the number of possible modes that can be supported by the fibre varies from one to more than a hundred thousand. Optical fibres can be divided into two categories: multimode and single-mode fibres, according to the number of modes they can propagate. Multimode fibres typically have a large core whereas single-mode fibre cores are small (typically around 10μm or less in diameter) allowing only the fundamental mode to be guided in the structure. Figure 2-2 shows typical RIPs for some fibres used in telecommunication applications. The refractive index is not necessarily constant in the core (step index) as presented in Figure 2-1 (a), but may be intentionally varied along the radius of the fibre to alter its optical properties. More complex RIPs are discussed in Section 2.2 in relation to application specific optical fibres.

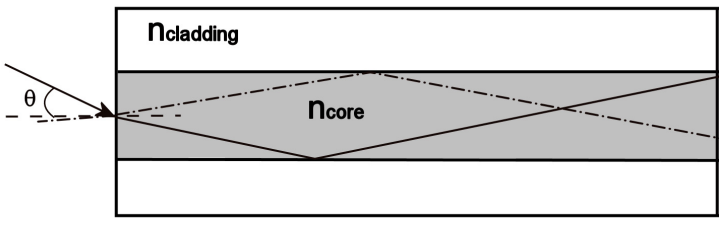

Figure 2-1. Diagram of the refraction of light entering a step-index fibre and total reflection within the fibre. θ is defined in Eq. (1).

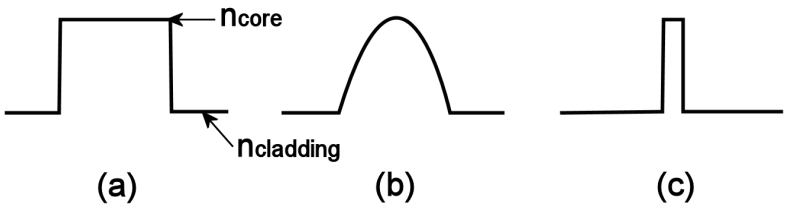

Figure 2-2. Graphical presentation of the three different types of RIPs in the core of the fibre; (a) multi-mode step index, (b) multi-mode graded index and (c) single-mode step index.

A basic parameter that characterises optical fibres is numerical aperture (*NA*). It is related to the refractive indices of the core and the cladding and for multimode fibres is the sin of the maximum angle at which light entering the end of the fibre will be propagated within the core, see also Figure 2-1.

$$NA = \sin\theta = \sqrt{n_{core}^2 - n_{cladding}^2} \qquad (1)$$

The relative core-cladding index difference, $\Delta = (n_{core}\text{-}n_{cladding})/n_{core}$, is also commonly used to characterise the RIP. The number of modes than can propagate is related to a dimensionless quantity *V* called the normalized frequency:

$$V = \frac{2\pi r}{\lambda} NA, \qquad (2)$$

where λ is the wavelength of light in vacuum and *r* is the core radius. When *V* is less than 2.405 for a step-index profile, the fibre is single-moded.

Optical fibres can be made of a variety of transparent materials. Various glasses such as chalcogenides and fluorides can be used as waveguide materials as well as polymers such as PMMA (polymethylmethacrylate). Silica glass is however the most widely used material due to the practical realisation of fibres exhibiting low optical loss (<0.2dB/km) and high information transmission capacity. Silica fibres also have high tensile strength and fabrication technology is available to realise high capacity production and so relatively low costs. Polymer optical fibres (POF) and composite plastic and glass fibres (plastic-clad silica PCS) typically exhibit much higher losses and

so are generally used for short distance data links or non-telecommunications applications. Fluoride and chalcogenide glass fibres may be used where transmission at longer wavelengths is required or as hosts for rare earths in optically active fibres.

In silica fibres the refractive index is modified by incorporating dopants such as germanium, fluorine, phosphorus, boron and aluminium. Ge, P and Al increase the refractive index whereas F and B decrease it. In a typical single-mode (SM) fibre design the core is doped with 3 - 7mol% of GeO_2 to give Δ = 0.3 - 0.7% [22]. As part of the power of the propagating mode lies in the cladding, the purity of the cladding is also very important. Depending on the manufacturing technique and desired refractive index of the cladding, a number of cladding compositions are typically used. Cladding can be composed of pure SiO_2 or SiO_2 doped with either F or P or both. P_2O_5 is typically included to lower the viscosity of the glass due to fabrication limitations. When matched cladding index is required, F is used to compensate for the increased index due to P. More details are given in [23].

2.2 Application specific and specialty optical fibres

Application specific optical fibres known also as specialty fibres typically have more complicated structures than those used for long-haul transmission. The structures are modified for example by introducing new dopants or by changing the geometry of the core or cladding or by introducing additional regions such as doped rings to the structure. The structure is modified in order to tailor specific optical properties or add functionality as required by the application. Some of the more common specialty fibres are briefly discussed below to give an idea as to the variety of designs that exist.

2.2.1 Fibres for dispersion management

Dispersion is an optical property, which causes a broadening of a propagating pulse with respect to time. In single-mode fibres the main source of the broadening is chromatic dispersion. The broadening is a result of the different spectral components of the pulse travelling at different speeds. Chromatic dispersion arises from two sources (i) material dispersion and (ii) waveguide dispersion. Material dispersion is due to the material refractive index variation with wavelength. Waveguide dispersion results from the changes in the power confinement of the mode as the core and the cladding have

different wavelength-velocity relationship. The total chromatic dispersion is the sum of the material and waveguide dispersion, see Figure 2-3 (a).

Pulse broadening can be prevented, or compensated for by modifying the fibre design. Such fibres are typically called dispersion-compensating fibres (DCF), zero- and nonzero-dispersion-shifted fibres (ZDF, NZ-DSF) and dispersion-flattened fibres. In these fibres the RIP has been modified to alter the waveguide induced component of the dispersion, resulting in specific dispersion characteristics. Figure 2-3 (b) shows examples of dispersion curves of the dispersion-shifted and dispersion-flattened fibre. Figure 2-4 shows the corresponding refractive index profiles.

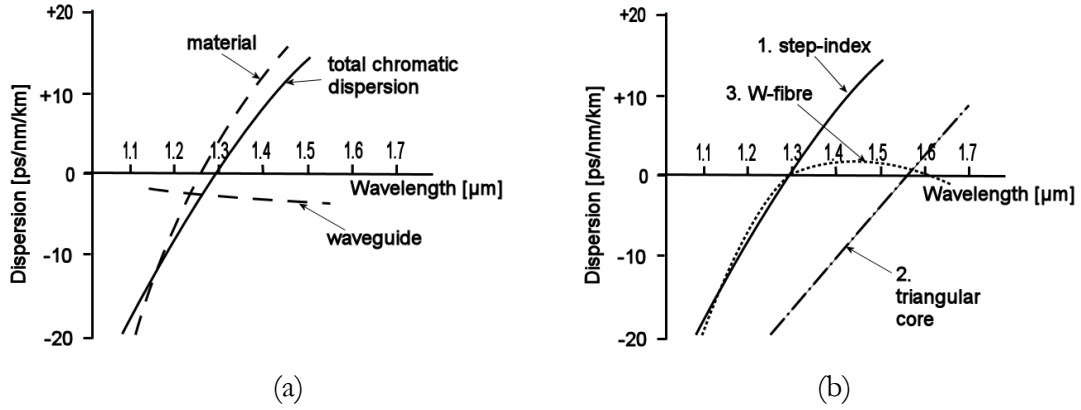

Figure 2-3. (a) Chromatic dispersion of a typical step-index single-mode fibre. Material and waveguide dispersion components shown as dashed lines. (b) Waveguide dispersion of 1. Step-index, 2. dispersion-shifted triangular core and 3. dispersion flattened W-fibre.

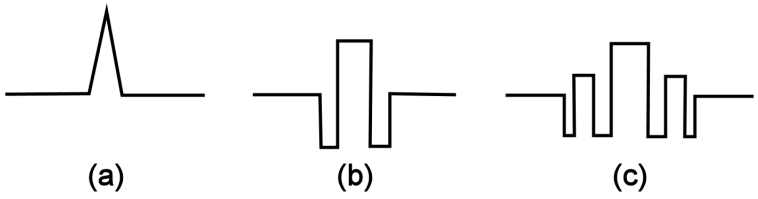

Figure 2-4. RIP designs of fibre cores for dispersion management; (a) dispersion-shifted triangular core, (b) dispersion-flattened double-clad fibre (W-fibre) and (c) dispersion-flattened quadruple-clad (QD) fibre [22].

2.2.2 Highly-birefringent fibres

Some applications require fibres that maintain the polarisation state of the light which it is guiding. Such fibres are typically called polarisation maintaining, polarisation-preserving or highly-birefringent fibres. These fibres are designed to introduce a large amount of birefringence that makes the fibre insensitive to small birefringent fluctuations typically present in fibres due to inhomogeneities in the geometry or mechanical perturbation. More specifically, they are designed with high birefringence to break the degeneracy of the fundamental mode and hence minimise any coupling between the two polarisations of the fundamental mode by giving them different propagation velocities. Birefringence can be introduced for example by making the core elliptical or by introducing stress-inducing elements on opposite sides of the core. Boron is typically used as the dopant for the stress inducing parts. The designs are called for example PANDA, bow-tie and 'elliptical clad' (or Tiger) fibre according to the shape of the stress-inducing regions, see Figure 2-5. The boron doping level is typically around 20mol% (depending upon the required birefringence) and the fibre cores are doped with germanium.

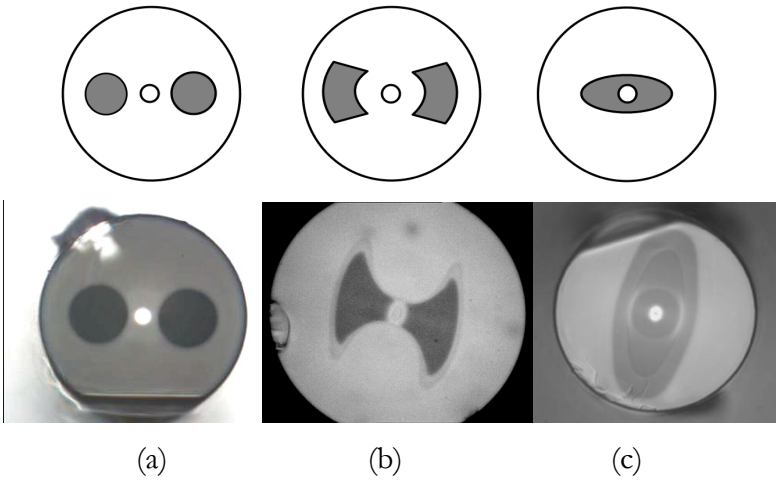

Figure 2-5. (a) PANDA and (b) bow-tie and (c) elliptical clad fibre. Photos of fibre (a) and (c) are courtesy of Nufern Ltd. Fibre (b) was fabricated at OFTC.

2.2.3 Photosensitive fibres

Photosensitive fibres, as the name indicates, are fibres that have been modified to enhance the photosensitivity[1] of the structure. Such fibres can be used to fabricate Bragg fibre gratings that have a multitude of applications in telecommunications. Gratings specifically play a role in WDM enabling components, amplifiers and fibre lasers. Gratings are also used in temperature, stress and strain sensors. More details are given in [24].

Germanium doped fibres have been found to be most suitable as photosensitive fibres. Photosensitivity is believed to result from formation of colour centres GeE' (GeO defects), densification, stress and the formation of GeH centres. Typically, higher Ge content results in greater photosensitivity. Germanium-boron co-doped fibres are the most common fibres employed. Boron provides an electron trap that stabilises the photoreactive change. Large amounts of germanium can also be incorporated whilst keeping the refractive index compatible to standard SM specifications by codoping with B. Figure 2-6 shows an example of the composition of boron co-doped fibre. Photosensitive regions can also be placed into other parts of the fibre if required. Tin codoped fibres can also be used and have some advantages over Ge-B codoped such as thermal stability and no additional loss related to B doping [24].

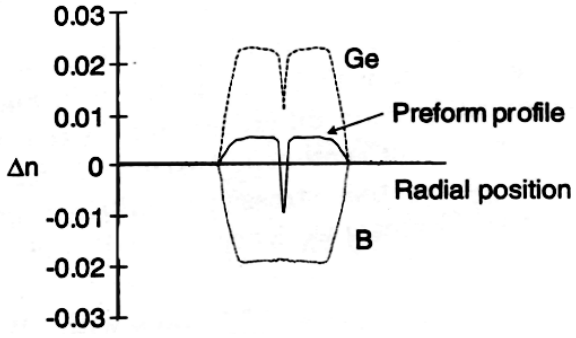

Figure 2-6. Refractive index components due to Ge and B contributing to the resultant RIP [24].

[1] Photo-induced change in refractive index due to exposure to UV-radiation.

2.2.4 Rare-earth doped fibres

The functionality of optical fibre can be enhanced by introducing optically active elements such as lanthanides. When these ions are optically excited with irradiation of an appropriate wavelength they act as a lasing or amplifying medium through stimulated emission. Fibre amplifiers are used to overcome transmission losses and restore the signal intensity in communication systems. The erbium-doped fibre amplifier is particularly interesting because it provides gain in the wavelength range typically used in fibre communication networks. By using suitable lanthanide-ion doped fibres, lasers can be made which operate over a wide range of wavelengths extending from 0.4 to 4μm (though silica transparency is a problem beyond 2μm). In addition to erbium, other lanthanides typically used in fibre lasers and amplifiers include neodymium, thulium, ytterbium, holmium and praseodymium.

Although the lasing properties are determined by the selection of the lanthanide ion and its concentration, the design of the silica fibre acting as a host to the ions is important to optimise the optical properties. Figure 2-7 shows an example of dopant distribution in an erbium-doped fibre preform. Rare-earth doped fibres typically use germanium to increase the refractive index of the core. Aluminium is often used as it increases the solubility of rare-earth ions in the silica matrix and prevents clustering [25]. Phosphorus can also be used to alter the silica structure and accommodate the lanthanide ions [25]. There are two major classes of fibre laser – core pumped and cladding pumped. The cladding in the cladding pumped fibres is commonly made non-circular to improve performance. Also novel structures such as air-clad structures are introduced into the fibre, acting as a low index cladding, enabling the use of higher optical pump powers [26].

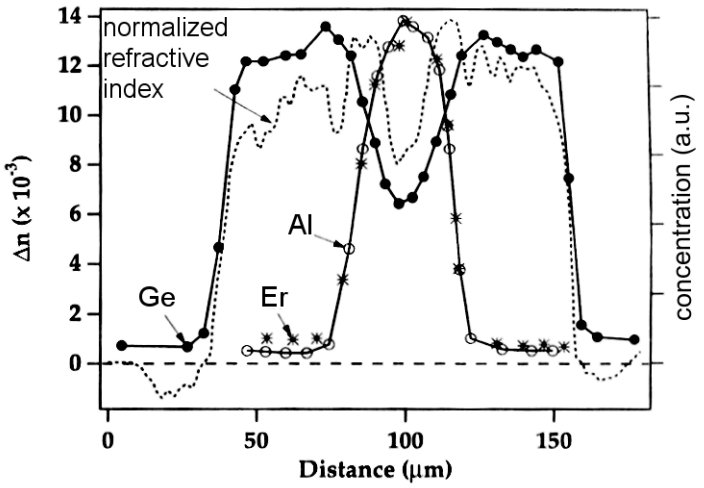

Figure 2-7. Distribution of Er, Ge and Al and RIP for an erbium-doped fibre preform [25]. (a.u. arbitrary units)

2.2.5 Photonic crystal fibres

The first air-silica structured claddings in optical fibres were introduced by Kaiser and Astle [27] in 1974. Their fibre consisted of pure silica with a solid core surrounded by an air-structured cladding. In the mid 1990s a new interest arose in using air structures in optical fibres when Birks *et al* [28] introduced Photonic Band Gap (PBG) fibres which used a highly periodic 2D lattice structure that would enable guidance of light in a lower refractive index core such as air via the band gap effect. The fibre was called photonic crystal fibre or PBG fibre. Although guidance in a hollow-core was not demonstrated until 1999, by Cregan *et al* [29], Russell and co-workers successfully fabricated fibre with air-structured cladding which used a solid core [30, 31]. These fibres did not exhibit PBG guidance, but light was guided by a so called modified total internal reflection and demonstrated a number of interesting phenomena such as endlessly single-mode behaviour, anomalous dispersion, high-nonlinearity and high birefringence [32]. These fibres are typically called 'index-guiding' fibres to differentiate them from PBG fibres. Both PBG and index-guiding fibres are frequently called PCFs but other names such as holey fibre [33], microstructured fibre [34], air-silica structured fibre [35] and Fresnel fibre [36] have been used. In this thesis PCF is chosen due to its wide use in the recently established industry.

The air-structure in the cladding of the PCF consists of an arrangement of small air holes running through the entire length of the fibre. Typically a periodical arrangement

of holes is used although it is not always necessary. The core can be solid or hollow depending on the type of PCF. PCFs are commonly made of silica, but polymers [37-39] and soft glasses [40] can also be used. The index-guiding PCFs have a solid core surrounded by the air-structure. An hexagonal close-packed array of holes is often used, as shown in Figure 2-8 (a). The guidance of these fibres has been compared to the conventional step-index fibre, where the air-structure represents a low refractive index cladding. Depending on the cladding air fraction, relative size of the holes and wavelength, an effective index can be computed for the cladding and some useful properties such as bending losses and dispersion properties can be qualitatively studied. For quantitative analysis the full vectorial nature of the electromagnetic waves must be taken into account.

One of the most intriguing properties of these fibres is that they can be made to be 'endlessly' single-moded. Whereas conventional fibres exhibit a cut-off wavelength below which they support more than a single mode, PCFs can be made to be single-moded over a large wavelength range [31]. This allows structures with ten times larger cores compared to conventional fibres to be single-moded [41] enabling, for example the delivery of high optical power. This property can be partly explained with the effective-index model by the wavelength dependent cladding mode refractive index where the effective cladding index increases with decreasing wavelength making the fibre single moded even at lower wavelengths [30]. A more accurate way of looking at this is that the higher order modes have a smaller transverse effective wavelength and will leak out along the silica bridges between the holes [32]. If these bridges are small enough the higher order modes are retained in the core and the fibre becomes multimoded.

Another interesting feature of PCFs is anomalous dispersion. With high air-fraction and small core design the wavelength of zero dispersion can be shifted to the visible end of the optical spectrum while keeping the fibre single-moded [42]. A number of interesting dispersion properties of PCFs have been reported in the literature [33, 42-46]. Unusual dispersion properties can be used for example in supercontinuum generation and soliton formation [47, 48]. Birefringence ten times larger than in conventional polarisation maintaining fibres can be induced in PCFs [49, 50].

The optical properties of these fibres are determined by the cladding air-structure and the core size. Typical geometric parameters defining the properties are hole diameter, d, centre-to-centre distance between neighbouring holes (pitch), Λ, number of rings, the air-fraction represented by d/Λ and the hole arrangement. Figure 2-8 (a) shows some of these parameters for fibre with an hexagonal arrangement of holes. For example these structures are single-moded when $d/\Lambda<0.4$ [51, 52]. In order to have useful optical properties the fibres do not always require absolute uniformity or order of the structure [53], although to realise low losses this is highly desirable. The lowest loss reported for an effective index guiding PCF is 0.37dB/km at 1550nm by Tajima *et al* [54].

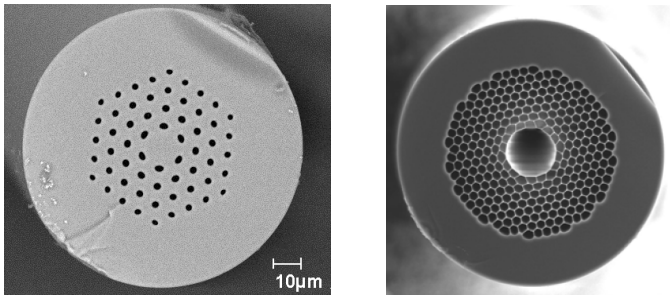

(a) (b)

Figure 2-8. Images of (a) effective index PCF fabricated for this theses and (b) PBG fibre by Mangan *et al* with 20µm hollow core [55].

PBG fibres have a lower refractive index core, such as air. In PBG fibres the air structure is highly periodic on the scale of the optical wavelength and consists of hundreds of holes with a very high air-fraction. When the periodic lattice of holes is appropriately designed, propagation of electromagnetic waves in certain frequency bands may be prohibited [32]. These photonic band gaps are analogous to electronic band gaps in semiconductors. If the hole structure surrounding the central defect (hollow core) is sufficiently regular, then strong confinement of light in the low refractive index core can be achieved. Figure 2-8 (b) shows an example of such fibre. In order to achieve PBG guidance a high degree of periodicity of the structure is essential. It is believed that this sensitivity of the band gap to structural fluctuations is the main obstacle in obtaining low losses [32]. The lowest loss PBG fibre reported to date is 1.72dB/km reported recently by Mangan *et al* [55]. Guidance in a hollow core is attractive because of the theoretical potential for extremely low transmission losses and significantly reduced optical non-linearity. Strong light-matter interactions can also be

achieved if the hollow core is filled with specific gas or liquid making the PBG fibre attractive in sensor applications for example.

2.3 Fibre fabrication

Optical fibre fabrication typically involves two stages; preform fabrication and fibre drawing. A preform is a large-scale replica of the fibre typically 100-1000mm in length and 10-50mm in diameter. (Large capacity manufacturing of long-haul optical fibre typically involves preform sizes of much larger dimensions, however emphasis here is on specialty fibre fabrication.) After fabricating the preform it is drawn down to fibre dimensions in a drawing tower. In most cases it is possible to conserve the relative preform cross-section (RIP) during the fibre drawing.

2.3.1 Preform manufacture

Special vapour deposition techniques have been developed to provide the necessary high purity levels of glass to realise today's low losses (<0.2dB/km) in silica optical fibres. There are currently three major processes used for making silica optical fibre preforms:

1. Modified Chemical Vapour Deposition (MCVD)
2. Outside Vapour Deposition (OVD)
3. Vapour-phase Axial Deposition (VAD)

The techniques are all based on manufacturing synthetic silica by vapour deposition, however the technologies used differ significantly and unique advantages and challenges arise with each process. These are discussed briefly in the following sections giving emphasis to MCVD which is the primary preform fabrication technique used in this thesis.

2.3.1.1 Modified chemical vapour deposition

MCVD is based on oxidation of halides of the required elements in a gas phase to form oxide particles that then deposit onto a substrate surface to form a thin layer of material (layer thickness ranging from a few microns to 100 microns). The substrate surface in MCVD consists of a silica glass tube, called the substrate tube. Deposition occurs on the inner surface of this tube. The preform is fabricated starting with an inner cladding

and finishing with a core by forming glassy layers (between 10 and 100) of pure or doped silica. Upon completion, the tube is collapsed to form a solid rod - the preform. The substrate tube becomes a part of the fibre cladding or can be removed by chemical etching.

Figure 2-9 shows a schematic diagram of the MCVD process. The high-quality silica glass substrate tube is mounted between rotating chucks of a glass-working lathe. An etching pass is typically performed first to improve the inner substrate tube surface. The halide vapours are delivered to the substrate tube by a carrier gas, e.g. oxygen, which is passed through the bubblers that contain the halide in liquid form. The more typically used halide precursors include $SiCl_4$, $GeCl_4$, BCl_3, BBr_3, PCl_3, $POCl_3$, SF_6, CF_4 and CCl_2F_2. The reagent vapours enter the rotating tube while an oxyhydrogen torch slowly traverses in the same direction as the gas flow. As the reagents enter the hot-zone created by the torch they react with oxygen by a homogeneous gas phase reaction to form glassy particles of submicron size. Typical reactions are shown below. [23, 56, 57]

$$SiCl_4(g) + O_2(g) \leftrightarrow SiO_2(s) + 2C1_2(g) \quad (3)$$

$$GeCl_4(g) + O_2(g) \leftrightarrow GeO_2(s) + 2C1_2(g) \quad (4)$$

$$4POCl_3(g) + 3O_2(g) \leftrightarrow 2P_2O_5(s) + 6C1_2(g) \quad (5)$$

$$4BBr_3(g) + 3O_2(g) \leftrightarrow 2B_2O_3(s) + 6Br_2(g) \quad (6)$$

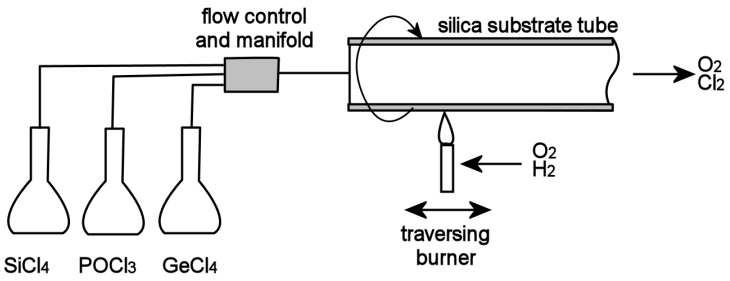

Figure 2-9. MCVD preform manufacturing process.

The particles formed deposit downstream of the torch by thermophoresis. Thermophoresis arises from the thermal gradient. Particles collide with the gas molecules that have different average velocities resulting in a net force in the direction of decreasing temperature. The particles thus deposit on the cooler tube surface downstream of the hot-zone. As the torch moves along, it sinters the individual soot particles into a consolidated glassy layer.

The relative proportion of the halide constituents are adjusted for each pass to provide the desired refractive index profile. The amount of each dopant in the final glass layer depends on the reactant proportions, the gas flow rates and on particle formation, deposition and consolidation [58]. The temperature is generally high enough so that the oxidation reactions Eq. (3)-(6) are not limited by reaction kinetics but by reaction equilibrium [23]. For example $SiCl_4$ (Eq. (3)) reacts almost 100% to form SiO_2 above a specific temperature, however, $GeCl_4$ has a temperature above which the $GeCl_4$ conversion is reduced. Figure 2-10 illustrates the conversion of $SiCl_4$ to SiO_2 and $GeCl_4$ to GeO_2 as a function of temperature. The equilibrium limitation for Eq. (4) means that 100% conversion of $GeCl_4$ is not achieved during the MCVD process. In addition to this the equilibrium shifts towards $GeCl_4$ at high chlorine concentrations, which results from the complete oxidation of $SiCl_4$, further reducing the oxidation efficiency of $GeCl_4$ [57]. Furthermore not all particles formed in the oxidation reactions deposit on the tube wall. Particles below a certain critical size stay in the gas stream and hence reduce the deposition efficiency. The deposition efficiency has been shown to depend on the ratio of the temperature of the gas and the tube wall and the reaction temperature [23]. The gas temperature is affected e.g. by torch speed, ambient temperature and tube wall thickness. The deposition efficiency is particularly low for GeO_2, 40-70% [23, 56-58].

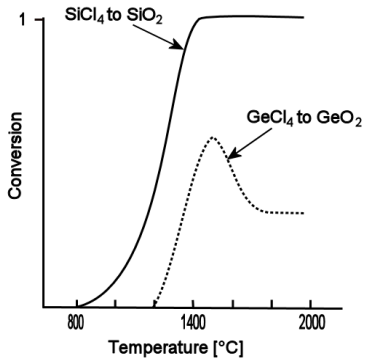

Figure 2-10. Conversion of $SiCl_4$ to SiO_2 and $GeCl_4$ to GeO_2.[2]

After the final core layer is deposited the tube is collapsed into a solid rod by increasing the torch temperature. The surface tension and the increased pressure from the torch [59] cause the tube to collapse. In the collapse stage small amounts of Cl_2 can be used to reduce OH incorporation in the glass. In order to increase the preform size and to improve productivity the core preform can be jacketed with a silica tube using a sleeving technique. Alternatively an OVD process (Section 2.3.1.2) can be used to grow additional cladding layers on to the outside of the preform.

Figure 2-11 shows a typical Ge-doped core single-mode fibre preform RIP with F-P_2O_5-SiO_2 cladding. There are some features that are frequently seen in fibres used in this thesis and are common in MCVD fibres. The layered structure of the MCVD preform is clearly seen in the cladding layers. Note that each layer has a refractive index gradient. These gradients are presumed to be due to different chemical diffusion rates, oxidation reaction equilibrium and particle formation during deposition and sintering. The Ge-doped core has a central refractive index dip characteristic of the MCVD process. At temperatures above about 1600°C the dioxide GeO_2 can be converted to the monoxide GeO according to reaction [58]:

$$GeO_2(s) \leftrightarrow GeO(g) + \tfrac{1}{2}\, O_2(g) \qquad (7)$$

[2] The figure is drawn for illustration purposes only and does not provide quantitative information. The illustration is based on results presented by Wood *et al.* [58].

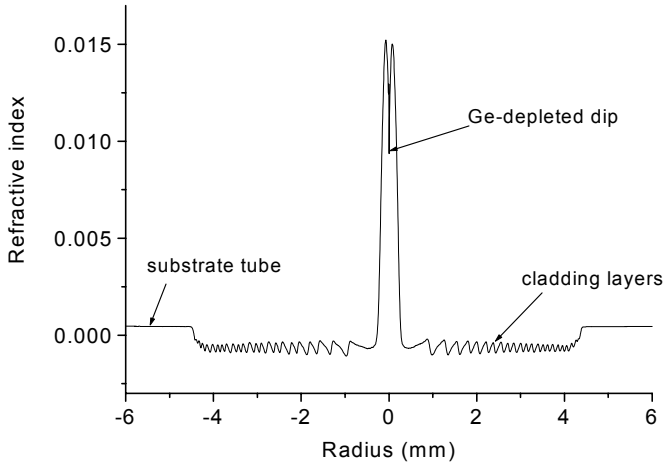

Figure 2-11. A typical single-mode preform RIP showing the layered structure and central Ge-depleted dip.

Due to the high temperatures used in the collapse phase, the above reaction can occur and may cause Ge-depletion from the surface of the innermost layer [56] because of greater volatility of GeO. Ge gradients could also be created due to tube radial temperature gradients where particles formed near the hotter tube wall will have a different GeO_2 concentration (either via equilibrium considerations of Eq. (4) or the reaction in Eq. (7)) [58]. If large soot particles form the Ge gradients would not have time to equalise via Ge diffusion. These particles deposit closer to the torch than the particles formed near the tube centre hence resulting in a Ge gradient across the layer. Typically the central refractive index dip does not cause a significant change in optical properties but can add to increased losses in high concentration single-mode fibres via scattering [60]. If required the central dip can be compensated by using small amounts of $GeCl_4$ during collapse or by removing the depleted area by etching prior to collapse [23].

2.3.1.2 Other deposition techniques

Plasma Chemical Vapour Deposition (PCVD) is similar to MCVD but reaction inside the tube is initiated by a nonisothermal microwave plasma that traverses the length of the tube. Deposition occurs directly on the tube wall and no particulate soot is generated. Reaction and deposition of both GeO_2 and SiO_2 are more efficient than in MCVD, approaching 100%, and very fast traverse speeds can be used to produce hundreds of layers in a relatively short period of time [57].

The Outside Vapour Deposition (OVD) process differs from MCVD in that vapour deposition occurs on the outside surface of the starting or target rod. The preform is thus built from inside to outside by forming soot layers. The chemicals are delivered into the torch where they react to form submicron glassy particles. A porous preform is formed layer by layer. Before consolidation the target rod is removed and the porous preform is placed in a consolidation furnace. The OVD method is preferred in large-scale production because of the relative ease associated with producing large preform diameters.

The Vapour-phase Axial Deposition (VAD) technique is similar to OVD in that vapour deposition occurs outside the starting rod. Differing from the OVD and MCVD processes, the layers grow axially rather than radially. In theory this method allows a continuous process, where a soot preform is grown, consolidated and drawn directly into the fibre. In the process the rod is rotated and the chemical vapours are delivered into the torches, which are placed at the end of the rod. As the soot particles build up, the starting rod moves upwards to make room for new growth. The refractive index profile is adjusted via precise control of the raw material flow, position of the preform tip and its surface temperature. The consolidation occurs in a similar manner as in the OVD process. More details of these deposition techniques can be found in [23].

2.3.1.3 Additional techniques used in specialty fibre fabrication

In the manufacture of specialty optical fibres additional processing steps are sometimes required. In highly-birefringent fibres, the so-called PANDA structure is made by using a rod-in-tube method. A preform with the required core is first fabricated and two holes drilled on opposite sides of the core. Boron-doped rods are then inserted into the holes to create the PANDA structure and the resulting structure is drawn. In fabricating the 'bow-tie' structure, additional burners are used in MCVD to etch parts of the stress-inducing B-doped layers away after which an inner cladding is deposited. Similar techniques can be used to create other complex structures requiring cylindrical asymmetry.

The so-called "rod-in-tube" method can also be used to make rare-earth doped fibres where a rare-earth containing rod is inserted into a tube which is subsequently collapsed

to form a rod. The more commonly used techniques involve either a solution-doping or vapour phase deposition. The solution-doping method involves the deposition of an unsintered porous layer of glass. The porous layer is then impregnated with a solution containing the lanthanide ions. After soaking, the solution is drained and the substrate is dried in a chlorine-oxygen mixture and collapsed into a solid preform. Various solvents can be used e.g. water, ethanol, methanol or acetone. More novel techniques such as chelate deposition [61], aerosol [62] and direct nanoparticle deposition [63] techniques have also been used to incorporate lanthanides into optical fibres.

Photonic crystal fibre preforms are fabricated typically by two methods (i) drilling or (ii) capillary stacking. In the drilling technique the required hole structure is drilled using an ultrasonic-drill in a solid silica rod. In capillary stacking the hole structure is created by stacking silica capillaries and solid rods inside a silica tube to generate a suitable pattern. These techniques are discussed in more detail in Section 3.1.2.

2.3.2 Fibre drawing

To produce the final fibre, the preform is drawn down in a draw tower. Typical optical fibre diameter is 125μm but specialty fibre diameters can range from 40μm to 2000μm. Figure 2-12 shows a schematic diagram of the fibre drawing process. The preform is fed vertically into a furnace, which is heated above the glass-softening temperature about 2000°C. As the glass softens a neck-down forms due to gravity and the pulling force. The pulling force is provided by a capstan, the speed of which is controlled to maintain constant fibre diameter.

2.3.2.1 Preform feed unit

The preform is mounted in a holding chuck attached to a preform feed mechanism that lowers the preform into a furnace. The preform feed rate, V_f, depends on the preform diameter, D_p, the fibre diameter, D_f, and the drawing speed, V_f, according to the conservation of mass (assuming constant density).

$$V_p = \frac{D_f^2 V_f}{D_p^2} \tag{8}$$

Typically the preform feed rate is held constant and draw speed used to control the fibre diameter due to the much faster response.

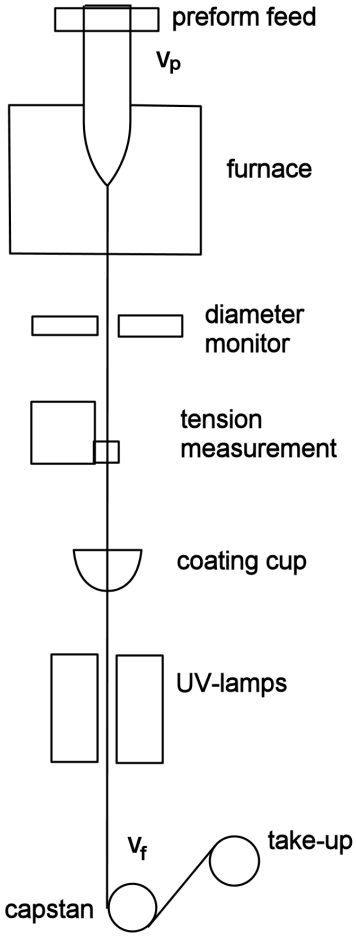

Figure 2-12. Schematic diagram of optical fibre drawing process

2.3.2.2 Drawing furnace

A variety of methods can be used to heat the preform to its "draw temperature" (1900-2200°C). As turbulence around the fibre causes unacceptably large variations in the fibre diameter, the furnace must provide laminar ambient gas flow and must also be clean, i.e. give off no particles that might impinge on the preform and degrade fibre strength. The most common furnaces used that meet these requirements are graphite resistance and induction furnaces, and zirconia induction furnaces. The advantage of the induction furnace is its compact size compared to resistance furnaces. Zirconia furnace elements emit fewer contaminating particles than graphite elements, but have more stringent operating procedures due to the large volume change when cooled below 1600°C.

Furnaces with graphite elements must use an inert gas, such as argon or nitrogen, during operation to prevent oxidising the element and hence increasing the particle contamination and reducing element lifetime. Several gas inlets are provided to give either resultant upflow or downflow of the gases. The furnace top and bottom irises are carefully adjusted, together with the inert gas flow to provide laminar flow of a sufficient quantity to maximize fibre strength and minimize diameter variations characteristic of turbulent gas flows. Furnace temperature is measured with an optical pyrometer from either the outer surface of the heating element or directly from the preform neck-down depending on the furnace set-up, the former being the more typical configuration. The temperature can be controlled to within 1°C, but it must be remembered that it does not necessarily coincide with the preform temperature. Fibre tension can be used to gauge the neck-down temperature. Fibre tension depends on the viscosity of the glass and hence will give a more accurate indication of the neck-down draw condition. Repeatability in fibre quality is improved by keeping the tension constant from draw to draw. On-line control of fibre tension can also be set-up while furnace temperature and/or preform feed rate can be used to alter the neck-down temperature.

2.3.2.3 Diameter control

In order to maintain a uniform fibre diameter, the drawing process includes a diameter control loop. The fibre diameter is monitored as it exits the furnace. The output signal from the diameter monitor is used to automatically adjust the speed of the drawing capstan using a PID controller to obtain the correct diameter. The diameter control is essential to minimize the effect of fibre diameter fluctuations on such properties as microbending sensitivity and splicing loss. Fibre diameter is usually specified as 125±1μm but even better control is routinely possible. Low frequency variation in the average fibre diameter can result from changes in preform diameter, drift in furnace temperature and the preform feed rate. This is minimised using PID control. Diameter variations with shorter period typically arise from perturbations in the neck-down region caused by thermal fluctuations of the furnace atmosphere, such as fluctuations in inert gas flows and acoustic and mechanical vibrations [57].

2.3.2.4 Coating

Before the fibre reaches the capstan it is coated with a protective polymer. Coating is required to protect the surface from abrasions and preserve the intrinsic strength of the silica by providing a barrier to moisture. The coating usually consists of two layers of acrylate, a softer inner layer and a harder outer layer. Acrylate is applied in a liquid state and is solidified by UV-curing. To provide other functionalities special coatings such as hermetic coatings or thermally curable coatings may be used. The final diameter of the fibre with coating is typically around 250μm. It is necessary that the fibre be cooled (<80°C) prior to coating. Between the furnace and the coater the fibre is cooled down by the surrounding air. At high speeds and with limited tower height it may be necessary to use forced cooling. Helium is often used for this purpose due to its improved heat transfer properties in specifically designed cooling tubes that enhance turbulence to remove heat more efficiently. After coating the fibre passes over a capstan onto a fibre take-up that winds the fibre onto a spool. Prior to coating, the fibre surface is exposed to potential contamination that will reduce the fibre strength. The fibres are therefore drawn in a clean room environment. Class 100 (see footnote[3]) is typically sufficient to provide the required high strength fibre.

2.3.2.5 Post-processing

After the drawing process fibres are proof-tested at a given stress level to minimise failure during the subsequent post-processes or fibre usage. Standard proof-test force is $0.7GN/m^2$ (100kpsi). During the proof testing the weak points of the fibre are removed ensuring a minimum tensile strength for the remaining fibre. The fibre is then characterised with regard to its optical properties. Depending on the fibre application the finished fibres can be coloured, made into ribbons and/or cabled or processed into optical device.

2.3.2.6 Draw-effects

The optical properties of the fibre are predominantly determined by the preform composition and structure and so the preform fabrication is the key process to optimise. The fibre drawing process can however modify the pattern laid down in the

[3] There exist no more than 100 particles larger than 0.5 microns in any given cubic foot of air.

preform and affect the final properties of the fibre. In the past the main effects studied include drawing effects on transmission losses and fibre strength [23]. Since the preform is drawn at very high temperatures followed by rapid cooling, modification to the glass structure is possible. It has been shown that defects such as E^I centres in silica and Ge-E^I centres in Ge-doped fibres, can result from the fibre drawing process [64-66]. These defects cause increased absorption losses in the fibre. To prevent draw-induced losses the fibres are commonly drawn in an optimal fibre tension range that varies according to fibre composition and design. In addition to tension, draw parameters such as furnace temperature and cooling rate affect defect formation [64].

The intrinsic strength of silica fibre can be compromised by the drawing process. As mentioned earlier cleanliness during drawing is an absolute prerequisite for high-strength fibre. Furnace and inert gas set-up play a significant role in reducing particle contamination as well as eliminating possible physical contact of the fibre with any surfaces prior to coating. The coating process itself can also be a cause of reduced fibre strength. The coating material should be filtered to remove any contaminants, should be bubble-free and applied concentric to the fibre and the curing process should be optimised. The drawing temperature has also been shown to play a role in high-strength fibre fabrication. Sometimes the required temperature ranges conflict with those required for minimized loss conditions. For example higher temperatures have been found to provide higher fibre strengths [23], but too high a temperature can result in changes in the refractive index profile via viscous flow and diffusion.

Modification of the RIP can also occur during drawing via residual stress. The differences in viscoelastic properties between the core and the cladding result in mechanical stress build-up during drawing [67]. As a consequence the refractive index is modified via the photoelastic effect. The modification depends on the particular fibre structure and the drawing conditions. A more detailed literature survey is given in Appendix I. A recent study in this area was published by Yablon *et al* [68] who state that refractive index perturbations result from frozen-in viscoelasticity during drawing[4].

[4] The term 'frozen-in viscoelasticity' used by Yablon *et al* [68] is not standard terminology. Author recommends the reader to refer to Ref. [68] for further details.

2.3.2.7 Specialty fibre drawing

Some modifications to the standard drawing process are required in specialty fibre fabrication. To produce circularly birefringent fibres the hi-birefringent preform can be spun during drawing (with spin speeds of 300-2000rpm). This requires a rotating preform chuck or spinning the fibre at the capstan. Some of the specialty fibres have non-circular cladding and require modification to the fibre diameter measurement and control. Fibres with air-structures such as PCFs, capillaries and poling fibres may require additional control for the air-structures.

Due to more complicated geometry and reduced fibre length requirements specialty fibres are drawn at considerably lower drawing speeds and with smaller towers than standard telecommunications fibre. Due to higher dopant concentrations and more complex fibre designs specialty fibres are likely to be more susceptible to draw-induced changes such as residual stress and RIP deformations. As stated in the Introduction chapter, the aim of the work reported in this thesis is to look at some of the specific drawing effects that must be taken into account in specialty fibre drawing. Dopant diffusion and geometry control of PCFs are the particular focus of this study.

CHAPTER 3 METHODS

The various methods employed in this thesis are presented in this chapter. The first section describes the designs used for the two fibre types studied, namely conventional silica fibre where doping is done by chemical vapour deposition techniques and silica photonic crystal fibre. The fibre fabrication techniques used to manufacture the studied fibres are described in Section 3.2. Section 3.3 encompasses the measurement techniques used to characterise the preform and fibre samples. In the course of this study it was found that no one particular measurement technique proved to be ideal, but that various complementary techniques had to be applied in order to obtain results, particularly in the diffusion study presented in Chapter 4. Some aspects of the measurement techniques were developed further in this work and are presented in depth here.

3.1 Fibre designs studied

3.1.1 Conventional silica fibres

The more common dopants used in silica fibres to modify the refractive index are germanium and phosphorus which increase the refractive index, and boron and fluorine which reduce the refractive index (as compared with pure silica). The most common dopant used to increase the refractive index in the core is germanium. In addition to standard telecommunications fibres most of the speciality fibres such as pigtailing, lasing and grating fibres also use germanium in the core to alter the refractive index, although lasing fibres typically also have aluminium. In addition to core doping, some fibre designs also employ germanium doped ring structures in the cladding region to alter the dispersion characteristics of the fibre. For all these fibres germanium distribution in the fibre plays a major role in defining optical properties. Hence germanium doped fibre designs were chosen as the focus of this study. Fluorine doped silica fibre was also studied in this thesis as fluorine is commonly used to reduce the refractive index of silica in the cladding of a multimode pure silica core fibres. These fibres play an important role for example in the medical industry. In addition to this, fluorine is frequently used as a co-dopant in other fibre designs to alter the refractive index profile.

Table 3-1 lists all the fibre designs used, with their geometrical properties. Three different fibre types were employed; Ge-doped core fibre, Ge-doped ring fibre and F-doped fibre. Figure 3-1 shows a schematic diagram of these fibre designs. In the germanium doped core fibre (code SS) the design was based on a pigtailing fibre with germanosilicate core surrounded by a silica cladding doped with phosphorus and fluorine. The fibre design gives an NA of 0.2 and a cut-off wavelength around 750 nm. In addition to a standard single-mode Ge-doped fibre, an asymmetric core preform (code SA) was also used. The structure of the preform was identical to the standard case however a strong cylindrical asymmetry was present in the core. The germanium distribution in the core was highly asymmetric causing the core-cladding refractive index difference to change from 0.028 to 0.018 within the core. This structure was selected in order to find out if such asymmetry would change during the draw. This result is important for other fibre designs such as elliptical core fibres where asymmetry is purposely introduced into the structure.

As shown in more detail in the results chapter, Chapter 4 *Dopant diffusion during fibre drawing*, some problems were encountered in using the single-mode core design (code SS) for diffusion study. It was found during the course of this study that the germanium distribution in the core changed along the length of the preform (code SS fabricated for this study) by an amount comparable to expected diffusion. In order to get reliable quantitative diffusion results the fibre design had to be altered from the germanium doped core design. A number of changes were made to the design. First of all to improve the longitudinal homogeneity of the preform the germanium depleted dip in the centre of the core had to be eliminated. It is know that the central dip changes along the length of the preform due to the nature of the collapse stage in the MCVD process. In order to prevent the effect of the Ge-depleted dip the design was changed from a circular core into a germanium doped ring (code 1R). Pure silica was deposited in the central region of the core, hence preventing any germanium depletion during the collapsing phase of the preform fabrication. Pure silica was also deposited outside the germanium doped ring to prevent cladding dopants interfering with the germanium diffusion.

A fibre with three Ge-doped rings (code 3R) was also made with different germanium concentration in each doped ring. This design was made to improve the etching and atomic force microscopy (AFM) technique (see Section 3.3.2) and to see whether concentration dependent diffusion could be observed. The refractive index profiles of all the Ge-doped preforms are shown in Figure 3-2 to 3-4. The fluorine doped fibre design (code F) is a multimode pure silica core fibre with fluorine doped cladding. A commercial preform SWU1.1 (03100906A) was used with a cladding to core diameter ratio of 1.1 and NA 0.22.

Table 3-1. MCVD fibre parameters

Code	*Preform number*	D_f *μm*	D_p *mm*	*Layer description*	*t or D μm*	*Composition*	*N*	*Δn*
SS	OD010	125	18	core	3	GeO_2-SiO_2	1	0.015
				cladding[1]	30	SiO_2-P_2O_5-$SiO_{1.5}F$	23	-0.007
SA	CD306	125	17	core	3	GeO_2-SiO_2	1	0.028/ 0.018[2]
				cladding[1]	30	SiO_2-P_2O_5-$SiO_{1.5}F$	31	
1R	OD0009	125	16	ring	3	GeO_2-SiO_2	9	0.025
				cladding[1]	5	SiO_2	3	0.000
3R	OD0032	125		innermost ring	4	GeO_2-SiO_2	9	0.021
				middle ring	4	GeO_2-SiO_2	8	0.009
				outermost ring	6	GeO_2-SiO_2	4	0.003
F	SWU1.1	110	25	core	100	SiO_2	-[3]	0.000
				cladding	5	F-doped SiO_2	-[3]	-0.017

[1]Cladding refers here to the layers deposited between the substrate tube before the first Ge doped core or ring layer.

[2]Preform SA had an asymmetric core. Δn values correspond to the maximum and minimum peaks within the core.

[3]The number of deposition layers is proprietary information of the supplier. The amount of layers is significantly higher than in MCVD process.

D_f is fibre diameter, D_p is preform diameter, t is ring or cladding thickness, D is core diameter, N is number of layers and Δn is refractive index difference to pure silica.

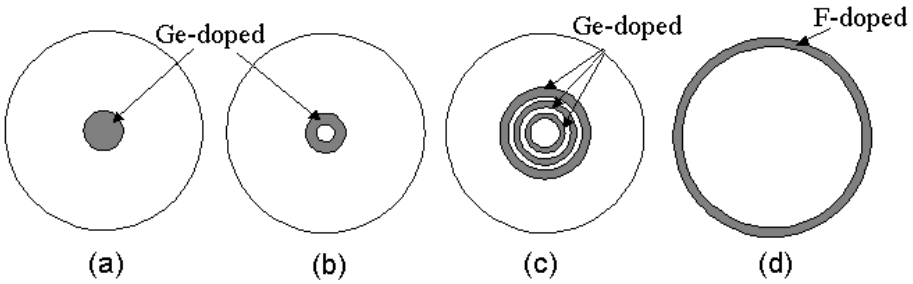

Figure 3-1. Schematic diagrams of fibres with Ge-doped (a) core SS and SA, (b) 1-ring 1R, (c) 3-ring 3R and (d) fluorine doped F fibre design.

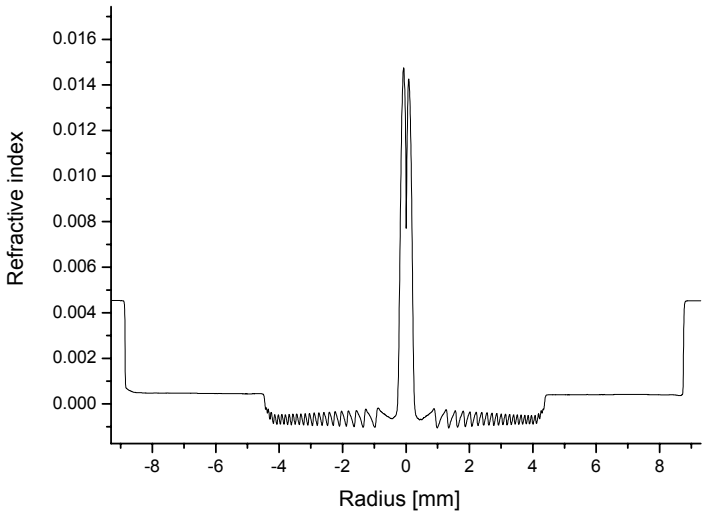

Figure 3-2. Refractive index profile of the Ge-doped core preform, SS

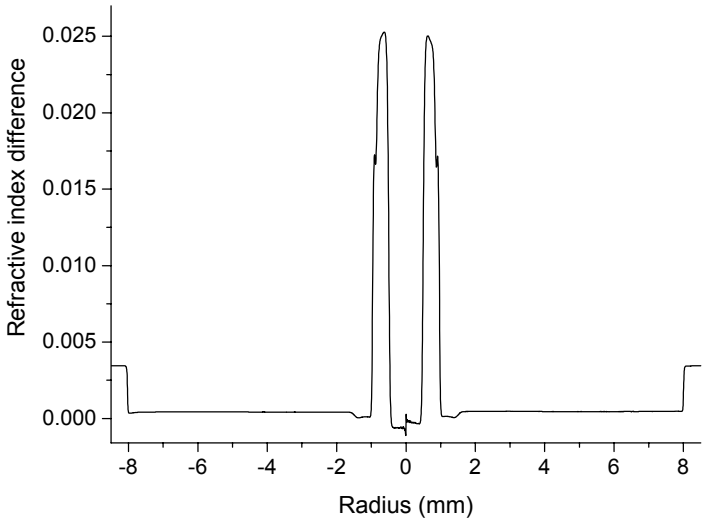

Figure 3-3. Refractive index profile of the Ge-doped 1-ring preform, 1R

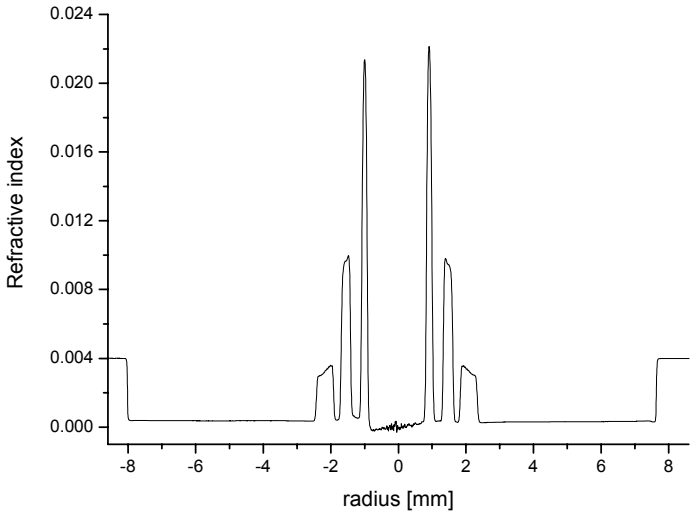

Figure 3-4. Refractive index profile of the Ge-doped 3-ring preform, 3R

3.1.2 Photonic crystal fibres

In PCFs the optical properties of the fibre are defined by the dimensions and position of the air holes as described in Section 2.2.5. The air structure can be created by two methods (i) stacking of capillaries and (ii) drilling holes in a solid rod. As the capillary stacking technique enables a relatively fast fabrication method of potentially large capacity preforms, it is the most common technique employed for silica PCF fabrication at present. Drilling techniques are more useful when the design requires the ability to create arbitrary hole positions and hole sizes. In this study the focus is on the drawing of capillary stacked preforms, though an experiment with drilled preform drawing is also included.

The most popular design used in the capillary stacked fibres is the hexagonal array of holes surrounding either a solid or air core. Figure 3-5 (a) shows such a fibre with hexagonal hole arrangement surrounding a solid core. In this structure the guidance properties of the fibre can be related to geometrical parameters such as the hole diameter d, hole-to-hole distance Λ, hole edge-to-edge separation Λ-d, ratio of hole diameter to pitch (approximately air-fraction) d/Λ and the number of rows surrounding the core, N, see Figure 3-5 (b).

The capillary stacked fibres used in this study had four rows of holes surrounding a solid core. This number of rows was chosen as it is sufficient to provide low confinement loss but not too complicated to stack due to the relatively small (60) number of capillaries required. The hole diameter and the air fraction were adjusted with chosen capillary hole size, the fibre diameter and the draw conditions. For a 125μm cladding diameter typical range of hole diameter was 1-5μm and hole diameter to pitch ratio (d/Λ) of 0.2-0.4. Figure 3-6 shows three fibres which were drawn using the same preform structure but different draw conditions. Note that (c) shows a fibre where the interstitial holes characteristic of a capillary stacked preform are preserved during drawing. As an example of how the preform design could be altered a schematic is shown in Figure 3-7 of (a) using thin walled capillaries (b) thick walled capillaries.

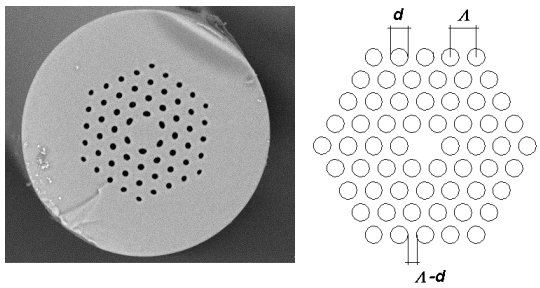

Figure 3-5. (a) Optical micrograph of fibre with hexagonal hole pattern. (b) Schematic of a hexagonal hole pattern surrounding a solid core

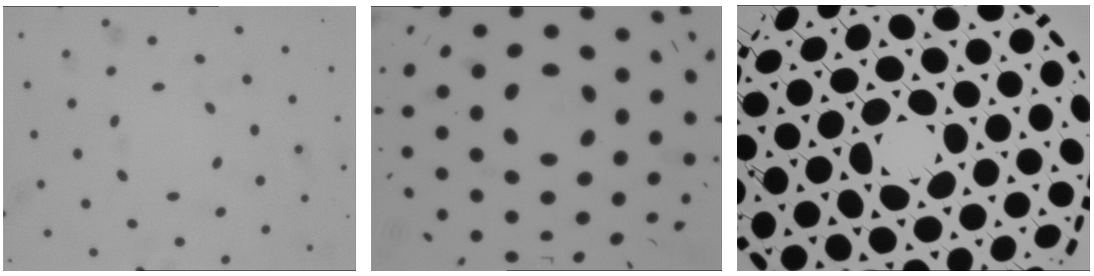

Figure 3-6. Optical microscope image of drawn capillary stacked fibres with air-fraction d/Λ of (a) 0.2 (b) 0.3 and (c) 0.6 with interstitial holes preserved

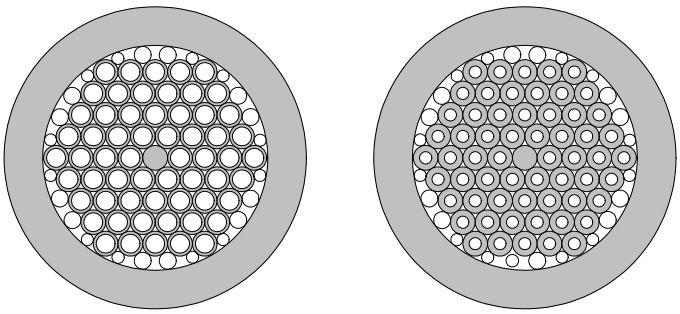

(a) (b)

Figure 3-7. Schematic of preform design using (a) thin walled and (b) thick walled capillaries.

Figure 3-8 (a) shows a photograph of a drilled preform design with non-hexagonal hole array structure. Figure 3-8 (b) shows the corresponding optical micrograph of the fibre. As can be seen from the figures the preform design is very different from that of the capillary stacked preforms. Most notably the interstitial holes created by the stacking of circular capillaries are absent in the milled preform and no separate cladding is required. Due to these differences it was expected that the drawing conditions required would differ from the capillary stacked preforms and results are presented in Chapter 5. The design used was a Fresnel fibre design where the hole positions and sizes were designed to create Fresnel zones around the air core. A detailed description of the design can be found in Refs. [36, 69]. The drilling technique was chosen for this design as it could not easily be achieved by the capillary stacking method.

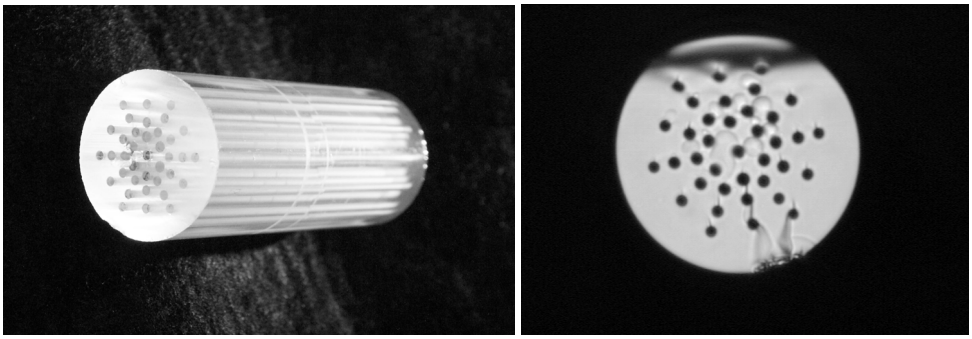

(a) (b)

Figure 3-8. (a) Drilled preform and (b) corresponding fibre with diameter of 125µm.

3.2 Fibre fabrication techniques

3.2.1 Fabrication of the preforms

3.2.1.1 MCVD preforms

The principles of MCVD are described in Section 2.3.1.The MCVD preforms used in this thesis were fabricated using a Heathway MCVD lathe. The lathe is based on a commercial glass lathe such as described in Chapter 2 Section 2.3.1 but has been modified to include etching burners to enable manufacture of circularly asymmetric preforms and an add-on chelate deposition system to allow the manufacture of novel rare-earth doped preforms. These special techniques were not however required for the fibres presented in this work and conventional MCVD techniques were used in their manufacture.

The preforms were manufactured to give designed dimensions for the standard 125μm fibre diameters. A one-metre pure silica substrate tube with outer and inner diameter of 25mm and 19mm was used for all preforms. Before cladding layer deposition HF was used to etch the substrate tube inner surface. For the germanium doped core fibres, SS and SA, a phosphorus and fluorine doped cladding was used whereas the germanium doped ring fibres had pure silica cladding. The number of cladding layers and the cladding thicknesses are listed in Table 3-1 on page 33, which also summarises the preform structure for each design.

For all structures the core or the rings were composed of a binary mixture of silica and germania. Depending on the structure, the core or the rings were deposited in one or more layers. The gas composition was changed in order to obtain the required refractive index. The halide compounds used as precursors are listed in Table 3-2. After core deposition the tube was collapsed by increasing the burner temperature. The refractive index profiles and longitudinal homogeneity are discussed in more detail with the results in Chapter 4.

Table 3-2. Halides used as raw materials in MCVD process

Dopant	SiO_2	GeO_2	P_2O_5	$SiO_{1.5}F$
Source	$SiCl_4$	$GeCl_4$	$POCl_3$	SF_6*+$SiCl_4$

*SF_6 is used for both etching and F doping.

3.2.1.2 Photonic crystal fibre preform

The main emphasis in this work was in the fabrication of capillary stacked fibres, as this is the most common technique used at the moment in the industry. However, as glass drilling enables arbitrary hole structures and thus is an important technique, one sample was included in the experiments. Both techniques are discussed below in relation to specific equipment and procedures used in this work.

The capillary stacking technique involved two stages: (i) the manufacturing of capillaries and (ii) stacking of capillaries in a cladding tube[5]. In the early stages of this work capillaries were obtained from a silica glass supplier. However, it was found that in order to perfect the stacking technique, tolerances for capillary geometry had to be very tight. Commercial capillaries of a reasonable price could not be found to fulfil these stringent requirements and an in-house capillary fabrication process was setup (see Chapter 5 *Geometry control of photonic crystal fibres*, Section 5.3.1).

Commercial MCVD substrate tubes were used both for the capillaries and the cladding tubes. Two different materials were used (i) synthetic silica (Heraeus-Tenevo F300) and (ii) natural fused silica (Heraeus-Tenevo LWQ300). Synthetic silica has a very low OH content, <1 ppm compared to ~150ppm in the natural fused silica. Natural fused silica also contains impurities such as Li, Na, Ti, Fe and Al although their content is typically <4 ppmw for the grade used in this work. For high strength and low loss fibres materials with highest purity should naturally be used.

The tube quality was selected according to the purpose of the preform. If low loss fibre was required, F300 tubing was used, whereas if the preform was used only for fabrication process condition optimisation lower quality tubing was used. Also a combination of the two could be used. The size of the tubing for both capillary and the outer cladding was selected according to desired thickness and air fraction in the final fibre design. Before the stacking process the cladding tube and the capillaries were cleaned with high purity solvent and dried with an inert gas. Note, that in order to increase the strength and to minimise defects from the capillary fabrication and

[5] Cladding tube here refers to the outer solid silica cladding that in conventional MCVD fibres is formed by the substrate tube.

handling, an additional HF etching step can be introduced in the preparation process to remove a fraction of the glass surface [54].

Figure 3-9 shows a typical hexagonal stacking pattern for four layers of holes. In order to stack the hexagonal pattern inside a circular cladding, '*filling*' capillaries or '*filling*' solid rods were used to support the main stack on each side of the hexagon. The stacking process proved to be one of the most important steps in the preform fabrication. The capillary sizes were selected carefully according to the measured inner diameter of the cladding tube, taking into account the variation of the cladding tube inner diameter. Typical cladding tube inner and outer dimensions and variations are shown in Figure 3-10 along the length of a substrate tube for two different quality tubes[6]. Note how the smaller size 16x10mm tube varies significantly more than the tube 20x17mm. The 16x10mm tube was natural quartz whereas 20x17mm synthetic. The different manufacturing process is a likely reason for the difference in variation.

To create a solid core a solid silica cane was stacked in place of the central capillary. The solid core canes were drawn in the same way as the capillaries (Section 3.2.2) from solid rods made either of natural quartz or high purity synthetic silica. After the stack was completed one end was collapsed to a neck-down and a handle tube attached to the other end for the draw. In addition to using fill capillaries or rods to support the hexagonal capillary stack, there are other ways in which the stacking can be done. The circular cladding tube can be replaced by a hexagonal tube or alternatively the circular cladding can be collapsed onto the capillary stack prior to drawing [70]. Capillary stacks can also be drawn without a cladding tube [70] though the strength of the fibre is compromised in this technique.

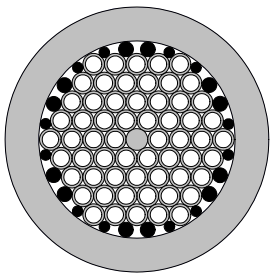

Figure 3-9. Schematic of a 4-ring hexagonal stacking pattern of capillaries with a solid core inside a cladding tube, fill capillaries/rods shown as black.

[6] The measurements were done at OFTC using a preform refractive index profiler (PK2600), see Section 3.3.1.1.

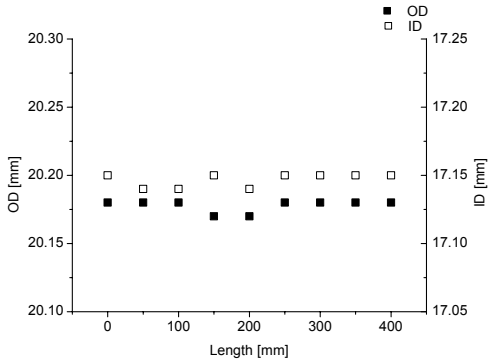

(a) 20x17mm

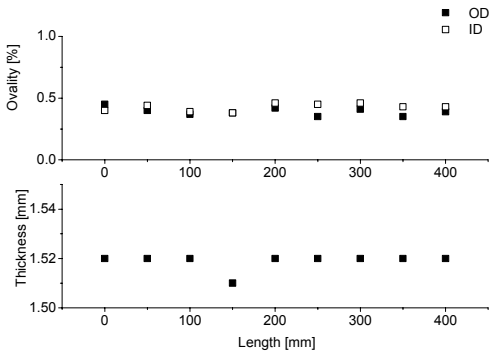

(b) 20x17mm

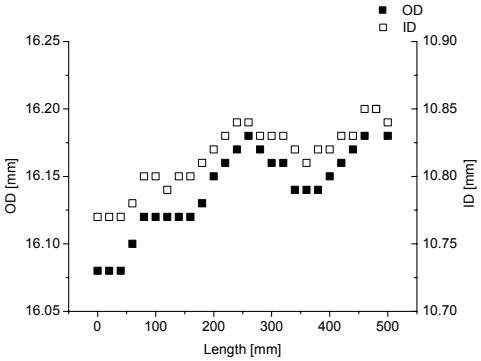

(c) 16x10mm

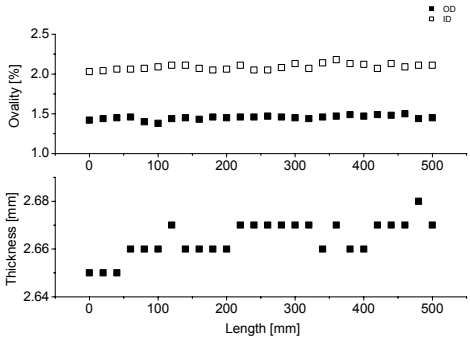

(d) 16x10mm

	OD (mm)	*ID (mm)*	*Thickness (mm)*	*Ovality (%)*
		20x17 mm synthetic		
Mean	20.18	17.15	1.52	0.39/0.43
Std±	0.004	0.005	0.003	0.03
		16x10 mm natural		
Mean	16.14	10.81	2.66	1.45/2.09
Std±	0.03	0.02	0.008	0.03/0.04

(e)

Figure 3-10. Longitudinal variation in the substrate tube (a) and (c) outer and inner diameter and (b) and (d) thickness and ovality also shown. Tube size (a) and (b) 20x17 and (c) and (d) 16x10mm. (e) The table shows a statistical summary of these data.

The drilled photonic crystal preform was fabricated using a sonic mill (Sonic-Mill Series 10) to drill a solid natural quartz silica rod of 17mm in diameter and 50mm in length. The material used was natural quartz. The preform design mentioned in Section 3.1.2 had 37 holes, each 1mm in diameter. After the drilling procedure, the preform was cleaned. The preform is shown in Figure 3-1 (a).

3.2.2 Drawing process

Two different drawing towers were used to draw the fibre samples. The towers are referred to in this text as (i) Nextrom tower and (ii) custom designed research tower (Heathway). The Nextrom tower was configured for drawing production-type speciality fibres, whereas the custom designed research tower was built for low speed drawing especially of preforms with length smaller than 150mm. The configurations of each tower are described below in detail. For an introduction to a typical drawing process refer back to the Background Chapter, Section 2.3.2.

3.2.2.1 Nextrom tower

The Nextrom tower has a nine metre frame which allows drawing speeds of up to 300 m/min. The frame includes a clean-air hood which encases the preform, furnace and the bare fibre providing a clean air environment (Class 100). The preform feeding chuck and the furnace are placed so that a maximum preform length of 800mm can be fed into the furnace. Preforms can be fed at speeds of up to 21 mm/min.

The furnace is a Centorr 11A graphite resistance furnace, wherein preforms with maximum diameter of 30mm can be heated. The hot-zone length of the furnace is 40mm and argon is used as the furnace atmosphere. The heating element and gas feeds are configured so that a major up-flow of the inert gas is obtained in operation. The argon is fed in at four inlets as follows (typical flows are noted in parenthesis); upper iris (1.4 litre/min), hot-zone (6 litre/min), bottom iris (2 litre/min) and chamber (1.2 litre/min). The flow into the chamber is not in contact with the preform but surrounds the heating element. Figure 3-11 shows a schematic of the furnace with argon flow inlets marked. A simulated neck-down shape is shown in the figure indicating the position of the preform and fibre relative to the hot-zone (for more details see Chapter 6). The typical drawing temperature range used was 1850°C to 2200°C. The temperature is measured from the back of the graphite element in the hot-zone with a pyrometer (Ircon Infrarail infrared thermometer, type E) with an accuarcy of ±20°C and repeatability of 6°C. The furnace is equipped with an extension tube to prevent thermal shock for the fibre at high drawing speeds. The extension tube is 200mm long with bore diameter of 20mm. Both top and extension tube irises are adjustable, with typical openings of 1.5 mm top (iris to preform gap) and 8 mm diameter on the bottom.

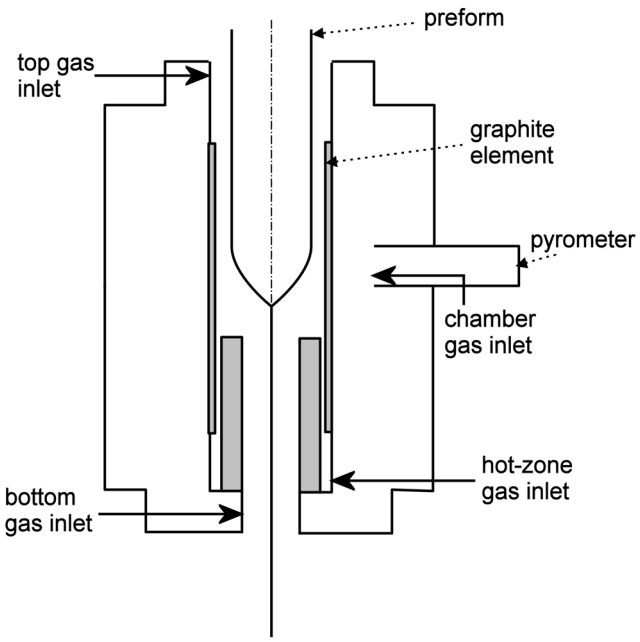

Figure 3-11. Schematic of a fibre drawing furnace with gas flow inlets marked.

As the fibre emerges from the furnace the bare fibre diameter is measured below the furnace using an Anritsu (KL151ATW) diameter measurement gauge, with averaging of 64 scans, for fibre with diameters below 300μm. The repeatability and reproducibility of the measurement is ±0.05μm for 125μm fibre. For diameters above 300μm a LaserMike (282-14 200FI) diameter measurement device is used. The measurement error is 0.25μm for fibre <500μm and 0.4μm >500μm and repeatability of ±0.13μm. Output from both of the devices can be used in the feedback PID controller to control the diameter of the fibre during drawing via the capstan speed. The diameter gauge also monitors the position of the fibre, and this information is used on-line to position the preform in the centre of the furnace.

Before the fibre is coated with a protective coating the bare fibre tension is measured using a non-contact measurement (Pullman 2+), which employs the velocity of a sound pulse to determine the tension. The tension measurement is used to indicate the temperature of the neck-down of the preform, and is considered more reliable than the furnace pyrometer since the latter measures the outside temperature of the graphite heating element temperature rather than the temperature of the preform itself.

Single or dual coating was applied to the fibre before winding. The coater used is a pressurised model with both pressure and temperature control. A UV curable acrylate

coating was used. The curing was performed with a single Fusion UV-lamp with variable power. The coated fibre diameter was monitored with an Anritsu (KL151A) diameter gauge before winding the fibre on a take-up spool. The tower did not include any additional forced fibre cooling as sufficient natural cooling times are provided even at full drawing speed.

The fibre samples corresponding to the different draw conditions were located on the spool according to the on-line data logging system and fibre length measurement. A data logging system was also used during drawing to log all the variables. Data were recorded at one second intervals. Figure 3-12 shows a graphical presentation of data from a typical experimental draw of PCF. The arrows show two samples with different preform internal pressure settings.

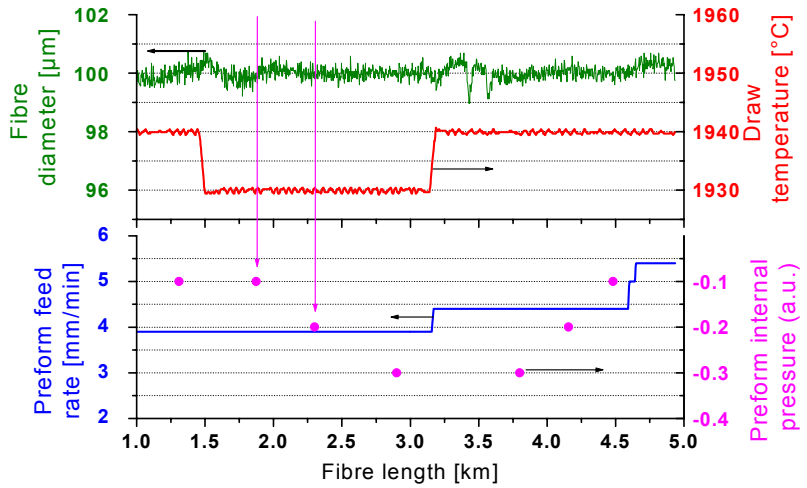

Figure 3-12. Graphical presentation of data from a typical experimental draw for a PCF draw. Arrows show two samples with different preform internal pressure settings.

When thick fibres and capillaries were drawn a different drawing capstan was used. The main fibre drawing capstan diameter limits the maximum fibre diameter due to bend radius limits. When thick fibres, also called canes, or thick capillaries were drawn a two-roller tractor-motor was used, wherein the fibre was not subjected to bending. The diameter of the capillaries and canes was controlled in a similar manner to the fibres. The PID control parameters were adjusted accordingly, as longer response times resulted from the lower drawing speed. Typically, drawing speeds ranged from 0.5 to 3 m/min and the diameter controller enabled capillaries to be drawn with diameter variation ≤ ±0.5% from nominal setting.

For the photonic crystal fibre and capillary draws a pressurisation system was set up in the drawing tower in order to control the preform internal pressure during drawing. The pressurisation had two purposes (i) to provide additional means to control the fibre and capillary geometry and (ii) to create an inert atmosphere inside the preform to reduce attenuation due to OH diffusing into the glass from the air as well as shield from other contaminants. Two pressure set-ups were used during the study. The initial pressure system was found to be inadequate to control the more sensitive structures and an improved system was built allowing for a more accuarate pressure control.

The schematic diagram of the pressure control set-up is shown in Figure 3-13. A constant flow (FIC, rotameter) of an inert gas such as nitrogen or argon was supplied to the system. A glass tube was attached to the top end of the preform which was connected to the gas line. The gas flow input was axial. The preform internal pressure was measured at the top of the preform and a feed-back control (PID) was used to adjust the gas flow into the preform. The accuracy of the preform internal pressure control was 1mbar.

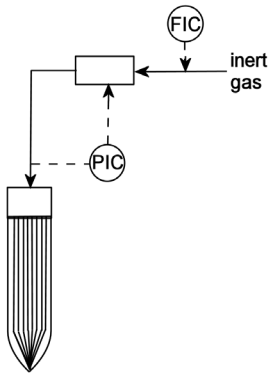

Figure 3-13. Schematic diagram of the pressure control system.

3.2.2.2 Custom designed research tower

The custom designed research tower is designed for small research preforms and for easy intervention and manual control by the operator when required. The small height of this tower also minimises the start-up waste, so the yield is higher from a small preform compared to a full length production tower. The custom designed tower was also equipped with a preform spinning system which enabled the manufacture of circularly birefringent fibres.

The furnace used in the custom designed research tower was supplied by Astro model GM. The furnace has graphite resistance heating elements and argon is used during drawing. The furnace is designed for downward argon flow, unlike the Centorr furnace in which the net flow is upwards. Only two argon feeds are used, the main flow being from the top iris and the smaller flow from the bottom iris. Typical flows are 2 litres/min and 1 litres/min. The preform is fed in a similar manner as described before, with speed of up to 10 mm/min. Maximum preform size is 25mm in diameter. As this tower has a smaller range of draw speed, 0-40m/min, no extension tube is required below the furnace.

The bare fibre is coated using an open coating cup based on gravitational flow. A single or twin coating set-up can be used. The coating is cured using a single UV-lamp (Fusion). Before the fibre is wound on the spool the coated fibre tension is measured above the capstan. The fibre diameter is measured with an Anritsu (KL151A, repeatability ±0.05 to ±0.15μm and reproducibility ±0.3μm) and PID feedback control is used to control the diameter during drawing. An optional logging system can be used to log the draw variables. After drawing, the fibre samples were wound onto separate spools, using the length data collected during drawing as with the production tower (Nextrom).

3.3 Preform and fibre measurement techniques

In order to study changes in the fibre structure during drawing various measurement techniques were employed to characterise the geometry and composition of the fibres and preforms. The most suitable techniques were selected according to the nature and magnitude of the change, the dimensions of the sample and the destructiveness of the measurement technique. For example preforms were measured by a non-destructive method along their entire length with a refractive index profiler, and only one sample per preform was analysed by electron micrsocopy due to the destructive nature of the sample preparation. The microanalysis of the preform was essential to correlate the refractive index profiles to dopant concentration profiles in the preform. As the preforms are relatively large and the features on a millimetre scale the spatial resolution of the measurement techniques was not an issue. Challenges were encountered when asymmetric preforms needed to be characterised with the refractive index profiler. Consequently in-house tomographic measurement software was developed [71, 72],

which enabled the computation of the refractive index profiles of preforms with arbitrary index distribution.

Changes due to dopant diffusion were expected to be on a submicron scale, so high resolution techniques had to be used to measure the effects in the fibres. The standard fibre refractive index profiler is only capable of spatial accuracy of about 0.5μm, so Transmission Electron Microscopy (TEM) was initially selected as the most promising technique for measuring dopant profiles across the cores of fibres. Although TEM measurement had the capability for accurate high resolution dopant concentration measurements with nanometre spatial resolution. The preparation of the ultra-thin samples (circa 80nm thick) was found to be very difficult and time-consuming. Unfortunately the ion-beam thinning used in the final preparation stage was found to preferentially etch germanium thus affecting the sample concentration profile. Due to these challenges an alternative measurement technique was used to profile the fibre samples. Atomic Force Microscopy (AFM) was identified as a suitable means of measuring changes on a sub-micron scale with a relatively simple sample preparation procedure. Refractive index profiling was used to complement the AFM measurements.

The draw induced changes in photonic crystal fibres were of a very different nature. Having only a single material no chemical analysis was required and the strong contrast between air and silica with changes on a larger scale suggested that an optical microscope would have sufficient capabilities. This was found to be the case for most of the samples studied, though, in order to increase resolution to submicron scale measurement with AFM and Scanning Electron Microscopy (SEM) were carried out for samples with very small features.

Whenever possible, several techniques were used to confirm findings and to complement each other. Each measurement technique used is described below, including descriptions of the techniques, limitations, accuracy, sample preparation, analysis and the purpose for which each technique was used.

3.3.1 Refractive index profiling

3.3.1.1 Preform

Due to its non-destructive nature, refractive index profiling of the preform is widely used in the industry. Standard commercial equipment has been designed to be used in the optical fibre production environment. Once the draw induced changes are known or eliminated, preform refractive index measurement can provide an accurate estimate of the drawn fibre refractive index profile and can be used in production to monitor the product and process quality. Consequently refractive index profiling of the preforms was the first choice for measuring the structure of the preform prior to drawing. Although, in addition to the material composition, other factors such as stress can affect the refractive index of the material the non-destructive profiling method proved to be invaluable in evaluating longitudinal and radial homogeneity of the preform in addition to providing information about the dopant distribution of the samples.

A commercial preform refractive index analyser (NetTest PK2600) was used to measure the refractive index profiles of all the MCVD preforms used in this study. In this instrument the preform is attached to a vertical tower and immersed in a tank containing index matching oil (index matched to silica at 633nm and 35°C). The preform can be rotated automatically to obtain scans at different rotational angles, the smallest step size being 1°. The system is fully automated so that several longitudinal positions can be measured in a single measurement routine. This is ideal for analysing both the longitudinal and radial homogeneity of the preforms prior to drawing.

The basis of the measurement method is to scan the output of a HeNe laser (633nm) radially across the preform and detect the deflected laser beam by a position-sensing detector. The displacement of the incident beam from the centre is computed from the measured voltages on the detector, from which the deflection function can be calculated. The deflection function is the ray exit angle as a function of the ray incident direction. The deflection function can then be transformed into a Refractive Index Profile (RIP) using Abel inversion of the function [73, 74]. The corresponding RIP calculated from the deflection data is shown in Figure 3-14 . The spatial resolution of the system is 5μm and the accuracy of the refractive index is 2×10^{-4} with repeatability of

5×10^{-5} [75]. However any problems with centering the deflection function (common with complex index profiles) will result in errors in the profile.

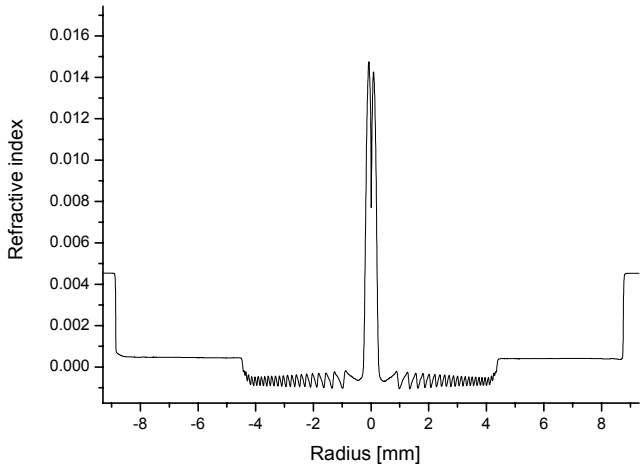

Figure 3-14. A RIP of a single-mode preform.

The basic software of the PK2600 has a limitation in that the computation from deflection data into refractive index profile assumes circular symmetry in the preform. Any departure from perfect symmetry causes inaccuracies in the profile. In order to measure asymmetric preforms a tomographic computation technique must be used. During the course of this study in-house software was developed to calculate refractive index profiles using a tomographic computation routine [72, 76]. This enabled the measurement of RIP for asymmetric preforms using the raw data from the PK2600 detector. Figure 3-15 shows a 3-dimensional plot of the refractive index of an asymmetric core preform and an RIP across the core.

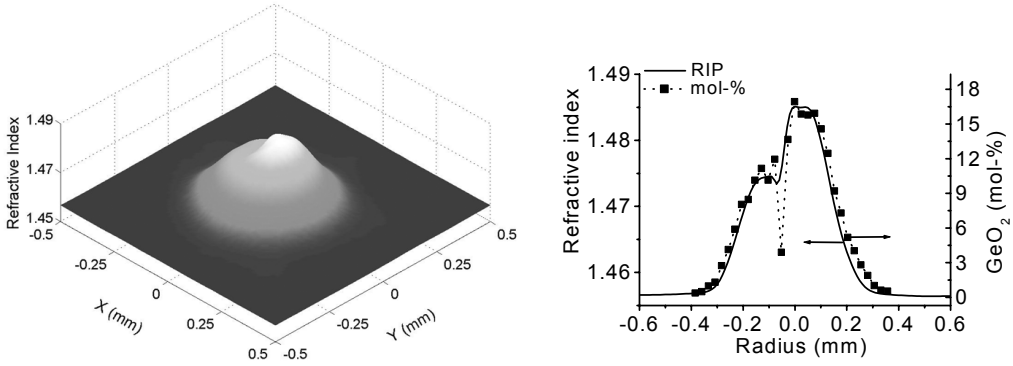

(a) (b)

Figure 3-15. (a) 3D RIP plot of an asymmetric preform core using the in-house tomographic computation and (b) a line profile across the core.

All the MCVD preforms used in the study were characterised using the preform refractive index profiler. Typically symmetric preforms were measured every 10mm along the length and in five rotational positions. Tomographic computations were performed when asymmetry in the preform structure was expected. For tomographic computations data was collected in 1° rotational steps for at least one longitudinal position. The refractive index plots provided two main functions (i) they were used to characterise the longitudinal and radial homogeneity of the preform enabling a selection of the best section for draw experiments and (ii) they were used to extrapolate the compositional profiles obtained from destructive microanalytical techniques on drawn sections of the preform.

Due to the very sharp step index profile of the fluorine doped preform the computed RIPs did not present a true picture of the preform. The sharp step in the profile could not be measured using standard profiling methods. This is discussed in more detail in Ref. [77]. In this thesis the preform RIPs were only used to give indication of homogeneity and microanalysis was used for the comparisons with fibre compositions.

3.3.1.2 Fibre

Unlike preform refractive index profiling, the fibre profiling is a destructive measurement technique and usually involves tedious preparation of measurement cells to guarantee successful results. As the fibre is 80 to 800 times smaller than the preform, similar relative spatial accuracy achieved in preform profiling cannot be achieved in fibres. Fibre refractive index profiling does however provide valuable information, as it is measured on the drawn fibre thus providing the refractive index profile which determines the guiding properties of the fibre. Consequently commercial fibre profilers are standard equipment in a fibre production facility.

As a complementary measurement technique the fibres used in this study were measured using a fibre refractive index profiler. Two commercial refractive index profilers were used, the on-site York S14 and an off-site EXFO NR9200-HR. Both instruments use the Refracted Near-Field (RNF) technique [78]. In RNF measurement the fibre end-face is scanned by a circularly polarised light and the refracted light not guided by the core is detected. The fibre is immersed in an index matching fluid with

refractive index slightly higher (S14 n_{oil}=1.468215 at 25°C) than that of the cladding to ensure that the refracted rays escape through the cladding to reach the detector. The detected signal variation is proportional to the refractive index change of the fibre.

The nominal spatial resolution of the refractive index profile reported by suppliers of both instruments was ≤ 0.5μm, which is 16% of a 3μm fibre core. As a comparison, the PK2600 preform profiler has a spatial resolution of 5μm which is 0.5% of a typical 1mm preform core. Table 3-3 shows the resolution of the profilers as reported by their suppliers. Although similar spatial resolution was reported for both instruments the second generation high resolution NR9200-HR was found to give more accurate profiles. For comparison of RIPs measured using both instruments see Figure 3-16.

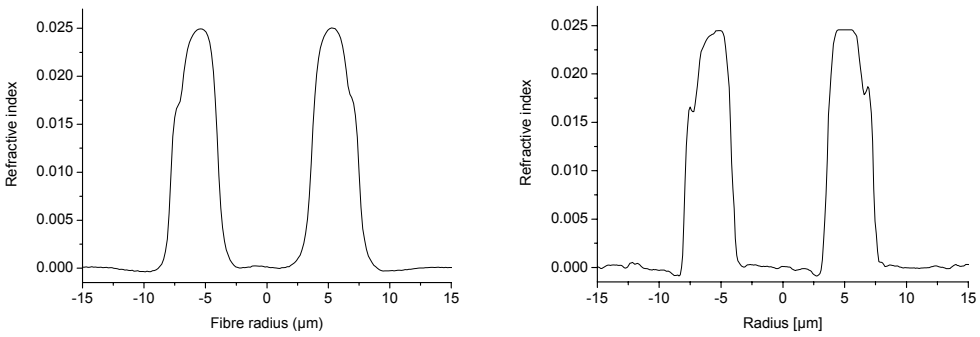

Figure 3-16. Ge-ring fibre core profile measured with (a) S14 and (b) NR9200-HR.

Table 3-3. Resolution of fibre refractive index profilers [75, 79]

	Wavelength (*nm*)	*Spatial resolution* (*μm*)	*Geometry measurement repeatability* (*μm*)	*RIP resolution*	*RIP repeatability*
S14	633	≤0.5	0.15-0.3	1×10^{-4}	2×10^{-4}
NR9200-HR	655	≤0.5	0.1	5×10^{-5}	7×10^{-5}

3.3.2 Etching and atomic force microscope technique

This section describes the use of AFM in characterising the dopant concentration profiles in optical fibre samples. Characterisation of optical fibres using an AFM was first reported in 1994 [80, 81]. Since this is relatively recent when compared to more traditional profiling techniques, such as RNF which dates back to the 1970's [82], a

summary literature review is presented on the use of the etching and AFM technique in profiling of optical fibres in Section 3.3.2.3. During the progress of this thesis further advances were made in producing quantitative dopant profiles using AFM and hence the sample preparation and data analysis is discussed in detail in this section. In the following paragraphs first the AFM technique is described and the application to optical fibres introduced. A more detailed discussion is then given on the acid etching process. Finally, the methods and equipment used for the samples are described and the section is concluded by the important data analysis relating the AFM data to the fibre dopant concentration profile.

3.3.2.1 Principles of AFM measurement

AFM is a scanning probe technique, where the measurement is based on attractive or repulsive forces between a sharp tip and the specimen surface. A piezo-electric scanner is used to translate either the sample or the tip. During the measurement the piezo-electric scanner maintains the tip force or the tip height from the sample surface constant depending on the measurement mode. The tip, made of silicon or silicon nitride, is attached to a thin and flexible cantilever beam which is typically 100 microns long and few microns thick. As the tip scans the surface, it moves up and down according to the surface topography and the cantilever is deflected. This deflection is measured using a laser beam which reflects off the back of the cantilever and is detected. In constant-force mode the piezo-electric transducer monitors the real time height deviation and a three-dimensional topographical map of the surface can be constructed. Unlike systems based on wave-optics the probe technique is not limited by diffraction but primarily by probe geometry. Since tip diameters as small as few nanometres can be made, nanometre resolution can be achieved with an AFM [83].

3.3.2.2 Etching of pure and doped silica glasses

To reveal the dopant concentration profile of the fibre a surface topography is created by etching the fibre end-face with hydrofluoric acid (HF) [81]. Differential etching rates create a 3D topography that can be related to the chemical composition of the fibre, i.e. dopant distribution. To determine dopant distribution from the topography the etching reaction and the reaction order must be known for the acid and the glass. In this study aqueous solution of HF was used as the etchant. The etching mechanisms of HF on silica are presented in more detail below.

The etching reaction of SiO_2 with HF can be represented with an overall reaction:

$$SiO_2 + 6HF \rightarrow H_2SiF_6 + 2H_2O \qquad (9)$$

The etching of silica is a surface reaction with kinetics similar to a catalytic reaction. The reaction can be presented as three distinctive steps [84]

1. HF adsorbs on a site S on the glass surface.
   $$HF + S \leftrightarrow HF \cdot S$$
2. The adsorbed acid breaks the siloxane bonds on the surface and the surface reaction takes place.
3. Desorption of the products occurs from the surface.

In Step 2 the hydrofluoric species in the HF solution break the covalent siloxane, $\equiv Si - O - Si \equiv$, bonds that form the silicate network structure due to the high electronegativity of the fluorine. Equation (9) is a greatly simplified equation and in reality the reaction happens in several reaction steps including the various hydrofluoric species taking part in the etching. Of these reactions it is the slowest step that is the rate-determining step for the etching of silica [85].

The hydrofluoric species in aqueous HF are formed according to equilibrium reactions, Eq. (10) [86, 87].

$$\begin{aligned} HF &\leftrightarrow H^+ + F^- \\ HF + F^- &\leftrightarrow HF_2^- \\ 2HF &\leftrightarrow H_2F_2 \end{aligned} \qquad (10)$$

The equilibrium constants, *K*, for the above reactions are [87]

$$K_1 = \frac{[H^+][F^-]}{[HF]} = 6.9\times10^{-4}\ mol/l$$
$$K_2 = \frac{[HF_2^-]}{[HF][F^-]} = 4.0\ mol/l \qquad (11)$$
$$K_3 = \frac{[H_2F_2]}{[HF]^2} = 2.7\ mol/l$$

In order to understand the etching kinetics, the influence of each species must be known. The reactivity of F^- has been shown to be negligible in the etching reaction [88, 89], however, the reactivity of the other species has been subject to numerous studies presented in more detail in refs [85, 86, 90]. To show the range of available models, some of the proposed reaction rate dependencies on reaction species concentration are shown below. r_{etch} is the reaction rate of silica in units of mol/area.time and C_i is concentration of species i, n is the reaction order and the various k_j are reaction rate constants of the related reactions.

$$r_{etch} = k_0 C_{HF}^n \qquad (12)$$

$$r_{etch} = \frac{k_{HF} C_{HF}}{1 + K_{HF} C_{HF}} \qquad (13)$$

$$r_{etch} = k_0"[SiOH_2^+][H_2F_2] + k_1"[SiOH_2^+][HF_2^-] + k_2"[SiOH][HF_2^-] \qquad (14)$$

Equation (12) shows one of the first models proposed [91] to describe HF etching of silica. The model was obtained by fitting to experimental etching data and hence can only describe the kinetics in a system similar to that of the experiment. Equation (13) was based on analogy to a catalytic reaction [84] and again can only represent the etching in a limited manner. Equation (14) is by Knotter [87] and is the most recent model presented in the literature. In his approach the reaction mechanisms are determined more from the phenomena occurring at a molecular level rather than just by fitting with experimental data. Importantly though, the model is verified against experimental data and results in the best fit to date in terms of the range of situations the model applies to.

The model by Knotter [87] is based on work presented by Osseo-Asare [92] where the protonation and deprotonation of hydroxylated silica surface groups (Si-OH) are taken into account. Depending on the pH of the etchant either positively charged sites ($Si\text{-}OH2^{+}$) or negatively charged sites ($Si\text{-}O^{-}$) are formed which then affect the surface concentration of the adsorbed fluoride and hence determine the reaction kinetics of etching. The main disadvantage of the earlier models was that these simple models could not explain the phenomena observed at various pH levels. By using the model in Eq. (14) Knotter [87] could fit the data for a range of solution pH where each of the components of Eq. (14) become dominant at specific range of pH. The proposed reaction mechanism is presented in Figure 3-17 and the full discussion can be found in Ref. [87].

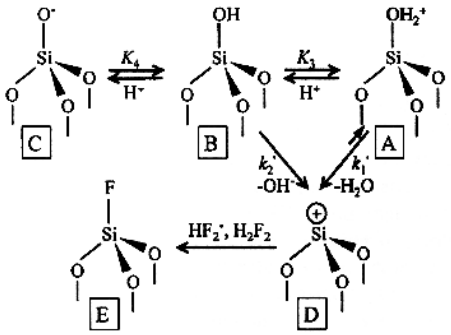

Figure 3-17. Reaction mechanism of the rate-determining step of the dissolution of SiO_2 in HF solutions proposed by Knotter. Replacement of the SiOH unit by an SiF unit. [87]

The aim of the above silica etching review is to show that etching kinetics are not simple and vary depending on the etching method and the environment. In this study doped silica was etched. The literature relating to this is reviewed in the following section. The basic molecular level reactions are, however, the same or similar to those presented above and the kinetics can be understood in terms of how the added dopants modify the silica network.

Also note that in the following review, studies which use Buffered hydrofluoric acid (BHF) are also reported in addition to studies with aqueous HF. In BHF NH_4F is added to the solution hence modifying the pH. The stoichiometry of the reaction between silica and HF is also altered from that of aqueous HF. To illustrate the issues relating to the selection of the etchant, see Figure 3-18 and Figure 3-19 where the etching rate of silica is shown as a function of HF and NH_4F concentration. The maximum in the BHF case can be explained with the model based on work by Osseo-

Asare [92] and Knotter [87]. Note also that the etching rate of un-doped silica can vary depending on the manufacturing technique. It has been shown for example that deposition temperatures and UV-exposure both affect the etching rate. This can be understood as resulting from the change of the bonding arrangement and porosity of the silica network [85].

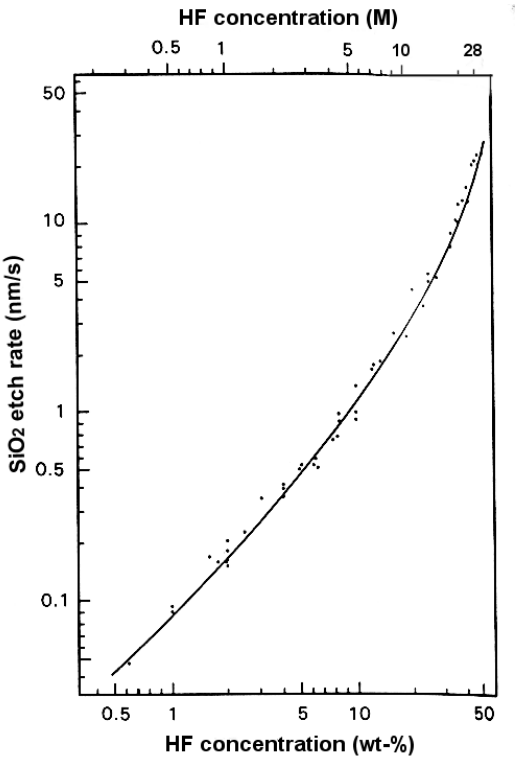

Figure 3-18. Reaction rate of silica with HF vs. molar HF concentration [85].

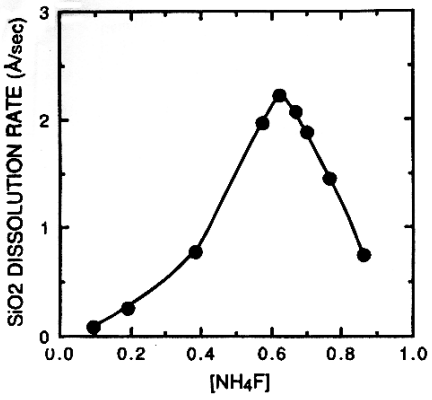

Figure 3-19. Reaction rate of silica with BHF vs. molar NH_4F concentration [89, 92]

As explained previously the etching and AFM method is based on the mapping of dopant concentrations due to the difference in etching rates of the various dopants in silica glass. How the dopants affect the etching rate depends on how the dopant is incorporated in the silica network and the properties of the created bonds. The etching rate is different due to the modified silica network where in addition to siloxane bonds the bonds created with the dopants must also be broken. It then depends on the chemistry of the bonds how the etching rate is changed.

The dopants can be classed as (i) network-forming oxides or (ii) network-modifying oxides. Common network-forming oxides are GeO_2, P_2O_5 and B_2O_3, which form $\equiv Si-O-A-$ and $-A-O-A-$ bonds [85]. Depending on the etchant chosen (HF or BHF) and the properties of the bonds, the etching is either faster or slower as compared to pure silica. If the bonds are broken more easily than siloxane bonds, the etching rate will be determined by the siloxane bonds and hence the overall reaction rate is faster than for pure silica. On the other hand if the bonds are more difficult to break, this becomes the rate determining step and in addition to slower etching rate the etching kinetics can be changed as a result of different chemistry.

Network-modifying oxides are incorporated in the silica network by breaking the siloxane bonds and forming non-bridging oxygen atoms. Examples of network modifiers include Na_2O, K_2O and CaO. The reaction of Na_2O with silica network is shown in Eq. (15) [85].

$$Na_2O + \equiv Si-O-Si\equiv \rightarrow 2\equiv SiO^{-}\cdot Na^{+} \qquad (15)$$

As the network-modifiers cause the silica network to partially break down, the etching rate is increased more than for network-forming oxides. The etching rate has been related to the concentration of non-bridging oxygens in the network [88, 93, 94].

The effects of various dopants, both network-forming and modifying, on etching rates are shown in Table 3-4. The findings from various past studies agree well overall, except for the effect of boron doping when etched with HF. The discrepancy has been explained by the substantially different boron concentration [85]. As described previously the etching mechanism can change if the way in which the dopant is

incorporated into the silica network is altered. For dopants commonly used in optical fibres, P_2O_5, B_2O_3, GeO_2 and F, the etching rate is increased compared to pure silica when HF is the etchant. However, when BHF is used, boron and germanium doped silica etches more slowly than un-doped silica. This is very useful because by using successive steps of HF and BHF etching the distribution of various dopants in a multidoped fibre can be revealed. This of course applies only to certain combination of dopants. However, it may be possible to determine the dopant distribution of all the dopants in the sample, if the magnitude of the differential etching rates are known and we have some prior knowledge of the composition of the sample.

Table 3-4. Etching rate of various dopants compared to un-doped silica, ↑ denotes higher rate that silica and ↓ lower rate.

Etchant	*P_2O_5*	*B_2O_3*	*GeO_2*	*As_2O_3*	*F*	*Al_2O_3*	*Vycor*[1]	*CaO*	*Na_2O*
HF	↑ [86]	↑ [85] ↓ [86]	↑ [81, 93, 95]	-	↑ [96, 97]	↑ [88]	↑ [98]	↑ [88, 93]	↑ [93]
BHF	↑ [86, 90]	↓ [85, 86]	↓ [81, 96]	↑ [85]	-	-	-	-	-

[1]Vycor consists of silica doped with 3% B_2O_3 & 0.5% Al_2O_3.

In order to obtain quantitative information of the sample composition, the qualitative information presented in Table 3-4 is not sufficient and the etching rate dependence of the dopant concentration must be quantitatively known. For multidopant samples this is a challenge, but for binary systems this data can be obtained from experiments. Only a few quantitative studies can be found in the literature and due to the complicated interactions with sample structure, etchant properties and the environment, one must be very careful when applying such data. In fact, for these reasons it was decided that the etching rate dependence on dopant concentration needed to be determined for the specific samples used in this study. It is useful however to review some of the results from past studies as they can demonstrate various issues when such experiments are made.

Figure 3-20 shows results from past studies of etch rate dependence on concentration for P_2O_5, B_2O_3 and As_2O_3 doped silica etched in BHF [85]. For phosphorus doped silica the relationship is linear and for arsenic nearly linear. The situation is more complicated for boron doped silica and is accounted for by the increased number of $=B-O-B=$ bonds at higher boron concentrations as opposed to $=B-O-Si\equiv$

bonds at lower boron concentrations. At higher B concentrations the hygroscopicity of the surface is increased hence changing the etching kinetics [85]. When the effect of etchant concentration is added to the boron doped silica etching data, as shown in Figure 3-21, one can understand the amount of complexity in the chemistry of boron etching with BHF.

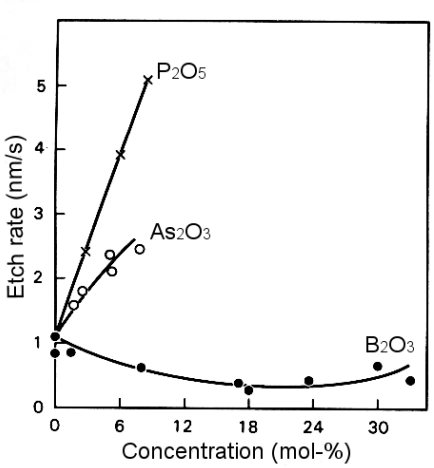

Figure 3-20. Etch rate as a function of dopant concentration for B_2O_3 , P_2O_5 and As_2O_3 [85]. Etching solution used was 10 parts 40wt% NH_4F and 1 part 49wt% HF [85].

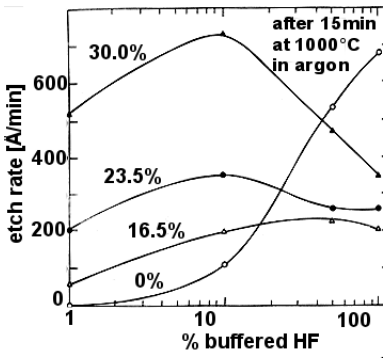

Figure 3-21. Etch rates of borosilicate glasses as a function of BHF concentrations. Curves labelled with B_2O_3 concentration (mol-%) [99].

3.3.2.3 Etching and AFM technique in optical fibre characterisation

Due to its superior spatial resolution compared to conventional fibre profilers, AFM has been recognised as a useful tool for studying optical fibres. The etching and AFM technique was first employed in optical fibres by Zhong and Innis [81] in 1994 and AFM was used to study the microheterogeneity of optical fibres without the etching step by Carter *et al* [80]. Since then the technique has been used for measuring a multitude of specialty optical fibres: D-shaped fibre [100], elliptical core fibre [101],

high NA fibre and twin-core fibre [95]. Also multimode fibre [97], fused-taper fibre couplers [102] and planar waveguides [101] have been studied using the etching and AFM technique. Most of the samples in these studies had a single dopant, either germanium or fluorine in silica, and the other dopants have been of small quantity typically residing in the cladding.

The reproducibility of the etching and AFM technique has been reported to be very good amounting to a 2% error for both etching depth and lateral distance measurements (e.g. core diameter) [81, 95]. The most relevant question relating to this work is, whether etching and AFM can provide quantitative information on dopant distribution in optical fibres. Although many of the above studies do compare the AFM profiles with fibre and preform refractive index profiles, each study usually encompassed only a single fibre type hence limiting the application of the data to this type of fibre and consequently to a limited range of concentrations and the type of dopant used.

The most comprehensive study to look at the relationship between etching depth and dopant concentration still remains that of Zhong and Innis [81, 95] although their study is limited to germanium doped fibres. They analysed several Ge doped fibres, with various index differences in the range 0.006-0.04, etched with dilute HF. Figure 3-22 shows the etching depth as a function of refractive index difference between fibre cores and cladding. If a reaction kinetic model, $r_{etch} = aC^n$, is used, the reaction order n can be determined from the data resulting in a value of n = 0.64 (R^2=0.97 (regression coefficient)), where a is a linear scaling factor and C species concentration. This kinetic model can be assumed reasonable in dilute HF, especially as bonds relating to germanium are shown to be weaker than siloxane bonds.

In the rest of this section sample preparation and the AFM equipment used in this study are described. It can be concluded from the literature survey that in order to compete with the standard optical fibre profiling systems, the etching mechanisms for each dopant and multidopant systems must be determined. This is however outside of the scope of this thesis and the necessary parameters, such as a and n have only been determined for dopant systems used in this study using empirical techniques. The determination of n is shown in Section 3.3.2.4.

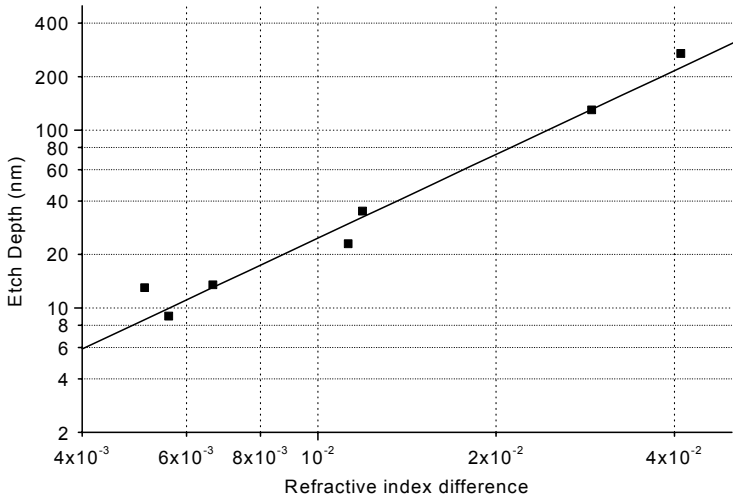

Figure 3-22. A correlation between refractive index difference and the etching depth of Ge-doped core optical fibres etched with 1 vol% HF [81].

Sample preparation of the fibre for AFM measurements involved first stripping off the coating by acetone and cleaving of the fibre by commercial fibre cleaver (York FK-11 or Siemens S46999-M9-A8). The fibres were then etched. The etchant used is this study was aqueous HF. Etching time and etchant concentration was chosen according to dopant type and to obtain optimal etching depths for AFM measurements. Table 3-5 lists the etching conditions used for each fibre type. Samples that were compared with each other were always etched together simultaneously to obtain the same etching conditions. After etching the fibres were rinsed with alcohol. It must be noted here that there is uncertainty about the quality of the etching solution for Samples SS, SA and 1R as the importance of the role of the etching solution concentration was only discovered later on during this study (with Sample 1R and 3R).

Table 3-5. HF concentrations and times used for the fibre samples

Sample	*SS*	*SA*	*1R*	*3R*	*F*
HF vol%	24	24	24	5	5
Time (s)	7	7	5	120	240

A Digital Instrument Nanoscope III AFM was used in this study. A V-shaped silicon nitride cantilever using a square pyramidal tip was used (NT-MDT, CSC21/SiN4/Al). The AFM was operated in contact mode. Figure 3-23 shows a typical topography measured using AFM for a Ge-doped ring fibre used in this study with a profile across the centre of the fibre. Figure 3-24. shows an AFM image of an photonic crystal fibre.

Note that in this case no etching step was required as the fibre is comprised of a single material, i.e. silica.

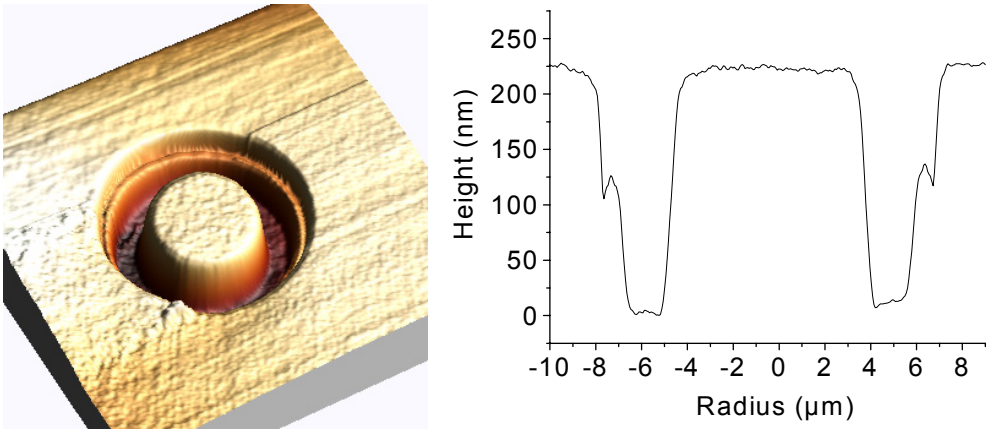

Figure 3-23. (a) AFM 3D plot of etched MCVD ring fibre core, (b) profile across the centre

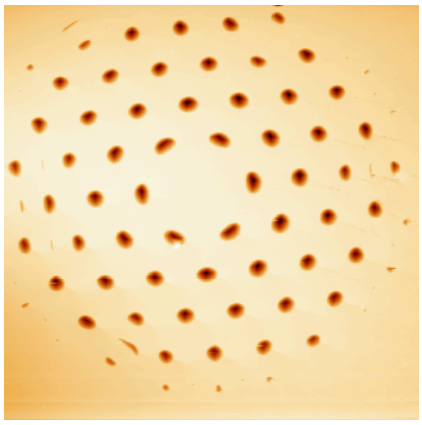

Figure 3-24. AFM image of air silica structured fibre core (2D plot)

3.3.2.4 Determination of etching reaction order

The 3R fibre with 3-rings each doped with different Ge concentration was used to determine the etching reaction order. The fibre was etched at different concentrations of HF for varying times. At constant dopant concentration and etchant concentration the etching depth was linearly dependent on the etching time, see Figure 3-25. The etching rate as a function of the GeO_2 concentration for HF concentrations of 2, 4, 6 and 12M is shown in Figure 3-26 and shows a non-linear relationship. The etching reaction order for each HF concentration was determined by fitting equation $r_{etch} = aC^n$ into the data as shown in the figure. More detailed description can be found in Ref. [103] by Pace *et al.*

Table 3-6. Measured reaction order for different HF solution concentrations

HF solution concentration [M] (vol%)	*Reaction order*	
	n	*1/n*
2 (4)	1.7	0.59±0.02
4 (8)	1.7	0.59±0.02
6 (12)	1.8	0.56±0.02
12 (24)	1.9	0.53±0.02

Once reaction order is known the AFM profiles can be transformed into concentration profiles. In this thesis $1/n$ is frequently stated as AFM profiles are transformed using (etch depth)^(1/*n*). Figure 3-27 shows AFM data of the 3R fibre etched in HF 5vol%, for 2min compared to concentration profile measured from the preform by EDS on SEM for (a) raw data and (b) transformed data with reaction order $1/n=0.6$.

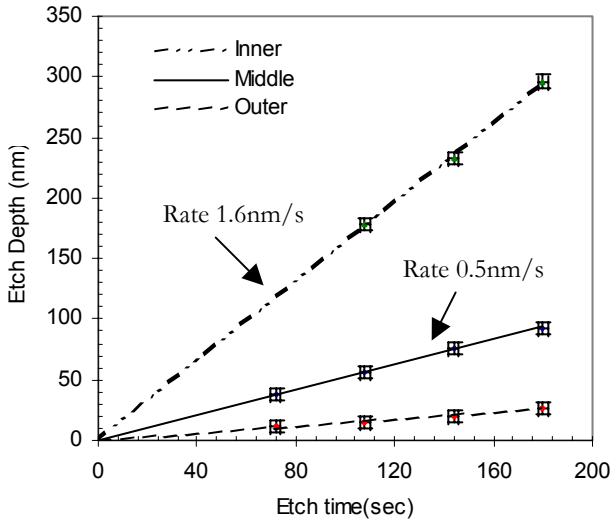

Figure 3-25. Etch depth vs. etch time with 2M HF for inner ring (17mol% GeO_2), middle (8mol%) and outer (4mol%) rings of the 3R fibre. The errors presented in Fig. 3-25 represent the uncertainty in the height measurements from the AFM. The timing error was assumed to be 2 sec. Figure courtesy of P. Pace, University of Melbourne [103].

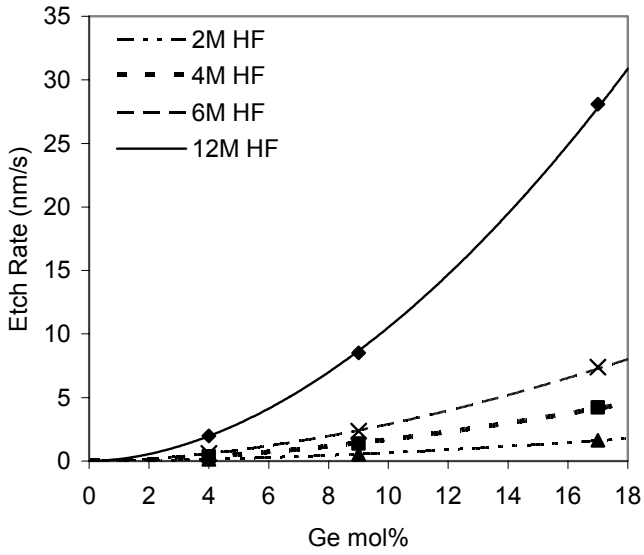

Figure 3-26. Etch rate vs dopant concentration for various HF concentrations for 3R fibre. Figure courtesy of P. Pace, University of Melbourne.

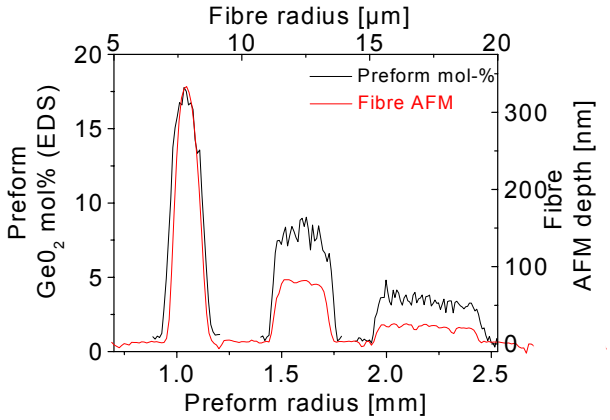

(a)

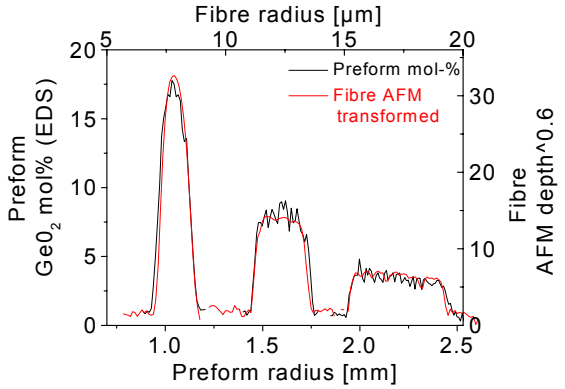

(b)

Figure 3-27. AFM profile comparison (a) without and (b) with transformation for the 3-ring fibre with germania concentration profile (EDS on SEM).

3.3.3 Electron microanalysis techniques

Electron microscopy measurements are based on the interaction between the electron beam and the sample. Electrons either passing through the sample, backscattered from the sample or emitted from the sample can be analysed to obtain structural and compositional information with very high resolution, down to atomic levels. Quantitative compositional maps and profiles can be obtained by analysing X-rays emitted from the sample. Due to the high spatial resolution, electron microscopy techniques are an attractive choice for studying compositional changes in preforms and optical fibres.

In this study Scanning Electron Microscopy (SEM) was used for compositional analysis of the Ge doped preform samples and Electron Probe MicroAnalysis (EPMA) was used for fluorine doped preform. Scanning Transmission Electron Microscopy (STEM) was used for a small number of fibre samples. In SEM and STEM measurements the chemical analysis was performed using X-ray analysis by Energy Dispersive Spectrometry (EDS) whereas Wavelength Dispersive Spectrometry (WDS) was used for the fluorine doped preform due to its superior detection resolution for light weight elements suchs as fluorine. Each technique is discussed in more detail in the following sections. Introduction to the techniques is given along with the measurement procedure and the sample preparation. Discussion of the suitability and limitations of each technique for analysing optical fibre and preform samples is also given.

3.3.3.1 Scanning electron microscopy

A schematic diagram of the electron optical column of an SEM is shown in Figure 3-28. The electron gun is operated at up to 50keV. The generated electron beam is demagnified down to a focussed spot by the condensing lenses (variable electro-magnets). The scanning coils close to the final lens move the beam in the form of a raster on the specimen surface. More details are given in [104]. As the electron beam strikes the specimen surface at a given point, interactions with the atoms in the sample generate a range of signals which are collected and amplified. Figure 3-29 shows a schematic for commonly used signals generated by the interaction between the incident beam and the specimen. The incident electrons are dispersed into an interaction volume causing two types of interaction: (i) elastic scattering where there is angular scattering

but no loss of energy and (ii) inelastic scattering or energy loss event where there is a loss of energy but only very small angular scattering.

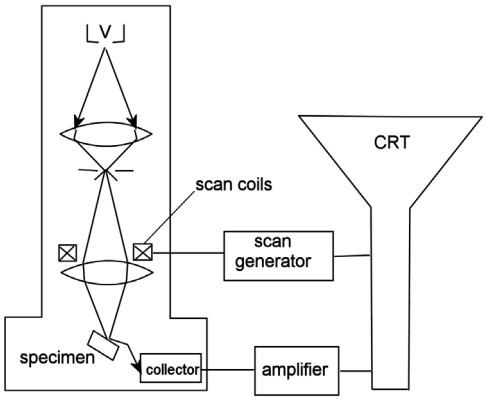

Figure 3-28. A schematic diagram of the electron optical column of the SEM [104].

The inelastic scattering produces backscattered electrons (BSE). Due to their strong interaction with the specimen, BSE provides an image with high atomic number contrast and are mainly used in compositional analysis. Secondary electrons (SE) are produced when a beam of electrons interacts with an atom and causes one of the outer shell electrons to be ejected from the atom. As secondary electrons are generated close to the surface they are mainly used for topographical studies. Images taken in secondary electron mode also have higher resolution as the interaction volume is smaller compared to backscattered electrons. More details can be found in [104, 105].

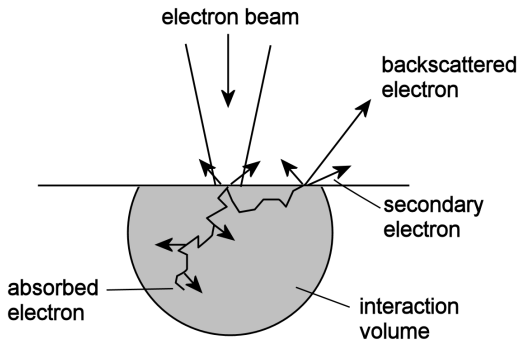

Figure 3-29. Schematic of signals generated by the interaction between the incident beam and the specimen [105].

In this study a Philips XL30 SEM was used to characterise MCVD preform samples and photonic crystal fibres. Due to the interaction volume, the spatial resolution of X-ray analysis was limited to about 4μm hence SEM was used only on preform samples. However the secondary electron imaging has better spatial resolution and was found

suitable for characterising photonic crystal fibres where no compositional analysis was required.

The MCVD preform samples were cut from the preform prior to fibre drawing using a diamond saw, into transverse sections with a thickness of about 5-10mm. The sections were then polished with #200 mesh emery followed by a 6μm and 1μm diamond paste. The samples were coated with carbon to prevent sample charging under the electron beam which was found to be a major problem with uncoated samples. All preform samples were measured under the same conditions with an accelerating voltage of 20keV and spot size of 5, corresponding to a 125nm beam diameter and using BSE mode. Figure 3-30 shows a typical BSE image of a preform sample showing a germanium doped core as a brighter region. Compositional analyses of the MCVD preform samples were performed by EDAX EDS detector attached to the SEM. This technique is based on analysing X-rays emitted from the specimen. The technique and measurement procedure are described in Section 3.3.3.3.

The photonic crystal fibre sample preparation involved cleaving of the fibre using a York FK-11 fibre cleaver. The surface roughness measured (with AFM) after cleaving is well below a micron and no additional polishing was required. The fibres were attached to a holder with carbon tape and carbon glue and coated with carbon. Typical accelerating voltage used was 20keV with spot diameter of 125nm, using SE imaging mode. Figure 3-31 (a) shows a cross-section of an photonic crystal fibre using SE imaging. An image using BSE mode is shown in (b) for comparison.

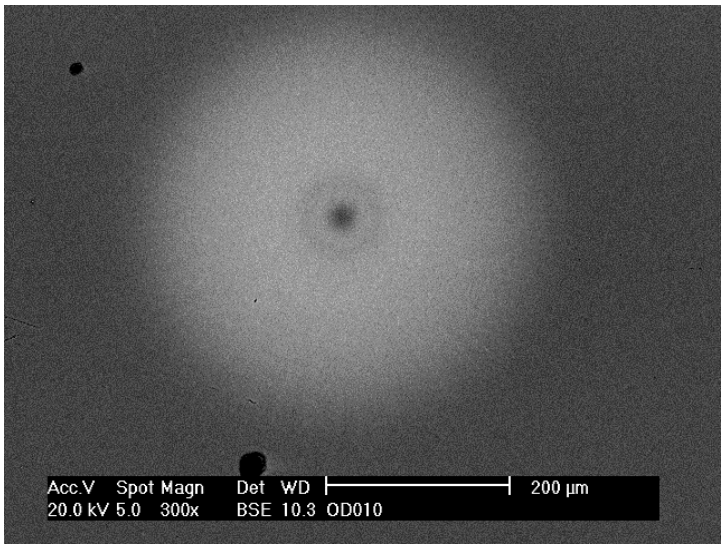

Figure 3-30. BSE image using SEM of a germanium doped preform core.

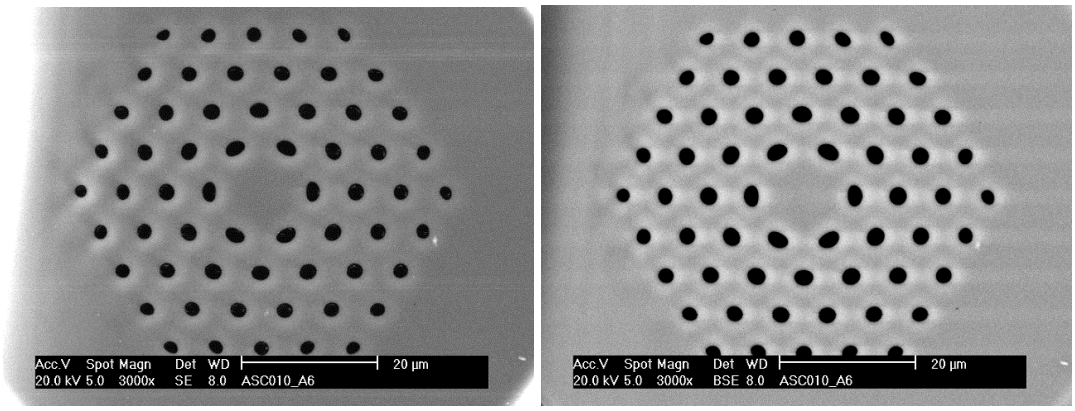

Figure 3-31. Cross-section of an photonic crystal fibre using (a) SE and (b) BSE

3.3.3.2 Scanning transmission electron microscopy

In Transmission Electron Microscopy (TEM) the analysis is based on electrons passing through a thin specimen, <100nm. As the electrons pass through the sample they interact with the material, giving information of its structure and chemical composition. The electrons experience either inelastic or elastic scattering. Elastic scattering forms the basis of TEM. Elastic scattering from crystalline samples gives rise to coherent diffracted rays to produce diffraction patterns which are used to analyse the structure of the sample. If only the transmitted beam (Bright Field Imaging) or one of the diffracted beams (Dark Field Imaging) formed are selectively allowed down the microscope column, an image of the specimen is formed. The image contrast is produced by the variation of intensities of the beam due to the differences in diffraction conditions.

In crystalline samples the images contain interference fringes due to the periodicity of the crystalline lattice and can provide information with near-atomic resolution. Improvements in electron optical lenses have produced microscopes that have point resolutions of less than 2Å. The use of Field Emission Guns (FEG) has improved image contrast and allows reconstruction of images containing information on finer scale than point resolution due to a coherent electron source. Because of the excellent resolution TEM is a popular technique in the structural study of crystalline materials where near atomic resolution can be achieved. For further details see [106].

Unlike in elastic collision, in inelastic collision electrons lose energy when interacting with matter. Measured energy losses due to this interaction can be used as a basis for chemical analysis in TEM equipped with Electron Energy Loss Spectroscopy (EELS).

Compositional analysis can also be done by analysing the characteristic X-rays using EDS detectors similar to the technique used in SEM. Since the TEM specimens are extremely thin the interaction volume is insignificant and spatial resolution in X-ray analysis is close to the beam diameter and submicron resolution can be achieved.

STEM works on the same principle as conventional TEM but the imaging set-up is reversed so that the electron gun is positioned below the specimen and the detector above it. The electron beam is scanned across the specimen to form a raster image as in an SEM. In this study a scanning transmission electron microscope VG HB601UX was used to analyse the MCVD fibre samples that required submicron resolution. The VG-STEM used in this study uses a room temperature FEG that provides the minute probe size and high beam intensity. The gun accelerating voltage used is 100keV and typical tip voltages 3.2-3.5 kV. Electrons are emitted from a facet of radius of about 20-2000Å. An apparent source radius of 5Å can be obtained which can be further demagnified for high resolution analysis. A very high vacuum is required to ensure proper operation of the FEG and to ensure a contamination free chamber and specimen. Typical operation pressures of the gun and column are $1.6\text{-}3.2\text{x}10^{-11}$ mbar and $2.0\text{-}11.0\text{x}10^{-9}$ mbar. Unlike a conventional TEM, VG-STEM does not contain any lenses after the objective but a variety of detectors are provided in the post-specimen chamber. The images are formed from the signals received from the various detectors. More details are given in [106].

The detectors used for the analysis of the optical fibre specimens were bright and dark field to locate the area of interest (e.g. the core) in the specimen and a large solid angle (0.208srad) windowless Link Pentafet EDS for compositional analysis (for more details see Section 3.3.3.3). One of the main challenges in electron microsocopy of fibre samples was the sample preparation. The most common technique used to produce the required thin sections, <100nm, for TEM is ultramicrotomy. In ultramicrotomy a diamond blade is used to cut thin slices from the bulk specimen by pressing the blade through the sample. The advantages of this technique is the relatively easy preparation process and the production of multiple sections within minutes once the sample has been mounted in the cutting stage. Unfortunately this technique was found to be unsuitable for the optical fibre samples. Although the fibres were embedded in resins with similar hardness to glass, no successful sections were obtained due to the brittle nature of glass.

A more promising technique involving various steps of polishing and ion beam thinning was developed at the Electron Microscope Unit (EMU) of the University of Sydney. As the preparation technique is not trivial a detailed description of the technique is given in Appendix II. Both longitudinal (Figure 3-32) and transverse (Figure 3-33) sections were made and thin enough samples were able to be fabricated. Unfortunately it was found that the ion beam thinning preferentially removed the germanium thus affecting the sample concentration profile. It was possible to however sometimes obtain profiles that showed a correct relative concetration profile across the core, but variations in the sample thickness resulted in variation in concentration and any comparison to profiles measured in other samples became thus unreliable. Further improvements in the technque may well improve these aspects and hence the results and procedures are presented here to benefit future studies.

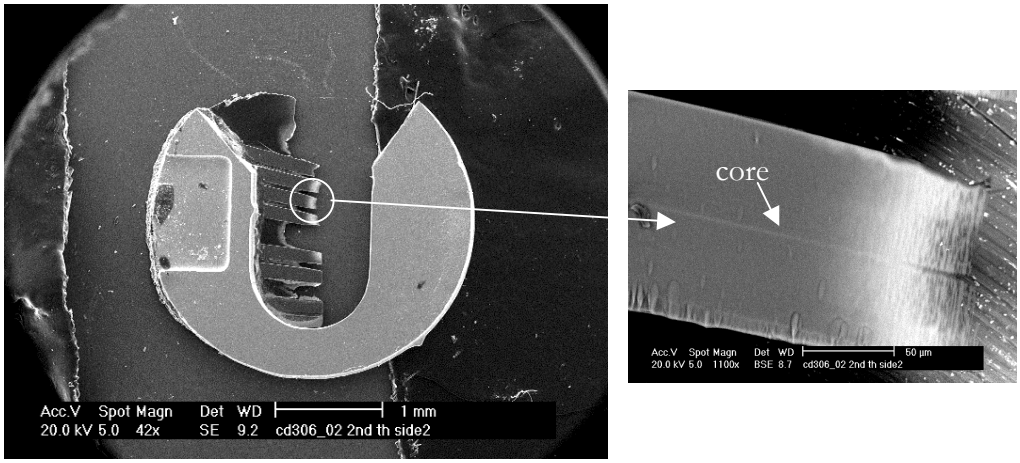

Figure 3-32. SEM image of longitudinal optical fibre TEM specimen with seven fibres. Inset shows magnified image of one fibre.

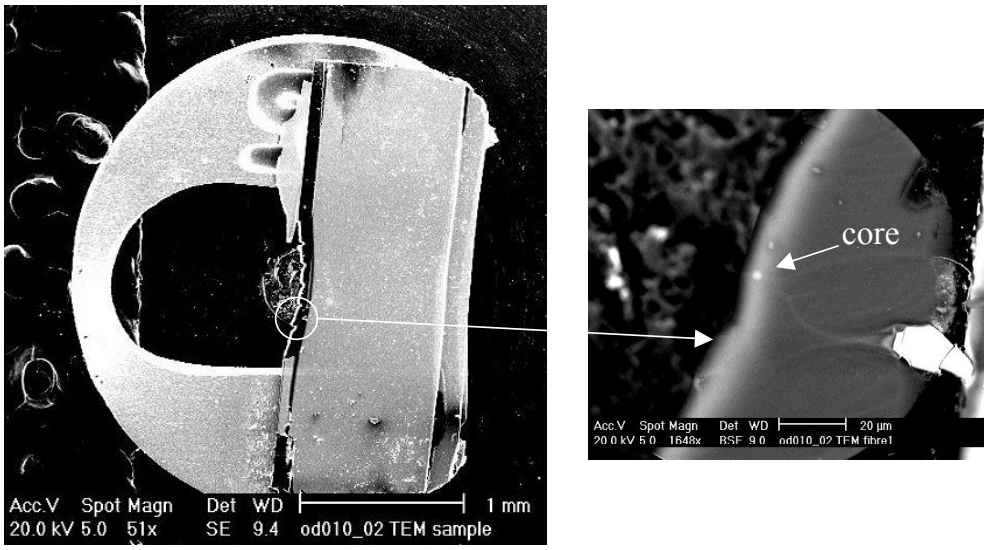

Figure 3-33. SEM image of the transverse optical fibre TEM specimen with four fibres. Inset shows magnified image of one fibre, core shown as bright spot near the edge.

Bright field image of the longitudinal specimen is shown in Figure 3-34. The image is taken at 20,000 times magnification and shows section of the fibre. The core of the fibre can be seen as a slightly darker strip in the centre of the fibre. A cross-sectional compositional line scan was performed perpendicular to the core to obtain a dopant concentration profile. Figure 3-35 shows a similar STEM image of a transverse of a fibre sample at magnification of 50,000 times. The fibre core is seen as a bright area with a dark region at its centre. The transverse sample was found to be more useful as the entire core could be seen and so it could be ensured that the profile was taken across the centre of the core. The actual compositional profiling of the samples was performed using an EDS X-ray detector and is described in the following section.

3.3.3.3 X-ray microanalysis

The X-ray analysis technique is based on analysing X-rays emitted from the specimen. When the electron beam interacts with the specimen some of the high energy electrons will cause ionisation of the atoms in the sample. This means that an electron from an inner shell of an atom is removed. The vacancy is filled with an electron from the outer shell and results in an energy release in the form of an emitted X-ray. The emitted X-rays are called characteristic X-rays and can be used to analyse the composition of the specimen. In order to excite characteristic X-rays, it is necessary for the accelerating voltage to exceed the critical excitation energy. For example 30kV accelerating voltage is sufficient to excite atoms with atomic number of up to 40 [104, 107].

Analysis of X-rays can be done in two ways using (i) Wavelength Dispersive Spectroscopy (WDS) or (ii) Energy Dispersive Spectroscopy (EDS). In WDS a crystal spectrometer is used. The crystal disperses the impinging X-rays in such a way that only photons of selected wavelength reach a counter, which emits a voltage pulse whose height is proportional to the energy of each X-ray photon. A series of interchangeable crystals with different lattice parameters must be used to accommodate a range of emitted X-ray wavelengths (0.1-10nm). To observe characteristic X-ray peaks for all the elements above atomic number nine requires three different crystals. The WDS method provides good resolution for distinguishing between neighbouring spectral peaks and is especially useful in trace element and light element analysis. However, as different crystals are used, this means the mapping of elements across the specimen must be done separately for each crystal, hence slowing the measurement. For details see [104].

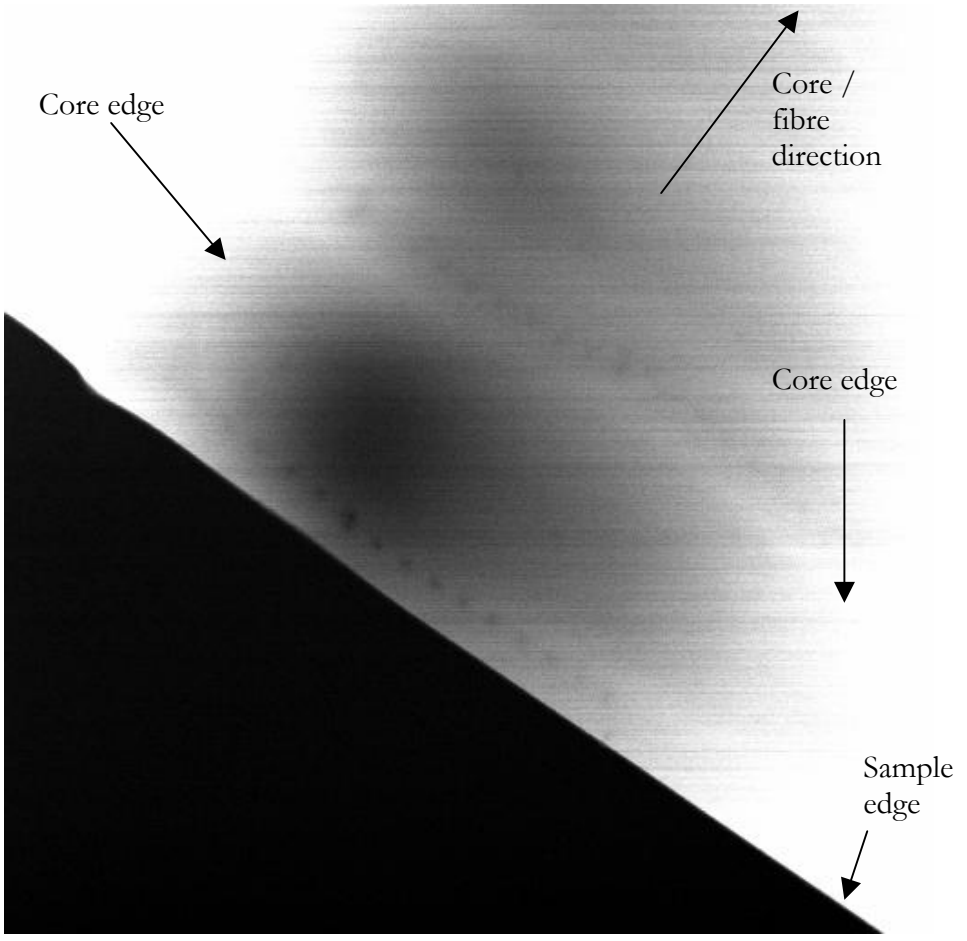

Figure 3-34. Bright field STEM image of the longitudinal specimen, magnification 20,000 times. Core is shown as darker area. Post-run image, where the beam damage can be seen as spots.

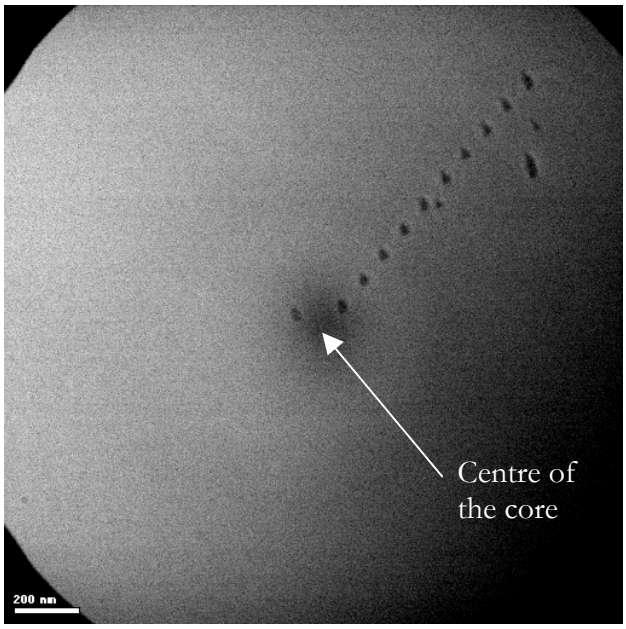

Figure 3-35. Bright field STEM image of a transverse specimen, magnification 50,000 times. Post-run image, the beam damage is shown as line of measurement spots. The dark spot in the centre is the dopant depleted area in the centre of the core.

In EDS a solid-state detector operating as a diode is located close to the sample and receives the whole wavelength spectrum of X-rays emitted from the sample. Usually either lithium drifted silicon or intrinsic germanium detectors are used. As the EDS system can accept simultaneously wavelengths from many elements it is a very fast technique and requires comparatively low probe currents. The resolution of a solid-state detector is about 150eV and unlike WDS cannot be used with X-ray energies less than 1 keV. Due to the large interaction volume in a bulk sample, the collection efficiency is decreased and resolution lost in detection. However, as all data is collected simultaneously from a single point, the EDS method is favoured in material composition studies relying on mapping and line scan analysis [104, 107]. For this study the EDS method was used for both MCVD preform and fibre samples. Typical detection resolution of an EDS is 0.1w% (0.2mol% GeO_2 in SiO_2). WDS technique was used for the fluorine doped preform sample. Significantly higher detection limits (0.01w%) are achieved with WDS.

The compositional profiles of the Ge-doped preforms were performed with an EDAX EDS spectrometer attached to the Phillips XL30 SEM microscope. A 10 mm section was taken from each preform from a location well above the hot-zone after drawing or if two draws were conducted, between the drawn sections. The dopant concentration

profiles could then be compared with the corresponding refractive index profiles to determine for example the suitability of the refractive index profiles for use in diffusion effect comparisons. The obtained dopant concentration profile also provided the required molar concentrations for the diffusion calculations. An automatic line-scan operation was used to produce compositional profiles across the core of the preform. The beam dwell time was adjusted to 30ms and typically 20-30 points were measured across the region of interest. A typical spectrum of a single measurement point in a germanium doped core is shown in Figure 3-36. The ratio of germanium to silica atoms can be obtained from the relative peak heights of Ge and Si signals, marked in the figure. Figure 3-37 (a) shows a BSE image of the core with a line marking the direction of the EDS line scan. Figure 3-37 (b) shows the resulting GeO_2 concentration profile computed from the spectra. The spatial beam positions were calibrated with a suitable calibration grid measured under the same measurement conditions as the preform samples (Figure 3-38).

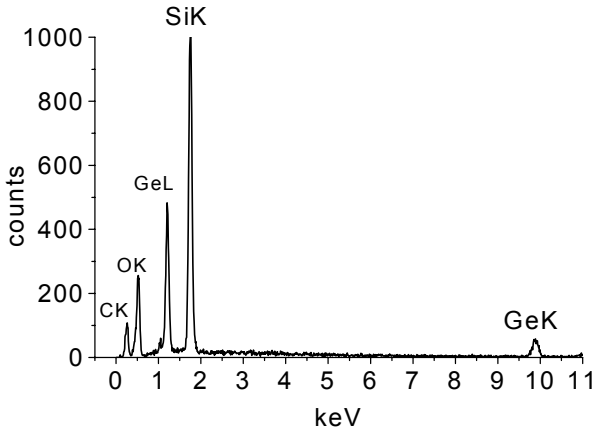

Figure 3-36. A typical EDS spectra of a Ge-doped preform core.

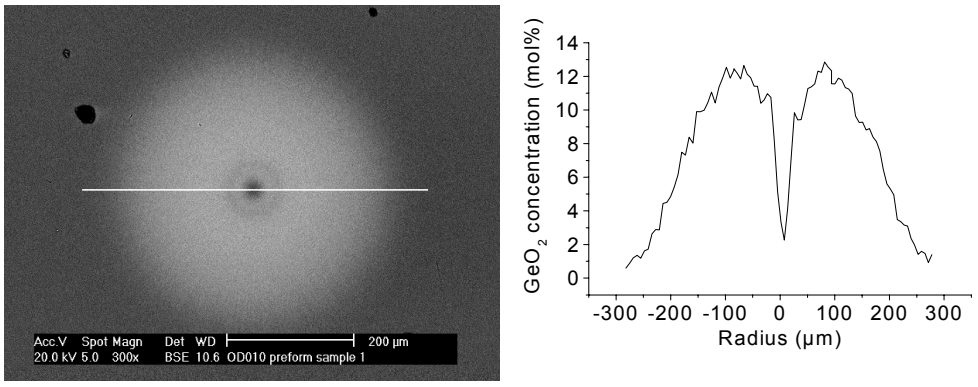

(a) (b)

Figure 3-37. (a) SEM micrograph of a preform core, line indicates the EDS line scan direction and (b) the corresponding GeO_2 concentration profile across the core.

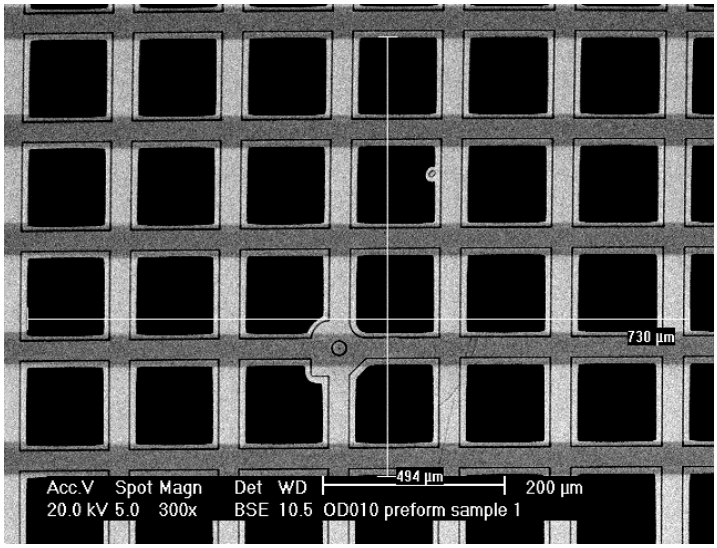

Figure 3-38. Calibration of the spatial line scan data on SEM showing six horizontal and four vertical mesh units. Mesh used 200/in.

The resolution of the SEM depends on the beam diameter, the interaction volume and signal-to-noise ratio, which in turns depends on the beam current, signal collection and amplification process [105]. The interaction volume for a given material can be simulated using Monte Carlo methods. A simulation program using [108] a Monte Carlo method was used to estimate the interaction volume of the measurements. The material selected for the simulation was pure silica. The accelerating voltage was chosen as 20keV and beam diameter 125nm, which are typical values used in the real measurement. The estimated diameter of the interaction volume was up to 4µm. To illustrate the effect of the interaction volume, an optical fibre core of diameter 3µm was measured using EDS on SEM and compared to EDS on TEM measurement for the same fibre, Figure 3-39. It is clearly seen from this figure that the measurement done on SEM is substantially averaged compared to the TEM measurement due to the large interaction volume of the SEM sample.

The compositional profiles of the fibre samples were analysed using a Link Pentafet EDS spectrometer attached to a VG-STEM microscope. An automated line scan feature was used to obtain quantitative element composition profiles across the region of interest, e.g. the core. Typical count rates used were 2.2-3.0 kcps, with 20-30 live second collection times per analysis point. A single profile usually had 10-20 points with about 80-160nm distance between them. The maximum profile length, ~1.5µm, was determined by the smallest magnification possible for the detector, x400,000. Due to

this limitation typically 3-4 profiles had to be measured across the region of interest (e.g. the core). The relative concentrations of the elements were automatically calculated from the spectra.

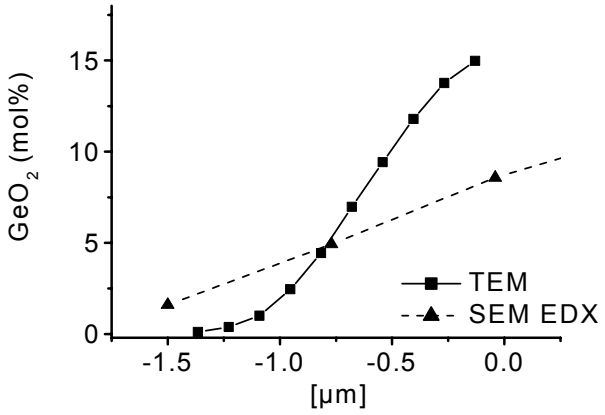

Figure 3-39. Illustration of the effect of interaction volume. EDS measurements with SEM and TEM for a Ge-doped fibre core. Zero on the x-axis is the centre of the core.

The electron beam typically causes some damage on the specimen and as a result the measured points can be seen in the sample. Figure 3-40 shows the centre of a core across which two line scans have been made. The exact distance between the points and the position of the profile in the sample can be determined using these markings. The germanium concentration profile across the asymmetric fibre (SA) core consisting of four line scans is shown in Figure 3-41.

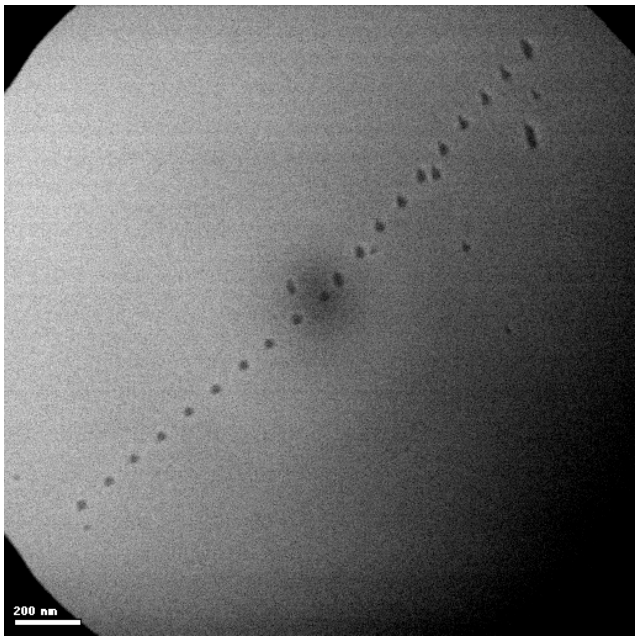

Figure 3-40. Marks after EDS line scan analysis on the asymmetric core fibre STEM sample

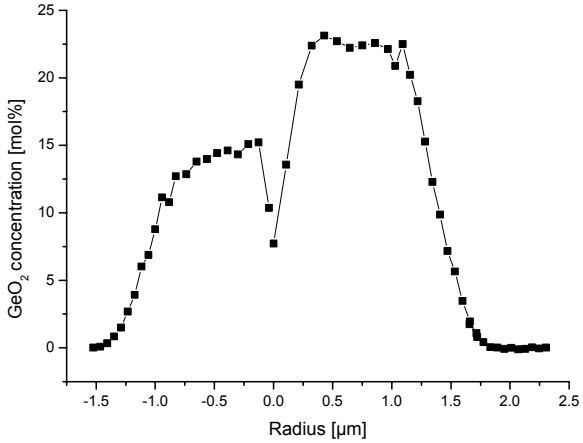

Figure 3-41. Concentration profile across the asymmetric core fibre measured with EDS on STEM

The fluorine doped preform samples were analysed using WDS on EPMA (Cameca SX50). Crystals used were TAP, PC4 and PC0. Fluorite, CaF_2, was used as a standard for fluorine measurements, the preform pure silica core as standard for silicon and oxygen. Quartz and sanidine ($KAlSi_3O_8$) standards were also used for Si and O measurements. Measurements at varying magnifications were conducted (2,200 – 800,000 times) at voltage and current of 8kV, 20nA and 60nA.

3.3.4 Other techniques

Due to the vast number of PCF samples and the high refractive index difference of silica and air, optical microscopy was used to characterise the majority of PCF geometries. An Olympus BH-2 microscope was used. Prior to imaging the fibres were cleaved using a York FK-11 cleaver and attached to a fibre holder. Images on both reflection and transmission mode could be obtained by illuminating the sample from the top or through the bottom end-face (Figure 3-42). In order to measure geometrical properties the reflected light should be used as in transmission mode holes appear larger due to the excitation of modes within the structure (for details see Ref. [70]). The resolution of the optical microscope is however limited to ~0.5nm. Techniques such as electron microscopy and AFM were also used to characterise a selection of the samples, however due to the problems in equipment availability, location and sample preparation their application was limited. As seen in Figure 3-42 and as mentioned in Section 5.3.5 the hole size can vary depending on its radial position. For the results presented in

Chapter 5 the hole size is determined as the average hole size in the second row of holes from the core unless otherwise stated.

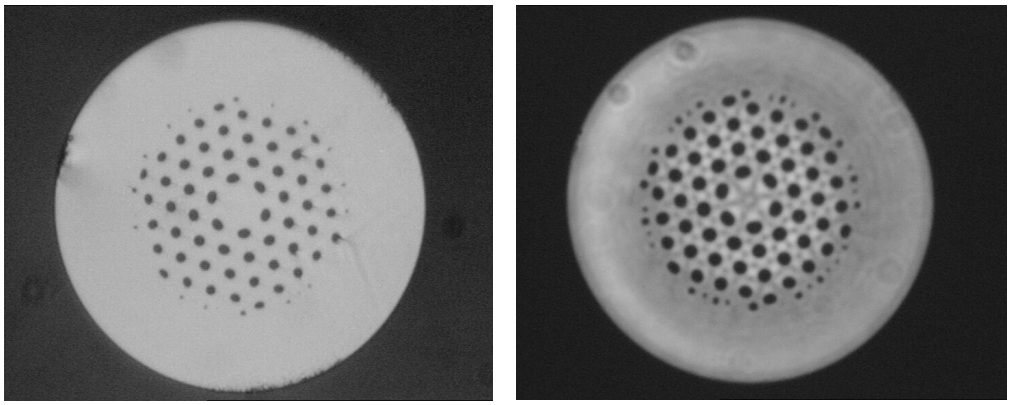

(a) (b)

Figure 3-42 Optical micrograph of a PCF fibre in (a) reflection and (b) transmission mode.

CHAPTER 4 DOPANT DIFFUSION DURING FIBRE DRAWING

4.1 Background

4.1.1 Structure of silica glass

Glass is an amorphous solid i.e. a solid that does not exhibit the long-range order of atoms found in crystalline materials. When glass is cooled it undergoes a gradual glass transformation during which the viscosity of glass increases rapidly and results in 'freezing in' an amorphous atomic structure if the cooling rate is fast enough. The structure, and therefore the properties, of the solid glass differ according to the cooling rate. The fictive temperature, T_f, characterises the glass structure, which represents the supercooled liquid structure at T_f. The glass transition temperature, T_g, is defined experimentally as the temperature at which the glass properties change to melt properties and is not necessarily a particular temperature but can also be a range. More details are given in [109].

The traditional model for the structure of glass was first suggested by Zachariasen [110]. According to the model the glass structure is formed by a continuous random network (CRN) of network forming oxides such as SiO_2, GeO_2, B_2O_3 and P_2O_5. A schematic of such structure in two dimensions is shown in Figure 4-1. The unit cell of the structure is the same as for the corresponding crystal such as the tetrahedron unit, SiO_4, for silica glass. These basic building blocks connect to each other in a way that lacks long-range order to form a random network. Other models for glass structure have also been suggested. The randomly dispersed crystallite model by Lebedev [111] deviates most from the CRN model. Although the CRN model describes well the structure of simple glasses, there are examples of multicomponent glasses that show microcrystalline-type inhomogeneities [109]. Some aspects of the glass structure are still under debate; one such being the medium range order of glass, MRO (from 10 to 20Å) [112-116].

The conventional CRN structure, however, can be used to describe the less complex glasses such as SiO_2 and GeO_2. The basic unit, SiO_4, of the structure in silica glass is presented in Figure 4-2, where two such units are linked by a bridging oxygen atom.

The unit cell consists of a tetrahedron, which has the silicon atom in the middle and four oxygen atoms in each corner. Each of the oxygen atoms is bonded to two silicon atoms, forming the SiO_2 network structure. The Si-O bond length is 1.6 Å and the tetrahedral angle is 109.5±0.7°. The variation in the network arises from the intertetrahedral bond angle, β, and bond torsion angles, α, that vary significantly, creating disorder in the structure. In the medium range, features such as chains and rings characterise the glass structure.

Germania glass has a similar cell unit to that of silica, where the silicon is replaced by a germanium atom. The Ge-O-Ge angle and bond length varies from that of SiO_2. In binary GeO_2-SiO_2 at small concentrations of GeO_2 the network is characterised by that of silica glass, however at a concentration range from 27 to 80mol% GeO_2, regions exist that are formed by the mixed Ge-O-Si bonds, altering the glass structure [117].

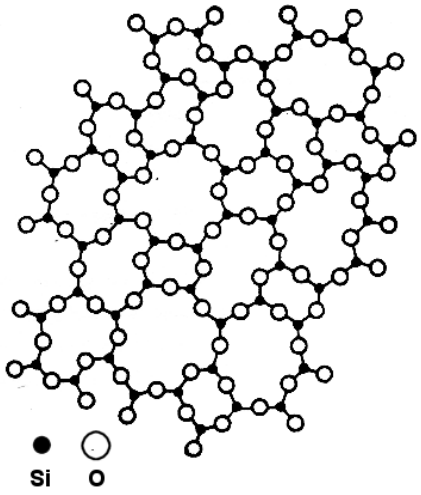

Figure 4-1. A random SiO_2 network, Varshneya [109].

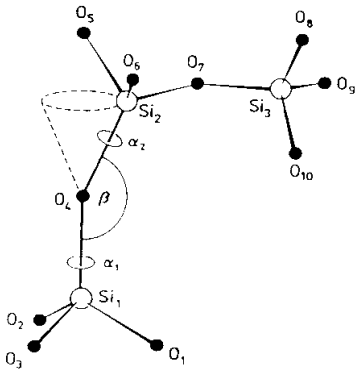

Figure 4-2. Three unit cells for silica glass in a glass structure, Varshneya [109].

Silica glass used in optical fibres also contains impurities such as Na, Ca and Al. Aluminium is used as a dopant for example in rare-earth doped fibres. Figure 4-3 shows a schematic of how a network modifier such as Na, K and Ca is positioned in the glass structure. The cations are located in the holes within the network, forming ionic bonds with the non-bridging oxygen atoms. Aluminium is a so called intermediate glass former, it does not form glass by itself, but acts like a glass former when combined with other glass forming elements. Other intermediate glass formers are e.g. Mg and Zn.

The properties of the glass depend on its structure. In 'simple' binary mixtures many of the glass properties such as density and refractive index can be estimated by rule of addition where the property is linearly dependent on the composition of the glass. Figure 4-4 shows the refractive index change with molar concentration of GeO_2-SiO_2 binary glass.

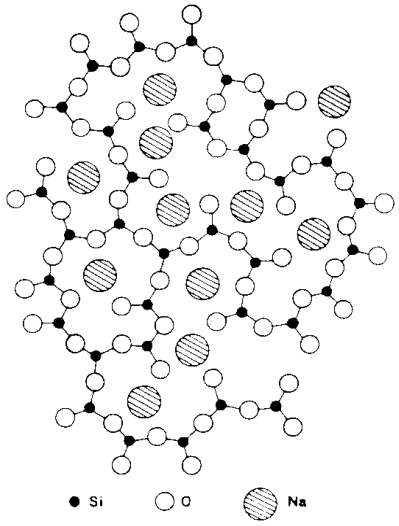

Figure 4-3. Network modifier within a glass structure [109].

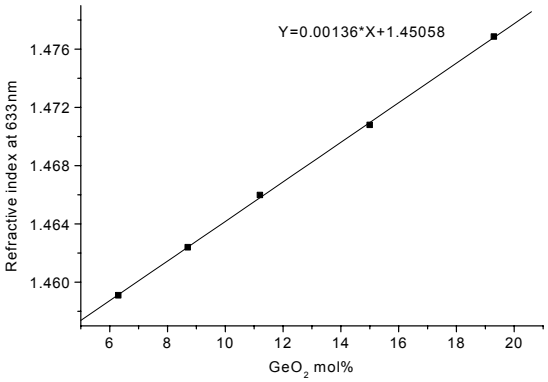

Figure 4-4. Refractive index of GeO_2-SiO_2 binary glass [118].

4.1.2 Mass transfer by diffusion

Diffusion is migration of an individual component in a mixture under the influence of a physical stimulus. Diffusion describes this movement in gases, liquids and solids. Typically diffusion arises from concentration gradients, where the component diffuses towards a lower concentration and if enough time is given equalises the concentration. Diffusion can also be caused by an activity gradient as in reverse osmosis, by a pressure or temperature gradient or by the application of an external force [119]. Here we consider only diffusion arising from concentration gradients.

In solids, diffusion can be presented in two ways. In crystals, migration of species can be described with a so-called atomistic model where point-defect interactions form the basis of the diffusion theory. In amorphous solids, such as glasses, diffusion can be presented by Fick's law. Fick's law states that the flux of diffusing species is proportional to the concentration gradient of the species, Eq. (16) [120].

$$J = -D\frac{\partial c}{\partial x}, \tag{16}$$

where J is the flux of the diffusing species through unit area of surface in unit time (mol/m^{2}s), c is the concentration of the species (mol/m^3), D is the diffusion coefficient (m^2/s) and x is the spatial coordinate in the diffusion direction (m).

If the diffusion coefficient is constant, then the diffusion equation in isotropic media at rest can be presented by Eq. (17) in one-dimension [121].

$$\frac{\partial c}{\partial t} = D\frac{\partial^2 c}{\partial x^2}, \tag{17}$$

where t denotes time (s).

For a case where the initial concentration profile is pulse like, where $c = 0$ everywhere else except at $x = 0$, the solution for Eq. (17) is [121]

$$c = \frac{M}{2(\pi Dt)^{1/2}}\exp\left(\frac{-x^2}{4Dt}\right), \tag{18}$$

where M is the total amount of substance diffusing. The expression is symmetrical with respect to $x = 0$ and concentration tends to zero as x approaches infinity positively or negatively for $t > 0$, see Figure 4-5 (a). The amount of substance diffusing remains constant and equal to the initial amount.

If the initial concentration profile is stepwise with thickness $2h$, the solution of Eq. (17) is [121]

$$c = \frac{1}{2} c_0 \left\{ erf \frac{h - x}{2\sqrt{Dt}} + erf \frac{h + x}{2\sqrt{Dt}} \right\}, \tag{19}$$

where c_0 is the initial concentration.

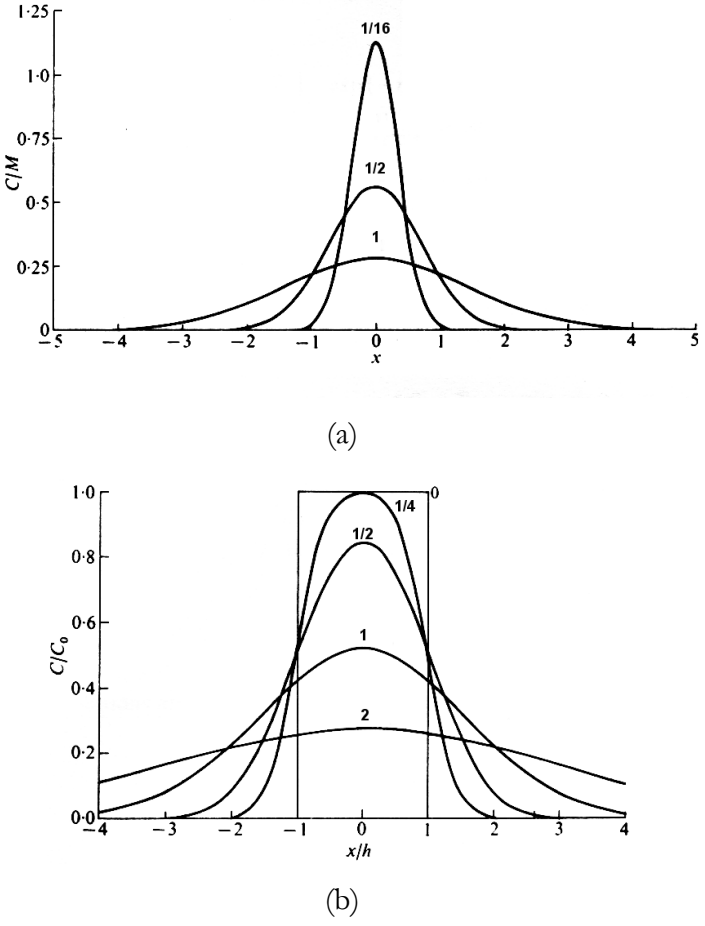

Figure 4-5. (a) Concentration profiles for an instantaneous plane source. Numbers on curves are values of Dt. (b) Concentration profiles for an extended source of limited extent. Numbers on curves are values of $(Dt/h^2)^{1/2}$ [121].

If the bulk fluid is in motion, the relevant momentum terms must be included in the diffusion equation. The resulting diffusion equation in two-dimensions is [122]

$$\frac{\partial c}{\partial t} + v_x \frac{\partial c}{\partial x} + v_y \frac{\partial c}{\partial y} = D\left(\frac{\partial^2 c}{\partial x^2} + \frac{\partial^2 c}{\partial y^2} \right), \tag{20}$$

where v_x and v_y are velocities in x and y direction respectively. The above equations assume that the diffusion coefficient, D, is constant. When the dopant diffusion in glasses is considered, there are two possible cases, which deviate from this assumption. The first one is the temperature dependence of the diffusion coefficient. The temperature dependence of the diffusion coefficient is a more radical function for solids than for liquids or gases. Typically the diffusion coefficient shows an Arrhenius temperature dependence as described by Eq. (21) [123]

$$D = D_O \exp\left(-\frac{E}{RT} \right), \tag{21}$$

where T is temperature (K), D_O is pre-exponential term (m^2/s), E is activation energy (J/mol) and R is the gas constant (J/(molK)).

The assumption of constant diffusion coefficient also fails if the diffusion coefficient depends on the concentration. This can arise if the magnitude of the concentration affects the local environment of the diffusing species. This is observed with macromolecules, for example proteins, which have very different diffusion coefficients at concentrated solutions [123]. In glasses it is possible that at low dopant concentrations the local environment of the dopant is characterised by the host glass, but above some critical concentration (or a range) the local structure is dominated by the dopant hence altering the diffusion coefficient. Ionic diffusion in glasses has been reviewed by Frischat [120]. Specifically the diffusion of sodium ion in silicates has been extensively studied. The studies show that the diffusion coefficient is strongly dependent on sodium concentration and that the fictive temperature of the glasses affected results due to structural changes in the environment of the diffusing ion.

The current study considers dopant diffusion as the primary source of concentration profile change during drawing. There are however other means by which the dopant

distribution can change at high temperatures when interfaces are considered. An interface between two fluids under thermodynamical equilibrium will take a specific geometrical form, which is compatible with mechanical equilibrium. If there is any deviation from this form, the system will seek to attain the equilibrium condition. The forces acting on the interface are those resulting from the surface tension of the fluid-fluid interface and the pressure of the fluids. If the densities of the fluids are different, gravity will play a role as well. A simple example of equilibrium shape of an interface is a mass of fluid immersed in another fluid, where the equilibrium shape is a sphere giving the minimum surface energy (least surface area) for a given volume [124]. Similarly in glass heated to sufficiently high temperature, interfaces that deviate from their equilibrium shape will tend to change towards that equilibrium shape. This has been observed for example in asymmetric optical fibre structures such as bow-tie fibres during drawing. These changes can however be minimised by using low enough temperatures hence increasing the viscous forces preventing flow.

There are also other ways than geometrical to minimise surface energy at an interface. In multicomponent systems segregation of species has been observed [125] based on the individual surface tensions of the species. This phenomenon has been observed in grain boundaries of metals [125] as well as in fluoride glasses [126]. This phenomena has not however been reported for silica glasses and is not considered further.

Other changes that involve flow of glass can occur if sufficient asymmetric thermal gradients are created whilst the glass is in motion (e.g. during drawing). The temperature gradients will cause viscosity gradients and induce velocity differences between regions of glass resulting in deformation of the dopant distribution. The processes are however carefully designed to avoid this and this is not typically observed in standard fibre manufacturing.

4.1.3 Literature review

This section presents a literature review of dopant diffusion in silica glass. The notations in the literature vary greatly and a few words are in place before presenting the review. The units for the diffusion coefficient, D, are typically reported either in m^2/s or cm^2/s. The units for activation energy, E, in the Arrhenius equation (21) are

J/mol, except for some cases where E/R has been replaced by E/k (k is the Boltzmann constant), in which case the units for E are in eV. The units for the pre-exponential coefficient D_0 are same as that of the diffusion coefficient. The magnitude of D_0 however changes if the authors have chosen to present the Arrhenius relation in base 10 or 2 logarithmic form instead of the natural logarithm. This applies to the activation energy as well. For clarity all the units reported here have been converted to m^2/s for D and D_0, kJ/mol for E and the expression in Eq (21) is used for the Arrhenius relation. In the literature the Arrhenius plot (logD vs. 1/T) is used frequently to compare the data, as D_0 and E can be derived from the linear fit of the data. Arrhenius plots are also used here to compare the data. The individual data points are not presented but linear fits are shown calculated from D_0 and E and plotted as lnD vs. 1/T consistent with Eq. (21).

Primarily the need for understanding the dopant diffusion in optical fibres arose from requirements for reduced fibre coupling losses and the interest in thermally expanded core (TEC) fibres. The focus on these applications meant that the diffusion experiments were mostly performed on drawn fibre by heating it in a controlled environment, and only a few studies have looked at the effect of the drawing process. Table 4-1 gives a summary of all relevant studies conducted up to date on diffusion in optical fibres. The most popular dopant-substrate system studied in optical fibres has been germanium in silica, but a number of diffusion studies have also been made in fluorine-doped silica. Only a handful of studies could be found for boron, phosphorus, aluminium and rare earth dopant diffusion. The main obstacle in studying the dopant diffusion in fibres is the small size of the fibre samples. As methods in microanalysis have advanced and quantitative data can now be achieved on the nanometre scale, some new studies have arisen where dopant diffusion in optical fibres plays a role.

The following sections summarise the findings from the past literature on dopant diffusion in optical fibres and preforms. These sections are organised according to dopant species and each section includes an Arrhenius plot of reported diffusion coefficients when available. As will be shown, there is significant scatter of the results and the possible reasons for such variations are discussed.

Table 4-1. Summary of past studies in dopant diffusion in optical fibres and preforms

Diffusion coefficients and observations D, D_0 [m^2/s] and E [kJ/mol]	Measurement technique	Ref.
Germanium		
• Diffusion observed	EDS, SEM	[6]
• No diffusion observed, estimation of $D<1.0\times10^{-18}$ (1400°C)	EDS, SEM	[127]
• $D=1.8\times10^{-14}$ (1790°C)	RIP, splice loss	[128]
• Diffusion observed in fused couplers (1100°C)	EDS, SEM	[129]
• Various Ge-doped SM fibres studied, range: $D_0=10^{-11}$-10^{-7}, E=150-290	EPMA	[130]
• MFD expanded from 5 to 30μm (TEC) (1700°C)	MFD meas.	[131, 132]
• Splice loss minimised using diffusion	Splice loss	[133, 134]
• No diffusion observed during fibre drawing	TEM, EPMA, EDS, RIP	[8, 9]
• Incorporation of F increased diffusion of Ge	Preform RIP	[135]
• MFD expanded from 10 to 40μm (TEC) (1300°C)	MFD meas., NFP	[136]
• $D_0=2.4\times10^{-6}$, E=310	EPMA, mode shape	[137]
• MFD expanded from 8 to 17μm (1000°C)	MFD meas., FFP	[138]
• Diffusion rates 1.86 times higher when codoped	Splice loss, MFD msr.	[139]
• Diffusion observed in tapered fibre	Etching and AFM	[102, 140]
• Indirect observation of diffusion (1400-1700°C)	Optical signal absorption	[141]
Fluorine		
• $D_0=1.52\times10^{-8}$, E=183	RIP, splice loss	[128]
• $D_0=1.2\times10^{-5}$, E=350, in preforms	EDS, SEM	[142]
• Diffusion observed and coefficients from Ref. [142] confirmed	RIP, splice loss	[143-145]
• $D=5\times10^{-17}$ (1300°C)	EPMA	[130]
• $D_0=8.3\times10^{-5}$, E=369, P-co-doped: $D_0=5.2\times10^{-6}$, E=287, OH content enhances diffusion	EPMA in preforms	[146]
• Diffusion observed (700, 1000°C)	Etching and AFM	[97]
• $D_0=3.7\times10^{-7}$, E=312, Ge-co-doped $D=2\times10^{-17}$ (1010°C), P-Ge-co-doped	RI modulation in gratings	[147]
• OH increases diffusion, Ge-co-doped, (1000°C)	SIMS	[148]
Boron		
• No diffusion observed (1200-1400°C)	EPMA	[130]
• $D_0=1.4\times10^{-8}$, E=210	EPMA, mode profile	[137]
• $D=10^{-12}$-10^{-14} (1800-2100°C) and varied B conc.	EPMA in preforms	[149]
Phosphorus		
• $D_0=8\times10^{-13}$, E=114	EDS, SEM	[127]
Aluminium		
• No diffusion observed	SIMS	[150]
• $D_0=4.8\times10^{-3}$, E=479	EPMA in preforms	[149]
Rare earth elements		
• Er, no diffusion observed	TEM, EPMA, EDS, RIP	[9]
• Yb, $D_0=4.8\times10^{-3}$, E=479	EPMA in preforms	[149]

4.1.3.1 Germanium diffusion in silica

Germanium is the dopant that has most frequently been reported in diffusion studies in optical fibres. As noted in Table 4-1 there are a number of studies, which show diffusion of germanium in optical fibres and some that report no observation of such diffusion. As diffusion depends on the temperature and time of the heat treatment, it is quite possible that low enough temperatures and/or times have been used in these studies to avoid diffusion. The resolution restrictions in measurement techniques can also limit the ability to observe diffusion.

Diffusion of germanium in silica optical fibres has been observed, for example, during splicing [128, 133, 134], manufacture of fused fibre couplers [102, 129, 140] and beam expanding fibres [130, 132, 136, 138]. The heat treatment temperatures vary from 1000 to 2000°C although a majority of the reported data is in the lower part of this range. Heating times vary from seconds to tens of hours and heating techniques vary according to the application. Measurement techniques are listed in Table 4-1 and include microanalysis and optical measurement techniques, such as MFD or loss measurements. The fibre samples used vary by manufacturing method (e.g. MCVD or VAD), germanium concentration and cladding composition. From the past studies a general conclusion can be made that germanium does diffuse under certain conditions. The important question is whether reliable diffusion data can be found from literature, which can be used for estimating germanium diffusion under a particular heat treatment such as fibre drawing.

Figure 4-6 shows the available data from past studies where diffusion coefficients have been reported. First, it is worth noting that the reported values have been measured at lower temperatures than typical fibre drawing temperatures. As diffusion has been reported to follow an Arrhenius law, it should be possible to extrapolate the data to higher temperatures, given that the structure of glass does not change significantly. There is noticeable scatter in the reported data. The variation in values reported for the activation energy, E, manifests itself in variations of the slope of the lines in the figure. This results in even larger variation of the diffusion coefficient if the data is used to extrapolate values to higher temperatures.

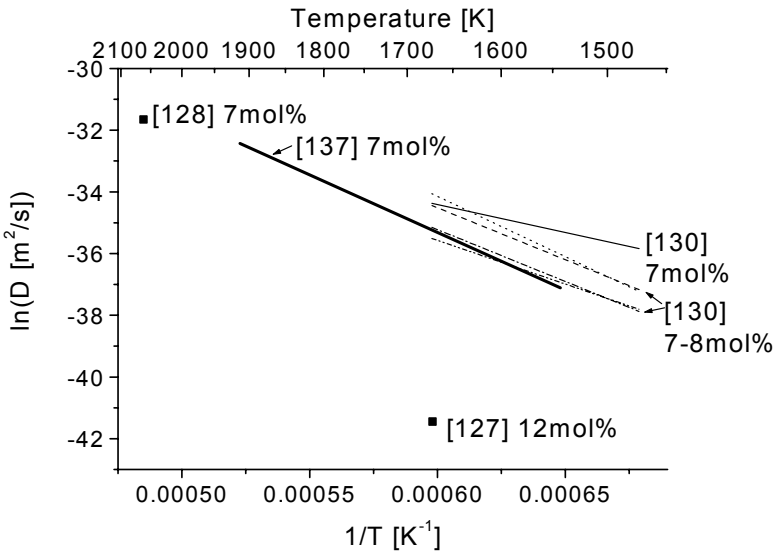

Figure 4-6. Arrhenius plot for germanium diffusion in silica reported in literature.

Diffusion coefficients for the greatest temperature range (1300-1600°C) were reported by Yamada and Hanafusa [137] who studied diffusion to create a mode shape convertor in PANDA fibre. The diffusion coefficient reported by Krause *et al* [128] agrees reasonably well with this data. Also, some of the results by Shiraishi *et al* [130] overlap with those of Yamada and Hanafusa [137]. Significant scatter of the results is, however, observed in their study. For example, the diffusion coefficient varied from 1×10^{-15} to 5×10^{-16} m^2/s at a given temperature. The fibres studied in this paper were varying in both fabrication method (VAD and MCVD) and their relative index difference (0.23-0.37%). Due to the number of variables, no clear cause for the scattered diffusion results was obtained. There is one reported value for Ge diffusivity that greatly disagrees with all the above studies. Fleming and Kurkjian [127] studied diffusion in MCVD fibres with binary GeO_2-SiO_2 cores. The study concluded that, within measurement accuracy, there was no evidence of germanium diffusion as a result of their heat treatment and calculated the diffusion coefficient plotted in Figure 4-6 based on this observation.

It cannot be said with certainty why such a scatter is reported for Ge diffusivities, but some likely reasons are given. There are a number of variables that could affect diffusivity of Ge, such as the manufacturing method of the preforms. For example preforms manufactured by the VAD method contain significant amounts of chlorine,

which could affect the diffusion. Also fibres made by different techniques can have different fictive temperatures affecting the structure of glass and hence the diffusion coefficient. The Ge concentrations of the reported fibres are fairly similar and thus should not affect the diffusion coefficient significantly. The cladding composition can affect Ge diffusion from the core in a similar way to the impurity content, by altering the diffusion environment. No details were available for some of the fibres, but it is likely that the P and F cladding doping levels varied between the fibres. It is also possible that the limitations in measurement resolution caused significant errors in the reported values. EDS and EPMA techniques typically have spatial resolution varying from one to several microns and detection limits can be as high as 1% (Section 3.3.3). The spatial resolution in optical measurements is unlikely to be better than 0.5μm. Despite the scatter in the results, some agreement was found among the various studies and approximate diffusion estimations could be based on these values.

4.1.3.2 Germanium diffusion in codoped silica

The studies reviewed in Section 4.1.3.1 were made for germanium surrounded by pure silica or a phosphorus and fluorine doped silica cladding. The following paragraphs describe studies made on germanium diffusion in codoped fibres. Not many publications are dedicated to this area, however two subjects can be identified: (i) germanium diffusion in PANDA fibre, which has a germanium doped core with two boron doped circular regions in close proximity to the core and (ii) rare-earth doped fibres, with high NA germanium doped cores. For a general description of the above-mentioned fibres see Chapter 2, Section 2.2. As discussed previously the local environment of the diffusing species can have a significant effect on the diffusion coefficient. This section looks at whether there is evidence in past studies on the effects of co-doping on Ge diffusion. If this was the case, some of the scattered results reported in the previous section might be explained for example via effects of cladding dopants.

Germanium diffusion in PANDA fibre was studied by Shiraishi *et al* [130]. As the boron-doped regions create stress across the core, they were able to study the effect of stress on dopant diffusion by measuring the germanium concentration profile in both perpendicular and parallel direction to the boron-doped regions. The study concluded that germanium diffusion was not affected by stress. This result disagrees with the

earlier study by McLandrich [129] who reported that there might be a mechanism enhancing the diffusion of Ge, which originates from axial stress applied to fibres during a tapering process. Germanium diffusion in PANDA fibres was also studied by Yamada and Hanafusa [137]. Both germanium and boron were found to diffuse under the heating conditions and overlapping diffusion of both germanium outwards from the core and boron towards the core was reported. No statement was made however whether boron affected the diffusivity of germanium. As discussed previously, their germanium diffusivities do agree to a degree with other reported values, Figure 4-6, indicating that boron did not greatly alter the diffusivity.

The rare-earth doped optical fibres typically consist of a core doped with either one or two rare-earth dopants as well as aluminium and germanium. The diffusion of each dopant is of interest due to the possible effects on the fibre performance. Germanium diffusion in rare-earth doped fibres has been studied by Stevenson *et al* [139] for the purpose of understanding the losses associated with fusion splicing such fibres. The codopants used in the studied fibres were ytterbium, phosphorus and erbium and a "reference" fibre having a Ge-doped silica core was measured as well. The study concluded that the germanium diffusion rate for the rare earth doped fibre was 1.86 times higher than for the reference fibre, showing that codoping affects germanium diffusion. This was also found by Kirchhof *et al* [149] who studied codoping effects on diffusion coefficients in silica. They stated that in all cases studied, codoping has led to higher diffusion rates. For example in their study [135] they found that co-doping with fluorine increased the diffusivity of germanium. Diffusion in rare-earth doped fibres has also been considered in a number of other studies [9, 131, 132, 141, 151] though no comparisons were made for single doped fibres or diffusion coefficients published.

In can be concluded from the few results published that at least some dopants such as erbium, ytterbium and fluorine increase the mobility of germanium. It is not known however whether the degree of this effect depends on the concentrations of the dopants for example. The enhanced mobility due to co-doping could explain some of the scatter in results presented in the previous section, for example if some of the cladding dopants had diffused towards the core and interacted with germanium. The effect of stress was found insignificant in PANDA fibres but due to lack of other studies no further conclusions can be made about the effects of stress.

4.1.3.3 Fluorine diffusion

The diffusion coefficients for fluorine diffusion in silica reported in the literature are plotted in Figure 4-7. The range of temperature for reported coefficients is greater than that for germanium diffusion and reaches the temperatures used in the drawing process. The fluorine diffusivities have been reported in five studies [128, 130, 142, 146, 147]. Although most of the studies cover a different temperature range from 1000 to 2000°C, there is a good agreement with studies by Hermann *et al* [142], Kirchhof *et al* [146], Fokine [147] and Shiraishi *et al* [130]. The higher fluorine mobility reported by Krause *et al* [128] was explained by Kirchhof *et al* [146] to result from the effects of co-doping with phosphorus. It must be noted that Krause *et al* [128] also noticed a significant difference with fluorine diffusivity when no co-doping was present in the fibres, however these results were not presented. As can be seen in Figure 4-7 the two data sets with phosphorus co-doping show reasonable agreement given the possible measurement limitations and varying glass composition.

Fluorine diffusion has also been studied in mode field expanding fibres [143-145] and fibres for sensor application [97, 152], however no diffusion coefficients were reported. It can be concluded from the published results for fluorine diffusion that there is reliable data available as long as the possible effects of co-doping are taken into account. It has been reported also that the fluorine diffusion coefficient is independent of concentration [142, 146].

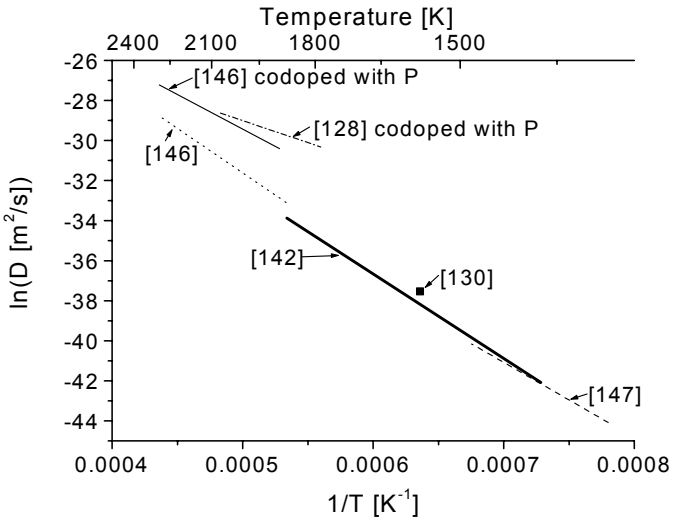

Figure 4-7. Arrhenius plot for fluorine diffusion in silica reported in literature.

4.1.3.4 Boron diffusion

Only a few studies can be found on boron diffusion in optical fibres or preforms [130, 137, 149]. Figure 4-8 shows the Arrhenius plot for reported values. Boron diffusion in heat-treated PANDA fibre was reported by Yamada and Hanafusa [137] in a temperature range from 1300 to 1600°C. A diffusion coefficient range for boron is given by Kirchhof *et al* [149] (possible area is shown in Figure 4-8) who also note that the coefficient was greatly affected not only by temperature but also by boron concentration.

Although publications about boron diffusion in optical fibres are scarce there are several studies made in semiconductors. A diffusivity literature review for boron in silica can be found in Ghezzo and Brown [153]. The diffusion coefficients reported in the survey are much smaller than those reported for optical fibres and it is noted that the values greatly depend on the boron concentration of the sources. Data from a more recent study in boron diffusion through a thin silica layer by Mathiot *et al* [154] is plotted in Figure 4-8 for comparison. The discrepancy between the coefficients can be explained by the different processing techniques of SiO_2 thin films [120]. It can be concluded that further studies would be required for boron diffusion in optical fibres, although rough estimates can be made based on the current values as long as the boron concentration is within the range reported. (For PANDA fibre boron level is typically 20mol%.)

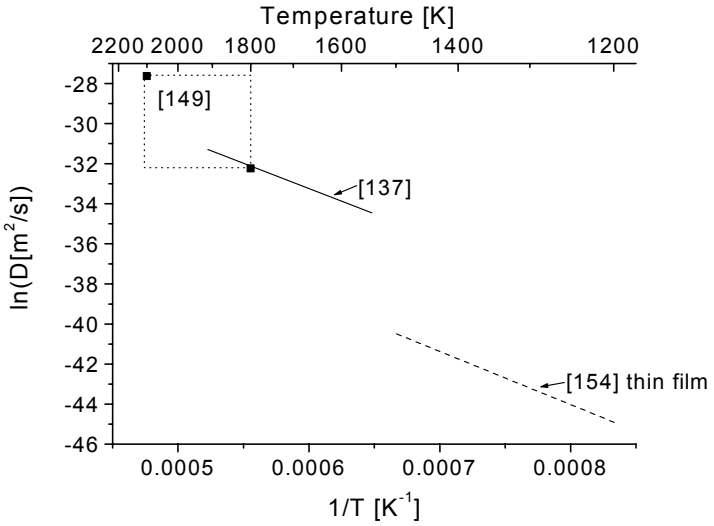

Figure 4-8. Arrhenius plot for boron diffusion in silica reported in literature.

4.1.3.5 Phosphorus

The literature for phosphorus diffusion in optical fibres is even scarcer. Phosphorus diffusion in MCVD fibres was studied by Fleming and Kurkjian [127] and diffusion coefficients were reported at temperature range from 1200 to 1950°C, see Figure 4-9. Due to lack of other studies, a data set from studies in semiconductors [155] for a thin oxide film is shown in the figure for comparison. It can only be concluded that the mobility of phosphorus seems to be lower than the other dopants, Ge, F and B. However even this conclusion must be made with caution as the result for Ge mobility by Fleming and Kurkjian [127] was much smaller than that reported in other studies.

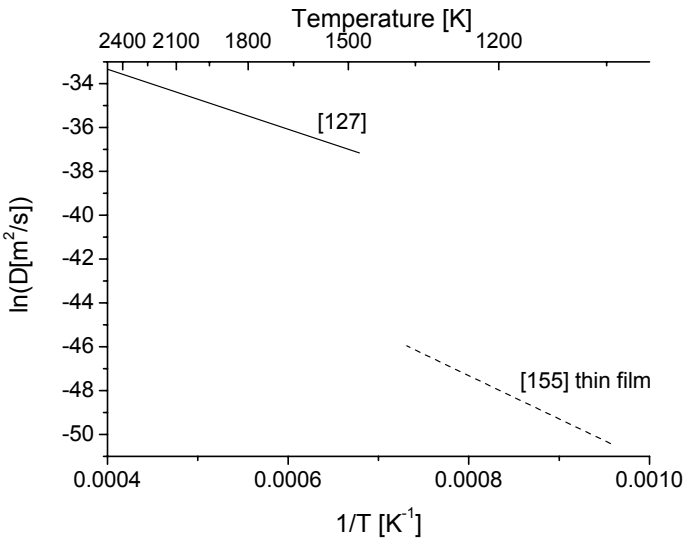

Figure 4-9. Arrhenius plot for phosphorus diffusion in silica reported in literature.

4.1.3.6 Diffusion during fibre drawing

There are very few publications dealing with the effect of the fibre drawing process on dopant diffusion. Germanium diffusion during drawing was observed by Hersener *et al* [6] who looked at the drawing induced changes of the GeO_2 profile in the neck-down of the drawn preform. No quantitative analysis was made but diffusion was observed as smoothing of the so-called 'ripples' characteristic in Ge-doped layers made by MCVD type process, see Figure 4-10. Germanium and erbium diffusion during drawing was studied by Pugh *et al* [7-9], but no diffusion was observed in the fibres. A Ge-doped elliptical core fibre was found to have altered ellipticity to that of the preform in a study conducted by Huntington *et al* [101], however no further study was conducted to

determine the cause of the change. Phosphorus has been reported to diffuse during drawing in highly phosphorus-doped silica fibres by Bubnov *et al* [156], the study however focussed on preform fabrication and not many details are given of the drawing related changes.

As opposed to dopant diffusion from within the core, impurity diffusion towards the core (from the jacketing tube) has been studied by Iino *et al* [150, 157]. Their study found that sodium and potassium were diffusing to the centre during drawing but that no aluminium diffusion was observed. Diffusivities for some impurities found in silica have been listed in Table 4-2. Alkali ions typically diffuse faster than the dopants used in optical fibres and aluminium has a diffusion coefficient in the order of glass network formers.

Due to the lack of drawing condition details in all the above references, it is difficult to compare the findings or to conclude any effects of drawing conditions other than that changes in dopant distribution have been observed during drawing. A qualitative comparison can be made on the mobility of various dopants by extrapolating the individual diffusion data to draw temperatures, see Figure 4-11. On the upper range of drawing temperatures fluorine has highest mobility followed by germanium and boron. On the lower range of temperatures the mobility of fluorine and boron is comparable whilst boron has the higher value. Phosphorus has the lowest mobility, but due to lack of measurement data to confirm this, it must be taken with caution. Boron was also found to have a diffusion coefficient depending on concentration and this will affect the relative mobilities.

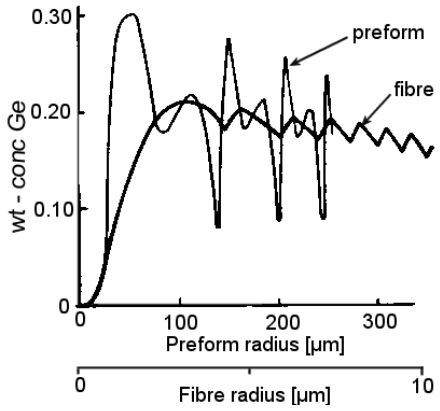

Figure 4-10. GeO_2 profile of doped preform and neck-down Ref. [6].

Table 4-2. Diffusivities for some impurities found in silica at 1000°C [118, 120].[7]

Ion	*Na*	*K*	*Ca*	*Al*
D m^2/s	7.9×10^{-10}	1×10^{-12}	2×10^{-12}	1×10^{-17}

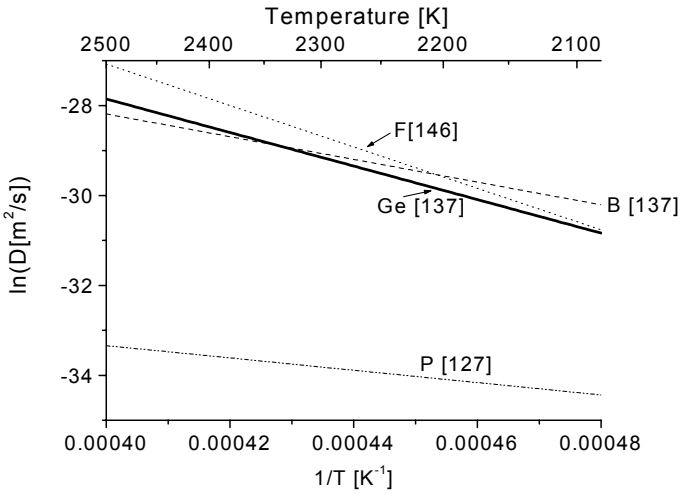

Figure 4-11. Arrhenius plot for various dopants extrapolated to draw temperatures from selected references.

4.1.3.7 Summary

Diffusion of most of the frequently used dopants in specialty optical fibres has been studied in the past. The most common dopants studied were germanium and fluorine. Very few papers were available on diffusion of other dopants such as boron, phosphorus and rare-earths. Diffusion data reported for fluorine in silica was by far the most consistent throughout the studies. Some scatter occurred but was explained by the increased mobility of fluorine in the presence of phosphorus. Significant scatter was reported for germanium, even within a study, although some agreement between different studies was found.

It is clear that although diffusivity information is readily available for all of the most important dopants, the data is scattered or too sparse. This complicates the selection of the most reliable and applicable results. The variations in the published data reflect both

[7] Note that 1000°C is much lower than the drawing temperature for silica. Unfortunately values at higher temperatures were not available in literature.

the limitations of the measurements used and the different fibre designs employed. The fibre samples in these studies vary in dimension, dopant concentration level, codoping and processing technique. The heat treatments vary from the use of splicer arcs to microburners and ovens. All of the above affect the accuracy of the results. In spite of the scattered diffusivity data, important qualitative observations were obtained, showing the importance of concentration dependence for boron and the effects of codoping on germanium and fluorine diffusion.

Very few studies have been made on the effects of the drawing process. Although reported diffusivities are very small, the fibres are drawn at very high temperatures. The times that the fibres are exposed to the heat in the furnace are very small which minimises diffusion, however some speciality fibres are drawn at speeds which are orders of magnitude slower than for the standard telecommunication fibres, thus increasing the dwell time inside the furnace.

The present study builds on past studies of dopant diffusion in silica optical fibres and specifically develops the area of dopant diffusion during the fibre-drawing step. Special consideration was given to reliable dopant concentration measurements in optical fibres and the selection of suitable fibre designs to observe diffusion.

4.2 Methods

The methods are described in detail in Chapter 3 and are only briefly summarised here. The fibre designs used for the diffusion study are shown in Figure 4-12. For dimensions and refractive index profiles see Section 3.1.1 on page 31. Three types of designs were used for Ge doped fibres: (a) Ge-doped core, (b) 1-ring-Ge-doped and (c) 3-ring-Ge-doped fibre. Both symmetric and asymmetric Ge-doped cores were studied. The 1-ring-Ge-doped design was adopted in order to improve the homogeneity of the refractive index profile along the preform length and to remove any effects of cladding dopants. The 3-ring-Ge-doped fibre had varying germanium concentration for each ring. This design was specifically made to improve the etching and AFM technique. Fluorine diffusion study was carried out on a pure silica core multimode fibre with F doped cladding. The Ge-doped preforms were fabricated using the MCVD technique. The Ge-doped core preforms had a SiO_2-P_2O_5-F cladding, whereas the ring designs had pure silica regions with no other dopants. The F-doped preform was supplied as a

standard product (Fluosil®) manufactured by plasma outside deposition. The drawing conditions for each preform are described with the relevant results, Section 4.3.

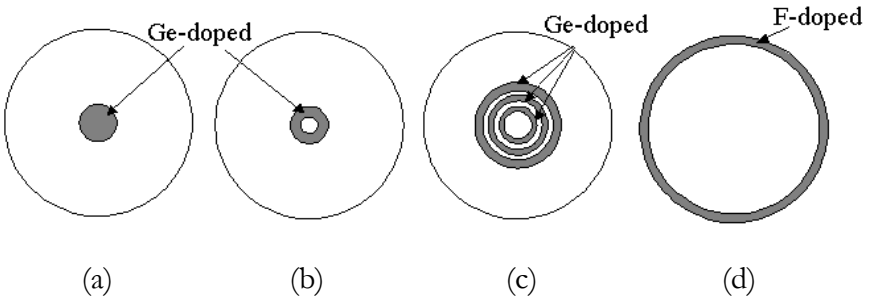

Figure 4-12. Schematic of the Ge-doped (a) core, (b) 1-ring and (c) 3-ring fibre design (d) F-doped fibre.

Table 4-3 summarises the measurement techniques used for the samples. The preforms were characterised radially and longitudinally with a refractive index profiler before the drawing to determine the homogeneity of the preform. When appropriate, tomographic computations were used to check radial homogeneity of the preforms. Chemical analysis was carried out by EDS for Ge-doped and WDS for F-doped samples for one section of each preform. The obtained dopant concentration profiles provided the required molar concentrations for the diffusion calculations as well as the initial concentration profile for comparisons with fibre samples.

The measurement of the fibre dopant profiles proved to be the most challenging task in studying the diffusion effects. No technique was found to give direct dopant concentration and submicron spatial resolution, consequently various techniques were used to confirm findings. Refractive index profiling, atomic force microscopy and electron microscopy techniques were all used to characterise the fibres, for detailed description see Section 3.3.

Table 4-3. Summary of fibre designs and characterisation techniques used in the diffusion study

Fibre type	*Preform code*[1]	*Nominal fibre diameter (μm)*	*Preform characterisation technique*	*Fibre characterisation technique*
Ge-doped core fibre	SS	125,800	RIP, EDS	AFM, EDS
Ge-doped asymmetric core fibre	SA	125	RIP, EDS	AFM, EDS
1-ring-Ge-doped fibre	1R	125	RIP, EDS	RIP, AFM
3-ring-Ge-doped fibre	3R	125	RIP, EDS	RIP, AFM
F-doped cladding, pure silica core fibre	F	110	RIP, WDS	RIP, AFM

[1]SS=Step-index Symmetric, SA=Step-index Asymmetric, 1R=one Ring, 3R=three Ring, F=F-doped

The notation for fibre samples follows that of the preform code listed in Table 4-3. For example, sample code **1R_125_1** is a fibre drawn from preform **1R** to a fibre diameter of **125**μm and has sample number of **1**. Each sample is drawn from a section of the preform and is typically given a *preform position* in mm together with the draw conditions. This value is measured as the longitudinal distance from the preform tip prior to drawing. The beginning of each draw would thus correspond to preform position 0.

4.3 Results

The study of diffusion during drawing proved to be more complicated than first anticipated. Challenges were encountered in finding suitable fibre design, drawing conditions and in measuring preform and fibre samples. The results are therefore reported in chronological order whereby the reader can follow the necessary steps required to finally quantify diffusion during drawing. This structure also enables a logical presentation of the improvements made in the various areas together with the relevant results. Note that a more detailed discussion on the measurements can be found in Chapter 3. Figure 4-13 gives the structure of the result section for the germanium diffusion study. Table 4-4 provides a summary of all the experiments, and can be used together with the figure to give an overview of the results sections. The sections are divided according to the different fibre designs. For each section, first the preform measurements are discussed and draw conditions presented. The fibre measurements are then presented and their implications for dopant diffusion discussed. The fluorine diffusion results follow the germanium study in Section 4.3.4.

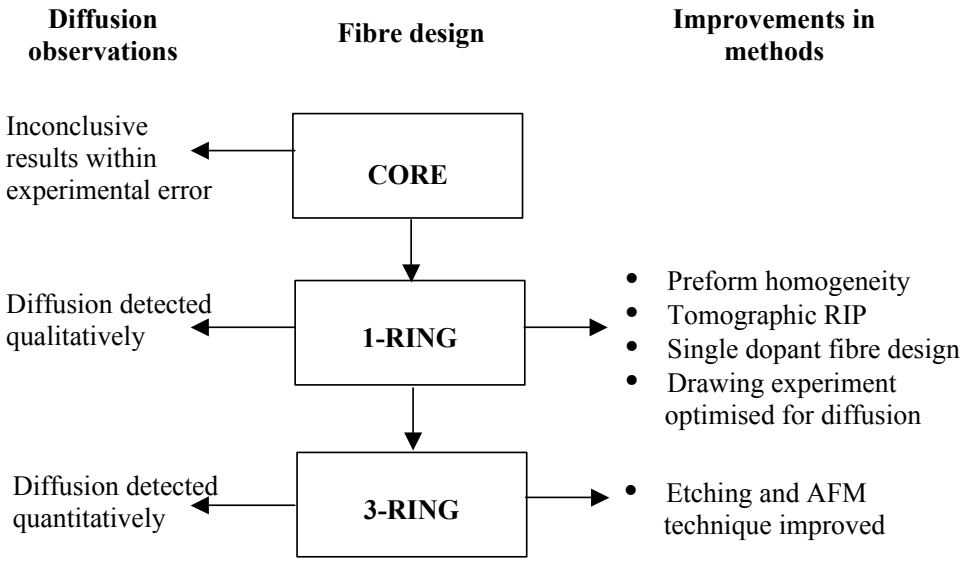

Figure 4-13. Structure of the Ge diffusion results section.

Table 4-4. Summary of the main results and draw conditions used in the experiments

Preform	*Nominal Fibre Diameter (μm)*	*Main Result*	*Temperature (°C)*	*Preform Feed Rate (mm/min)*	*Draw Speed (m/min)*
SS	125	No diffusion detected	1890-2020	2-9	30-170
	800	Results inconclusive within experimental error	1900-2100	2-7	1-4
SA	125	Results inconclusive within experimental error	1560[1]	1	20
1R	125	Diffusion detected	1800-2100	0.5-2	10-35
3R	125	Diffusion detected	1800-2100	0.5	10
F	110	Diffusion detected	1900-2100	0.04-0.2	2-10

[1]Different furnace used, absolute temperature not comparable to other experiments

4.3.1 Ge-doped core fibre

The first experiment was performed on a fibre design which was selected on the basis of being both simple and commonly used in industry. The PF1 pigtailing fibre has a relatively high germanium concentration in the core, thus increasing the chances for diffusion detection. The preform was drawn into the usual 125μm fibre diameter and to a special 800μm diameter. The capabilities of the measurement techniques were not yet established conclusively at the time, therefore a fibre with relatively large diameter (800μm) was drawn which could be analysed using SEM, avoiding spatial resolution limitations. Draw conditions were chosen based on the typical ranges used for the optical fibre drawing at OFTC. The fibres were drawn under various temperatures and draw speeds (Table 4-5).

Although diffusion could not be conclusively measured during this experiment, the following presentation of the results demonstrates the problems in studying dopant diffusion in optical fibre drawing and illustrates how these problems were overcome. This first section emphasises more the methods used than the diffusion phenomena, which is demonstrated and discussed in Sections 4.3.2 to 4.3.4. This section presents the results as follows:

- Preform homogeneity using RIP and EDS measurements
- Comparison of different drawing conditions using etching and AFM and EDS measurements
- Comparison of fibres to preform

Table 4-5. Draw conditions for SS samples

Fibre	*Diam (μm)*	*Sample*	*Draw Temperature[1] (°C)*	*Preform Feed Rate (mm/min)*	*Draw Speed (m/min)*	*Tension (g)*	*Preform Position (mm)*
SS	125	1	1980	1.6	30	10	290
		2	1890	1.6	30	40	330
		3	1840	1.6	30	90	350
		4	1970	5.3	100	40	430
		5	2010	8.5	160	40	470
		6	2020	9.0	170	40	500
SS	800	1	2100	1.7	0.8	-	50
		2	2000	1.7	0.8	-	70
		3	1900	1.7	0.8	-	90
		4	1900	7.3	3.5	-	130
		5	2000	7.3	3.5	-	170
		6	2100	7.3	3.5	-	220

[1]Draw temperature is measured by pyrometer from the back of the heating element, not the preform. Measurement has ±20°C accuracy and repeatability ±6°C.

4.3.1.1 Preform homogeneity

In Table 4-5 the corresponding preform longitudinal position is shown for each fibre sample. Numerous draw conditions could be studied during each fibre draw, eliminating variations between preforms. However, Samples SS_125_1 and 6 are sourced from relatively distant sections of the preform and longitudinal inhomogeneities become an issue when comparing the samples. Figure 4-14 shows the preform outer diameter, core diameter (computed using equivalent step-index, ESI, method) and their ratio along the length of the preform measured with a refractive index profiler. As the fibre diameter is controlled during the draw, it is the ratio of outer to core diameter that is important in order to obtain constant fibre core diameter.

The draw sections are shown in Figure 4-14. For these sections the ratio of the outer diameter to the core diameter varied by less than 4%. As the core diameter is computed using an ESI model it does not reflect the shape of the core profile. In order to look more closely at the preform homogeneity, several preform RIPs were compared. Figure 4-15 shows the preform core RIP at three different longitudinal positions corresponding to Samples SS_125_1, 2 and 6. As can be seen from the figures there is a variation in the peak refractive index difference. As the standard RIP computation assumes cylindrical symmetry, the asymmetry seen in the RIPs might not be presented

correctly. However, it can be concluded that there is a difference between the RIPs and that some asymmetry is present.

In addition to longitudinal variation, it is possible to have cross-sectional variation in the preform. Figure 4-16 compares the refractive index profiles for the core of the preform at the 500mm longitudinal position corresponding to Sample SS_125_6 at three different angles. This comparison shows that not only is there longitudinal but also cross-sectional variation in the preform. For the 800µm fibre draw the corresponding preform core refractive index profiles for Samples SS_800_1, 4 and 6 are shown in Figure 4-17. Although some variation is present it is less than for the SS_125 fibre draw section. In order to determine the asymmetry, tomographic RIP should be computed for the preform. Unfortunately the tomographic capability was not available prior to drawing of the preform.

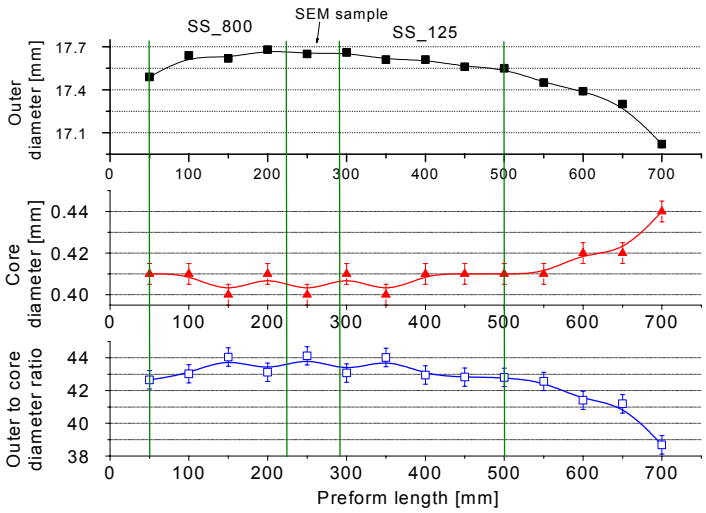

Figure 4-14. Preform SS homogeneity along the length. Draw sections marked for SS_800 and SS_125 with vertical lines.

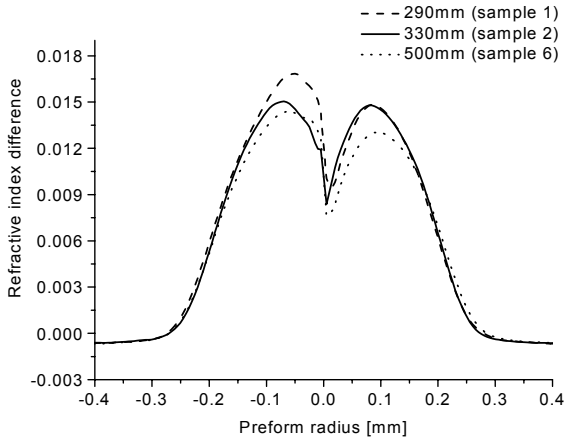

Figure 4-15. Preform core RIP in three different longitudinal positions, SS_125_1, 2 and 6.

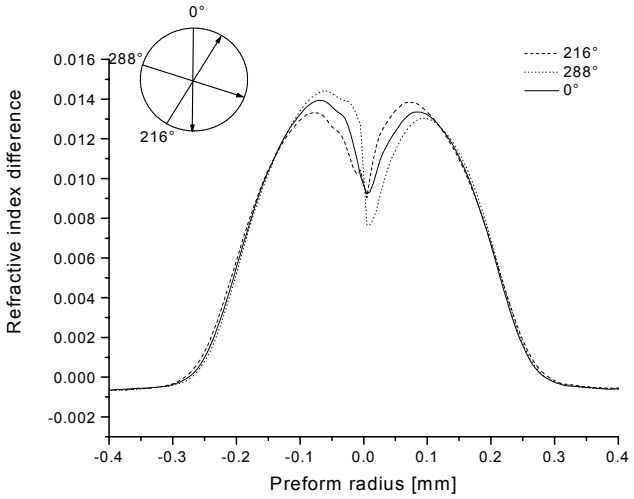

Figure 4-16. Preform core RIP at single position, 500mm, for three angular positions, 0°, 216° and 288°.

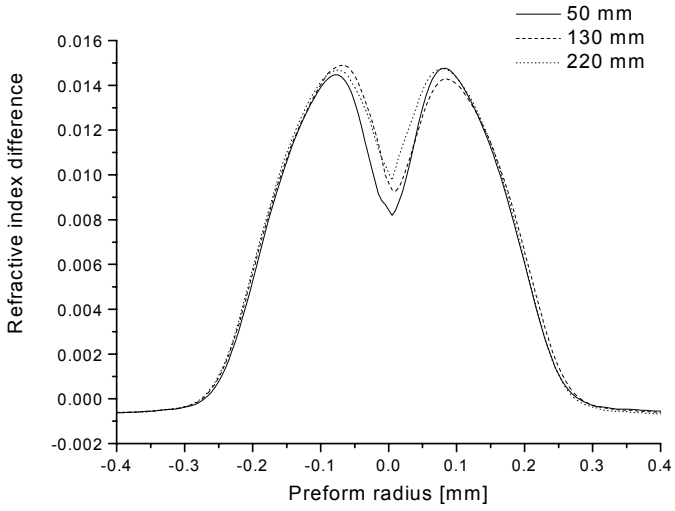

Figure 4-17. Preform core RIP in three different longitudinal corresponding to SS_800_1, 4 and 6.

The preform section at the 260mm position was also analysed using EDS on SEM. Figure 4-18 shows a BSE image of the preform cross-section. The core looks symmetric, more so than that which is shown in the RIPs. In the centre of the core a Ge-depleted area is shown with another small depleted ring surrounding the centre. Note that the "star-burst" shape core edge sometimes results from the MCVD process and is studied in [158]. Figure 4-19 shows the GeO_2 concentration profile measured using EDS compared to the corresponding preform RIP. The RI profiler does not resolve the small Ge-depleted ring in the final profile but this feature could cause an

error in the selection of the core centre, which would then translate into the final RIP as asymmetry. Also the central Ge-depleted dip is much deeper than resolved by the RI profiler. The core outer edge follows the concentration profile well.

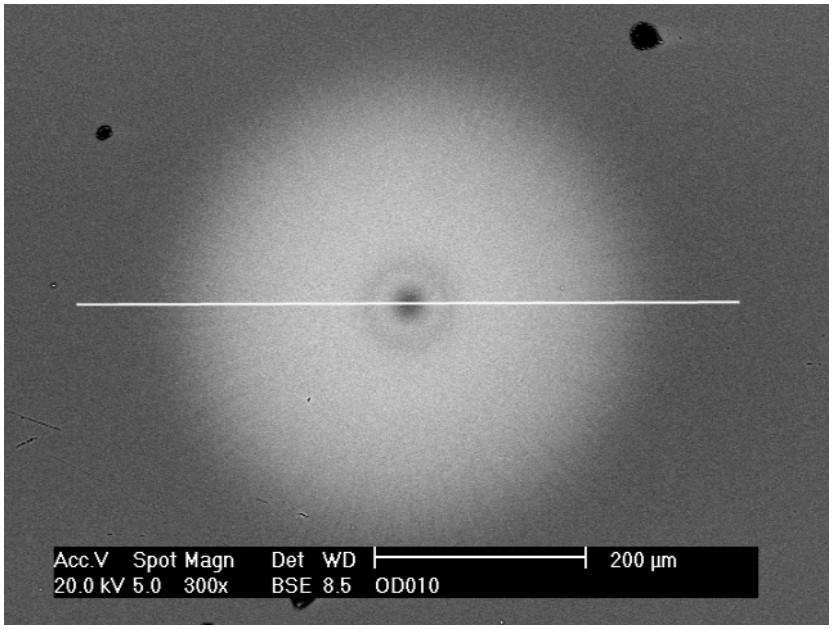

Figure 4-18. BSE image for SS preform using SEM. White line indicates the EDS line scan position.

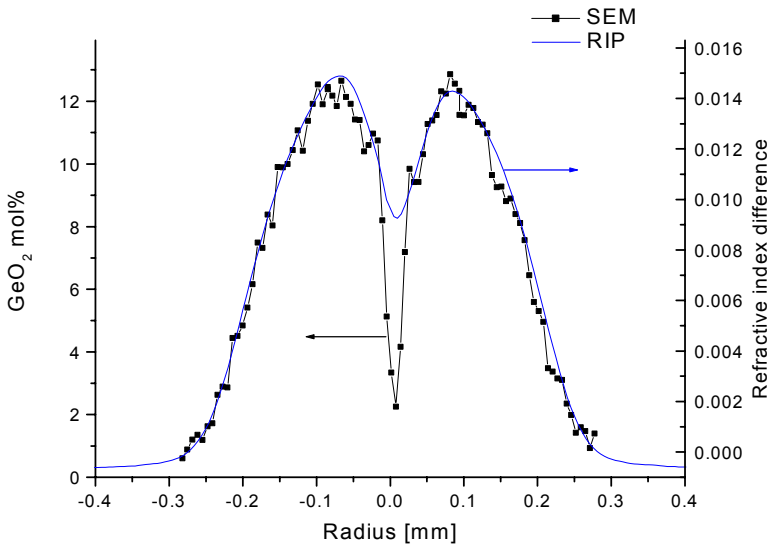

Figure 4-19. GeO_2 concentration profile of SS preform compared to the corresponding RIP

4.3.1.2 SS 125μm fibre

The 125μm fibres were measured using two methods (i) etching and AFM technique and (ii) EDS on TEM. For clarity, comparison of only three fibre samples is shown here. Samples SS_125_1 with a high draw temperature of 1980°C and SS_125_2 with a low draw temperature of 1890°C were chosen as they would present the greatest difference in the profile due to diffusion. Sample SS_125_6 was chosen to compare the effect of drawing speed. The draw conditions are presented for these samples in Table 4-6.

Table 4-6. Draw conditions for Samples SS_125_1, 2 and 6

Sample	*Draw Temperature (°C)*	*Preform Feed Rate (mm/min)*	*Draw Speed (m/min)*	*Tension (g)*	*Preform Position (mm)*
SS_125_1	1980	1.6	30	10	290
SS_125_2	1890	1.6	30	40	330
SS_125_6	2020	9.0	170	40	500

Figure 4-20 shows the AFM profiles for Samples SS_125_1, 2 and 6. All the samples show the deep Ge-depleted centre and also the small ring surrounding it. Sample SS_125_6 has a much lower peak height than the other samples. To illustrate the challenges of AFM data analysis three profiles are plotted for Sample SS_125_2 taken at different angles 0, 45 and 90° across the core in Figure 4-21. There is some variation in peak height but mostly in core width. Figure 4-22 shows the reason for this. In Figure 4-22 the data is presented in two-dimensions. The intensity of the colour represents the height of the sample. During scanning the sample has moved slightly resulting in what seems to be an oval core (~20% ovality). When line profiles are taken at different angles, the data is correspondingly broader or narrower depending on the angle. In this case the AFM data for Sample 2 is not reliable in spatial dimensions. The cause of the drift was later removed by modifying the way the fibres were attached to the sample holder. The lower peak height of Sample SS_125_6 was not however explained by the sample drift. The noise seen in Figure 4-21 (at 45° and 90°) is due to variation in the baseline height from scan to scan.[8] This feature is typical for an AFM image and is

[8] An AFM image is constructed from multiple scan lines. The tip (or sample) moves back and forth in the fast scan direction after which it moves an increment perpendicular to this direction. The profile at 0° is smooth as it comprises data from only a single scan.

removed by a flattening process found in standard AFM software. The line height variation is also seen in the raw AFM data in Figure 4-22.

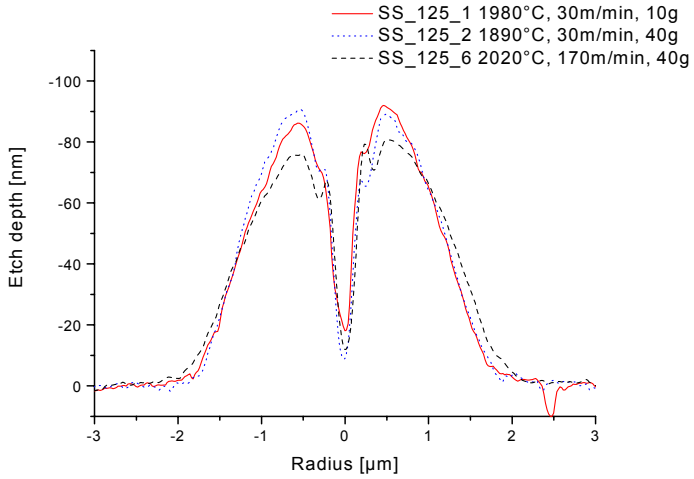

Figure 4-20. Core profiles for SS_125_1, 2 and 6 using the etching and AFM method.

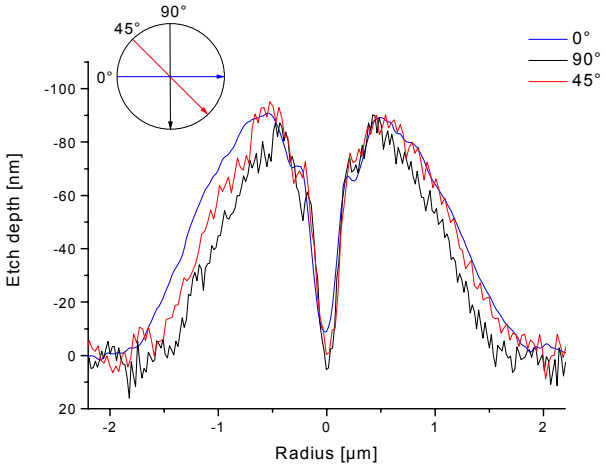

Figure 4-21. AFM core profiles for Sample SS_125_2 taken at 0, 45 and 90° angles.

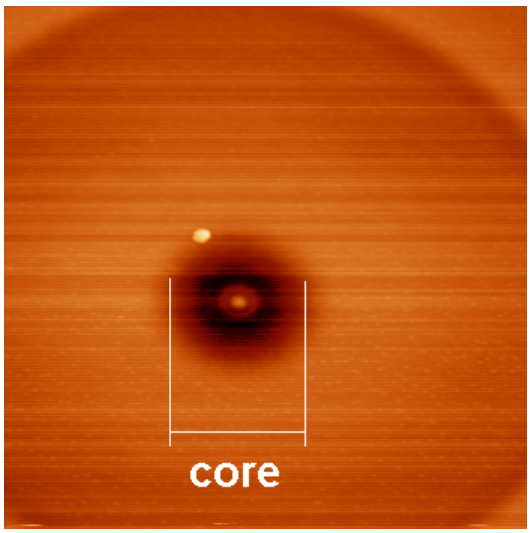

Figure 4-22. 2D presentation of the AFM data for Sample SS_125_2. The bright speck near the core edge is a contamination particle.

In parallel with the AFM measurements TEM was also attempted to determine the germanium concentration profiles in the fibre samples. Figure 4-23 shows concentration profile measured using EDS for Samples SS_125_1, 2 and 6. Again Sample SS_125_6 shows lower peak concentration than the other samples. Only one scan for each sample is shown in Figure 4-23 as it was found that the scan locations in the sample could not be accurately determined[9]. No further comparison was made with the TEM data as uncertainties in the position of the line scans caused substantial decrease in the spatial resolution of the data. It was also shown later that ion beam thinning preferentially removed germania, thus affecting the concentration profile. For further discussion see Section 3.3.3.2.

As a final comparison, each of the 125μm fibre samples was compared with the preform RIP corresponding to the section from which the fibres were drawn. Figure 4-24 shows the comparison for Samples SS_125_1, 2 and 6. Each of the figures has the same scaling and it can be concluded that the maximum peak height follows reasonably the corresponding preform profile for each sample indicating that the changes in the fibres are due to preform non-homogeneity. Although the RI profiler does not resolve fully the Ge-depleted dip in the centre nor the ring surrounding it, it is likely that these features change along the preform length. Due to the preform inhomogeneities and the challenges in fibre measurements, no drawing induced change in the profiles was conclusively detected.

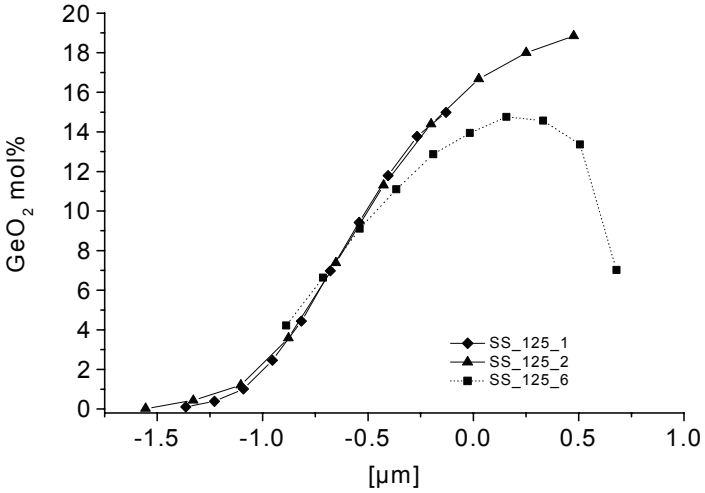

Figure 4-23. Core profile comparison for SS_125_1, 2 and 6 measured using EDS on TEM

[9] The scan width was limited to ~2μm and thus scans spanning the width of the core were not possible. Due to the difficulty in positioning, the scan SS_125_1 did not reach as far into the core centre.

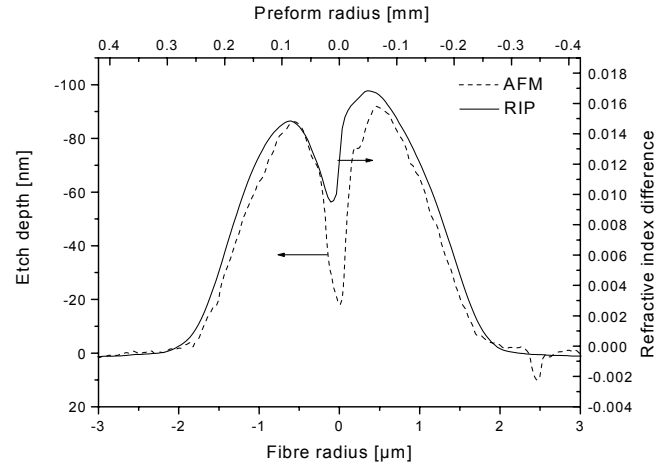

(a)

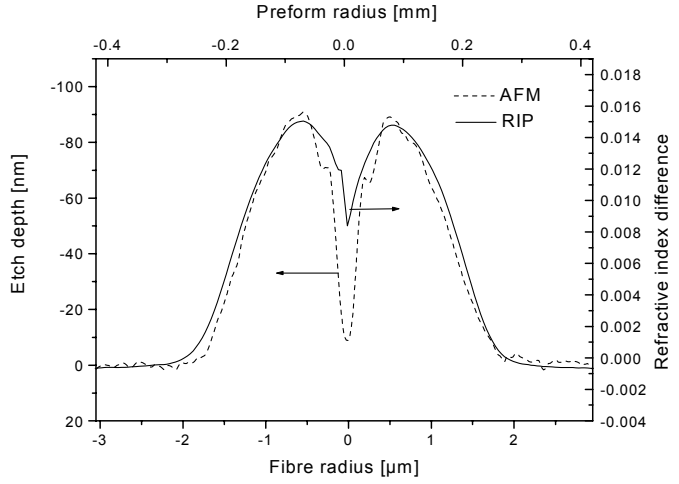

(b)

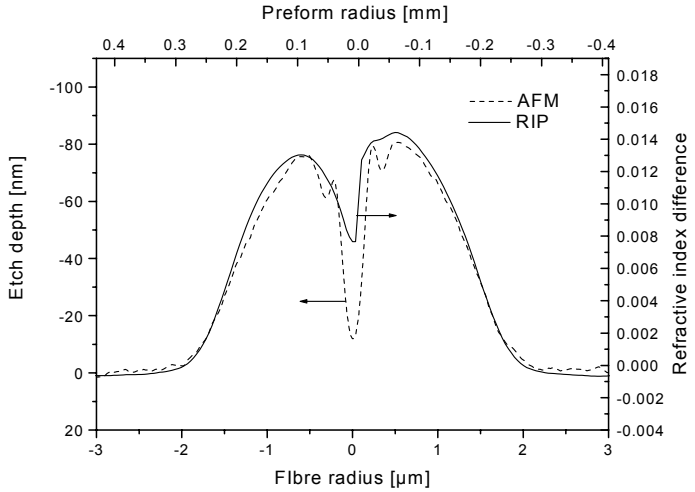

(c)

Figure 4-24. Comparison of preform RI and fibre AFM profile for (a) Sample SS_125_1, (b) 2 and (c) 6.

4.3.1.3 SS 800μm fibre

In an attempt to mitigate the problems in fibre measurements, fibres with very large cores were drawn. The 800μm fibres were drawn at various draw temperatures and speeds. Five samples (Table 4-7) were chosen to study the following effects on diffusion: (i) effect of temperature at low preform feed rate (SS_800_1 and 2), (ii) effect of temperature at high preform feed rate (SS_800_4 and 6) and effect of preform feed rate at constant temperature (SS_800_2 and 5). The fibres were analysed with EDS on SEM to obtain GeO_2 concentration profiles across the core.

Figure 4-25 shows the GeO_2 concentration profiles across the core for the samples. The error bars represent the interaction volume of the measurement. The concentration measurement at the point is an average of the volume resulting in larger errors when greater gradients exist. A free hand line is drawn through the points to guide the eye. Figure 4-25 (a) shows the comparison between fibres drawn at the lower draw speed of 0.8m/min at 2000°C and 2100°C. Figure 4-25 (b) shows the profiles for draw speeds of 3.5m/min and temperatures 1900° and 2100°. Figure 4-25 (c) shows the Samples 2 and 5 drawn at the same temperature of 2000°C but at different draw speeds. No significant differences between the profiles can be seen within the measurement accuracy, except for Samples SS_800_4 and 6 (Figure 4-25 (b)) where the central Ge-depleted region has higher Ge concentration, possibly indicating increased Ge diffusion at 2100°C compared to 1900°C. Finally Sample SS_800_4 is compared with the preform profile both measured with EDS on SEM, Figure 4-26. The preform sample was taken relatively close to the section drawn into the fibre sample. The most noticeable difference is that the central Ge-depleted dip has higher Ge content in the fibre, indicating possible diffusion of Ge during drawing. Despite the large core (30μm), the interaction volume hinders the detection of draw-induced changes. As with SS_125 samples the preform inhomogeneity could result in the changes observed in the Ge-depleted centre region.

Table 4-7. Draw conditions for Samples SS_800_1, 2, 4, 5 and 6

Sample	*Draw Temperature (°C)*	*Preform Feed Rate (mm/min)*	*Draw Speed (m/min)*	*Preform Position (mm)*
SS_800_1	2100	1.7	0.8	50
SS_800_2	2000	1.7	0.8	70
SS_800_4	1900	7.3	3.5	130
SS_800_5	2000	7.3	3.5	170
SS_800_6	2100	7.3	3.5	220

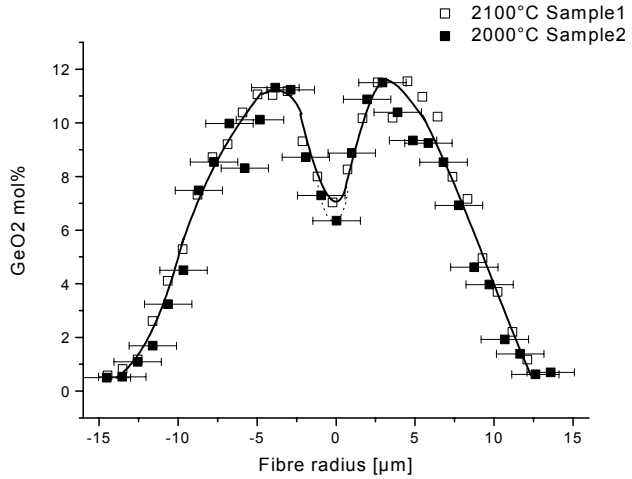

(a)

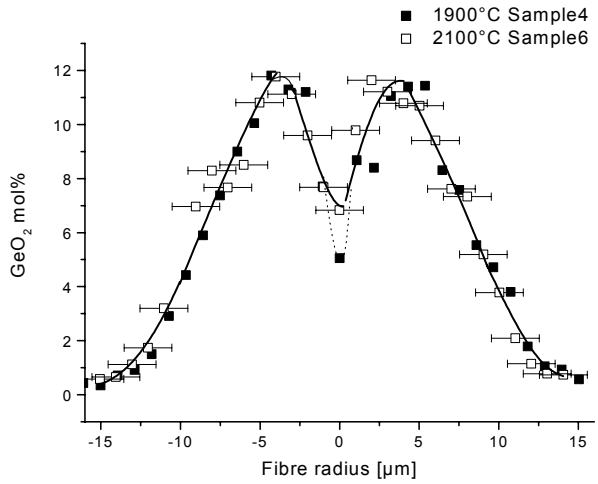

(b)

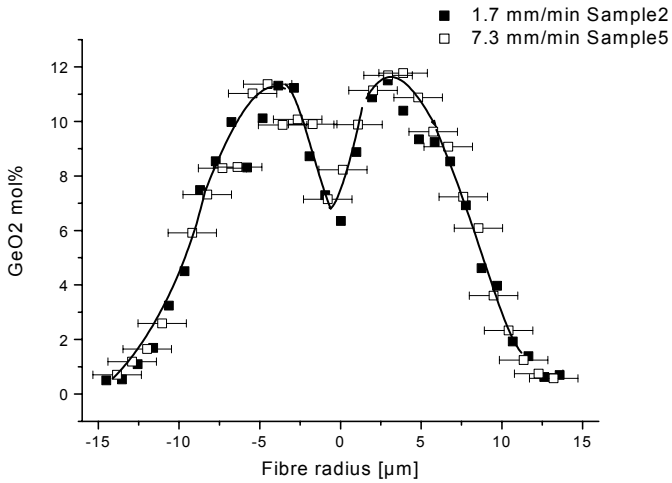

(c)

Figure 4-25. EDS GeO_2 concentration profiles for SS_800 effect of temperature (a) at low feed speed and (b) at high feed speed and (c) effect of feed speed. Only one experiment set per figure has error bars for clarity. The interaction volume is same for each point.

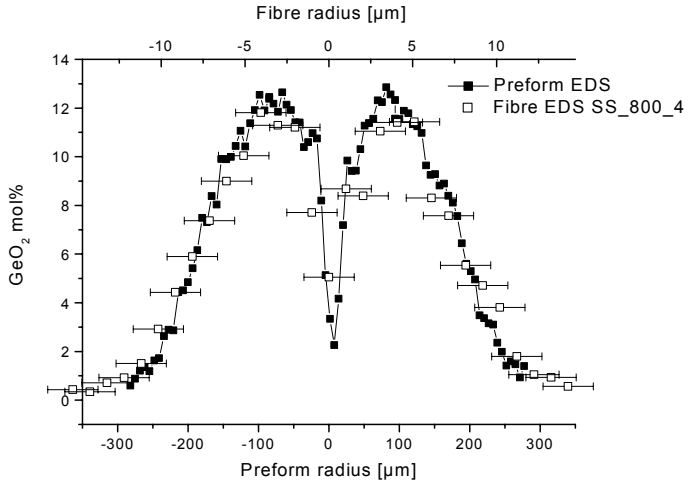

Figure 4-26. Comparison SEM profiles of Sample SS_800_4 and preform sample. Preform scaled to fibre dimensions. The width of the error bar of the preform measurement corresponds to the size of the label.

4.3.1.4 Asymmetric-core fibre

In order to verify whether asymmetry in a Ge-doped core would be affected by diffusion, a preform that had a Ge-doped core with high asymmetry was drawn (Sample SA_125). The fibre sample was drawn at a draw speed of 20m/min, preform feed rate of 1.1mm/min at 1560°C using the modified tower. The furnace temperature is not comparable with the other tower but the draw tension was 65g, a bit higher but comparable to the tension employed in the other draws.

Figure 4-27 shows a BSE image acquired with SEM of the asymmetric preform core. The drawn line indicates the radial position of the measured GeO_2 concentration profile. Figure 4-28 shows SEM and RIP scans, showing the large variation in the peak germanium content. It should be noted that the tomographic RIP was measured at a different position to the preform SEM section and the preform section drawn into fibre. However it is shown here to demonstrate the similar asymmetry found in the RIP as compared to SEM. The central dip is much smaller in the RIP and this could be due to the limitations of RIP measurement or longitudinal variation of the dip along the preform.

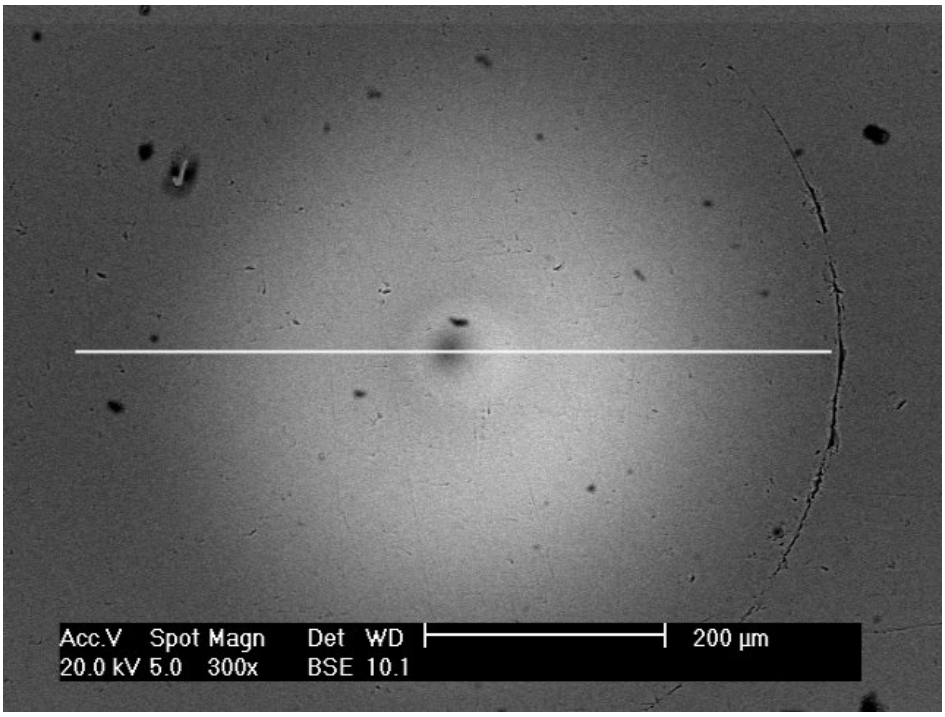

Figure 4-27. BSE image performed on SEM of the asymmetric preform core with the line indicating the diameter with maximum asymmetry.

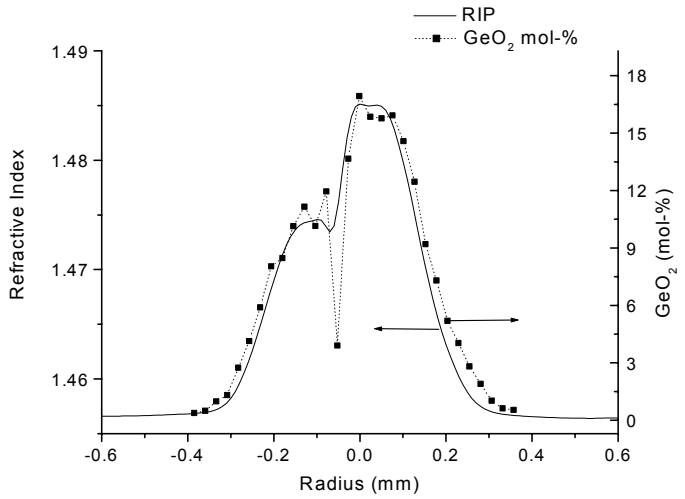

Figure 4-28. Preform SEM and tomographic RIP along the diameter with maximum asymmetry

Comparison of the preform EDS and fibre AFM profile is show in Figure 4-29.The index dip in the centre of the core is slightly less than that of the preform and the asymmetry seems greater in the preform. These may indicate that some profile alteration has occurred during drawing. The exact relationship with the etching depth and Ge-concentration could not be determined for this sample limiting the comparability of the profiles.

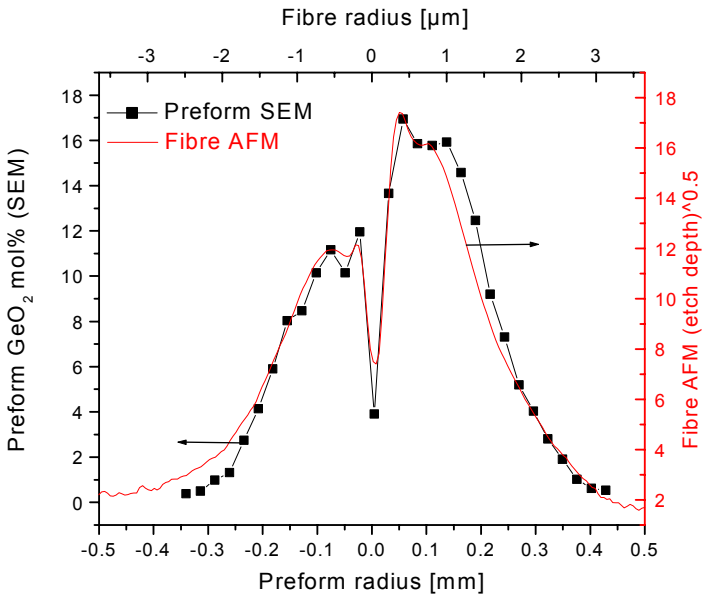

Figure 4-29. Comparison of fibre core profiles for Sample SA_125 (etching and AFM) and preform GeO_2 concentration profile (EDS on SEM).

In conclusion, due to the difficulties in measuring an asymmetric structure, where exact profile position is essential for comparisons and preform longitudinal variations are likely (unfortunately tomographic profiling was not available prior to drawing), no diffusion or viscous deformation could be observed. It can however be noted that significant asymmetry prevails in the fibre drawn at these specific conditions. Although not much was learned of diffusion in this experiment, the asymmetric fibre proved to be very useful for highlighting the challenges in the various analysis techniques.

4.3.1.5 Summary

Due to the longitudinal and radial fluctuations in the preform composition and the limitations of the measurement techniques, no conclusive results were obtained for drawing induced changes in the profile. The experiments however highlighted the problems in studying such changes and resulted in valuable information as to the improvements required in both experimental set-up and measurement techniques. These improvements are listed below, most of which were implemented in the following studies presented in Sections 4.3.2, 4.3.3 and 4.3.4.

Experimental techniques:

- Preform homogeneity must be improved.
- Fewer draw conditions should be used to minimise preform length used.
- A draw condition should be chosen, which maximises diffusion e.g. higher temperature and lower draw speed.
- A single dopant fibre design should be used to eliminate the effect of cladding dopants.

Measurement techniques:

- A tomographic RIP should be used to verify radial homogeneity and improve resolution.
- Etching depth should be correlated to dopant concentration, as it is not linear.
- Single dopant design should be used in order to remove the effect of other dopants on the etching process in the etching and AFM technique.
- Sample drift should be eliminated from the AFM measurement.
- TEM sample preparation reduced the germanium content of the samples and cannot be used for the study unless improvements are made in the preparation process.
- EDS on SEM has too limited spatial resolution even for large diameter fibres.
- An alternative fibre measurement technique should be used to verify findings made from etching and AFM technique, such as high-resolution fibre RIP.

4.3.2 1-ring-Ge-doped fibre

A Ge-doped ring design was selected to improve the longitudinal homogeneity of the preform. In the ring design the central dip resulting from the depletion of germanium during collapse was removed by depositing a thick layer of pure silica in the centre of the core prior to collapse. Draw conditions were carefully selected according to diffusion rates estimated from the literature and the number of samples were minimised so that the corresponding preform locations for the samples were as close together as possible, thereby maximising the comparability of the samples. Three different draw conditions were chosen (Table 4-8). Sample 1R_125_1 and 1R_125_2 were drawn at

very low speed, namely 10m/min with temperatures of 1800°C and 2100°C. Based on estimated results it was expected that at 1800°C minimal diffusion would occur but that at 2100°C some diffusion would be evident. Sample 1R_125_3 was drawn at high temperature but at a faster speed of 35m/min. Due to the faster speed less diffusion was expected than Sample 1R_125_2 as the sample spends less time in the hot-zone.

First the homogeneity of the preform was checked. Figure 4-30 shows the cladding ring dimensions along the preform length (measured from the preform RIPs). The draw section is shown in the figure. The longitudinal variation for cladding OD was <0.5% and variation in ring dimensions by less than 3%. The ratio of cladding OD to ring OD varied less than 1%. To look in more detail at the preform RIPs for the sections from which the samples were drawn, refer to Figure 4-31. This figure shows the refractive index profile at two different positions corresponding to the beginning and end of the draw section. The RIPs are almost identical.

Table 4-8. Draw conditions for Ge-doped ring fibre 1R_125

Sample	*Nominal Diameter (μm)*	*Furnace Temperature (°C)*	*Preform Feed Rate (mm/min)*	*Draw Speed (m/min)*	*Preform Position (mm)*
1R_125_1	125	1800	0.5	10	240
1R_125_2	125	2100	0.5	10	210
1R_125_3	125	2100	1.8	35	190

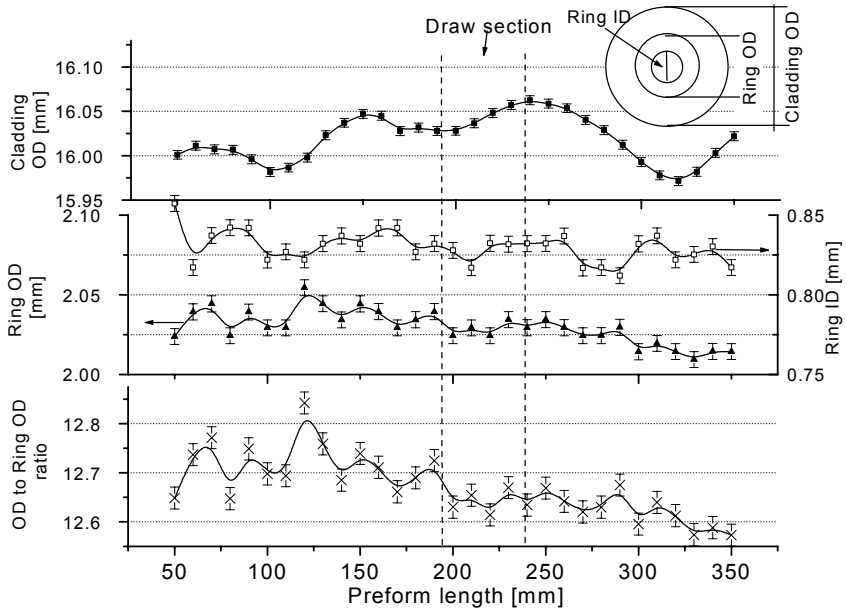

Figure 4-30. Longitudinal homogeneity of the Ge-ring preform, 1R.

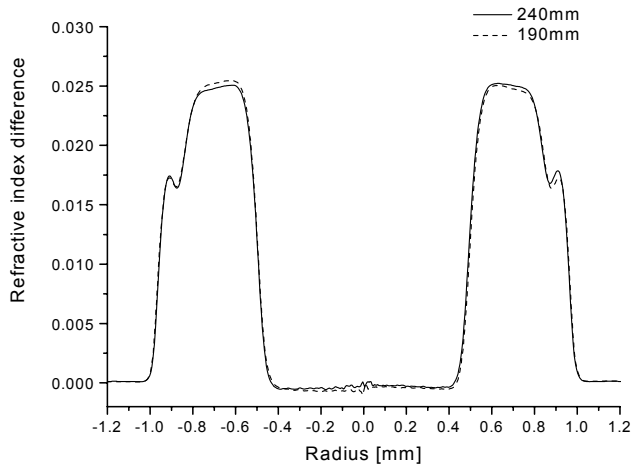

Figure 4-31. Preform RIP at positions 240 and 190mm corresponding to Samples 1R_125_1 and 3.

To check the cross-sectional homogeneity a tomographic RI profiling was used. The two-dimensional contour plot of the RIP is shown in Figure 4-32, where it can be seen that the preform is symmetric. In addition to this a tomographic RIP at an arbitrary angle is compared with an RIP assuming circular symmetry in Figure 4-33. The tomographic profile shows a more symmetric profile than the profile computed assuming circular symmetry. The presumably artificial asymmetry can be created in the computation of the RIP when the centre of the core is not located accurately. The profiles match relatively well and as the tomographic profile shows high symmetry it is concluded that the cross-sectional homogeneity is very good for the preform. The small peak in the outer part of the ring resulted from the preform manufacturing phase (Section 3.2.1.1) and proved to be useful in comparing the different fibre samples.

To determine the germania concentration profile SEM was used. Figure 4-34 shows the BSE image of the preform core. Comparison of the EDS line-scan and preform profile is shown in Figure 4-35. The peak on the outer edge is resolved with both methods, although SEM measures higher Ge content of this peak. This discrepancy may be due to the stress profile of the ring design resulting from the different thermal expansion coefficients of pure silica and the doped ring altering the RI (see Appendix I).

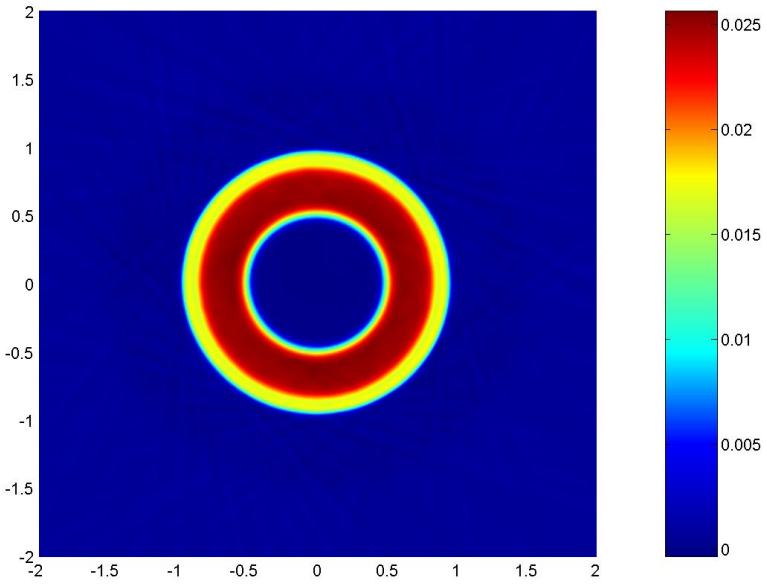

Figure 4-32. Tomographic RI contour plot of the preform 1R. Colour represents refractive index change and X and Y are positions in mm.

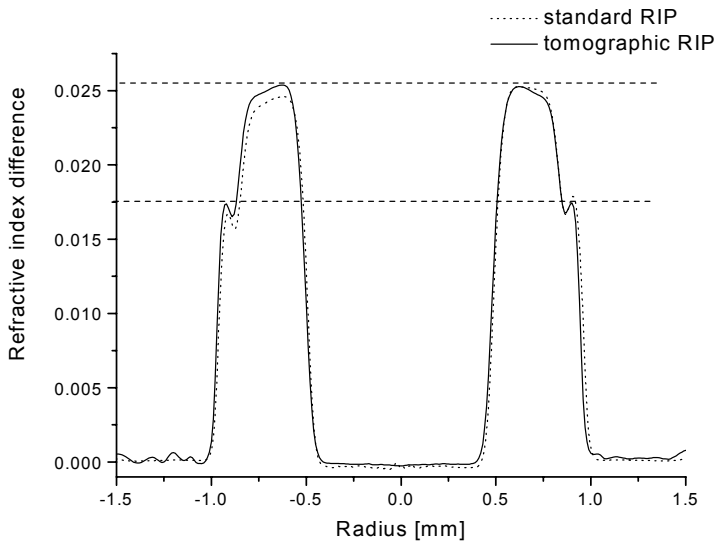

Figure 4-33. Preform RIP with symmetric assumption and tomographic profile for 1R.

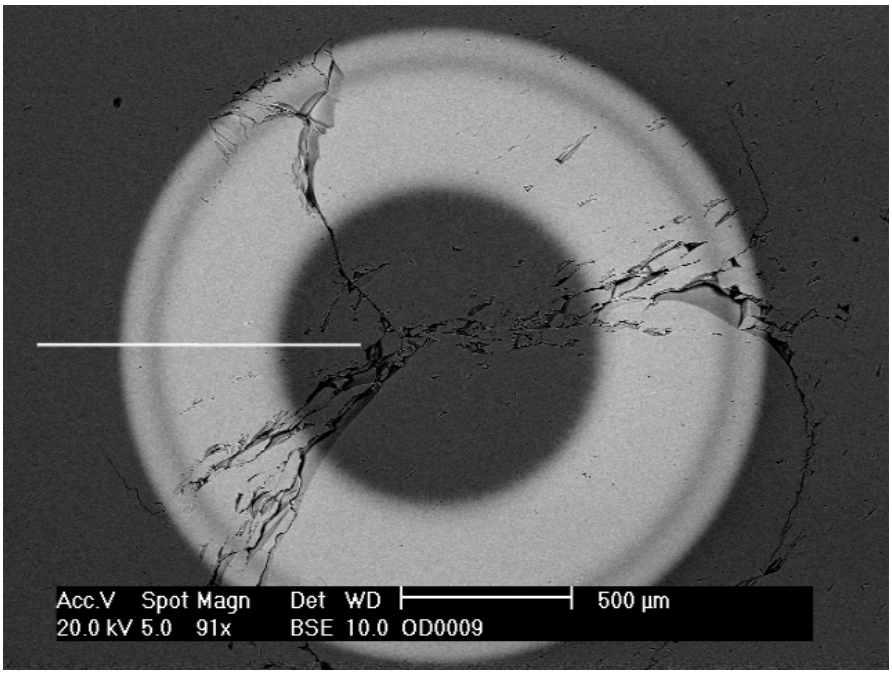

Figure 4-34. BSE image of the preform 1R. The cracks shown in the image are due to the cutting of the sample owing to high stresses resulting from the relatively high Ge content. EDS line scan measurement position shown as a white line.

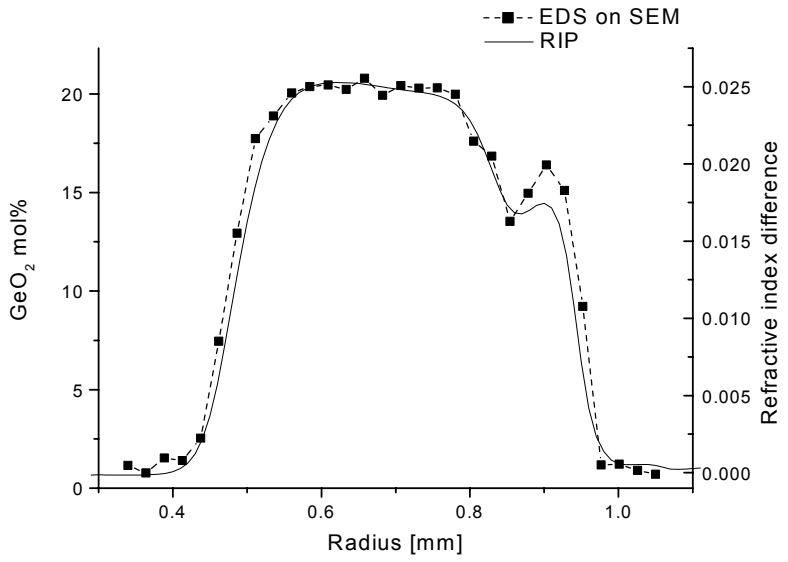

Figure 4-35. Preform SEM profile and RIP comparison for 1R.

The drawn fibres were analysed by etching and AFM and high-resolution RI profiler. Figure 4-36 shows the AFM profile for Samples 1R_125_1 and 1R_125_2, which were drawn at 10m/min and 1800°C and 2100°C, respectively. It can be seen that substantial broadening of the features has resulted at the higher of the two temperatures most likely due to diffusion. Figure 4-37 shows the inner edge of the Ge-doped ring for Samples 1R_125_1, 2 and 3 again showing broadening for the higher temperature samples. Sample 1R_125_3 was drawn at high temperature but the draw speed was increased from 10m/min to 35m/min corresponding to a preform feed rate increase from 0.5mm/min to 1.8mm/min. This results in the preform travelling a distance of 10mm in 5.6min instead of 20min in the furnace. Correspondingly a 125μm fibre spends 0.3s instead of 1.2s travelling a distance of 0.2m. This reduced dwell time of the preform and fibre in the furnace should result in less diffusion. As expected Sample 1R_125_3 exhibits less diffusion than Sample 1R_125_2. However, due to higher temperature, Sample 1R_125_3 has diffused more than Sample 1R_125_1. Not surprisingly it can be concluded that diffusion occurs during high temperature drawing and that not only temperature but also the duration of exposure to heat affects the amount of diffusion.

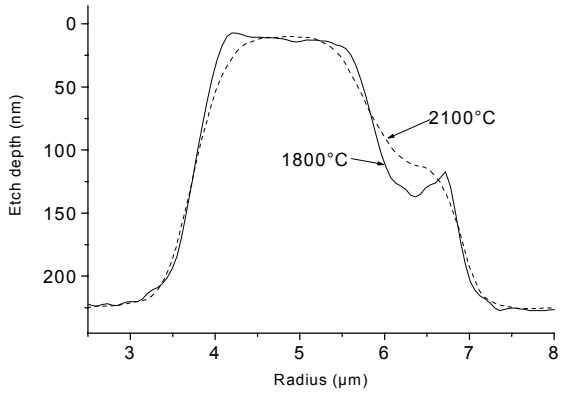

Figure 4-36. Fibre AFM profile for Samples 1R_125_1 and 2.

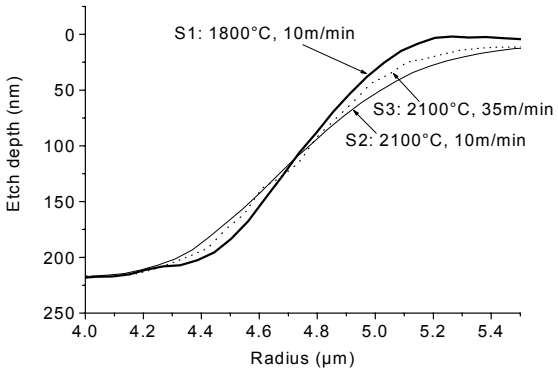

Figure 4-37. AFM profiles of the inner edge of the ring for Samples 1R_125_1, 2 and 3.

To confirm the results a high-resolution fibre refractive index profiler (Section 3.3.1.2) was used to analyse the fibre samples. Figure 4-38 shows the comparison between the refractive index profiles of the Samples 1R_125_1, 2 and 3. Although the resolution of the fibre refractive index profiler is less than the AFM, the diffusion is still evident from the comparison. The ring inner edge comparison is shown in Figure 4-39. Here the resolution limitations are significant and differences between the samples are not so obvious, although consistent with the AFM profiles.

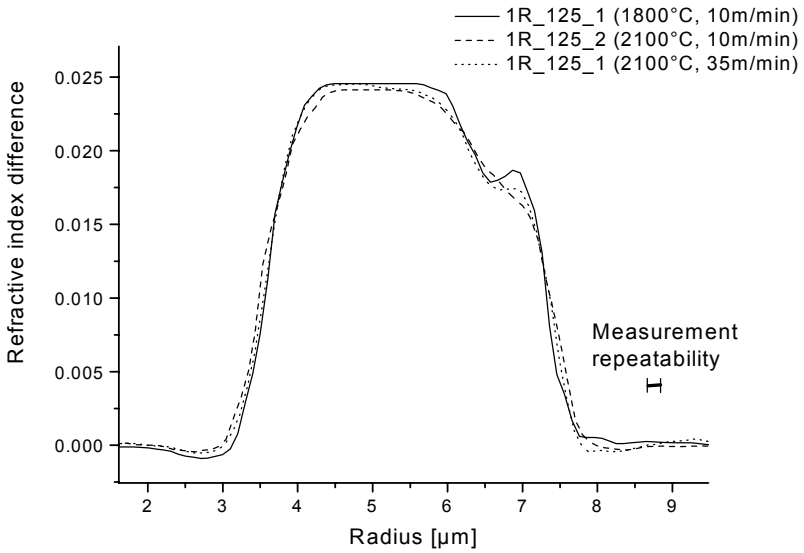

Figure 4-38. Fibre RIPs of Samples 1R_125_1, 2 and 3.

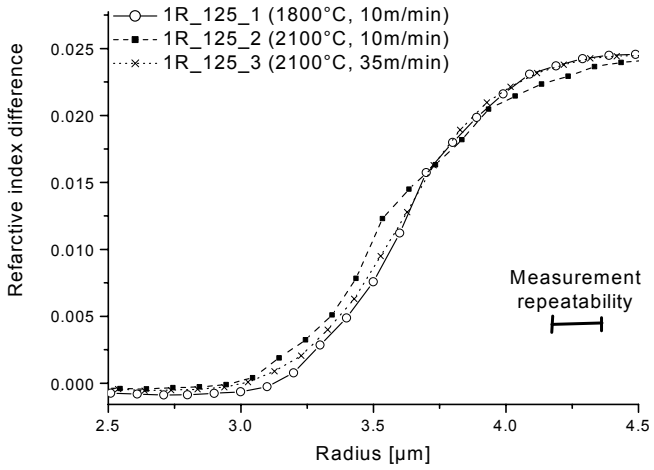

Figure 4-39. Fibre RIPs of Sample 1R_125_1, 2 and 3, inner edge of the ring.

Finally the preform and fibre samples were compared. The comparison between the preform EDS profile and etched fibre profiles is shown in Figure 4-40. The fibre drawn at colder temperature shows similar inner peak shape as that of the preform whereas the hotter sample is more diffused. There is some discrepancy between the shape of the preform and fibre samples, which is most likely due to inaccuracy in determining the etching depth relation to concentration as relatively high HF concentration was used. The corresponding RIPs for preform and fibre samples are compared in Figure 4-41, showing that for the low temperature sample the shape of the small peak is similar to that of the preform RIP confirming the findings with previous comparison. The preform RI is higher at the ring but lower for the small dip on the outer edge. These differences may be due to different stress profiles of the preform and fibre. It has been shown that axial stress is released at cleaved fibre ends (and a couple of microns into the glass) [159]. If any stresses would prevail, the fibres would have 'frozen-in' viscoelasticity at high draw tension [68].

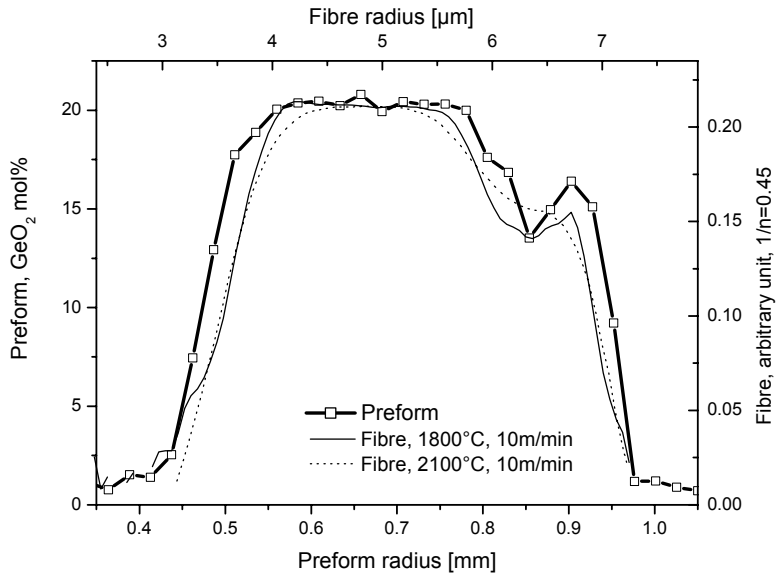

Figure 4-40. Comparison of preform SEM and fibre Samples 1R_125_1 and 2 measured with AFM. (*n* is the etching reaction order used, refer to Section 3.3.2.4.). Preform concentration error is 0.2mol% and spatial resolution 0.004mm. Statistical fibre concentration error from etching analysis is <1% for lower concentration range and <0.01% for higher concentration range.[10] Fibre spatial resolution is in order of tens of nanometers.

[10]Note that the accuracy of the AFM and etching method depends on the correct determination of the etching reaction order, which for this sample is questionable due to the uncertainties of the etching process at the time. The relative comparison of the fibre samples is however reliable as etching conditions were identical.

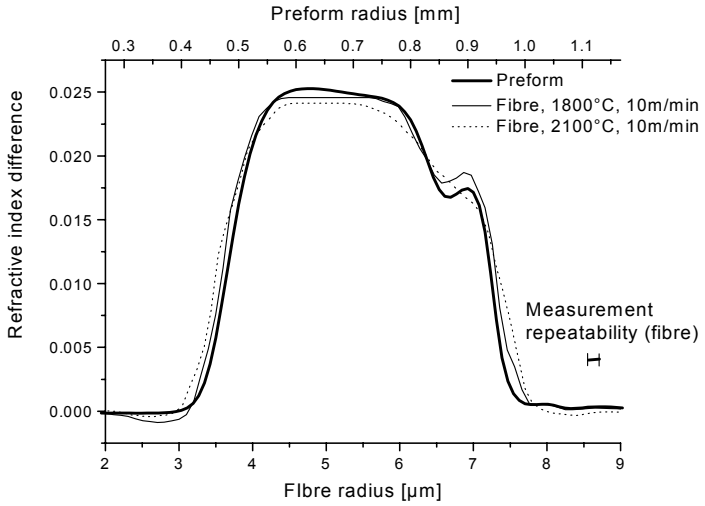

Figure 4-41. Comparison of preform and fibre RIP of Samples 1R_125_1 and 2.

In order to determine whether the differences in fibre profiles are due to diffusion, computations were performed using the measured profiles. It is shown in Chapter 6 that diffusion during drawing results in the measured profile change although the discrepancy remains with the preform concentration profile and etched fibre profiles. For more accurate diffusion computations the relationship with etching depth and dopant concentration was determined for the 3-ring fibre (Section 3.3.2.4) and experimental results presented in the next section (4.3.3)

4.3.3 3-ring-Ge-doped fibre

In order to quantify diffusion the relationship with etching depth and germanium concentration had to be established. The 3-ring design was chosen as the most suitable for the task. Each ring was doped with a different amount of germanium giving three concentrations against which the etching depth could be determined. For details see Section 3.3.2.4. The preform longitudinal homogeneity was expected to be an issue due to the relatively complex design and only two fibre samples were drawn to ensure their proximity in the preform. The fibres were drawn at 10m/min with a furnace temperature of 1800°C and 2100°C.

Table 4-9. Draw conditions for 3-ring fibre 3R_125

Sample	*Nominal Diameter (µm)*	*Furnace Temperature (°C)*	*Preform Feed Rate (mm/min)*	*Draw Speed (m/min)*
3R_125_1	125	1800	0.5	10
3R_125_2	125	2100	0.5	10

Only 20mm of preform was consumed during drawing. The preform RIPs corresponding to the fibre samples are shown in Figure 4-42. The profiles are almost identical and the refractive index level for each ring is the same in both longitudinal positions. To study the radial homogeneity a tomographic RI measurement was obtained at the position corresponding to Sample 3R_125_1. A 2D plot of the RIP is shown in Figure 4-43. There are no deformations in the ring shapes. Figure 4-44 shows tomographic RIPs taken at four angular positions. There is no significant variance in the inner most ring, however the refractive index difference varies about 10% for the mid and outermost ring. To determine the GeO_2 concentration profile EDS on SEM was used. A BSE image of the preform is shown in Figure 4-45. The concentration profile is compared with the tomographic RIP in Figure 4-46. The concentration variance in each ring corresponds to the number of MCVD layers in the preform fabrication. Note that the RI profiler does not resolve these layers but they are seen in the micrograph taken with optical microscope in Figure 4-47. If the refractive index is scaled to match the outermost ring a large difference is seen in the inner-most ring and some difference in the middle ring. The thermal stress in the preform can cause about 8×10^{-4} increase for 9mol% Ge-doped fibre core due to compressive stress in the doped core [67]. This agrees with the middle ring. The difference is larger for the highly doped inner ring, which is consistent with increased difference in thermal expansion coefficients.

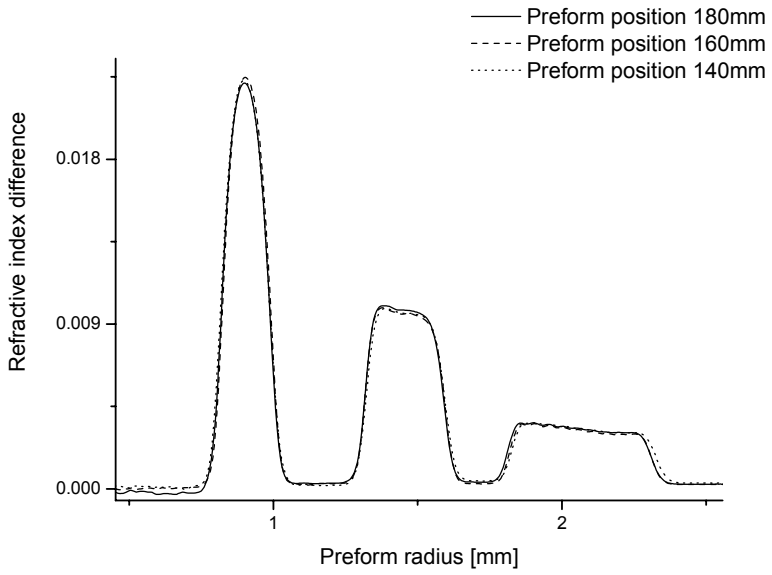

Figure 4-42. Preform RIPs corresponding to fibre samples 3R_125_1 and 2.

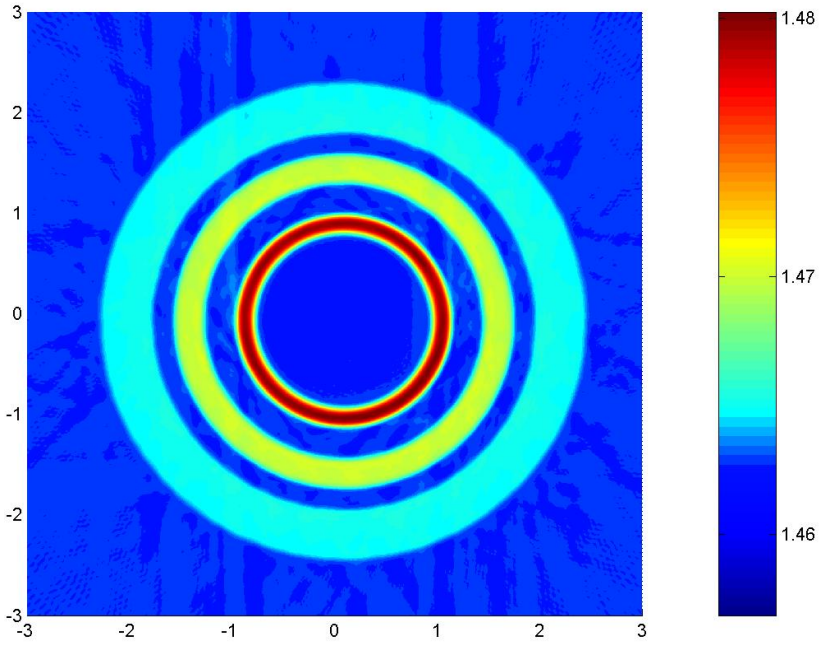

Figure 4-43. Tomographic RI contour plot of the preform 3R. Colour represents refractive index and X and Y are positions in mm.

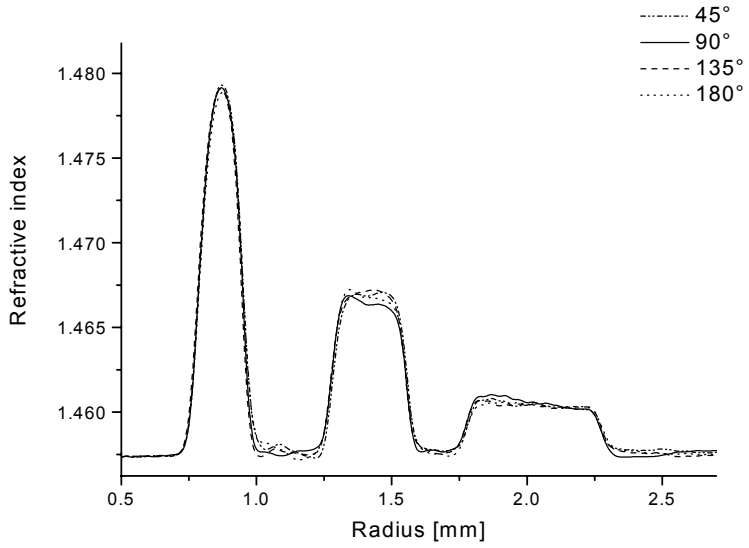

Figure 4-44. Preform tomographic RIPs for 3R at four angular positions, 90°, 45°, 135° and 180°.

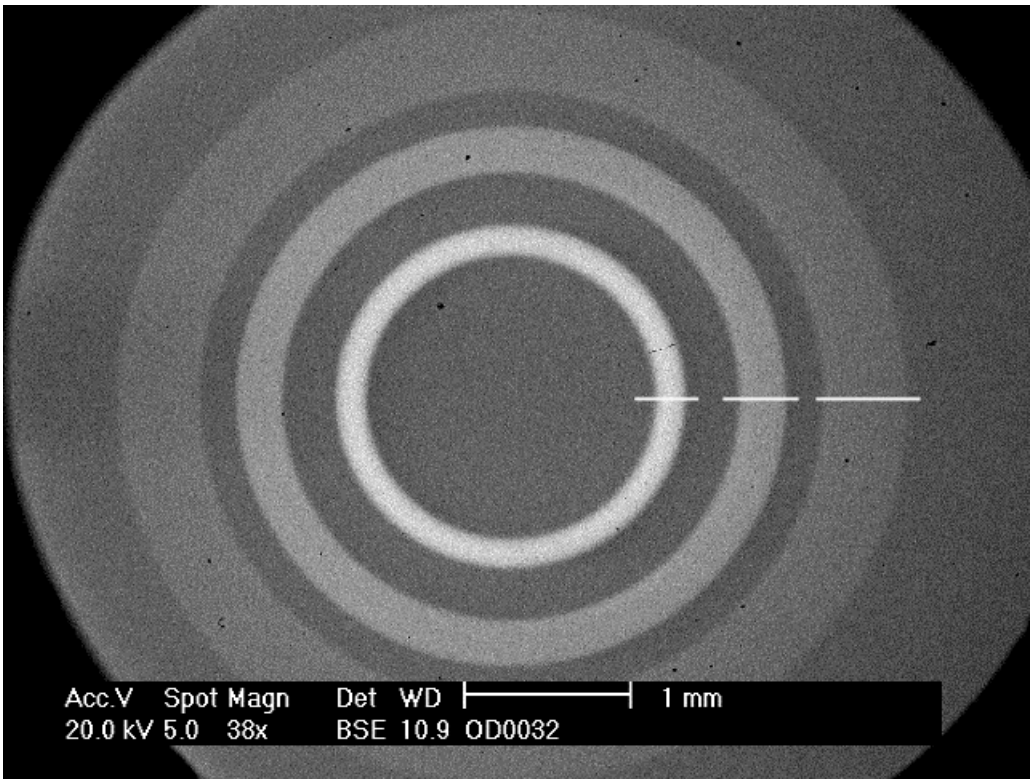

Figure 4-45. BSE image of the preform 3R. The lines indicate measured line scans for each ring.

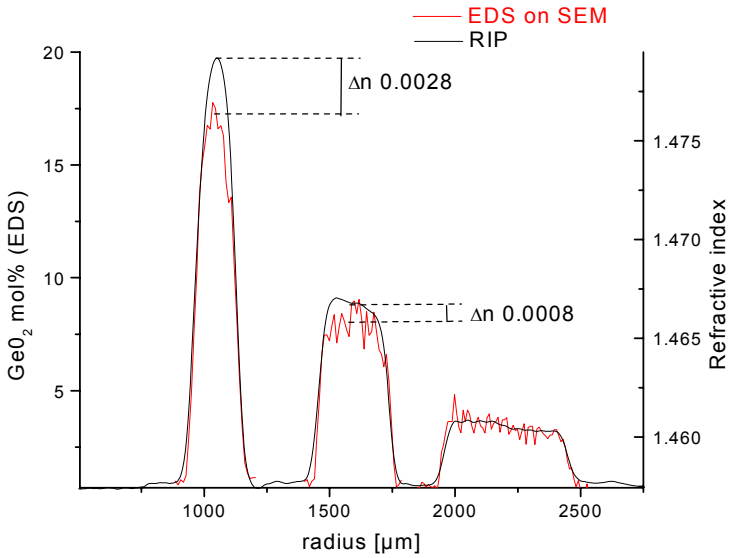

Figure 4-46. GeO_2 concentration profile measured using EDS in SEM and RIP for preform 3R.

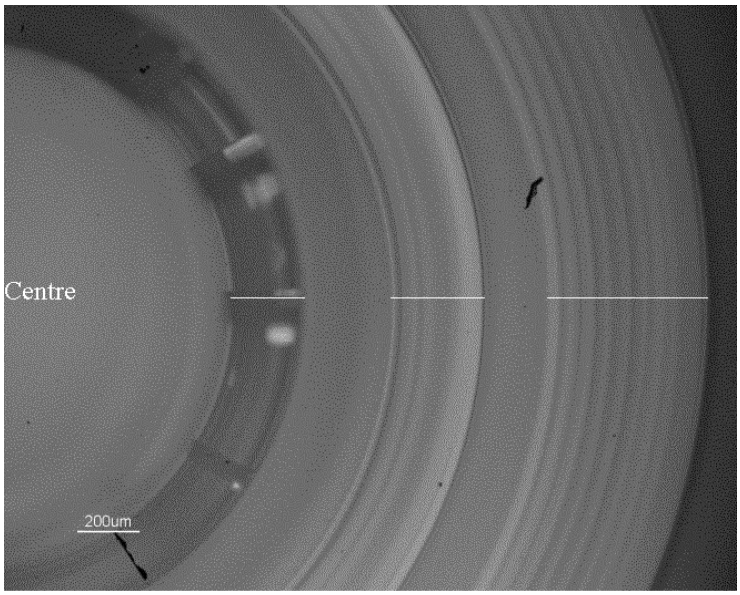

Figure 4-47 Optical micrograph of preform 3R showing the layer structure of the outer rings.

The fibres were analysed by the etching and AFM technique and RI profiler. The raw AFM profile for the fibres is shown in Figure 4-48. HF concentration of 5vol% was used. The difference of the profiles is evident for the inner-most ring with highest Ge concentration. The fibre that was drawn at hotter temperature has etched less indicating a lower Ge concentration. The difference in the two outer rings is not so clear. Figure 4-49 show the profiles for each ring after transforming the raw data to represent GeO_2 molar concentration (3.3.2.4). The innermost peak shows broadening of the profile, which very much resembles change originated from dopant diffusion. It is possible that the middle ring also has undergone some change at the higher temperature, however this change is within the 10% variance found in the preform. The outermost ring seems to have changed the least if at all implying no significant diffusion.

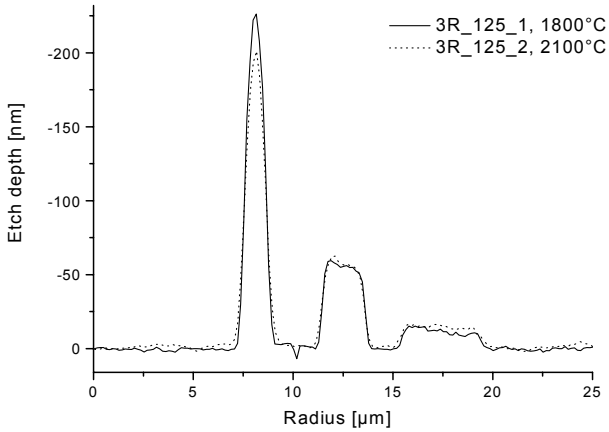

Figure 4-48. AFM profiles (raw data) of Samples 3R_125_1 and 2. HF concentration was 5 vol%.

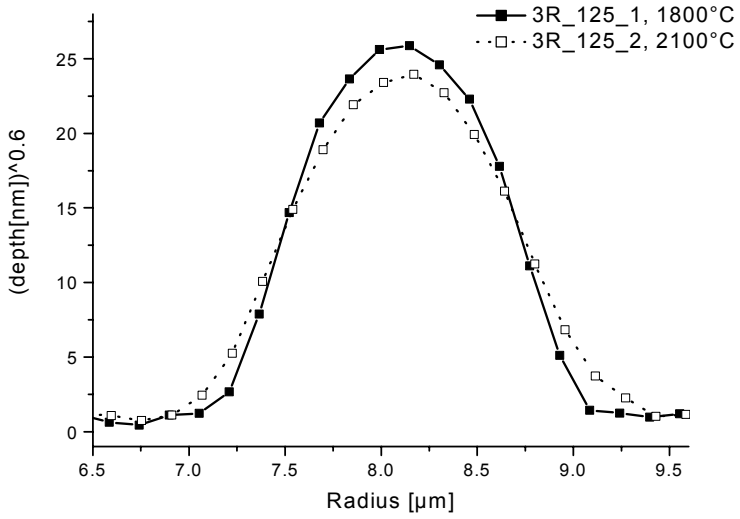

(a)

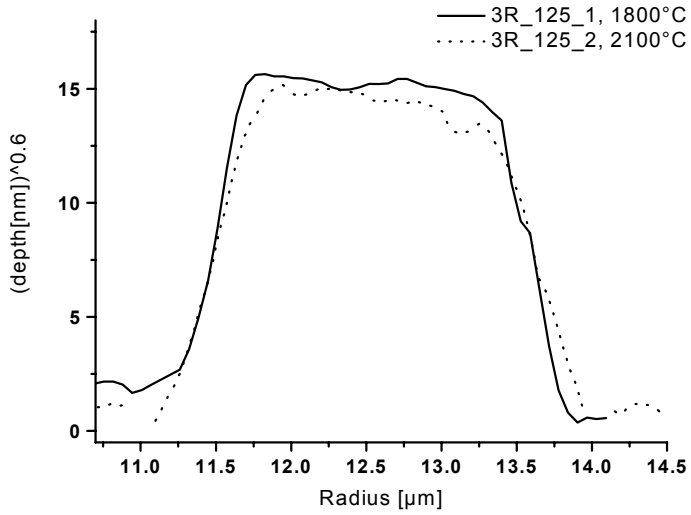

(b)

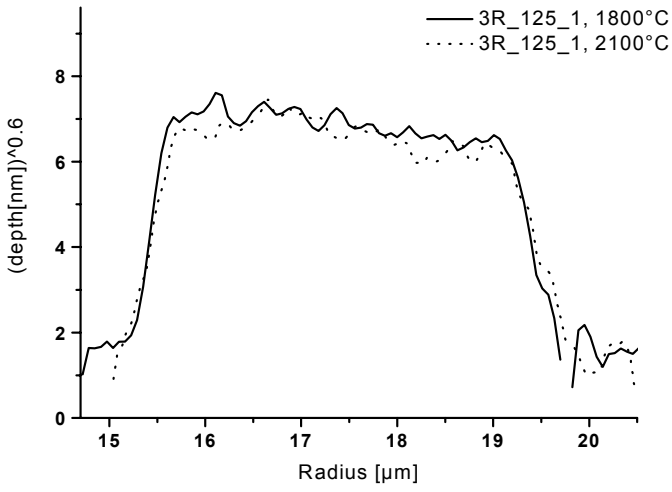

(c)

Figure 4-49. Transformed AFM profiles of (a) the inner ring, (b) mid and (c) the outer ring of Samples 3R_125_1 and 2.

The fibre RIPs are shown together with the preform RIP in Figure 4-50. The greatest difference between the fibre samples is seen in the innermost ring, which is consistent with the etched fibre profiles. The peak refractive index is higher for the sample drawn at a colder temperature. Note that the innermost ring has a full width at half maximum of only 1.5μm making accurate RI profiling difficult. No significant change is seen in the width of the peak within the measurement accuracy. The preform RI is higher for all the rings but most significantly for the inner most ring. As with the comparison of the 1-ring preform (1R) this can be explained by release of the axial stress when the fibres were cleaved. Note however that when the fibre RI for the silica centre is set to zero the cladding RI is negative. If no axial stress is present the RI should be same as that of the centre. It must be noted that the focus for fibre RIP was difficult to adjust and could result in some error. If stresses are present, the reduced RI may be due to draw induced mechanical stress, as the outer cladding would solidify first, bearing most of the tensile stress [67, 68].

It can be concluded that there is significant change between the samples drawn at different temperatures. It is shown in Chapter 6 that dopant diffusion during draw accounts for the change in profile of the innermost ring. The diffusion coefficient for Ge is obtained using the etched fibre profiles and preform concentration profiles in Section 6.4.2.

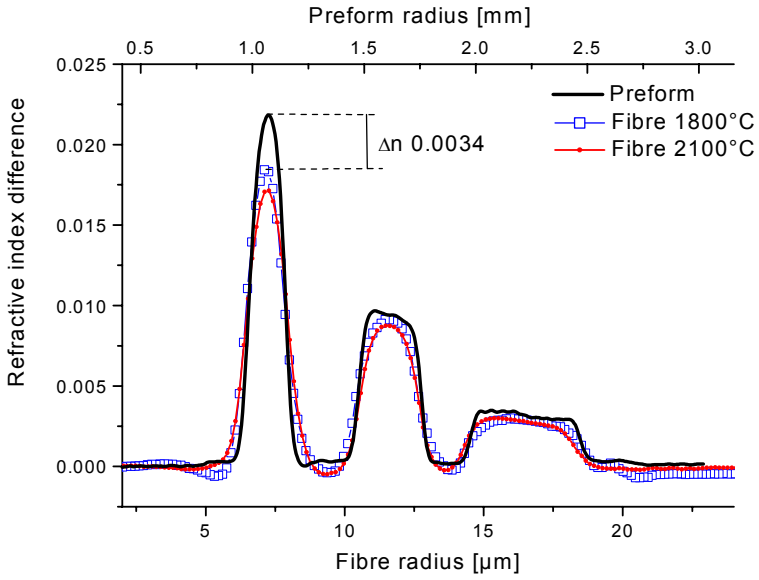

Figure 4-50. Fibre RIPs of Samples 3R_125_1 and 2 and preform RIP. The symbols for fibre measurements present the standard deviation of the RI for each measurement set.

4.3.4 F-doped cladding pure silica core fibre

Fluorine diffusion during drawing was studied using the same techniques as for Ge diffusion. A silica core, fluorine-doped cladding, preform was drawn at four different drawing conditions (Table 4-10) to a nominal diameter of 110μm. Due to the very slow speed (2m/min) the diameter controller was not used and diameter varied in Samples F_112_2 and F_130_4. The preform was analysed with the RI profiler and chemical analysis was acquired using WDS on EPMA. The fibres were analysed using etching and AFM technique and RI profiling. Note that for comparisons the 112 and 130μm samples were scaled to 110μm.

Only 30mm of preform was used during drawing. The preform was not pre-treated prior to drawing (for example by fire polishing) to avoid any thermal processing. The homogeneity was expected to be excellent as the preforms are commercially produced. The refractive index profiles along the length of the preform are shown in Figure 4-51. A tomographic 2D RI plot is shown in Figure 4-52 and corresponding radial scans at 5 angles in Figure 4-53. Note that although the core-cladding interface is shown as rounded, this is an artefact resulting from the very steep RI gradient of the step-index profile ([77], Section 3.3.1.1). This is evident from the fluorine concentration profile measured using WDS on EPMA (Figure 4-54), where the change from average cladding fluorine concentration of 4.3w% to pure silica occurs within 30μm. This corresponds to 0.1μm in 110μm diameter fibre. On the outer edge of the preform the RIPs show a fluorine-depleted region. Although the width of this region is difficult to define due to the inaccuracy of the profile, importantly this feature stays constant both in longitudinal and radial comparisons of the preform. The WDS profile shows the first measurement point as having F concentration of 2.9w%, which is 30% less than the average cladding concentration. The fluorine concentration varies in the cladding from 3.9 to 4.7w%. The variance seems to correspond to the layered structure resulting from the preform fabrication process [160].

Table 4-10. Draw conditions for F-doped cladding pure silica core fibres

Sample	*Diameter (μm)*	*Furnace Temperature (°C)*	*Preform Feed Rate (mm/min)*	*Draw Speed (m/min)*
F_110_1	110	1900	0.2	10
F_112_2	112	1900	0.04	2
F_110_3	110	2100	0.2	10
F_130_4	130	2100	0.04	2

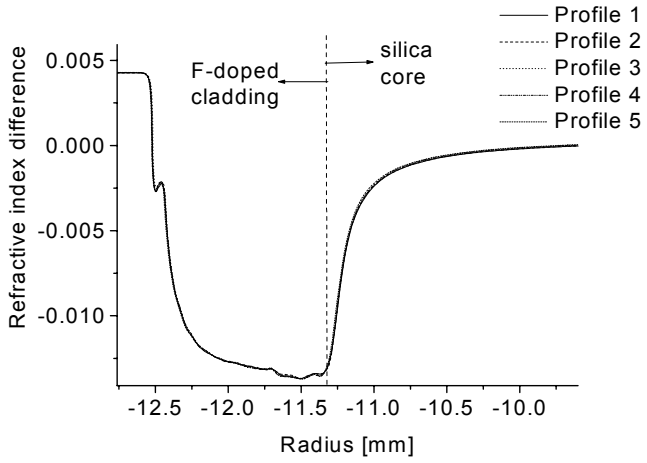

Figure 4-51. Five RIPs at 10mm intervals along the length of the preform with F-doped cladding.

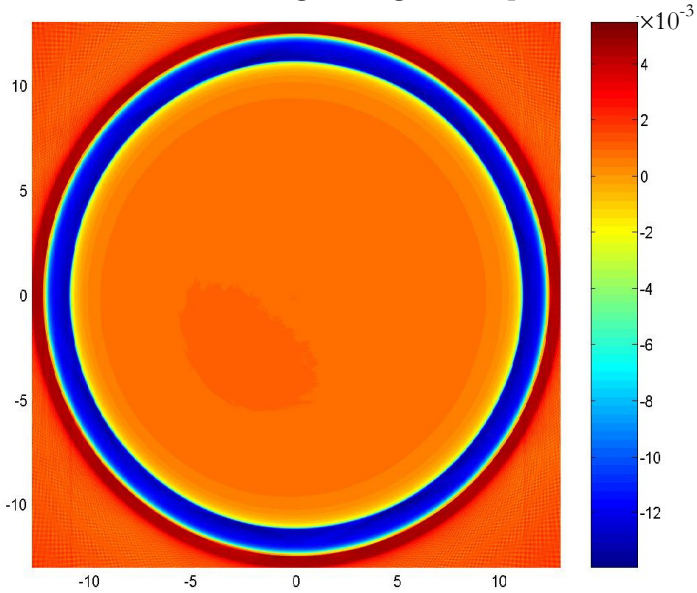

Figure 4-52. Tomographic 2D RI plot of the preform F.

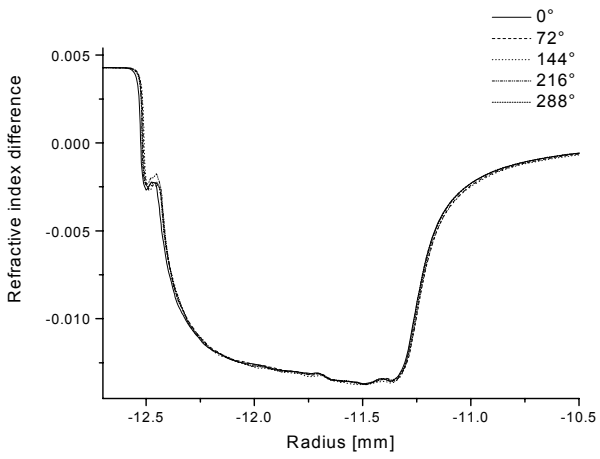

Figure 4-53. RIPs for preform with F-doped cladding at 5 different angular positions

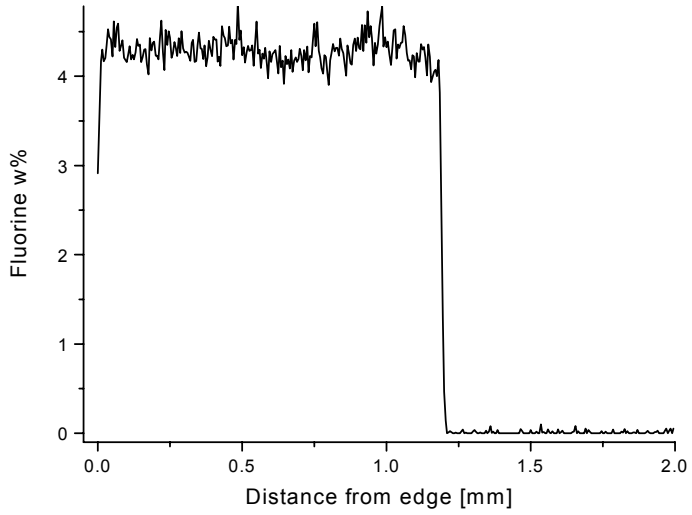

Figure 4-54. Fluorine concentration profile measured using WDS in EPMA.

The etched fibre profiles are shown in Figure 4-55 and Figure 4-56. At both 10m/min and 2m/min the fibre drawn at hotter temperature shows similar changes in the profiles. At hotter temperature the F-depleted region in the outer edge of the fibre has etched less indicating lower F concentration. At the core-cladding interface the slope of the interface is reduced for the fibre drawn at hotter temperature. Both changes indicate higher mobility of fluorine, both towards the core and out of the fibre. The effect of draw speed at constant temperature is shown in Figure 4-56. For both temperatures when the draw speed is reduced, the same changes are seen as explained above. The F-depleted region has lower F content and the core-cladding interface has reduced slope. As no 3-ring structure (or equivalent) was available for fluorine-doped fibre, the relationship of etch-depth to F content could not be established, and no quantitative diffusion comparison could be carried out with the samples.

To confirm the changes in profiles the fibres were also measured with the RI profiler. Similar comparisons presented for the etched samples were made for fibre RIPs and are shown in Figure 4-57 and Figure 4-58. The profiler does not resolve the F-depleted region in the outer edge of the fibre but shows the change in core-cladding interface slope. The trends are similar to those shown with AFM profiles.

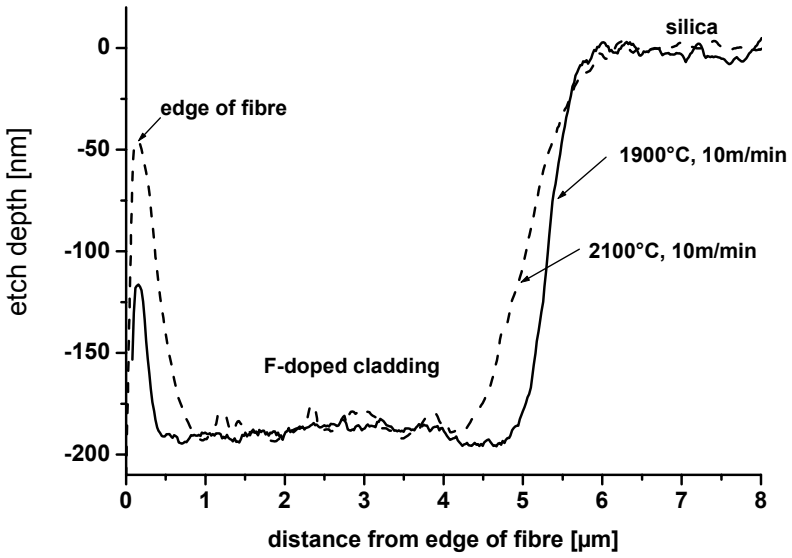

(a)

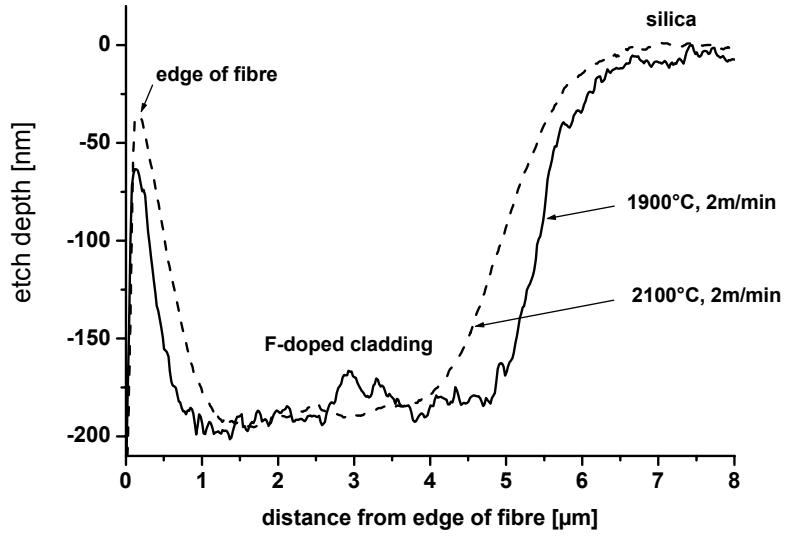

(b)

Figure 4-55. AFM profiles of (a) high draw speed samples F_110_1 and F_110_3, (b) low draw speed samples F_112_2 and F_130_4. Data scaled to 110µm diameter fibre.

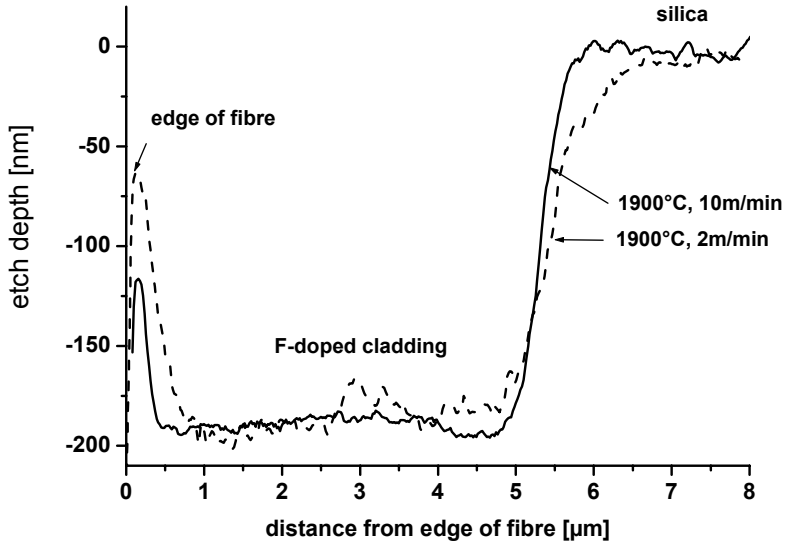

(a)

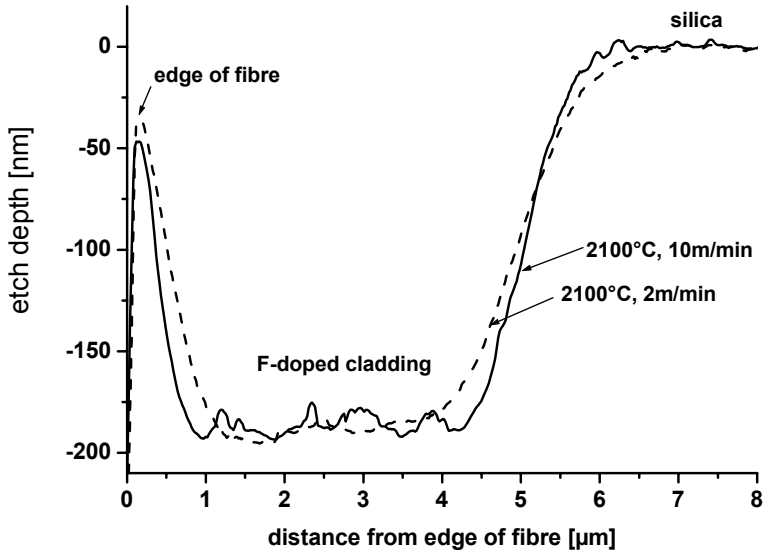

(b)

Figure 4-56. AFM profiles of (a) low temperature samples F_110_1 and F_112_2, (b) high temperature samples F_110_3 and F_130_4. Data scaled to 110µm diameter fibre.

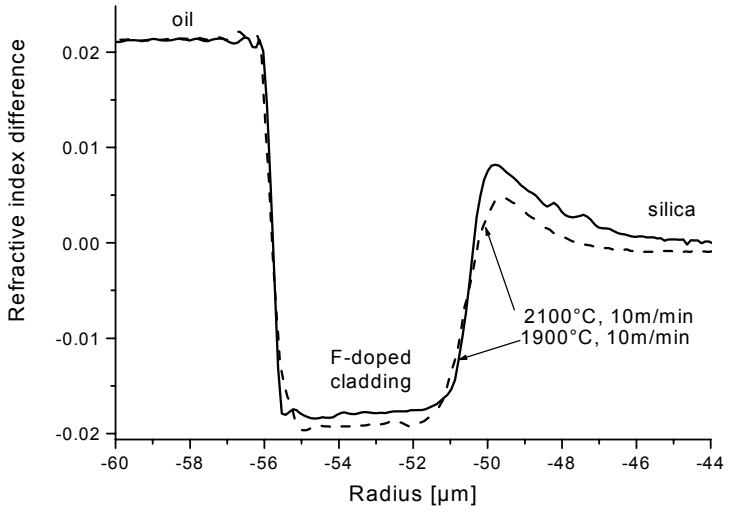

(a)

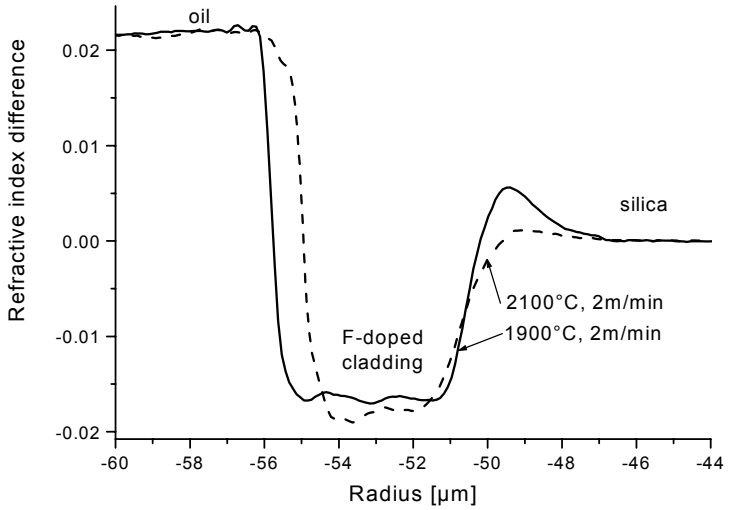

(b)

Figure 4-57. RIPs of (a) high draw speed samples F_110_1 and F_110_3, (b) low draw speed samples F_112_2 and F_130_4. Data scaled to 110μm diameter fibre. Note that F_130_4 was etched to reduce the fibre outer diameter. Note that the peak at the core-cladding interface is believed to be a measurement artefact resulting from the high refractive index of the oil compared to the cladding. The peak does not appear in the AFM measurements. It is believed that this artefact does not affect the conclusions as they agree well with the results from AFM measurements.

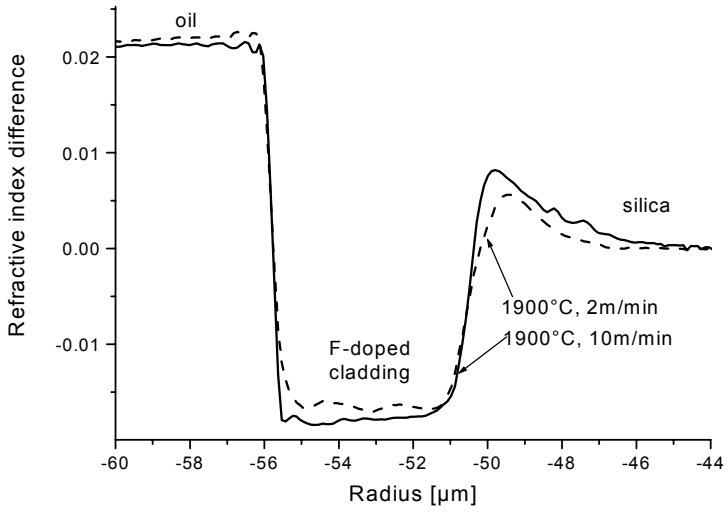

(a)

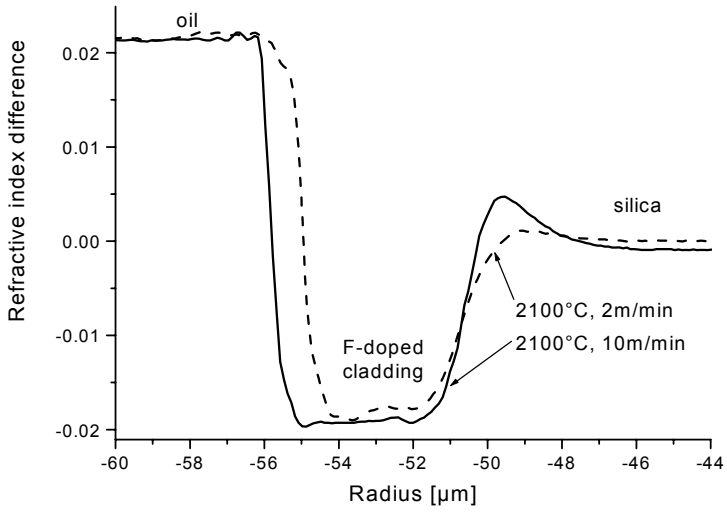

(b)

Figure 4-58. RIPs of (a) low temperature samples F_110_1 and F_112_2, (b) high temperature samples F_110_3 and F_130_4. Data scaled to 110μm diameter fibre. Note that F_130_4 was etched to reduce the fibre outer diameter.

To compare all four draw conditions, the etch depth of the F-depleted region on the outer edge of the fibre and the slope of the core-cladding interface are plotted in Figure 4-59 and Figure 4-60. The lowest F concentration in the edge of the fibre is for fibre drawn at 2100°C and 2m/min. The slope of the core-cladding interface is lowest for this sample as well. The highest F concentration in the edge of the fibre is for the sample drawn at 1900°C and 10m/min. This correlates with diffusion, which is increased at higher temperatures and at lower draw speeds due to increased dwell time in the furnace. Note that the trend in slope is the same measured both with AFM and RIP. The magnitudes of change are different which is not surprising as the etching depth is unlikely to be linear with fluorine concentration.

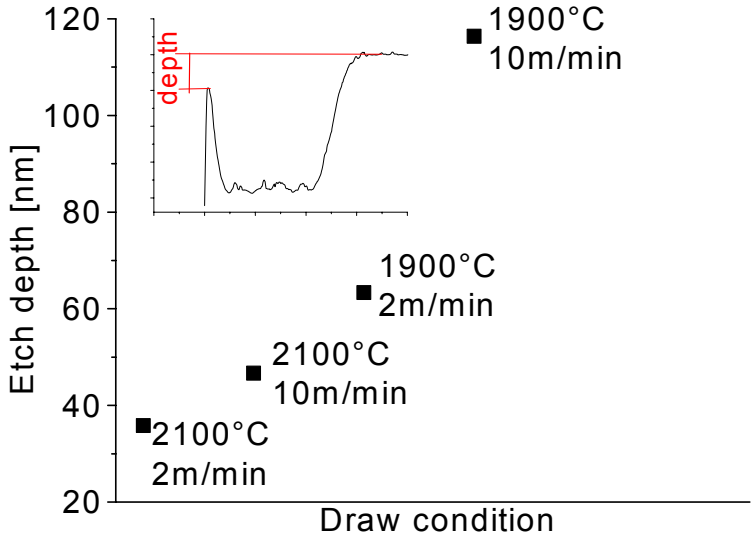

Figure 4-59. AFM etch depth measurements of the peak at the outer edge of the fibre.

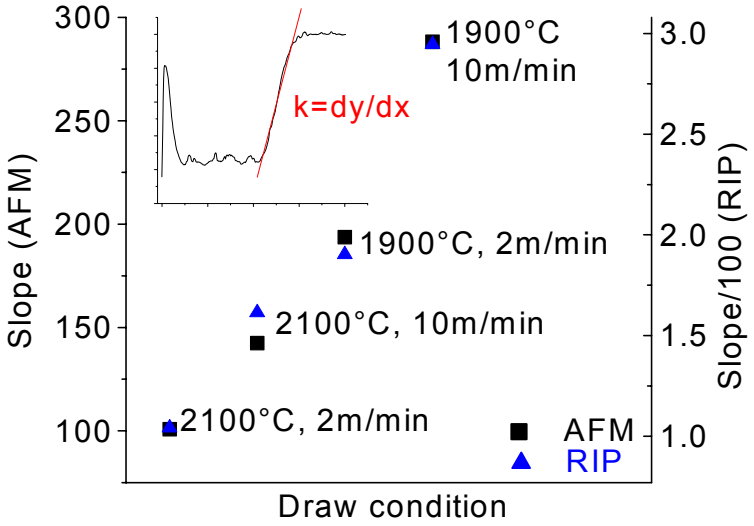

Figure 4-60. Cladding-core edge slope measurements from AFM and RI profiles.

Finally the fibre profile measured using the etching and AFM technique for the least diffused sample F_110_1 was compared to the concentration profile of the preform (Figure 4-61). Any conclusions from the comparison must be taken with caution, as it is unlikely the etching depth is linearly dependent on the concentration. The fibre cladding F content variation seems to follow that of the preform and the F-depleted region on the edge is of same magnitude. The inner edge of the fibre seems diffused compared to the preform. It is plausible that the mobility of the fluorine is different in the outer edge of the fibre to that inside the fibre. This may be possible for example if the removal mechanism of fluorine from the fibre edge affects the diffusion profile. If this were the case, then the furnace atmosphere may have an effect. Factors such as selection of furnace gas, the amount of oxygen and humidity in the gas as well as the furnace temperature may affect the surface chemistry on the preform and fibre. The diffusion towards the core is unaffected by these factors but would be affected by the quality of the silica, i.e. OH and impurity content.

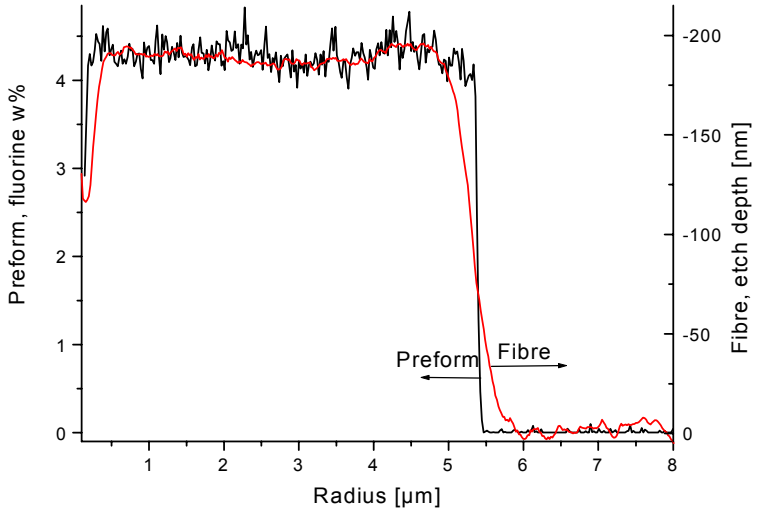

Figure 4-61. Preform F profile compared to fibre AFM profile for Sample F_110_1.

4.4 Discussion

4.4.1 Ge and F diffusion

Dopant diffusion experiments were carried out by drawing preforms into fibres using various draw conditions. The preform and fibre samples were characterised using various techniques including RI profiling, X-ray microanalysis and the etching and AFM technique. Modification of the profiles was found to occur during drawing for both germanium and fluorine doped fibres under high draw temperature (2100°C) and low draw speeds (<40m/min). The profile change was characterised by reduced peak dopant concentration and broadening of the profile indicating dopant diffusion as the source of the change.

At low draw temperature (1800°C) germanium doped fibre profiles were found to have insignificant change. The draw speed was found to affect the profile alteration by having a greater effect at slower speeds. This is consistent with diffusion-induced change where at slower speeds the preform and fibre are exposed to high temperature for longer times during drawing. The profile change was not similar in all parts of the fibre. For the 3-ring Ge-doped fibre the outer ring with low Ge concentration had very little or no change in profile even at extreme draw conditions. In terms of diffusion, this could be due to either a temperature gradient in the cooling fibre or concentration dependent diffusion coefficient.

The fluorine doped fibre profile was found to alter even at the low temperature of 1900°C. The fluorine was found to be mobile in both the outer and inner surface of the cladding. At both interfaces the broadening of the profile indicated diffusion-based mobility. The broadening occurred progressively from sample to sample from low temperature and faster draw speed to higher temperature and slow draw speed. It is possible that the diffusion in the outer edge of the cladding is altered by a mechanism by which the fluorine is removed from the preform and fibre surface. This surface chemistry may be affected by the furnace atmosphere as well as the temperature.

4.4.2 Limitations of the measurement techniques

Although the major challenges for the diffusion measurements were overcome during this study, there are some limitations to both the fibre refractive index measurement and the etching and AFM technique. Both residual stress and silica fictive temperature have been shown to affect the refractive index. These effects presumably both arise from the change in density of silica. The effects have been widely studied and reported in the literature (see Ref. [161] and Appendix I). The etching and AFM technique however is more recent and such effects are not fully established yet, although no such effects have been found significant to date in the etching and AFM technique [162]. A brief discussion is provided below on the possible effects and implications on the results of the current study.

The fictive temperature of glass is determined by the thermal history of the glass. In particular, the cooling rate affects the fictive temperature. For silica the higher the cooling rate the higher its fictive temperature [163]. During drawing, depending on the drawing temperature and the drawing speed, the cooling rate can change, causing the fibres to have different fictive temperatures. It has been shown that silica with different fictive temperature exhibits a different refractive index and a different HF etching rate [164]. Hence it is possible that the fictive temperature affects the profiles obtained by the etching and AFM method and the refractive index profiles.

The cooling rates for the fibres used in the diffusion study were estimated using the heat transfer calculations (see Chapter 6). Due to the low draw speed used for all the samples, the cooling rate is about 2500°C/s, a relatively moderate rate in terms of typical fibre drawing. This cooling rate differs by no more than a few tens of °C/s between the fibre samples so that the change in fictive temperature resulting from the difference in cooling rates is insignificant. Due to this relatively moderate cooling rate the temperature dependence of the density is also insignificant [165]. A typical range of fictive temperatures measured for optical fibres with varying manufacturing methods are 1600-1700°C [166]. It is expected based on the above arguments that the fictive temperature of the fibres does not significantly vary. There have also been reports on radial fictive temperature gradients in Ge-doped core silica fibres [167, 168]. However, a

study by Kim and Tomozawa [166] which re-examined the earlier results showed that such gradients did not occur in fibres .

Although it is unlikely that the fibres used here exhibit significantly different fictive temperatures, it must be noted for future studies that if the fictive temperatures of the samples are significantly different, this may cause an increased error in measurement of both RI and differential etching rate. For example a 300°C higher fictive temperature increases the RI by 3×10^{-4} for high purity synthetic (F300) silica glass [161]. For fluorine doped silica the effect was found to be less. Similarly it has been shown that a 300°C higher fictive temperature increases the HF etching rate of silica (natural) by about 30% [164]. This however does not indicate any trend for differential etching rates of doped samples. Most importantly it has been shown by Zhong and Innis [81] that the dopant concentration has the dominant contribution for differential etching rate. They found that fibres manufactured with various methods and conditions and dopant concentrations showed that differential etching rate was dependent on the dopant concentration irrespective of the fibre type or manufacturing method (thus fictive temperature and stress state) and a consistent relationship could be established for the dopant concentration and the differential etching rate.

In summary it has been shown that significant profile change can be induced during drawing. In order to prevent such change or use it to advantage, the effects of draw parameters such as furnace temperature, drawing speed and preform diameter must be known. Based on the experimental results presented in this chapter, diffusion computations were carried out. The diffusion coefficient for germanium in silica was estimated and was subsequently used to calculate diffusion effects on the fibre compositional profile using thermal history data from heat transfer calculations. These simulations allowed studying of the diffusion effect of the different draw parameters. The techniques and results are presented in Chapter 6.

CHAPTER 5 GEOMETRY CONTROL OF PHOTONIC CRYSTAL FIBRES

5.1 Background

Photonic crystal fibres and their guiding properties were presented in the Background Chapter 2 in Section 2.2.5. As was discussed, the guidance of light and optical properties of the fibre depend on the geometry of the air structure surrounding the core. PBG fibres are specifically vulnerable to structural inhomogeneities because the guidance is based on a structure where high periodicity with tight dimensional tolerances is required to form the band gaps [32, 169-172]. Photonic crystal fibres that guide light based on the so called average index effect tolerate geometrical changes better, however properties such as micro and macro-bending losses and dispersion are affected significantly by fine adjustments in the geometry [46, 173, 174]. Accurate control of the properties of these fibres also requires fine control of the geometry and therefore of the fabrication process.

A few studies have used theoretical modelling in trying to understand the basic single capillary drawing process. Fitt *et al.* [11] studied capillary drawing theoretically and derived analytical relationships between draw parameters and capillary geometry. Stability in capillary drawing has also been studied [175, 176]. In photonic crystal fibres where multi-capillary drawing is critical, Deflandre [12] made a theoretical study on hole deformation in the neck-down region of a drawn photonic crystal fibre with an hexagonal hole pattern. Although the above studies give useful qualitative results, the necessary approximations for both analytical and numerical studies greatly limit their quantitative usefulness in practice.

Although numerous papers on photonic crystal fibres briefly describe the fabrication process and mention the importance of various draw parameters in obtaining the required structure, there are very few papers that discuss in detail aspects of the fabrication process itself. The fabrication of various air-silica structures has been discussed by Knight et al. [70] who give practical guidelines for obtaining desired parameters such as air-filling fraction and hole separation based on experimental results.

They suggest that the main draw parameter controlling the air structure is the drawing temperature and note that due to surface tension forces the maximum obtainable air-fraction reduces as the fibre dimensions are reduced. Drawing temperature was also used in a study by Bennett *et al* [177] to control the air-filling fraction.

The lack of details in the literature makes it difficult to compare these studies with the results of this thesis. However, Fitt *et al* [11] have provided an in depth study on capillary drawing, of which selected findings will be provided here. Fitt *et al* [11] used mathematical modelling to study the capillary drawing process. In capillary drawing a large diameter annular cross-section tube is drawn into a capillary tube. The capillary drawing process is the most simplified case of PCF drawing process. Since the PCF structure typically contains tens or even hundreds of holes, it is not expected that modelling of the capillary draw will provide comparable quantitative results. However some of the findings may apply at least qualitatively for a single hole in a PCF structure. The experimental results in this thesis will be discussed in relation to the theoretical findings of Fitt *et al* [11] when relevant.

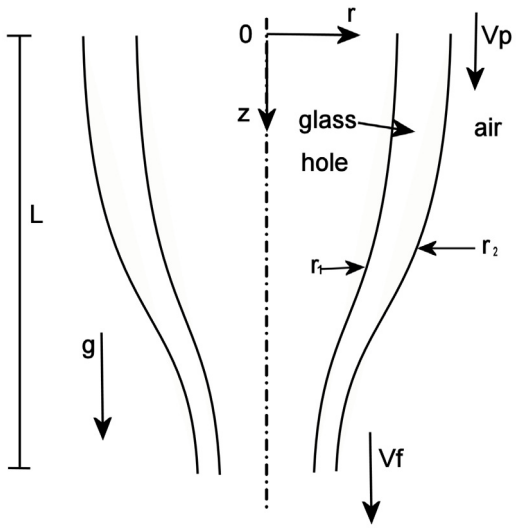

Figure 5-1. Schematic diagram of the capillary drawing process

In their study Fitt *et al* [11] constructed a fluid mechanics model using asymptotic analysis with assumptions specific to capillary drawing. The governing equations derived by Fitt *et al* [11] are shown in Eq. (22) to (25), see also Figure 5-1. Following the authors' notations, the derivatives are denoted by subscripts. These equations are the leading-order equations derived from the Navier-Stokes and convection-diffusion equations where the main assumption exploited is that the radius of the capillary is much smaller than the characteristic length of the neck-down ($r \ll L$). Since the derivation of these equations is lengthy and out of the scope of this thesis, it is not presented here. The details can be found in Ref. [11]. A more detailed background for the use of fluid dynamics modelling in the area of optical fibre drawing can be found in Chapter 6, Section 6.1 and 6.2.

$$\rho\left(r_2^2 - r_1^2\right)\left[v_t + vv_z - g\right] = \left[3\mu\left(r_2^2 - r_1^2\right)v_z + \xi\left(r_1 + r_2\right)\right]_z \tag{22}$$

$$\left(r_1^2\right)_t + \left(r_1^2 v\right)_z = \frac{p_0 r_1^2 r_2^2 - \xi r_1 r_2 \left(r_1 + r_2\right)}{\mu\left(r_2^2 - r_1^2\right)} \tag{23}$$

$$\left(r_2^2\right)_t + \left(r_2^2 v\right)_z = \frac{p_0 r_1^2 r_2^2 - \xi r_1 r_2 \left(r_1 + r_2\right)}{\mu\left(r_2^2 - r_1^2\right)} \tag{24}$$

$$\begin{aligned} &\frac{r_2^2 - r_1^2}{2}\left[\rho c_p\left(T_t + vT_z\right) - k\left(T_z\right)_z - \sigma\varepsilon'\left(T_a^4 - T^4\right)\right] \\ &\qquad = r_2 h\left(T_a - T\right) \end{aligned} \tag{25}$$

where t is time, z is distance along the axis of capillary, r_1 and r_2 are the inner radius and outer radius of the capillary, v is velocity, ρ is density, g is acceleration due to gravity, μ is viscosity, p_0 is pressure difference between internal hole pressure and atmosphere and ξ is surface tension. In Eq. (25) c_p is heat capacity, T is temperature, T_a is ambient temperature, k is thermal conductivity, σ is Stefan-Bolzmann constant, ε' is material constant involving emissivity and h is heat transfer coefficient.

The findings listed below are based on the above equations together with assumptions and initial and boundary conditions relevant to each case. The major assumptions are listed below together with the findings. The equations are only presented when they are

used in this thesis. The derivation of the equations is not presented here since it is lengthy. Details can be found in Ref. [11].

Findings by Fitt *et al* [11]:

- Order of magnitude of terms in the governing equations, Eq. (22)-(24), for capillary drawing were analysed. The relative importance of inertial, gravitational and surface tension is shown by the non-dimensional parameters:

$$\frac{LV_f\rho}{\mu}, \quad \frac{gL^2\rho}{\mu V_f}, \quad \frac{\xi L}{\mu R_f V_f}$$

  L is the characteristic hot-zone length (10-50mm), V_f is the characteristic draw velocity (10-300m/min) and R_f is the typical drawn capillary size (0.1-10μm single hole in PCF and 0.1-2mm in cane draw). Typical material parameters for silica are ρ = 2200kg/m^3, μ = 10^4-10^5 Pas and ξ = 0.3N/m. From the comparison of the above non-dimensional parameters, it can be seen that viscosity effects are always important, inertial effects are negligible and gravitational effects are significant, especially when large diameter capillaries are drawn. The analysis also showed that in many draw regions surface tension and viscous effects compete. Internal hole pressurisation is similarly characterised by the following parameter:

$$\frac{Lp_0}{V_f\mu}$$

  p_0 is the pressure difference of the hole pressure to atmospheric pressure (up to 10kPa). The non-dimensional parameter $Lp_0/V_f\mu$ has to be of order of unity for hole internal pressurisation effects to be significant.

- In the absence of surface tension and internal hole pressurisation, the hole does not experience any collapse or expansion, hence preserving the initial outer to inner diameter ratio.

- When the assumption is made that surface tension has a very small effect (but that such effect is still present) and thus the viscous effects dominate, the equations predict that the degree of hole collapse depends on the ratio of surface tension and viscosity, ξ/μ. The analysis further predicts that under these assumptions the hole collapse is more sensitive to the preform feed speed

than the draw speed. As the glass viscosity depends on temperature, the hole collapse is sensitive to the temperature as well. Hole collapse is encouraged by low viscosity (high temperature), slow feed rate and long hot-zone. Note that in this analysis an isothermal assumption was made and inertial, gravitational and hole pressurisation effects were ignored.

- If inertia, gravity and surface tensional effects are ignored for the isothermal case, the qualitative finding can be made, that the sensitivity to internal hole pressurisation is increased with long hot-zone, low viscosity and slow feed rate.
- When both surface tension and internal hole pressurisation are taken into account, sensitivity of the process to internal hole pressurisation can be estimated. By assuming a relatively small hole and ignoring inertia and gravitation for isothermal drawing, following sensitivity parameter S was derived by Fitt *et al.* [11].

$$S = \frac{L\xi}{\mu r_{ID} V_p \log\left(V_f / V_p\right)}, \tag{26}$$

where r_{ID} is initial tube inner radius and V_p is preform feed rate, see Figure 5-1. When $S \ll 1$ internal hole pressurisation may be a suitable means of control, but if $S \gg 1$ the system is highly sensitive to pressurisation and control may not be feasible. It can be seen from Eq. (26) that the parameter S is more sensitive to the preform feed rate than the drawing speed. Since the hot-zone length is typically fixed and the surface tension of silica is constant, the sensitivity factor then depends only on the viscosity of glass (i.e. the drawing temperature), initial hole diameter, preform feed rate and the draw ratio V_f / V_p. The sensitivity parameter increases for lower drawing temperature, smaller hole size, lower preform feed rate and smaller draw ratio. Some examples of S values for different sets of parameters are shown in Table 5-1.

Table 5-1. Sensitivity parameter for typical drawing range for a hole diameter of 1.5mm, V_f 190m/min, V_p 3mm/min and T 1930°C.

1.	Draw speed	$0.2\times V_f$	V_f	$1.6\times V_f$
	S	1.9	0.4	0.2
2.	Feed rate	$0.2\times V_p$	V_p	$1.6\times V_p$
	S	1.9	0.4	0.2
3.	Draw temperature	T-100°C	T	T+200°C
	S	0.1	0.4	3.7

One of the main assumptions in the above analysis is that the problem is isothermal. Although the effect of temperature may be taken into account in the glass viscosity, the radial and axial temperature gradients are ignored. It is shown in Chapter 6, *Heat and mass transfer simulations of the fibre drawing process,* that significant temperature gradients can exist during fibre drawing process making this assumption invalid. It is however acknowledged that without certain assumptions, obtaining analytical correlations is impossible and that such correlations may prove to be valuable in studying the effects of PCF drawing.

The analysis of Fitt *et al* [11] implies that the main parameter governing hole collapse is the ratio of surface tension to viscosity. There is not much data on the surface tension of silica but it is typically considered not to vary significantly with temperature. However, as silica viscosity greatly depends on temperature, it is clear that furnace temperature is one of the main draw parameters affecting hole collapse. It is also important then to find out the effect of other draw parameters and the preform structure on temperature profile during the fibre drawing process. This is specifically looked at in Chapter 6. The preform feed rate was noted as playing an important role in the hole collapse, more so than e.g. drawing speed. In experimental studies it must be remembered that preform feed rate will also have an effect related to time exposed to temperature and change of viscosity. Perhaps the most interesting implication of the analysis is the use of preform internal pressure to control the hole dimensions. Although Fitt *et al* [11] do not directly recommend using pressurisation as a means of controlling PCF structures, they recognise that this may prove to be useful under limited draw conditions.

There is an additional issue which is not discussed in detail in the paper by Fitt *et al* [11]. If a force balance in the direction normal to the surface is applied over an element in the neck-down of a capillary with cylindrical symmetry it can be seen that the capillary dimensions depend on the rate of change of the thickness of the capillary wall along the drawing direction[178]. This will be affected greatly by the neck-down shape, i.e. the curvature of both the inner and the outer surface of the capillary. In solid fibre drawing, the neck-down has been shown to depend on most of the drawing parameters, such as

the preform feed rate, the drawing temperature, preform and fibre dimension and the draw speed (see Chapter 6).

In this thesis the use of the above-discussed parameters on controlling the hole structure of a PCF was studied experimentally. More specifically the use of draw temperature, preform feed rate and preform internal pressure was examined as a means of controlling the geometry during the fibre drawing process. Capillary-stacked preforms with a solid core were used in this work although one milled hollow core preform was used for comparison. The capillary stacking itself was found to be extremely important and Section 5.3.1 is dedicated to capillary draw experiments that resulted in ability to fabricate the high precision capillaries necessary for successful fibres. The results of the fibre geometry control experiments are presented in Sections 5.3.2 to 5.3.5.

5.2 Methods

The preform fabrication methods for PCFs were described in Chapter 3, Section 3.2.1.2 and the fibre drawing process and equipment in Section 3.2.2. The draw experiments and sampling technique are discussed in more detail below and the measurements are briefly reviewed in Section 5.2.2; a full description of the measurement techniques can be found in Section 3.3.

5.2.1 Experiments

Table 5-2 gives a summary of the various parameters studied and the effects observed in both the capillary drawing and the fibre drawing experiments. The parameters studied can be divided into two categories, (i) draw parameters and (ii) structural parameters. Draw variables included the process variables that can be changed during drawing and directly relate to the drawing process. Structural variables relate to the preform and fibre structures and geometric dimensions. The most important process variables i.e. draw temperature, preform feed speed and preform pressure effects were studied. In studying the effect of structural variables the effects of milled vs. capillary structure, cladding and capillary dimensions were considered. Majority of the preforms were fabricated by the capillary stacking method but one milled preform was included in the study.

The effects of the draw and structural variables on various aspects of final fibre geometry were studied. Depending on the aim of the particular experiment, the geometric properties such as hole diameter, spacing of the holes and size of the interstitial holes were measured. To study structural homogeneity, stack deformations were observed in addition to the above-mentioned properties. Homogeneity along the length of the fibre was judged by measuring the diameter variation during draw, geometric property changes along the length and attenuation of the fibres at various lengths. The above-mentioned experiments also revealed the structure dependant sensitivity to process variables, which is of utmost importance when optimal process conditions are chosen. The experimental conditions are described in detail before each result is presented.

Table 5-2. Summary of variables and effects studied in capillary and PCF draw experiments

	Capillary	*Fibre*
Draw variables studied	Draw temperature Furnace gas flow Tube internal pressure	Draw temperature Preform feed rate Preform internal pressure
Structural variables	Tube dimension Variation in tube dimension	Preform structure -type (milled/capillary) -cladding and capillary dimensions Fibre diameter Capillary stacking quality
Effects observed on	Inner diameter Diameter variations	Hole diameter Air fraction Stack deformations

To cover all the above-mentioned experiments 14 PCF preforms were fabricated. Each draw variable effect with a specific preform structure was typically studied on a single draw. For example the draw temperature would be changed to various values during one draw. Using a single preform for a set of draw conditions guaranteed that changes from preform to preform arising e.g. from the stacking process or different capillary batch being used, would not affect the results. However, sometimes the experiments required more than one preform and hence care was taken to copy the preform structure for each consecutive experiment. The preforms are identified with a preform number, which is presented with the related experimental conditions and results.

5.2.2 Measurements

In order to determine the drawing induced changes in the final fibre structure the fibre samples were analysed using various methods. An optical microscope was used for the majority of the samples. For more precise images and analysis AFM and SEM were used. A York FK11 cleaver was used to cleave the fibre samples to ensure a clean and level cross-section cut. Inspection with the optical microscope and AFM did not involve any further preparation, however the SEM imaging required a conductive coating. Once the images were obtained of the fibre samples, image analysis software was used to determine the various geometric characteristics such as hole size, core size, hole spacing and any deformations occurring for each sample and correlated with the corresponding draw conditions. As will be discussed in Section 5.3.5 the hole size can vary depending on its radial position. For the results presented in this chapter the hole size is determined as the average hole size in the second row of holes from the core unless otherwise stated. Preform structure was documented carefully with cladding and capillary material and dimensions during the stacking process and images were taken with a digital camera when necessary. For detailed description of the measurement equipment, procedure and the sample preparation refer to Chapter 3, Section 3.3.

5.3 Results

5.3.1 Capillary drawing

The importance of the fabrication of the capillaries themselves, which are used as building blocks for PCF preforms has already been discussed in Sections 3.1 and 3.2. Significant effort was made to improve the capillary fabrication technique as well as to understand the effects of draw variables on capillary dimensions and quality. As the capillaries are a simplified version of a PCF it was also a good starting point to begin the study by looking at the geometry control of the capillaries.

The capillary properties that can be changed during drawing are the capillary outer diameter (OD) and inner diameter (ID), which determine the capillary thickness. Note that the ratio of the outer and inner diameter can be changed during drawing by controlling the collapse and expansion of the structure. When the ratio of outer to inner diameter, OD/ID, is greater than the original tube OD/ID ratio, partial collapse has occurred during drawing. When the ratio is smaller than the original tube OD/ID,

expansion has occurred during drawing. In addition to the nominal dimensions of the capillary at any one point, the variation of these properties along the length of the capillary is extremely important to obtain good stacking in the preform.

The draw variables that affect the capillary dimensions are the same as those in PCF drawing, namely, draw temperature, feed rate, draw speed and pressure. There are typically however some restrictions of these variables in comparison to fibre drawing. In this study, for example, the capillary collection during draw was done manually[11], which limited the maximum capillary draw speed to about 3m/min. The draw capstan can also be a limiting factor, as for very thick capillaries ~10mm or more, a special heat resistant wheel surface is required and issues with grip and glass weight would have to be solved. This limits the size of the capillaries. These factors in turn limit the preform feed rate and for this practical reason the main draw variable that was used to control the structure was the furnace temperature.

5.3.1.1 Control of OD/ID ratio

The control of the wall thickness of the capillary in addition to diameter is of great importance, as the capillary wall thickness will define the range of air fractions possible in the PCF. As the OD/ID ratio describes the air-fraction of the capillary it is frequently used to report the results here. The wall thickness of the capillary together with OD or ID relates to this ratio as shown by Equation (27).

$$\frac{OD}{ID} = \frac{OD}{OD - 2t} = \frac{ID + 2t}{ID} \tag{27}$$

As was discussed in the introduction the viscosity plays a major role in defining the capillary dimensions during draw. The tube internal pressure can either prevent or aid collapse depending on the pressure difference in the inside and outside of the tube/capillary. Temperature affects the viscosity and hence changes the viscous forces. On one hand it might be desirable to prevent any collapse during draw, which can be accomplished by simply maximising the viscous forces by using as low temperature as possible. On the other hand it can be useful to be able to control the capillary OD/ID

[11] In standard fibre drawing the fibre is collected automatically on a spool by a take-up rewinder. The diameter of the capillaries (1-3mm) does not allow bending and hence collection on a spool, instead the capillaries are cut into short lengths and collected manually.

ratio as a single starting tube can be used to manufacture a range of capillary thicknesses.

Figure 5-2 shows an experiment where temperature was changed from 1850°C to 2030°C and the OD/ID ratio measured whilst keeping the outer diameter constant at 2mm. The nominal OD/ID ratio of the original tube is marked as a horizontal line on the graph. It is seen that as temperature is increased the tube collapses more hence increasing the OD/ID ratio. No internal tube pressurisation was used during the experiment.

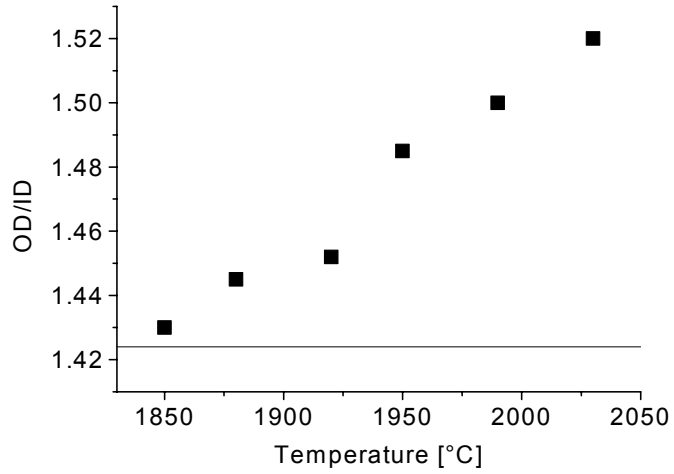

Figure 5-2. OD/ID change of a capillary with draw temperature. The nominal tube OD/ID marked as a solid horizontal line.

The OD/ID variation along the drawn capillary length was also measured and compared with the tube OD/ID variation. The OD diameter control is discussed in the next section and the OD/ID results are summarised in Table 5-3. Two different tube sizes were used, 17x12mm and 30x10mm. In both cases the standard deviation is significantly worse for the capillary OD/ID than for the tube. In addition to variations in the starting tube diameter and thickness, other external factors affect the collapse of the capillary during draw and can make the OD/ID variation of the capillary worse. In order to control the variation of OD/ID internal pressure should be controlled as well as the wall thickness measured on-line during drawing. This was not implemented during this study, as such a measurement device was not readily available. Given that the tube is of excellent quality having minimal variation of both the OD and ID,

acceptable quality capillary can be made when external disturbances during draw are minimised.

Table 5-3. Comparison of OD/ID variation of tube and capillary

Tube ODxID (mm)	*Tube*		*Capillary*	
	Average OD/ID	SD (%)	Average OD/ID	SD (%)
17x12	1.42	0.01	1.45	0.28
30x10	3.07	0.16	3.00	1.25

5.3.1.2 Diameter control

The longitudinal outer diameter variation is as important as the control of the capillary OD/ID ratio. In order to have good capillary stack in the PCF preform, outer diameter variation must be minimised. There are several sources of diameter variation as is known from conventional fibre drawing, such as variations in the preform, draw variables, mechanical vibrations and furnace gas flows [179-186]. In addition to these effects, the tube internal pressure must also be considered for capillary drawing. The capillary diameter was controlled with a conventional PID controller, where the diameter was measured below the furnace and the pulling capstan speed adjusted accordingly. The main sources of capillary diameter variation were studied and are presented below.

First the starting tube diameter variation was compared with the capillary diameter variation. If the tube variations were translated directly to capillary diameter, the variation along 1mm of 25mm diameter tube would spread over 160mm of 2mm diameter capillary. However, the diameter variation of the tube will affect the neck-down shape and the furnace gas flows hence affecting the drawing dynamics. Numerical studies have shown that even few percent changes in preform diameter can be amplified in the final fibre [187].

In the experiments the tube diameter variation was compared to the capillary diameter variation for four different tube sizes, 17x12mm, 30x10mm and 20x17mm and 25x19mm tubes. Table 5-4 shows a summary of the statistics of diameter variation of tube and capillary for each tube size. PID control parameters were kept the same for all

the tubes. The drawing conditions were kept as similar as possible, although the temperature and feeding speed had to be adjusted due to the dimensional differences of the tubes.

Table 5-4. Comparison of tube diameter variation to the capillary diameter variation

Tube ODxID (mm)	*Tube*				*Capillary*	
	Average (mm)		SD (%)		Average (mm)	SD (%)
	OD	ID	OD	ID	OD	OD
17x12	17.02	11.95	0.07	0.07	2.00	0.08
30x10	29.99	9.76	0.06	0.07	2.50	0.06
20x17	20.01	16.95	0.25	0.27	2.00	0.14
25x19	24.79	18.82	0.02	0.02	2.05	0.06

The diameter variance in the selected tubes varied considerably from tube to tube. The tubes 17x12 and 30x10 had a medium level variation of SD<0.1% and the corresponding capillary diameter SD was very similar, 0.06-0.08%. This showed that the drawing did not significantly increase nor decrease SD of the outer diameter of the capillaries. Tube 20x17 had relatively large SD of the diameter, 0.25%. The corresponding capillary diameter SD was 0.14%. This is worse than for the tubes 17x12 and 30x10, however the capillary diameter variation could be improved during the draw. The best quality tube in terms of the diameter variation was the 25x19 with SD of 0.02%. The capillaries drawn from this tube had a higher diameter variation with SD of 0.06%, which is the same as that for the 30x10 tube. This indicates that it is difficult to obtain a better diameter variation than 0.06% even if the tube quality is better with the current draw set-up.

Figure 5-3 shows the diameter variation along the length of the capillary during draw for the tube 17x12 measured on-line. The graph contains data along 20m of drawn capillary. The frequency of the diameter variation is much greater than that of the tube, which is characteristic also for fibre drawing. In conclusion the capillary diameter variation can be controlled to an extent during drawing, however the tube diameter variations are likely to reflect in one way or another in the capillary diameter and it is preferable only to use the best quality tubing when capillary diameter is of great importance. If required the individual capillaries can be sorted according to their diameter variation manually and hence very high precision capillaries can be selected.

A number of other possible sources of diameter variation were examined. Due to the much thicker capillary diameter compared to the usual fibre diameters, the furnace gas flows were expected to have different optimal settings. Figure 5-4 shows the diameter variation along the length of the capillary during draw at the standard 2 litres/min used for fibres and the new optimal gas flow, 4 litres/min, for capillary drawing. The minimum diameter variation was improved from ±7μm to < ±3μm.

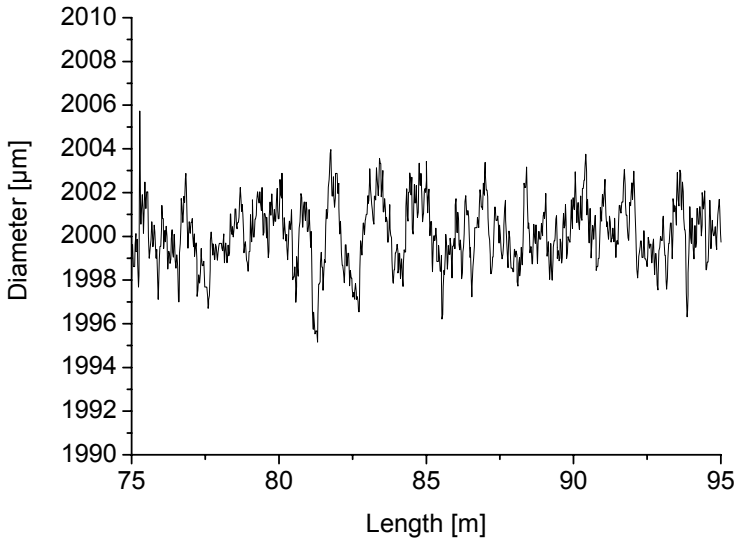

Figure 5-3. Capillary outer diameter variation during draw of tube 17x12mm.

The changed gas flow was the gas feed into the lower part of the furnace below the hot-zone. In order to keep the gas velocity similar in the lower part of the furnace compared to fibre draw, one would have expected a lower volumetric flow feed due to the significantly larger dimensions of the tube lower neck-down and the final capillary diameter. Instead, the optimal flow was larger. This could be explained by a stabilising effect of the resulting cooling of the capillary due to the higher gas flow. A 125μm fibre cools down faster due to the smaller volume of glass per unit length as opposed to a 2mm diameter capillary, hence requiring less gas flow to have a similar effect. A thick capillary also better withstands higher gas velocities due to reduced flexibility so that any vibrations associated by high gas velocities are avoided.

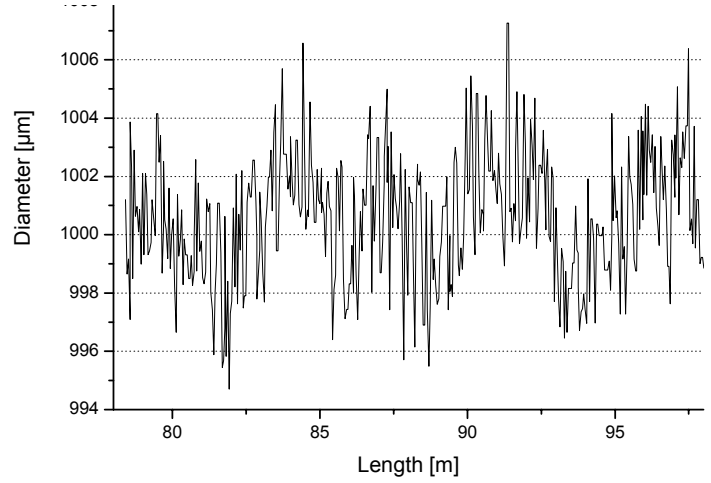

(a)

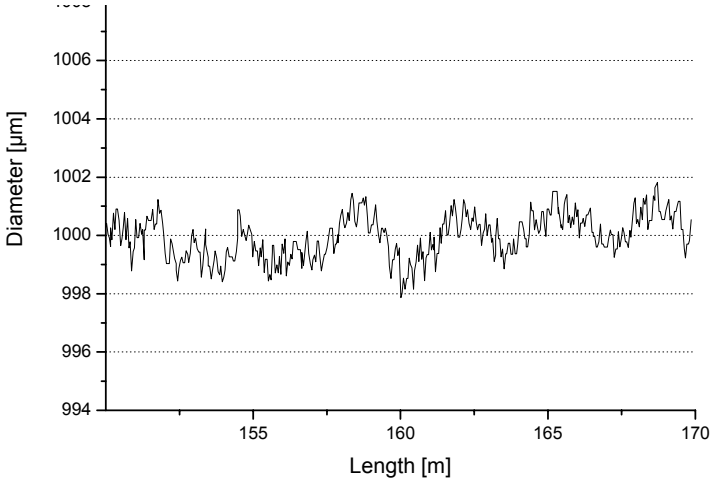

(b)

Figure 5-4. Outer diameter variation of capillary drawn from 17x12 tube at bottom iris gas flow of (a) 2 lpm and (b) 4 lpm.

Other possible source for high frequency diameter variation could be the diameter controller itself if not tuned properly. A test was conducted where the capillary diameter was monitored with and without the diameter control. A section of the draw was selected where the draw was stabilised and all other external disturbances minimised. It was found that the diameter variation was very good even without control, however an improvement on both the range and SD of the diameter was achieved when the controller was on, see Table 5-5. Naturally the benefits of diameter control are much greater when a disturbance is introduced to the system.

Table 5-5. Statistical summary of capillary diameter with control off and on

(μm)	*Control off*	*Control on*
Mean	1000.9	1000.4
SD	0.69	0.60
Range	3.5	2.7

In order to provide an inert atmosphere inside the tube during drawing the tubes were pressurised and the pressure controlled during drawing. Table 5-6 shows the comparison of diameter variation when draw was done under atmosphere without pressure control and under an inert gas with controlled pressure. There are no significant differences between the different draws. With pressurisation the relative capillary diameter range is slightly higher than that of the tube. However, as both the outer diameter variation and the thickness variation is higher for Tube 2 than for Tube 1 used for the atmospheric draw, this is most likely the source for the increased variation. Tubes were from same batch with nominal dimensions of 25x19mm.

Table 5-6. Comparison of capillary diameter variation under atmosphere and with tube pressurisation

Diameter	*Tube1* *(mm)*	*Capillary from Tube 1, under atmosphere* *(mm)*	*Tube2* *(mm)*	*Capillary from Tube 2, with pressurisation* *(mm)*
Mean OD	24.79	2.0499	25.11	2.0510
SD %	0.02	0.06	0.08	0.09
Range %	0.3	0.3	0.3	0.4
Thickness SD %	2	-	3	-

As a result of the experiments on capillary diameter control, the capillary drawing process was improved to an extent that capillaries with diameter control an order of magnitude better than commercial capillaries could be manufactured. A commercial and in-house fabricated capillary diameter measurement along the length of a typical capillary is shown in Figure 5-5. In a summary, in order to minimise capillary diameter variation the starting tube diameter variations have to be minimised, on-line diameter control used and furnace gas flows optimised. The tube pressurisation did not improve diameter control as such but is essential in order to obtain low water content and contamination free capillaries. The pressurisation can also potentially be used to control the thickness of the capillaries providing an on-line measurement is setup.

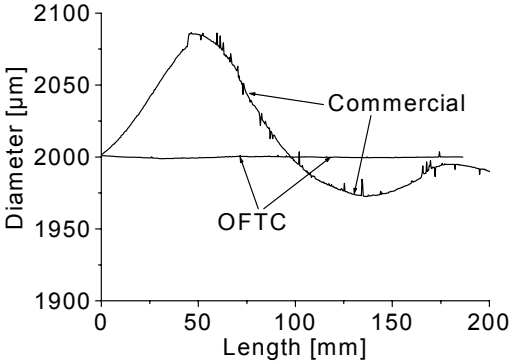

Figure 5-5. Diameter variation in a commercial and in-house fabricated capillary along the length measured off-line using LaserMike diameter measurement system.

5.3.2 Draw temperature

In a similar manner as for the capillary draws, the temperature affects directly the collapse conditions in the PCF by changing the viscous forces within the preform and fibre structure. A number of draw experiments were made to determine the temperature effect on the air structure. Table 5-7 lists the preforms used with the structural variables and temperature range used.

Six capillary-stacked preforms were chosen and one milled preform. The capillary-stacked preforms all had the same cladding tube, 25x19mm, except for ASC021, which had a 21x17mm tube. Capillary OD/ID ratio was typically 1.3, with exception of ASC005, which had ratio of 1.4, and ASC021 with ratio of 1.2. Both low quality and high quality materials were tested. Fibres were drawn to a standard diameter of 125µm and a smaller diameter of 100µm. One preform was drawn into a larger diameter of 500µm. Feed rate was kept to a constant except for one test point where a higher value was employed (ASC014). The large diameter draw also had a higher feed rate. Internal pressure was kept constant and at the same nominal value when the preform had the same structure, except for ASC005 where the preform was open to atmosphere. Temperature ranged from 1860 to 1970°C, where typically 5°C, 20°C and 30°C change was studied. In Figure 5-6 a typical hole size change with decreasing temperature can be seen in a sequence of optical micrographs taken of fibre samples drawn with different temperatures. As the temperature is decreased the hole collapse is less.

Table 5-7. List of preforms and draw conditions for temperature experiment

Preform code	*Capillary OD/ID*	*Material*	*Fibre diam. (μm)*	*Feed rate (mm/min)*	*Temperqture*[3] *range (°C)*
ASC005[2]	1.4	LQ[1]	125	2.5	1880-1900
ASC010	1.3	LQ[1]	125	2.7	1930-1970
ASC012	1.3	F300	100	2.7	1920-1940
ASC014	1.3	F300	100	3.9	1930-1960
ASC019	1.3	F300	500	8.0	1950-1955
ASC021	1.2	F300	100	3.0	1915-1920
ASM001[2]	milled	LQ[1]	125	2.7	1860-1880

[1]LQ=low quality (natural quartz), [2]Tube not pressurised, [3]Element temperature measurement has ±20°C accuracy and repeatability ±6°C.[12]

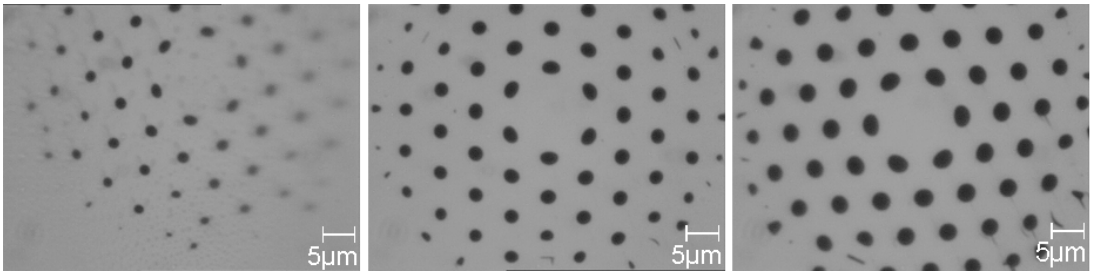

(a) (b) (c)

Figure 5-6. Sequence of optical micrographs of fibre samples (ASC014) drawn at decreasing temperatures (a)1950°C, (b)1940°C (ΔT to (a) is –10°C) and (c)1930°C (ΔT to (a) is –20°C).

Figure 5-7 shows the hole size vs. the draw temperature for all the fibres listed in Table 5-7 except for ASC019 which was drawn at 500μm. Surprisingly it was found that for all fibres drawn to 100μm or 125μm irrespective of the preform structure, material, draw temperature range or preform feed rate exhibited same rate of hole size vs. draw temperature of 0.057±0.01μm/°C amounting to 1.1±0.2μm increase change of hole size for a 20°C decrease in temperature. This observation is of course within the measurement error, which is quite high. The fitted lines have been drawn across the entire temperature range. This is to guide the eye and is not expected to hold true in the physical sense. A linear relationship applies only to a limited range of temperatures at each experiment set. If temperature is increased high enough the holes collapse and this has been observed to happen within a relatively small temperature range. For example fibre ASC010 had holes fully collapsed at temperature of 1970°C while holes where still

[12] The accuracy and repeatability values are those reported by the manufacturer and apply to the measurements from draw to draw. It has been experimentally observed that the temperature change within a single draw reflects better repeatability than that reported by the manufacturer.

open with dimeter above 3µm at 1960°C. The hole collapse from 3µm diameter occurs thus over only 10°C. If temperature is decreased low enough the hole dimension determined by the preform structure is obtained and hole expansion will only occur if for example, pressure inside the preform is increased.

The range at which this useful temperature response can be obtained varies from preform to preform as seen in Figure 5-7. In the remainder of this chapter this range will be called *the optimal temperature range*[13]. Preform feed rate seems to play an important role if results from ASC012 and ASC014 are compared. The preforms are otherwise identical but preform feed rate is higher for ASC014 resulting in increased hole size. Due to lack of data points it is highly speculative to state the effect of fibre diameter or capillary OD/ID ratio.

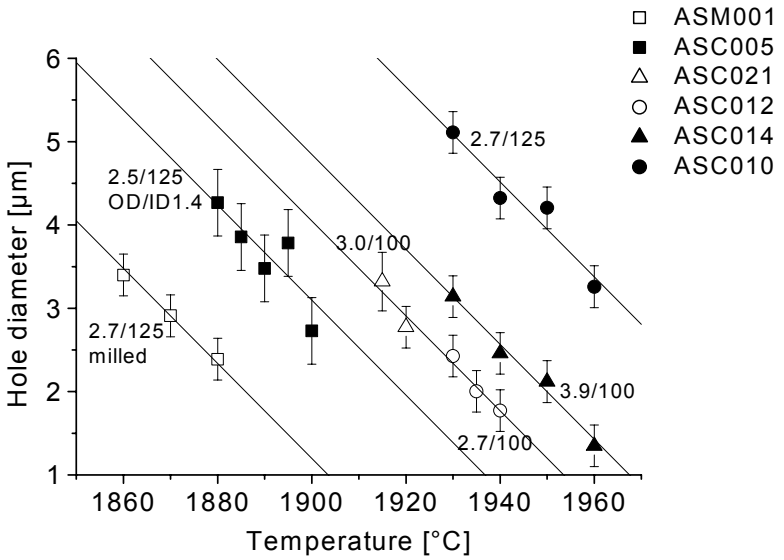

Figure 5-7. Hole size vs. draw temperature. Fitted lines drawn with same gradient of 0.057µm/°C. Feed rate (mm/min) and fibre diameter (µm) shown as V_p/D_f beside each experiment set.

It must also be noted that the temperature is measured from the heating element and has repeatability error of 6°C. Furthermore the milled preform ASM001 had smaller preform diameter, which would affect the preform temperature. The important point to extract from the data is the strikingly similar hole diameter response to temperature

[13] The optimal temperature range is defined here as the drawing temperature range at which the holes stay open in a stable manner and where the minimum temperature is limited by the strength of the fibre.

change irrespective of the varied parameters such as quality of silica used, milled or capillary technique, preform feed rate and fibre diameter.

To further look at the possible effect of fibre diameter, ASC019 was drawn to a much larger diameter, 500μm. Two different temperatures were used and a 5°C change in temperature resulted in a 1.9μm change in hole diameter. This results in a much higher response rate of 0.38μm/°C. This would indicate that a large difference in diameter affects the rate of change, but it must be noted that the preform feed rate is also much higher, 8mm/min. It is interesting to note though that the relative change in diameter is 10%, which agrees much better with the other data. Further experiments would however be required to confirm this.

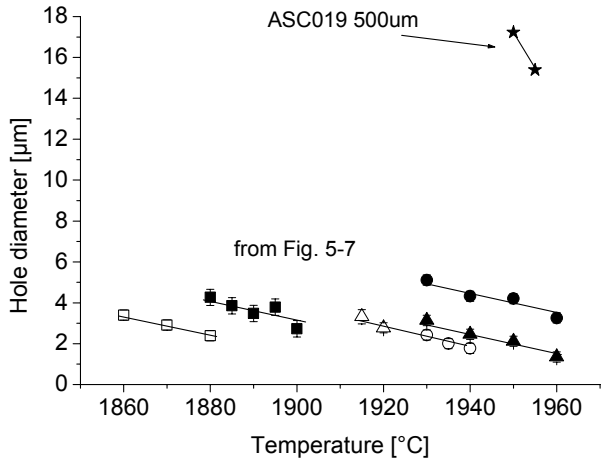

Figure 5-8. Hole size vs. draw temperature. Large diameter draw ASC019 shown with data from Figure 5-7.

It can be summarised that hole size for fibres drawn to 100-125μm diameter with a modest range of preform feed rates and variation in preform structure exhibit a constant response to draw temperature within their optimal draw temperature range of about 20°C. Such behaviour can be considered very useful in terms of controlling the hole dimensions; the same controlling scheme can be used for various preform structures as long as the optimal temperature range is known. In relation to the theoretical modelling presented by Fitt *et al* [11] the following can be observed. The viscosity plays an important role and hole dimensions can be altered by changing the temperature. Viscosity is known however to depend on temperature according to Eq. (28) [188].

$$\mu = 10^{-7.24-26900/T}, \tag{28}$$

where temperature T is in Kelvin and μ in Pas. Although the relationship is by no means linear, for a small temperature range such as 20°C at about 1900°C (typical draw temperature) a linear approximation can be done, perhaps partly explaining the hole size response to temperature. As predicted by the theoretical analysis, preform feed rate plays an important role in hole collapse. This was further explored experimentally and results presented in the next section.

Although temperature seems like an ideal way to control the hole size, the response times to a control variable must also be taken into account. The drawing experiments show that the temperature effect is not instantaneous. Due to the relatively large mass of glass and gas in the drawing furnace, it can take a long time to stabilise the heat transfer after the furnace temperature is changed. For the preform diameter range of up to 30mm the stabilisation typically takes from a few minutes up to 10min depending on the magnitude of the change and the absolute temperature. This amounts to hundreds of metres of fibre, which clearly indicates that temperature is not the most suitable means of on-line hole diameter control, as this results in substantial fibre scrap length. Temperature is, however, a suitable means of adjusting the hole diameter and hence the air-fraction of the fibre when a single size fibre is required to be drawn from a preform.

5.3.3 Preform feed rate

Preform feeding rate changes the temperature of the preform and fibre inside the furnace by changing the time the preform dwells in the hot-zone. The faster the preform is fed, the shorter the time it spends inside the hot furnace, hence reducing the exposure to the furnace temperature. Via the effect on temperature the preform feed rate will affect the viscosity distribution in the preform neck-down and the hole collapse. The theory of capillary drawing also predicts that the hole collapse is sensitive to preform feed rate even at isothermal conditions [11]. There is thus a possibility of using the feed rate to control the air-structure of a PCF in a manner similar to the use of furnace temperature.

Table 5-8 lists the preforms used to study the effect of preform feed rate. Three preforms were used for the experiments of which one was a milled preform. ASC001

and ASC014 had the same outer cladding but ASC001 had thicker capillaries and was drawn open to atmosphere. ASC001 and ASM001 were drawn to 125μm and ASC014 to 100μm diameter. For all preforms the fibre hole diameter increased with increasing preform feed rate as shown in Figure 5-9 (a) and (b). Although fewer data are available than for the draw temperature experiments it can be noted that the hole size change rate with feed rate is not constant. As the fibres were drawn at very different feed rate regions and the preform structures were different their comparison is very difficult. It can be concluded however that feed rate affects the hole diameter significantly and should be taken into account when optimal drawing conditions are established. The relative hole diameter change vs. preform feed rate is shown in Figure 5-9 (b). It is noted here that within the error, fitted lines can be drawn that intersect at about feed rate of 2mm/min and relative hole diameter of 0.4. It is not intuitively clear what this means in physical terms and further studies are necessary. It has been experimentally noticed that if preform is fed at very low feed rate, which results in full collapse, a small increase in feed rate will cause a large change in hole diameter initially. The practical limit for minimum feed rate has evolved to about 2.0mm/min by experience, and may be related to the intercept around this value.

In summary, the preform feed rate can be used to control the hole geometry although the response of hole diameter change varies greatly with draw conditions and/or preform structure. It was also found that the preform feed rate had a strong effect on radial hole size gradient, which increased with increasing feed rate. This is discussed in Section 5.3.5. The effect of preform feed rate to stabilise also takes a long time and is comparable to the stabilisation time of a draw temperature change. The preform feed rate thus does not seem ideal as a mechanism for hole size control.

Table 5-8. List of preforms and draw conditions for preform feed rate experiment

Preform code	*Capillary OD/ID*	*Material*[1]	*Fibre diam. (μm)*	*Temperature (°C)*	*Feed rate range (mm/min)*
ASC001[2]	1.4	LQ	125	1900	2.2-2.5
ASC014	1.3	F300	100	1940	3.9-5.4
ASM001[2]	milled	LQ	125	1840	2.65-3.5

[1]LQ=low quality (natural quartz), [2]No pressure control used.

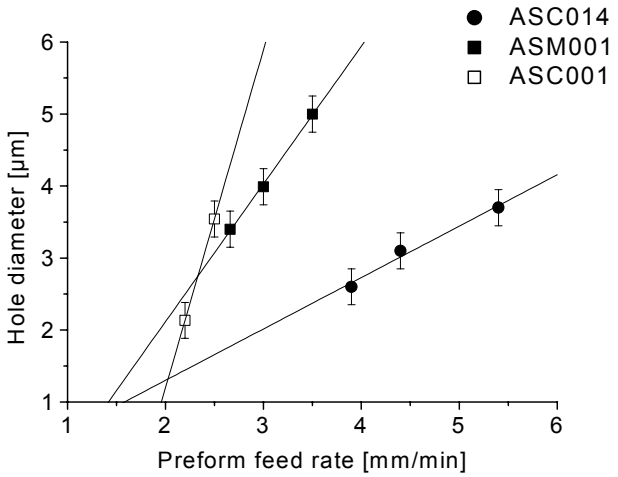

(a)

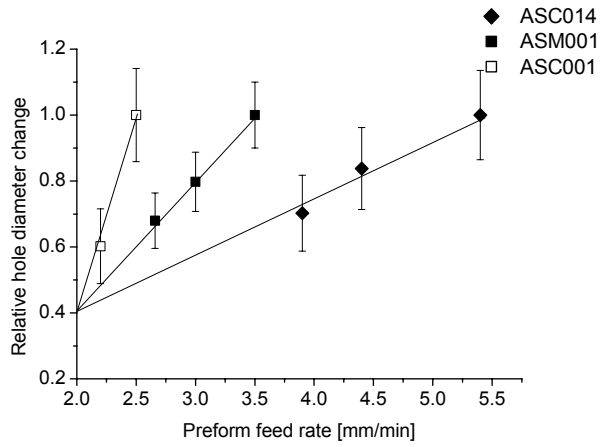

(b)

Figure 5-9. Hole diameter increase with increasing preform feed rate (a) absolute diameter in µm and (b) relative diameter change (the largest hole diameter).

5.3.4 Pressure control

Even though the furnace temperature and the preform feed rate can be used to control the hole collapse, the degree of control was never satisfactory until preform internal pressure control was introduced. Figure 5-10 shows a cross-section of a typical fibre with and without the preform internal pressure control. The preform structure was similar for both fibres with four rings of capillaries stacked into a 25x19mm tube.

Without the pressure control the structure become irregular especially between the air-structure and the outer cladding. The air inside the preform gets hot as the furnace is

heated thus expanding and changing the gas pressure. As the conditions change continuously during the draw, that is, the top end of the preform gets closer to the top of the furnace, the temperature distribution and the pressure in the air structure may never stabilise. The air-fraction is typically greatest between the hexagonal capillary stack and the solid cladding due to the fill capillaries, thus making the control of the structure even more difficult due to the uncontrolled air pressure. The radial temperature gradient may play a role as well because outer parts of the preform and fibre are at higher temperature. Using solid fills and filling all the spaces between the hexagonal air-structure and the cladding or alternatively by using hexagonal cladding would improve this, but nevertheless the pressure control is essential to fully control the air-structure.

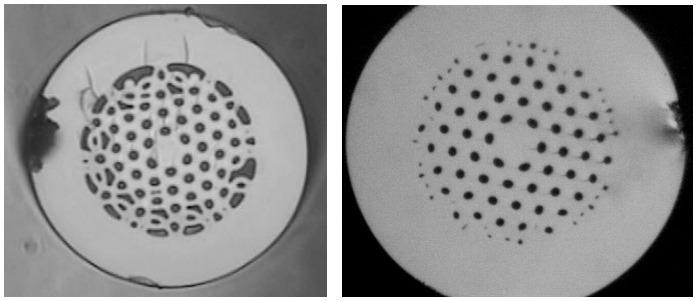

(a) (b)

Figure 5-10. Optical micrographs of a typical fibre cross-section (a) without (ASC005) and (b) with a preform pressure control (ASC026). Fibre diameter is 125µm for both fibres.

Table 5-9 lists the preforms and draw conditions used in the pressure control experiments. Ten preforms were drawn with varying structure, fibre diameter and draw conditions. It is important to note that the pressurisation system was changed in the middle of the experiment series to gain more accurate pressure control. Preforms ASC010 to ASC014 were drawn using the old system and preforms ASC16 to ASC26 were drawn using the new system. ASC015 was drawn using both systems for comparison. As the old pressurisation system was very different in terms of control principle and had a different type of pressure sensor located at a different position in the system, the pressure change listed in the Table 5-9 and in the related figures are not comparable with the new system. This has been taken into account so that no quantitative results with the old system are compared with those of the new system.

The pressure control by itself is not sufficient to control the structure, but both temperature and preform feed rate have to be within an optimal range. This is demonstrated in Figure 5-11 where optical micrographs of fibres drawn with various conditions are shown. Figure 5-11 (a) and (b) show fibres drawn at too high a temperature. When the pressure is also high the holes expand too much distorting the entire air-structure. When the pressure is low the holes collapse fully. Figure 5-11 (c) and (d) show fibres drawn at optimal temperature range using the same pressure as in Figure 5-11 (b). The holes are open and the structure is uniform. Working at the high temperature end of the optimal range gives a low air fraction fibre, whereas working at the low temperature end of the range gives a high air fraction structure.

Table 5-9. List of preforms and draw conditions for preform pressure control experiments

Preform code	*Capillary OD/ID*	*Material*	*Fibre diam. (µm)*	*Feed rate (mm/min)*	*Temperature (°C)*	*Pressure change (kPa)*
ASC010	1.32	LQ	125	1.0-2.7	1930-1970	5[1]
ASC012	1.32	F300	100	2.7	1920/1930	5[1]
ASC014	1.32	F300	100	4.4	1940	3[1]
ASC015	1.18	LQ	100	4.0	1910	3[1] / 0.1
ASC016	1.18	F300	100	2.7	1910	0.2
ASC017	1.23	F300	100	2.7	1910	0.4
ASC019	1.32	F300	500	8	1950	1.0
ASC020	1.23	F300	125	3.5	1900	0.4
ASC021	1.23	F300	100	3	1915	0.7
ASC026	1.32	F300	125	3.9	1930	0.3
ASC030	1.32	F300	100	2.7	1910	0.6

[1]A different pressurisation system was used and changes are not comparable to the results with new system.

Figure 5-11 (e) and (f) show fibre cross-sections drawn at too low a preform feed rate. The preform is exposed to the temperature too long and gets hot enough to cause full air-structure collapse. An unfavourable change in neck-down shape is also suspected as even at very high pressure the air-structure cannot be opened, Figure 5-11 (f). Images (g) and (h) show the same fibre drawn at higher feeding speeds using the same pressure and temperature setting. The air-structure is uniform and the air-fraction is changed at different preform feed rates. The pressure sensitivity factor *S* (Eq. (26)) derived by Fitt *et al* [11] is calculated for each condition in Figure 5-11. Qualitatively the factors agree in that S is reduced for lower temperature and higher feed rate. However the sensitivity factor is never much larger than unity as predicted from the theory for conditions where pressure control is not suitable.

In summary, it is important to operate at the optimal temperature and feed rate range when pressure control is used. The optimal ranges vary with the preform structure and more importantly depend on the control capability of the pressurisation system. If the pressure can be controlled with better accuracy the optimal range for temperature and feeding speed is greater.

The above experiment was done using the old pressure control system. To compare the capabilities of the old and the new pressure control system, a preform stacked with very thin capillaries (ASC015) was fabricated and drawn using both systems. Thin walled capillaries were chosen as they were found to be more sensitive to the pressure change as will be discussed in Section 5.3.4.2. Temperature and feed speed were held constant during these experiments. Figure 5-10. shows optical micrographs of two fibre cross-sections drawn with the old system with pressure adjusted by the smallest possible step the resulting in air-fraction of <10% and 70%. Fibres with air-fractions in between these values were easily attained using the new pressure control system, an example is shown in Figure 5-10(c). A pressure change step size of 0.1kPa could be attained providing a better control even for high air-fraction preforms.

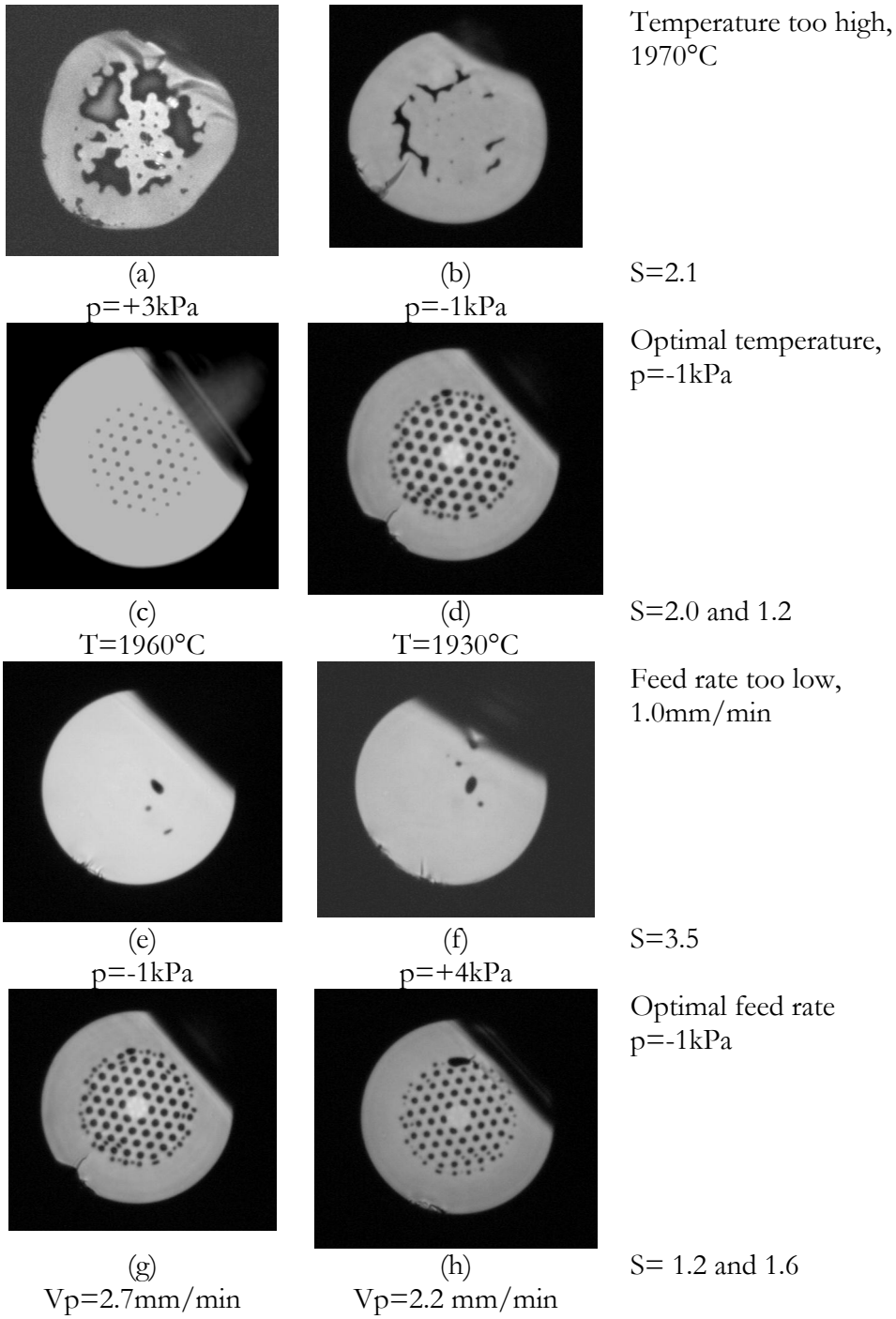

Figure 5-11. Pressure control at too high temperature (a) and (b), at optimal temperature range (c) and (d), at too low preform feed rate (e) and (f) and at optimal preform feed rate (g) and (h). S is pressure sensitivity factor from Fitt *et al* [11]. Experiment was done with ASC010 and pressure is relative to atmosphere.

As discussed previously both temperature and preform feed rate had to be optimal for pressure control to be effective. Based on this it should be asked whether the pressure also has an optimal range. Naturally it can be concluded that if pressure is too low the structure collapses and if it is too high it expands and distorts and finally breaks the fibre at high enough pressure. In addition to these obvious extremes it was found that a combination of low pressure and very low temperature resulted in the holes becoming flattened instead of keeping their round shape. This is shown in Figure 5-13. The effect was found to be more severe with low-air fraction preforms. The same phenomenon was observed with capillary draws.

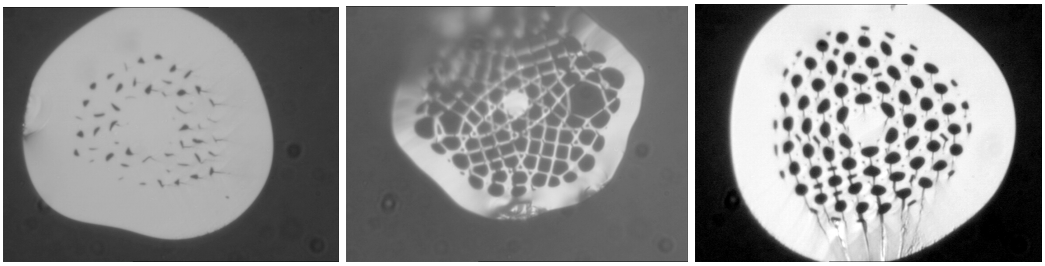

(a) (b) (c)

Figure 5-12. ASC015 fibre cross-sections drawn with old pressure system with (a) small and (b) large pressure and (c) a 'medium' air-fraction obtained by the new pressure system.

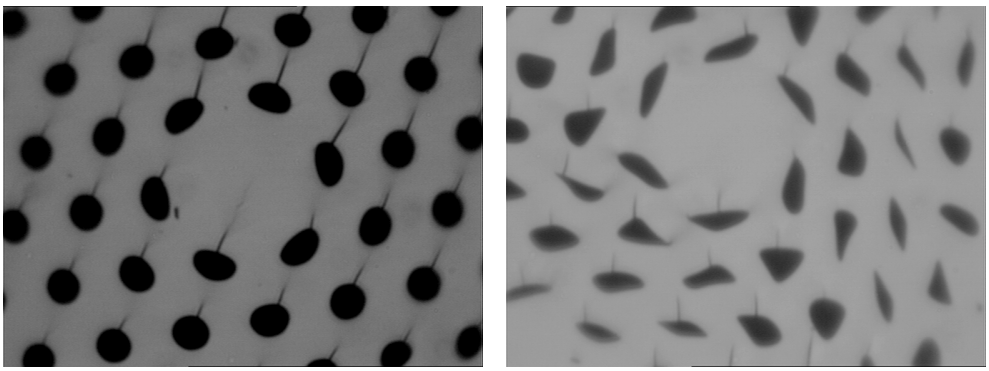

(a) (b)

Figure 5-13. Hole collapse with (a) moderate pressure and temperature (ASC021), and (b) low temperature and pressure (ASC015). Core diameter is ~15µm.

Another unwelcome effect of pressurisation was an unstable regime found at higher pressures. Figure 5-14 shows a draw log of on-line fibre diameter and draw speed measurements. The diameter was controlled by a PID controller, which adjusted the draw speed accordingly. The large fluctuations in the draw speed indicate an unstable fibre structure for which the diameter controller is compensating. When the pressure was adjusted to a lower level, the draw speed stabilised significantly. The pressure was controlled within 0.1kPa accuracy at the top of the preform for both conditions, which indicates that the instability occurs in the neck-down region. Due to this instability an upper pressure limit exists that can be used in controlling the fibre structure. This limit is dependent on preform structure and draw conditions.

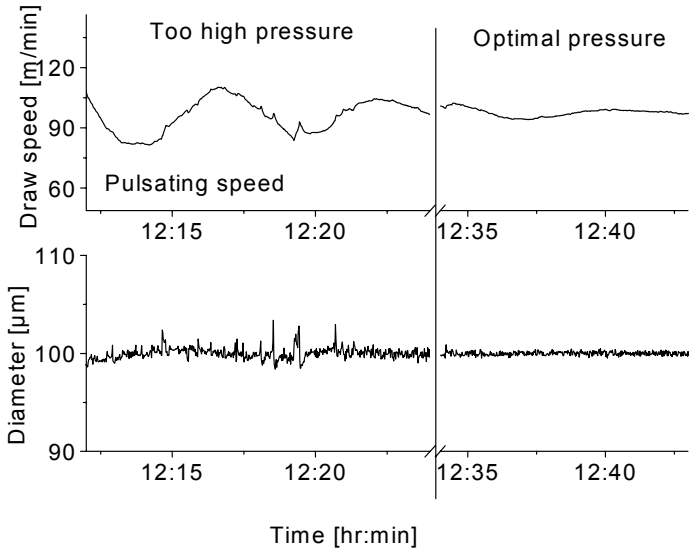

Figure 5-14. Fibre diameter and draw speed during draw of ASC016 showing unstable geometry regime at high pressure and stabilisation at lower pressure setting.

5.3.4.1 Control of hole diameter and pitch

The main objective in controlling preform internal pressure is to be able to (i) prevent unwanted deformations of the air-structure and (ii) to adjust the hole diameter and air-fraction. Figure 5-15 shows an experiment where the pressure was used to change the hole diameter and the air-fraction. The fibre was drawn down to 100µm diameter and pressure changed whilst keeping the draw temperature and feed rate constant. Figure 5-15(a) shows the hole diameter change with pressure change[14]. A 0.6kPa pressure increase increased the hole diameter from 2.0µm to 2.9µm. Within the measurement

[14] For each figure the reference pressure is chosen as the lowest pressure used in the experiment set i.e. the pressure change is always positive.

error the change is linear. Figure 5-15(b) shows the corresponding change in the hole to pitch ratio d/Λ and the silica bridge thickness (d-Λ). For an increase in pressure of 0.6 kPa d/Λ increased from 0.3 to 0.4 and d-Λ decreased from 5.2 to 4.7μm. It appears that whilst d/Λ changes linearly, (Λ-d) may decrease exponentially, although measurement error in this case is too high (d/Λ=±0.05, (Λ-d)=±0.5) to make conclusive findings.

Figure 5-16 shows hole diameter change with change in pressure for four different fibres drawn at different drawing conditions and diameters. ASC017 and ASC021 were made using thinner capillaries (OD/ID=1.23) than preforms ASC026 and ASC030 (OD/ID=1.32). Within the experimental error the change rate is estimated as 2.3μm/kPa. This seems to apply irrespective of the temperature, feed rate or diameter of these samples. Experiments were also done with fibre drawn to 500μm diameter with significantly higher feed rate (8mm/min). The change rate was 2.5μm/kPa within the experimental error, indicating insensitivity to the draw parameters.

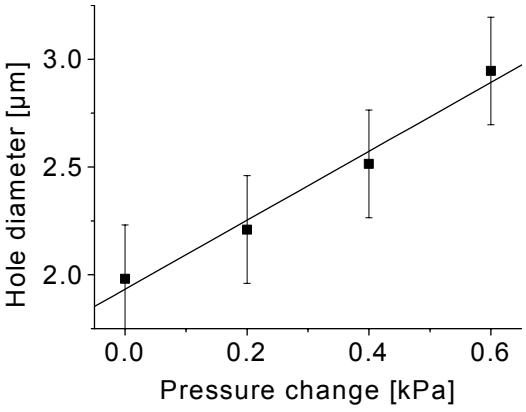

(a)

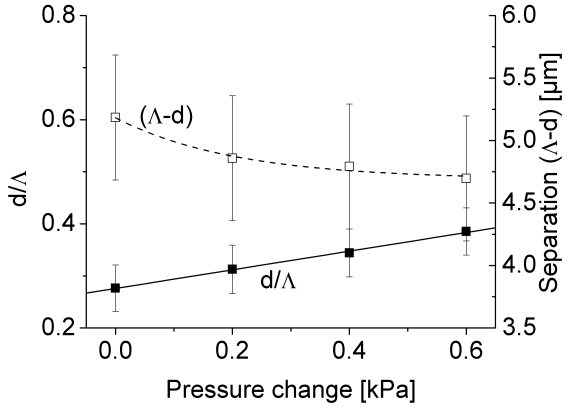

(b)

Figure 5-15. (a) Hole diameter vs. pressure change and (b) change in d/Λ and Λ-d for 100μm fibre drawn at 1910°C and feed rate of 2.7mm/min (ASC030).

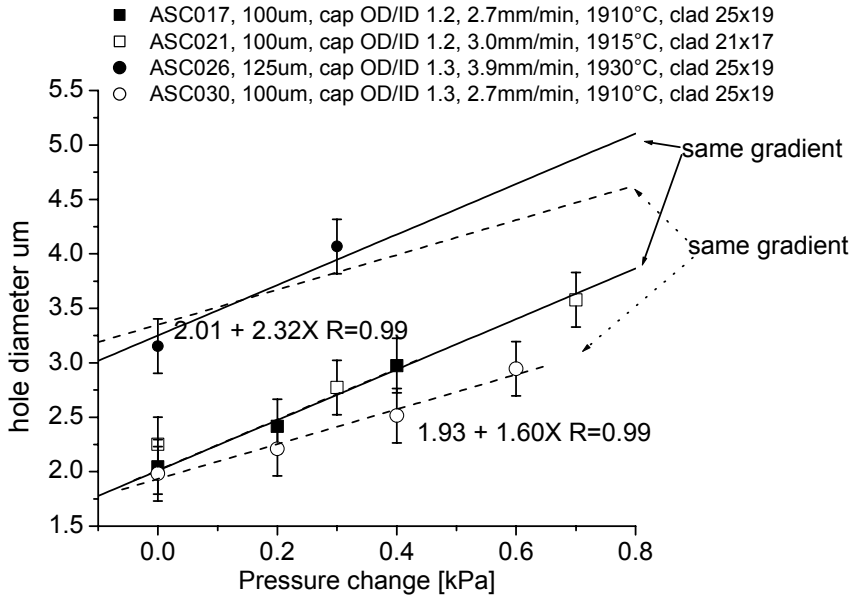

Figure 5-16. Hole diameter vs. pressure change for fibres drawn at different draw conditions.

It would seem obvious that draw parameters such as temperature and preform feed rate would affect the rate of diameter change with pressure via the effect on viscous forces. At higher temperature the viscous forces are reduced thus enhancing the effect of pressure. Surface tension forces depend both on the structure of the fibre and the dimensions of the preform. As the temperature distribution within the preform and the fibre is also affected by the air fraction of the design and the cladding dimensions, the pressure effect dependence on furnace temperature is further complicated. Although it has already been shown that effectiveness of the preform internal pressure control greatly depends on draw temperature and feed rate, the above results indicate that once operating at the optimal range, the hole diameter response to pressure change is relatively constant for fibres with similar structure and hole size.

5.3.4.2 Structural sensitivity to pressure

To further look at the pressure sensitivity issues the effect of the preform structure was studied by using stacks with different capillary wall thickness. The hole diameter change with pressure for a preform made with thin capillaries ,OD/ID=1.23 (ASC017), and for a preform made with thick capillaries, OD/ID=1.32 (ASC030) is replotted in Figure 5-17. Although the relatively large measurement error allows lines with the same

gradient to be fitted in the two measurement sets, it appears that the structure with thinner capillaries is more sensitive to pressure change. This is also supported by an observation that a fibre with very thin capillaries, OD/ID=1.18, was found to be extremely sensitive to pressure (see Figure 5-10) and significant deformation of the holes occurred during the draw. It is possible that this can be improved by optimising other draw parameters such as temperature and preform feed rate or by using more accurate pressure control.

The effect of the outer cladding was also looked at. Figure 5-18 shows two fibres with otherwise identical structure but with different outer cladding thickness. ASC017 had a cladding tube 25x19mm and ASC021 21x17mm. The cladding tube does not affect the hole diameter change significantly.

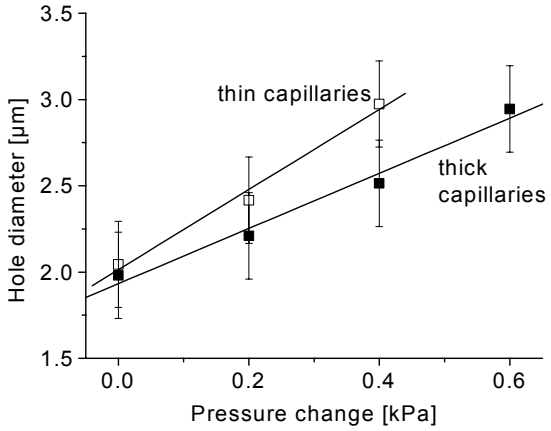

Figure 5-17. Relative holes size vs. pressure change for fibres with stacked capillaries with OD/ID ratio of 1.23 and 1.32 (ASC017 & ASC030). Both fibres drawn at 1910°C and 2.7mm/min.

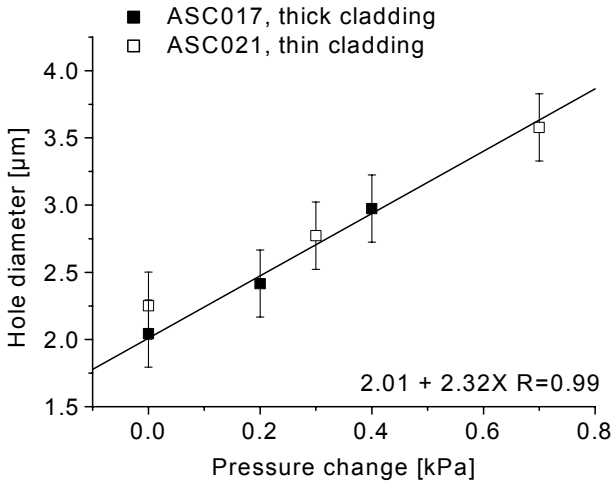

Figure 5-18. Hole diameter vs. pressure change for fibres with thick (25x19) and thin (21x17) outer cladding. ASC017 drawn at 1910°C and 2.7mm/min and ASC021 at 1915°C and 3.0mm/min

The majority of the preforms were fabricated by leaving the interstitial holes between the capillaries open. This allows fibres to be fabricated with either these interstitial holes open or collapsed during the draw. Two preforms with the same structure, ASC021 and ASC020, were drawn with different draw conditions so that ASC021 did not have any interstitial holes and ASC020 retained the interstitial holes open and the effect of pressure was studied. Figure 5-19 shows the relative hole size change for these fibres with increasing pressure. The interstitial holes compete with the main holes in expansion resulting in decrease of the hole diameter with increased pressure. This points out a limitation of the pressure control with fibres when interstitial holes are required in the structure.

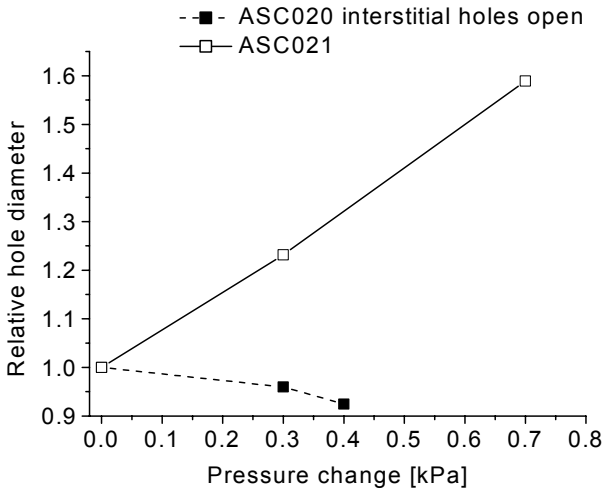

Figure 5-19. Relative hole size change with pressure for fibre with and without interstitial holes.

Although preform internal pressure control did not provide as large a change in hole diameter as draw temperature, the hole diameter can be tuned during the fibre drawing stage using pressure control to obtain the required geometrical dimensions for the fibre. One of the advantages in using the pressure is the fast response of the structure to pressure changes compared to draw temperature or feed rate changes. When operating at an optimal range the structural response to pressure was of the order of a minute. Great care must be taken when choosing the correct pressure ranges, as the sensitivity of a very thin capillary preform may be greater than that of a preform made with thicker capillaries. This can be used to advantage. When fine-tuning of dimensions is required a preform with thicker capillaries is more suitable, whereas when larger range of dimensional changes are sought, a thinner capillary preform can be used. It is noted that the use of pressure has its limitations, especially for the higher air fraction structured fibre designs in terms of retaining an ordered structure.

5.3.5 Cross-sectional hole size gradients

During the experiments it was noted that in some fibres a radial hole gradient was observed where the holes closer to the outer cladding were smaller. Figure 5-20 shows the hole diameter gradient across fibres drawn at three different draw conditions. Both the preform feed rate and the drawing temperature affect the hole size gradient. It is believed that this gradient results from a radial temperature gradient in the structure. As the preform is heated from the outside the structure closer to the cladding gets hotter and results in more collapsed holes.

In order to control the temperature gradient it is important to understand the heat transfer during fibre drawing. This is dealt with in Chapter 6 where results from heat transfer simulations are presented. It will be shown that the temperature gradient across the preform is substantially larger for an air-structured preform compared to that in a solid preform. It will also be shown that the cross-sectional temperature gradient varied strongly depending on the preform feeding rate. By making use of the existing temperature gradients in the air-silica structure, pressure control may be used to preferentially collapse holes in the outer rings of the structure. If temperature gradients need to be avoided, there exists an upper limit for preform feed rate and an optimal range for temperature hence limiting their use for controlling the hole structure.

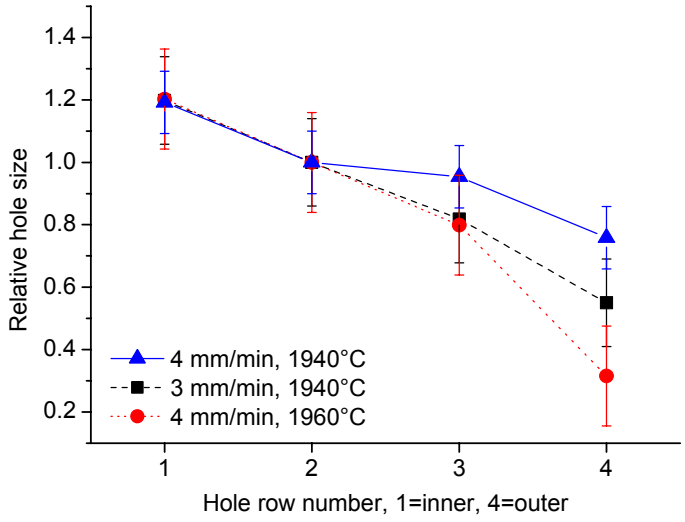

Figure 5-20. Relative hole diameter (relative to hole at row no. 2) across the cross-section of the fibre drawn at different draw conditions. X-axis shows the row number, 1 is the innermost row of holes and 4 is the outermost row of holes.

5.4 Discussion

As is the case with conventional silica fibre fabrication the PCF characteristics depend on the preform structure. Although the air structure allows greater change in the structure during drawing than for conventional fibres, the fibre is typically only as good as the preform it was drawn from. In the capillary-stacked fibres it was found that stringent dimensional specifications for both the cladding tube and the capillaries were required in order to fabricate good quality fibres. The capillary dimensions were found to reflect both the characteristics of the starting tube and the capillary drawing process. By optimising the capillary drawing process and introducing a tube internal pressure control good quality capillaries were manufactured providing high precision building blocks for the preform stack.

Due to the hole structure the fibre geometry can be more readily changed during drawing than conventional solid silica fibres. The holes can collapse, expand and deform depending on the drawing parameters. This makes the PCF fabrication more difficult but also offers greater flexibility in the various structures that can be fabricated from one preform design. In order to achieve this, suitable control parameters must be identified. The literature review revealed that the most common control parameter used during drawing was the drawing temperature. A theoretical study on capillary drawing by Fitt *et al* [11] also recognised the importance of preform feed rate on hole collapse and the possibility of using tube internal pressure for controlling the hole size. These three draw parameters, namely draw temperature, preform feed rate and preform internal pressure, were studied experimentally in this thesis for their suitability for geometry control of PCFs.

Hole size control by draw temperature was found to exhibit a relatively constant hole diameter response over a moderate range of feed rates, fibre and preform diameters and preform structures. The temperature range at which this behaviour occurred was dependent on the draw conditions and preform structure. This uniform hole size response would indicate that draw temperature is an ideal candidate for controlling the hole size. The stabilisation times for a draw temperature change however were found to be very long, up to tens of minutes, which is not acceptable for on-line control when fast response times are required.

A relatively large change in hole size during drawing was also achieved by adjusting the preform feed rate. The hole size change rate varied however, greatly depending on the draw conditions and possibly the preform structure. Unless this behaviour can be predicted accurately the feed rate may not be the most suitable control mechanism for PCF drawing. The findings however point out that the feed rate must be carefully chosen when different preform structures and sizes are drawn. Both feed rate and temperature were found to affect the radial hole size gradients believed to result from a temperature gradient during the draw. This is discussed in more detail in Chapter 6.

Preform internal pressure was found to have by far the fastest response in the fibre geometry. This is a very attractive feature when on-line control is considered. Some limitations were however discovered in using the preform internal pressure control. The pressure control was useful only when operating at optimal draw conditions. This was also predicted by the theoretical study of Fitt *et al* [11] although calculated sensitivity values only agreed qualitatively. Low enough draw temperature and high enough preform feed rate were required for obtaining a suitable geometry control. Once these were established an upper limit for pressure was found above which the geometry control became unstable. These limitations resulted in a somewhat smaller range of hole sizes than could be achieved by preform internal pressure control. The hole size response to a given pressure change at different drawing conditions was found to be relatively constant although preform structures with thin capillaries were found to be more sensitive to pressure. Taking into account the advantages and limitations, pressure control seems suitable for finer adjustments of the geometry and specifically promising in on-line control where fast response times are essential. The limitations can possibly be removed or at least the operating range increased by having a more precise control of the pressure.

CHAPTER 6 HEAT AND MASS TRANSFER SIMULATIONS OF THE FIBRE DRAWING PROCESS

6.1 Background

6.1.1 Introduction

Most of the draw-induced changes in optical fibres are dependent on the thermal history that the drawing process imposes on the fibre. As shown in Chapter 4, dopant diffusion depends on the temperature and exposure time during the drawing. Chapter 5 showed the importance of draw parameters in PCF fabrication, where the hole deformation is greatly affected by the viscosity dependence on temperature. The optical and mechanical properties of the fibre can also be altered by residual stresses (Appendix I), viscous deformation, defect centres [64, 65, 189, 190] and varying fictive temperatures [191, 192] that result from this high temperature process.

Although experimental studies are essential, they are often time consuming and costly. In addition, it is sometimes impractical or impossible to carry out required measurements. For example, great difficulties were faced in the measurement of diffusion during this study. It was also determined that on-line measurement of preform neck-down temperatures was impossible without affecting the temperature distribution. Theoretical analysis can offer a fast and cost-effective means of studying complicated problems and give insight to the phenomena that govern the fabrication processes. This is why in addition to the experimental analysis, theoretical heat and mass transfer analysis was also applied to the optical fibre drawing process.

The thermal history of a material depends on the heat and mass transfer processes involved and the thermal and mechanical properties of the material. Heat can be transferred in three modes, by conduction, convection and radiation. Heat conduction is typically the dominant mode of heat transfer in solids and depends on the spatial temperature gradient and the heat conductivity of the material. Heat transfer by convection arises from the movement of fluid and is important when gases are involved. Heat transfer by radiation is different from the other two in that it depends on the absolute temperature of the objects not temperature differences. Radiation

usually dominates in high temperature processes and its magnitude is determined by the surface characteristics of the objects such as emissivity and absorbance as well as the 'view' that the surfaces have of each other. For detailed description of the heat transfer processes see [122, 193]. Due to the high temperatures and speeds involved, all three modes of heat transfer are important during the optical fibre drawing process [194, 195].

Figure 6-1 shows a schematic of the heat transfer phenomena during fibre forming. The preform is heated radiantly in a cylindrical furnace. The furnace temperature of about 2000°C causes the viscosity of the glass to drop dramatically and together with the pulling force cause the preform to neck down into a fibre. Outside the furnace, the fibre is exposed to room temperatures or cooling tubes. Large geometrical changes occur within the relatively short (50-100mm) neck-down[15] region where the diameter changes from tens of millimetres down to 0.1mm fibre. Typical draw-down ratios range from 100 to 200, but can be up to 1000 in long-haul fibre fabrication. It results from the mass conservation that the velocity of the glass in the preform is of the order of 1-20mm/min and the velocity of fibre four or even five orders of magnitude higher. These large changes in temperature, dimensions and velocity make the heat and mass transfer processes during drawing complicated and the relative magnitude of the three modes of heat transfer vary accordingly along the length of the preform and fibre.

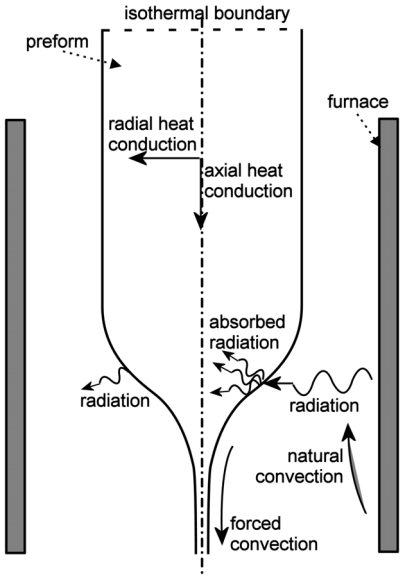

Figure 6-1. Heat transfer phenomena during drawing process.

[15] In some literature the neck-down region is divided into two (i) upper part which is called neck-down and (ii) lower part which is called draw-down. Here neck-down is used to refer to both unless otherwise stated.

Looking at the material parameters for silica glass also tells us about the heat transfer characteristics. The heat conductivity of silica is about 2 W/mK at 2000°C [188] which is low compared to metals (400W/mK for copper [122]) but high compared to air, (0.003W/mK [122]), or for example polymers (PMMA=0.2W/mK [196]). Due to the relatively low heat conductivity, there exist considerable radial thermal gradients in the preform stage of drawing, which however diminish when the fibre achieves its minute dimensions. Specific heat capacity defines the amount of heat required to raise the temperature of 1 kg of material by 1°C. The specific heat capacity of silica is about 1000 J/kgK at 2000°C. This is much higher than for metals (copper 385 J/kgK) but comparable with air and PMMA. The density of silica is about 2200 kg/m^3, which is low compared to metals (copper 8900 kg/m^3) but higher than PMMA polymer (1200 kg/m^3). This means the volumetric heating and cooling of silica is faster than PMMA but slower than metals. Most of these material parameters are highly temperature dependent for silica, which will also affect the relative magnitudes of modes of heat transfer due to the large temperature variations in the fibre forming process. The characteristics of radiation transfer for silica are discussed in Section 6.1.2.2.

The complex nature of the heat transfer processes in fibre drawing together with temperature dependent material properties make an analytical approach to the fibre drawing problem very difficult if not impossible. During the past decade computational resources have become abundant making a numerical approach to the problem attractive. In this chapter numerical heat and mass transfer analysis is used to study the effect of draw variables and preform structure, both in doped silica and air structured optical fibres. First a literature review is provided for work in the area of numerical analysis of optical fibre drawing. Subsequently details of the model used for this work are presented, followed by the simulations, results and discussion. Dopant diffusion is further studied using the results from the heat transfer simulations and draw experiments and finally an example of diffusion effects on non-zero dispersion-shifted fibre is presented.

6.1.2 Literature review

Numerical simulations have been used to study the optical fibre drawing process since the late 1960's when Glicksman [16] was the first to study the glass spinning and fibre cooling process. He showed that analytical predictions were inaccurate in describing the

heat and mass transfer in the fibre-forming region and showed the importance of radiation heat transfer and convection in this region. For the next two decades numerous papers were published [13-15, 180-182, 184, 197-204] exploring issues such as fibre cooling, laser drawing and instabilities during drawing. Due to the limitations in computational resources, many assumptions had to be made in these early numerical studies, which made them applicable only to a specific problem or region of fibre drawing. However these studies demonstrated the usefulness and the possibilities of such numerical analyses in the fibre drawing process.

Even today, simplification of the drawing problem is necessary in order to speed up the calculations and minimise computational costs. The most common simplifications are presented below. The literature from the past decade can then be reviewed in light of this, leading to the assumptions made here. The fibre drawing problem can be divided into several sub problems, see Figure 6-2. Based on the physical aspects (Figure 6-2(a)), drawing can be divided into two consecutive stages:

1. Fibre formation and heat transfer inside the furnace
2. Cooling of the fibre after the furnace.

The heat transfer problem is very different in the two areas and great simplifications can be made if one is only interested in aspects of fibre cooling. The various materials taking part in the drawing problem have very different heat transfer characteristics and the problem could be divided into heat and mass transfer in

1. glass
2. gas
3. furnace.

If the study is only interested in the gas flow patterns inside the furnace the other two materials can in some circumstances be omitted.

In terms of the computational aspect (Figure 6-2(b)) either

1. steady-state or
2. transient problem is solved.

If time-dependency is not a matter of interest, then steady-state calculations are appropriate. However, for example, when studying fibre diameter control, one has to

solve the transient equations. If the mass transfer does not affect the heat transfer, or vice versa, then only one of them needs to be solved, greatly simplifying the problem. For example when the neck-down shape of the preform is known *a priori*, only heat transfer equations need be solved. When both are solved simultaneously the problem is called *coupled* or *conjugated*.

The computational problem can be further divided according to the number of spatial variables. For example in 1-dimensional heat transfer, temperature varies only in one direction. In fibre drawing this could be the longitudinal direction. The 2-dimensional problem is typically axisymmetric in fibre drawing, where the variables change in longitudinal and radial directions but stay constant around the axis of symmetry. Various combinations of these subdivisions can be used and are not limited to the ones listed here. Typically the computational time and the difficulty in convergence increase with the number of problems that are simultaneously solved. Within recent years it has become possible to merge most of these subdivisions into one large computational problem. The term *fully coupled* problem is used in this text to describe such computations.

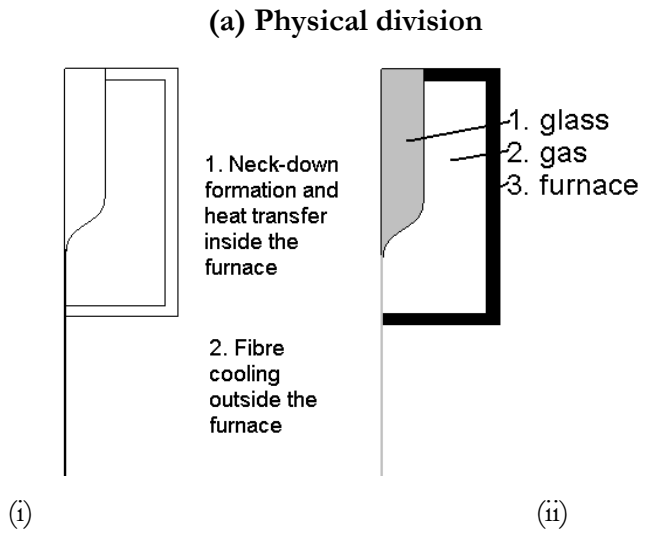

Figure 6-2. Examples of subdividing the draw problem by a) physical or b) computational aspect.

6.1.2.1 Neck-down formation

The flow of glass can be described by momentum and continuity equations. If radial velocity gradients are assumed insignificant, 1-dimensional calculations are sufficient. In the fibre drawing problem the axial (draw directional) velocity changes are much greater than radial, however 2-dimensional computations have been done to study the effect of this assumption [194, 195, 205, 206]. Rosenberg *et al* [205] and Papamichael and Miaoulis [194] showed that radial velocity gradients exist in the neck-down region and that the 2-dimensional model provides a more accurate neck-down profile. The former study was however isothermal and a latter study assumed temperature independent material properties of glass, except for viscosity. Choudhury *et al* [207] and Lee and Jaluria [195, 206] showed that the radial velocity gradients are very small, giving a maximum difference between the centre and surface velocity of only 1.5%-2.5%. In their simulations the corresponding maximum surface to core temperature difference was ~30°C [195] and ~220°C [206]. Also Choudhury and Jaluria [17] point out in their analysis that it is more important to take into account the 2-dimensionality in heat transfer than in glass flow. In the present work the glass flow was assumed to be 1-dimensional, however a 2-dimensional model was used for heat transfer.

The shape of the neck-down depends on the forces acting on the preform and fibre. The following force balance can be written for the cross-section of the neck-down at an axial position for 1-dimensional case [204].

$$F_T + F_g = F_\mu + F_\xi + F_I + F_e \qquad (29)$$

where F_T is the draw tension and F_g gravitational force both aiding the neck-down formation. F_μ is the viscous force, F_ξ force due to surface tension, F_I is inertial force and F_e shear force exerted by external fluid. A number of studies show that the inertial and surface tensional forces and the shear force due to external gas are not significant and can be ignored [17, 208, 209]. It is seen then from Equation (29) that the gravitational force aids the pulling force and that the viscous force plays a major role in neck-down formation. In the present work also, F_ξ, F_I and F_e are ignored. The temperature dependence of viscosity couples the neck-down formation to the heat transfer equations.

The effects of drawing parameters on the neck-down shape have been studied by the above researchers. The neck-down shape is mainly determined by the temperature distribution and the viscosity dependence on temperature [17, 183, 207, 209, 210]. When the draw speed is increased the change in temperature profile causes the neck-down to start further down the furnace [17, 207, 209]. If the mass flow-rate is kept constant but preform or fibre radius changed, the neck-down shape is very similar. However, if drawing velocity is kept constant but preform radius changed (i.e. preform feeding rate changed) the necking shapes are different [207]. Furnace temperature profile is an important factor in determining the temperature profile of the glass and thus affects the neck-down shape drastically [17]. Other heat transfer related parameters that affect the neck-down shape include the heat transfer coefficient on the surface of the glass which is affected by the gas flows in the furnace. Neck-down shape is shown to be affected by the gas flow velocities and gas inlet positions [17, 208]. The preform structure would affect the neck-down shape only if the structure were composed of large regions with considerably different viscosities [18, 209].

6.1.2.2 Heat transfer

In the past decade numerous studies have emerged on computational analysis of the heat transfer during fibre drawing. Radiation was found to be the dominant mode of heat transfer early on [16, 182, 184, 199, 204, 211] and new methods for calculating radiation are being developed [212]. The most common model used for radiation transfer between glass and furnace is the enclosure model [17, 194, 195, 207-209]. This model includes an enclosure of surfaces that participate in the radiation heat transfer. The fraction of radiation leaving one surface and reaching another surface depends on the geometrical orientation of the surfaces with respect to each other. A detailed description of this method and application to the drawing problem can be found in Refs. [193, 213]. Using the enclosure model Lee and Jaluria [213] studied the effect of different pre-set neck-down shapes on the radiative heat transfer. They showed that the neck-down shape significantly altered the heat flux between the geometry of the preform and that in order to provide accurate simulations the neck-shape profile should be solved coupled with the heat transfer equations. In the current work this approach is followed and the conjugated problem solved where the enclosure model is used for radiation heat transfer between glass and furnace.

The radiation heat transfer must be also considered inside the glass. To simplify the computations the Rosseland approximation [193] is typically applied within the glass [17, 194, 195, 207-209]. As the resulting diffusion equation is like a heat conduction equation, this greatly simplifies the computation of radiative heat transfer within the glass. The Rosseland approximation is only valid when a medium is optically thick and temperature gradients are moderate. The effect of this approximation for heat transfer during drawing was studied by Nicolardot and Orcel [18]. The so called "zonal method" has been used in recent work by Yin and Jaluria [214, 215] who found that the radiative heat flux is strongly influenced by the radial temperature variation within the preform but that if this temperature variation is small, the optically thick approximation gives good results. Liu *et al* [20, 212] used a Fresnel interface approach to calculate the radiation transfer but found that the differences in temperatures to the diffusion approximation were only 1-2%. In order to simplify the computations the Rosseland approximation is used in the present work.

Another important mode of heat transfer is the convection transfer between the surrounding gas and the glass surface. Inert gas is used in the fibre-drawing furnace to prevent contamination of the hot preform-glass surface. Typical gases used are argon or nitrogen, which are blown through a number of inlets into the furnace. The flow configuration can be either cocurrent or countercurrent relative to fibre draw direction. The feed rates of gases, feed position configurations and properties of the gas all affect the thermal processes in the furnace. Particularly in high-speed drawing or at high gas feed rates, convection transfer from fibre to gas is greatly affected.

In order to compute the heat transfer coefficient required for convection transfer the velocity field of the gas must be known. Computing the velocity field in the gas inside the furnace greatly increases the computational time and complicates the model, thus typically a prescribed heat transfer coefficient is used on the glass-gas boundary. The effect of the magnitude of the coefficient has been studied by Choudhury *et al* [17, 207] and Lee and Jaluria [195]. The value for the heat transfer coefficient ranged from 50-300W/m^{2}K dating back to the work of Paek and Runk in 1978 [14]. The studies show that the selection of the coefficient affects the temperature distribution and neck-down profile, but only towards the end of the neck-down. The velocity fields in the gas were computed coupled with the heat transfer equation by Choudhury *et al* [17, 208, 210,

216] and Yin and Jaluria [215] showing that the heat transfer coefficient depends on the gas velocity and becomes significant at high gas flows, draw speeds and near the gas inlets and depends on the direction of gas flow. The gas flow patterns themselves have been a subject of some studies [217-220]. In order to simplify the present study gas flows are not computed. Since the draw velocities in specialty fibre drawing are considerably slower than the velocities used in the above simulations the importance of convective heat transfer is even smaller. However it should be noted that this assumption may cause inaccuracies in the produced temperature profiles.

Most of the studies presented here have assumed a prescribed temperature profile along the furnace wall. Choudhury *et al* [17, 207] and Lee and Jaluria [195] showed that for different furnace wall temperature profiles the necking shape and temperature distribution were considerably different. If the temperature profile of the furnace can be reliably measured, a prescribed temperature profile can be assigned to the model. However, if such measurements are not available or a new furnace design is being considered, then the temperature profile should be computed within the model. Such an approach has been used by Nicolardot and Orcel [18] and Cheng and Jaluria [21]. In the current work the structure of the furnace is included in the heat transfer calculations and no prescribed temperature profiles are used inside the furnace.

Another important source of heat during drawing, which has not been discussed above, is viscous dissipation in glass. Viscous dissipation arises from the velocity differences in glass and also changes due to temperature dependence of glass viscosity. It has been shown that viscous dissipation has an effect on the temperature distribution [206]. However, the effect is significant mostly in the exit fibre temperature. The velocity gradients also are more significant at high-speed drawing. The same study showed that it is also important that the temperature dependency of the material properties is taken into account. The most important is the viscosity of the glass, but also thermal conductivity and specific heat capacity are functions of temperature in glass. The current work takes into account the temperature dependency of the material properties for glass but viscous dissipation is ignored to simplify calculations and is justified by the low draw speeds used.

There are areas of heat and mass transfer computations in fibre drawing that have not been discussed above. A number of studies have modelled heat transfer during cooling of the fibre [15, 179, 217, 219, 221-223]. The discussed work also only involved studies made for the steady-state process, which is the subject of the current work. However numerous studies have been made in transient computations for the fibre drawing process [19, 180-184, 186, 187, 201, 224, 225] and more specifically in the area of drawing process control [203, 226-230].

As discussed in Chapter 5, Section 5.1, there are very few studies done on drawing of fibres with air-structures. A model that would take into account all the above-mentioned heat transfer effects, neck-down formation and the deformation of the internal air-material structure would be very complicated and three-dimensional simulations would be required. Deflandre [12] reported simulation of a PCF drawing where heat transfer was also taken into account. No details were however given of the parameters and only one simulation result was shown. It was evident from the simulation that issues with heat transfer caused a higher deformation rate of the holes close to the surface of the fibre. One of the aims of this thesis is to study the effects of the air-material structure on the heat transfer during the drawing process. Two-dimensional heat transfer simulations were carried out as a full three-dimensional model with deformation accounted for was outside the scope of this thesis. The results are reported in Sections 6.3.6 and 6.3.7.

6.2 Fluid dynamics computations

6.2.1 Model description

The model includes the preform, the furnace and the gas surrounding the preform, Figure 6-3. The furnace is composed of a graphite heating element with heat source and insulator structure to represent the real furnace structure. The model is extended below the furnace, to include a cooling part for the fibre. The neck-down shape is calculated for the preform, where 1-dimensional flow is assumed. A 2-dimensional axisymmetric heat transfer equation is solved in the preform, the furnace and the gas. Simulations are steady state and temperature dependent.

Figure 6-3 shows the model geometry and typical dimensions. The properties for each material are given in the Appendix III. Temperature dependence for glass viscosity, conductivity and specific heat capacity were taken into account. Gas properties were taken as those of argon. The conductivity was temperature dependent and other properties constant at the mean temperature of the furnace.

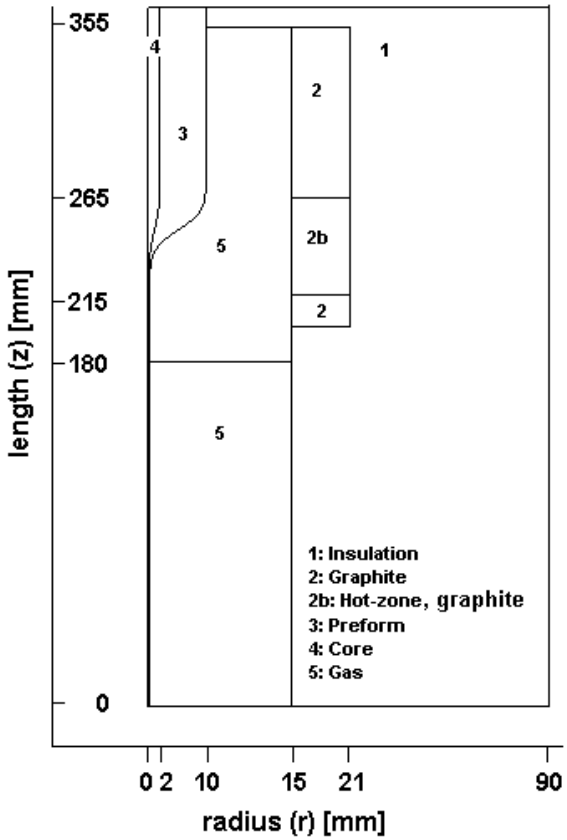

Figure 6-3. Fibre drawing and furnace model geometry.

6.2.2 Governing equations

As discussed in the Background Section 6.1 the heat transfer in the furnace is a complex system. The shape of the preform neck-down depends on the temperature profile and affects the view factors for radiation heat transfer, therefore the conjugate problem is solved. The nomenclature used in this chapter is listed in Table 6-1. The equations (30, 33-35) and (41-42) can be found for example in text books by Bejan [122] and Siegel and Howell [193].

Table 6-1. Nomenclature for Section 6.2.

G	Gebhardt factor	ρ	Density, kg/m^3
H	Internal heat generation, J/m^{3}s	σ	Stefan-Boltzmann constant
L	Length of the model, m		
T	Temperature, K	Subscript	
S	Surface area, m^2	c	Conduction
c_p	Specific heat capacity, J/kgK	e	External fluid
g	Acceleration of gravity, m/s^2	ext	External
k	Heat conductivity, W/mK	f	Fibre
n	Normal to the surface or refractive index	g	Gravity
q	Heat flux, W/m^2	I	Inertia
r	Radial coordinate, radius m	i	Surface participating in radiation
v	Velocity, m/s	k	Surface participating in radiation
z	Axial coordinate, length m	p	Preform
		r	Radiation
α	Absorption coefficient, m^{-1}	T	Tension
ε	Emissivity	ξ	Surface tension
η	Kinematic viscosity, m^2/s		
μ	Dynamic viscosity, Pas		

6.2.2.1 Heat equations

The steady state axisymmetric heat equation for the preform is expressed as [122]:

$$\rho c_p \left(v_z \frac{\partial T}{\partial z} + v_r \frac{\partial T}{\partial r} \right) - \frac{\partial}{\partial z}\left(k \frac{\partial T}{\partial z} \right) - \frac{1}{r}\frac{\partial}{\partial r}\left(rk \frac{\partial T}{\partial r} \right) = 0 \qquad (30)$$

For the preform the radiative energy reaching a point (r,z) in the preform is computed using the Rosseland approximation, Equation (31), giving the '*effective*' conductivity of the glass, Equation (32) [14]. n is here the refractive index of glass.

$$q_r = \frac{4n^2}{3\alpha}\sigma\nabla^2\left(T^4\right) \qquad (31)$$

$$k = k_c + \frac{16n^2\sigma T^3}{3\alpha} \qquad (32)$$

The heat equation for the insulation, the graphite and the gas is [122]:

$$-\frac{\partial}{\partial z}\left(k\frac{\partial T}{\partial z}\right)-\frac{1}{r}\frac{\partial}{\partial r}\left(k\frac{\partial T}{\partial r}\right)=0 \tag{33}$$

The furnace heating element includes a heat source, giving

$$-\frac{\partial}{\partial z}\left(k\frac{\partial T}{\partial z}\right)-\frac{1}{r}\frac{\partial}{\partial r}\left(k\frac{\partial T}{\partial r}\right)=\rho H\,, \tag{34}$$

where H is the internal heat generation (J/m^{3}s) [122]. A typical value of 18 kJ/m^{3}s was used in simulations.

6.2.2.2 Neck-down profile calculation

The velocity distribution in the neck-down region is calculated from the momentum equation, Equation (35). Surface tension, inertial or shear stress from external gas are not taken into account as the contribution is insignificant [17].

$$\frac{\partial}{\partial z}\left(3\mu r^2\frac{\partial v}{dz}\right)=-gr^2\rho\,, \tag{35}$$

For incompressible and one dimensional flow the continuity equation yields:

$$r^2 v=r_p^2 v_p\,, \tag{36}$$

For calculating the neck-down profile Equations (35) and (36) were combined to give

$$\frac{\partial}{\partial z}\left(3\eta\frac{1}{v}\frac{\partial v}{dz}\right)=-\frac{g}{v} \tag{37}$$

A transformation of variables, as shown in Equation (38), was performed to obtain Equation (39). As the effect of gravity is small, Equation (39) becomes almost linear and is thus easier to solve.

$$f(z) = \log v(z) \tag{38}$$

$$\frac{\partial}{\partial z}\left(3\eta \frac{\partial f}{dz}\right) = -ge^{-f} \tag{39}$$

For the neck shape calculations the preform radius, fibre radius and draw speed are given. Typical values are

$$\begin{aligned} r_p &= 6 - 12 \times 10^{-3} m \\ r_f &= 62.5 \times 10^{-6} m \\ v_f &= 0.4 - 3.0 \, {}^{m}\!/_{s} \end{aligned} \tag{40}$$

6.2.3 Boundary and initial conditions

The furnace is water-cooled and thus enables the use of the Dirichlet boundary condition for the external furnace walls, where the temperature is set to 289K. The temperature at the top of the preform is also set to 500K. The enclosure model was used to account for radiation heat transfer [193]. A diffuse gray radiation boundary condition [193] is applied to the enclosure consisting of the furnace inner wall, irises and the preform-fibre surface. The discrete version of the boundary condition gives Equation (41). See Appendix III for the calculation of Gebhardt, G_{ik}, and view factors. Emissivity for the preform-fibre surface is dependent on the radius of the preform-fibre, as is taken from Myers [184] and Homsy and Walker [13].

$$\begin{aligned} &-\left(k_k \frac{\partial T_k}{\partial n}\right)_{body1} + \left(k_k \frac{\partial T_k}{\partial n}\right)_{body2} = \\ &\sigma \varepsilon_k \left(T_k^4 - \frac{1}{S_k \varepsilon_k} \sum_{i=1}^{N} G_{ik} \varepsilon_i T_i^4 S_i\right) \end{aligned} \tag{41}$$

where n is component normal to the surface.

For a fibre surface in the cooling section below the furnace, idealized radiation cooling is included as this part is not within the enclosure. The external temperature is set to 298K. A number of convection heat transfer coefficients were tested from literature [216], however the shape of the neck-down was found to correlate with experiments better when convection was neglected.

$$-k\frac{\partial T}{\partial n}=\sigma\varepsilon\left(T^4-T_{ext}^4\right), \tag{42}$$

where n is component normal to the surface.

In the symmetry line of the model the following applies:

$$\frac{\partial T}{\partial r}=0 \tag{43}$$

Boundary conditions for Equation (39) are

$$\begin{aligned} f\left(L\right)&=\ln\left(v_p\right)\\ f\left(0\right)&=\ln\left(v_f\right)\end{aligned} \tag{44}$$

where L is the length of the model and 0 is at the bottom of the fibre as in Figure 6-3. The preform velocity v_p and fibre draw velocity v_f are predefined. The velocity of the glass is set to zero and the temperature is set to 1000K for the entire computation domain as the initial conditions.

6.2.4 Numerical scheme

A computational software package ELMER [231] was employed to solve the coupled partial differential equations. The equations were discretised using the finite element method. Stabilization was used for the convection-dominated heat equation [232]. The view factors, needed for the diffuse-gray radiation modelling, were computed for each pair of boundary elements participating in radiation, by numerical integration. From the view factors the Gebhardt factors could be determined by solving a set of linear matrix equations. The radiation boundary condition was linearized by an explicit iteration scheme for the first few iterations and thereafter fully implicit Newton iteration was employed.

The matrix equations resulting from the finite element discretisations were solved with a band matrix solver from LAPACK based on LU decomposition. To reduce the execution time reverse Cuthill-McKee bandwidth optimisation was employed before the direct solver. The coupled set of equations was solved iteratively until the solution fulfilled simultaneously the convergence criteria of all the equations. After a new neck-down profile was obtained the mesh was readjusted with linear mapping and new view factors for radiation heat transfer were calculated. To ensure convergence, relaxation was used with a relaxation factor of 0.7. Typically 5 to 12 iterations were required for the heat equation and only 1-2 iterations for the neck-down iteration. Around seven coupled iterations were required to obtain a fully consistent solution. As the computational domain included the furnace structure and the gas in addition to the preform, a nonuniform grid was employed. Denser mesh was applied in areas where greater changes in gradients of the variables were expected. The mesh consisted of 3500 bilinear elements. With this mesh typical simulation took around 135 CPUs on a single processor of SGI Origin 2000 computer.

6.2.5 Experimental validation

The simulated neck-down shape was compared with an experimentally produced neck-down. For the simulation the draw parameters, such as the drawing temperature, preform and fibre diameter and the draw speed were matched to those of the experiment. The resulting neck down shape from the fibre drawing experiment was measured using a preform diameter measurement gauge and compared to the calculated shape.

As can be seen from Figure 6-4 the neck-down profiles match well considering that the furnace structure has been simplified for the simulations and that the material properties of glass used in the simulations are taken from literature and could be different for the actual preform. Simplifications performed in the computational model relating to viscous dissipation and 1-dimensional flow of glass could explain the discrepancies. The drawing tension was also calculated for simulations and compared well with the typical range of real tensions measured during draw. No material or heat transfer parameters were changed according to experimental results, nor did the numerical scheme contain any artificial constants that would have been adjusted to

match the experimental data. Material properties were taken from published measurements when available as referred in Appendix III.

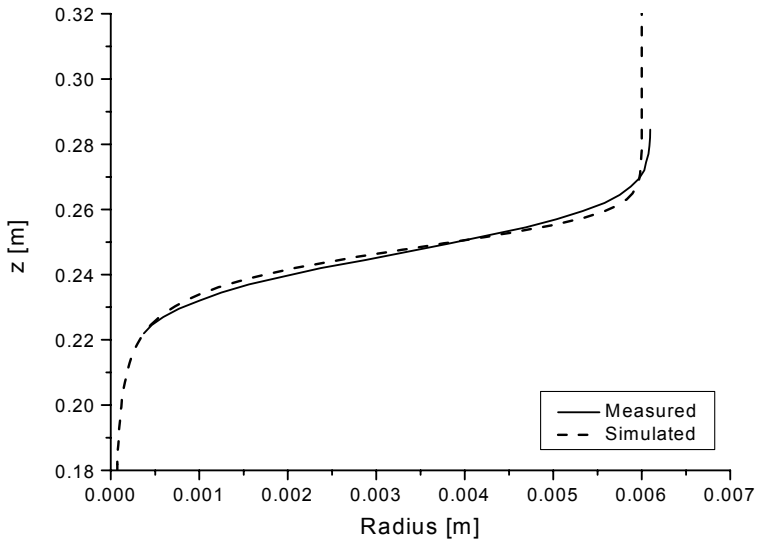

Figure 6-4. Comparison of simulated and measured neck-down for 12mm diameter preform at draw speed of 0.4m/s.

6.3 Heat transfer simulation results

The following sections present the heat transfer results from fibre drawing simulations. First the effects of draw parameters such as furnace temperature and drawing speed are presented, then the heat transfer in a solid preform structure is considered, including the effect of preform diameter and the presence of a highly doped core. The influence of furnace structure is also studied by considering two different structures. The structures are simplified models of furnaces from different suppliers. Finally the effect of air-structures in preforms is studied including a study of heating microstructured polymer optical fibre preforms.

Figure 6-5 shows a typical temperature field in the preform and furnace during drawing of silica fibres. The maximum temperature in the glass is experienced in the neck-down region where the preform forms into fibre. The neck-down occurs at the same longitudinal position as the position of the heating element. The preform entering the furnace heats up and a slight radial thermal gradient is observed in the preform. The fibre cools down as it exits the hot-zone and is radially almost uniformly heated. Note

that this computed temperature field together with the computed neck-down shape and glass velocities are then used in Section 6.4 to estimate dopant diffusion during drawing.

Note that the results are mostly presented with graphs where the studied variable such as temperature is the y-axis and the longitudinal coordinate (z) the x-axis, see Figure 6-7 for an example. The length (z) and the radius (r) always correspond to the coordinates given in Figure 6-3. The top of the preform is in the right hand side of the figure and the bottom of the model (i.e. fibre) are in the left had side of the figure. To show the position relative to the neck-down, the radius of the neck-down is drawn as a dotted line using the second y-axis. Only neck-down for one of the cases in each figure is drawn for clarity. The case of the neck-down drawn is indicated in the figure caption.

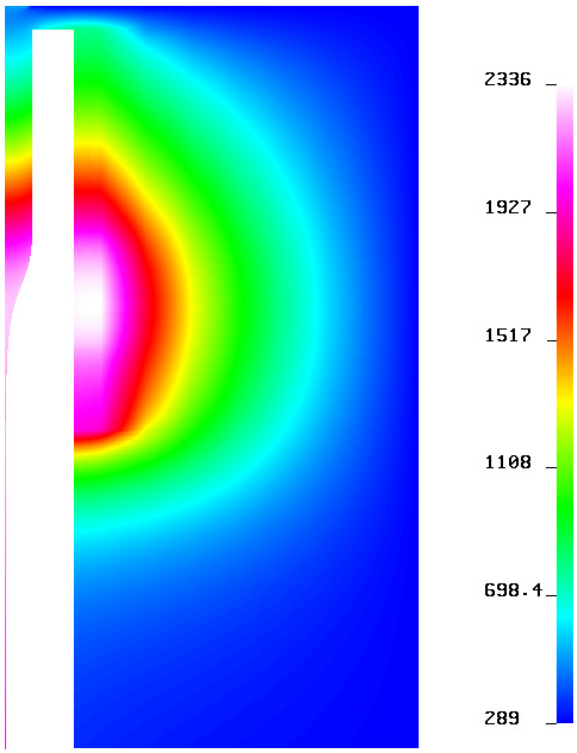

Figure 6-5. Temperature contour plot, 12mm diameter preform, draw speed of 3.0m/s, x-axis has been scaled by 2 and gas temperature hidden for clarity. Temperature in K. Note orientation and dimensions as in Figure 6-3.

6.3.1 Drawing temperature

To study the effect of drawing temperature, the furnace heat source was varied from 18 to 20 kJ/m^{3}s. Preform diameter was 12 mm and drawing speed 0.4 m/s. As the heat source was increased, the hot zone element temperature increased from 1860°C to 2060°C and the fibre tension decreased from 70g to 10g. The necking started slightly earlier for hotter temperatures, as seen in Figure 6-6. The difference however is not large. Figure 6-7 shows the preform and fibre centre temperature along the length. The maximum temperature in the preform increased 140°C due to heat source increase. The difference in neck-down temperature for the two cases was 150°C and for the fibre temperature difference was 65°C. The shape of the temperature profile along the length stays similar between the cases. Note that the "kink" in the temperature profiles at a z-position of about 0.18m is a local artefact of the boundary conditions between the furnace and the bottom iris and does not significantly affect other parts of the model.

Figure 6-8 shows the difference between glass surface and core temperatures along the length of the preform and fibre. For the element temperature of 2060°C, the preform surface is 11°C hotter than the core. The fibre core is 4°C hotter than fibre surface. These are similar to the lower temperature.

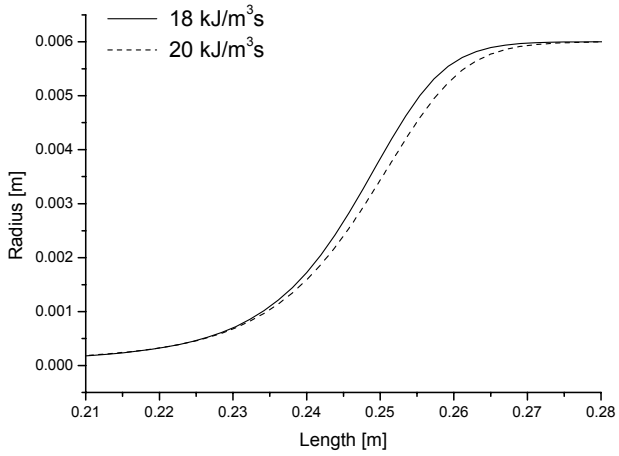

Figure 6-6. Neck-down shape at two different furnace temperatures.

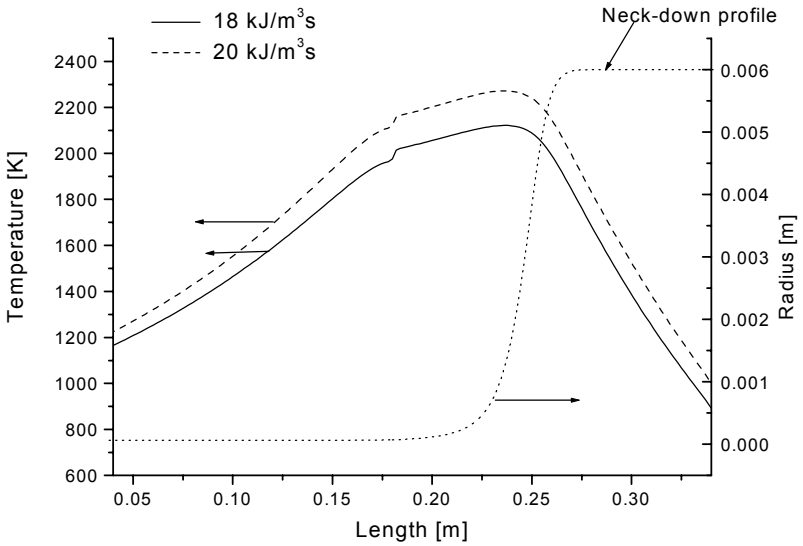

Figure 6-7. Core temperature along the length of the model at different draw temperatures. The neck-down profile is for the case of 18kJ/m³s.

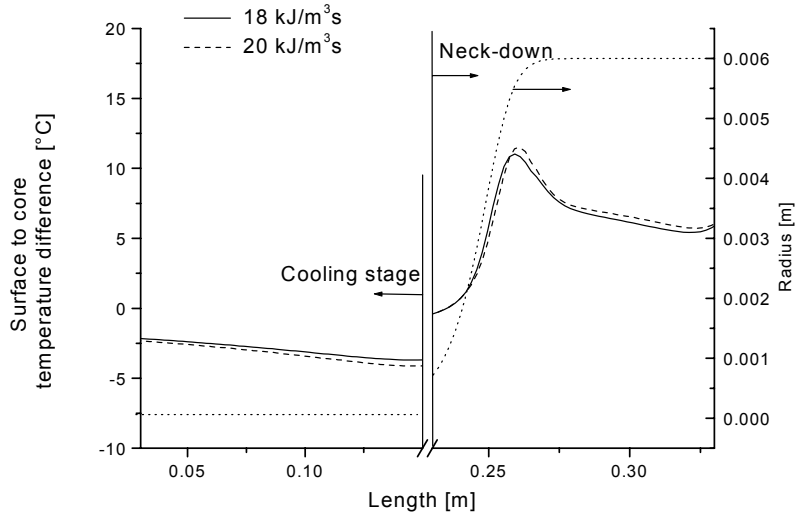

Figure 6-8. Surface to core temperature difference along the length of the preform-fibre at different draw temperatures. The neck-down profile is for the case of 18kJ/m³s.

6.3.2 Feed and draw speed

Simulations for a 12mm diameter preform were performed at two different speeds, at a "low" speed of 0.4m/s and a "high" speed of 3m/s. As the preform and fibre diameter (12mm and 125μm) were kept constant the corresponding preform feed rate was 2.6 and 19.5mm/min and mass flows were 0.7 and 4.8g/min. As noted in the literature [17], if the mass flow is held constant, the neck-down profile is very similar, although the fibre or preform diameter is changed. However change in mass flow will cause change in the neck-down shape. This is also seen in Figure 6-9, where the neck-down for higher draw speeds is slightly more elongated and starts further down the hot-zone.

The effect of draw speed on core temperature can be seen in Figure 6-10. For the same hot-zone temperature, the fibre at the exit of the furnace is hotter for higher draw speed, as is expected. Also the fibre is considerably hotter well below the furnace. It is noted that although an increase in draw velocity increases the fibre temperature at a particular position, the cooling occurs more quickly [209]. Above the neck-down region the preform temperature is 240°C colder at higher draw speed. This may be part of the reason why PCFs retain their structure better at higher preform feed rates.

Figure 6-11 compares the differences in surface temperature to core temperature along the length of the model. The difference is substantial for higher draw speed just above the neck-down, being 65°C more than at slow speed. In the lower neck-down region and the fibre, the difference between high and low speed is not significant, amounting to 3°C degrees.

The considerable surface to core temperature difference in the upper neck-down region and just above neck-down shows the importance of draw speed for speciality fibres with large doped areas as well as air-silica-structure fibres, where changes in structure are more likely due to radial temperature gradients. Due to the extremely strong temperature dependence of the viscosity, surface to core temperature differences of this magnitude could affect the residual stresses of specialty fibres with heavily doped regions. Radial velocity differences in doped areas could also arise, given that the viscosity of the different regions were considerably different.

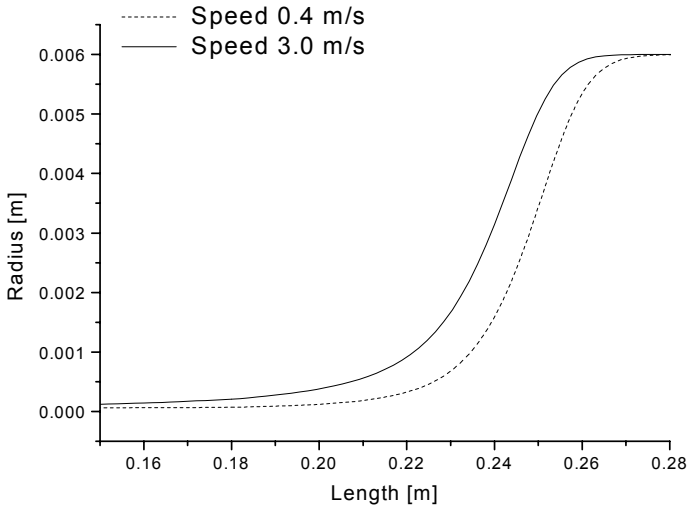

Figure 6-9. Neck-down profiles at different draw speeds.

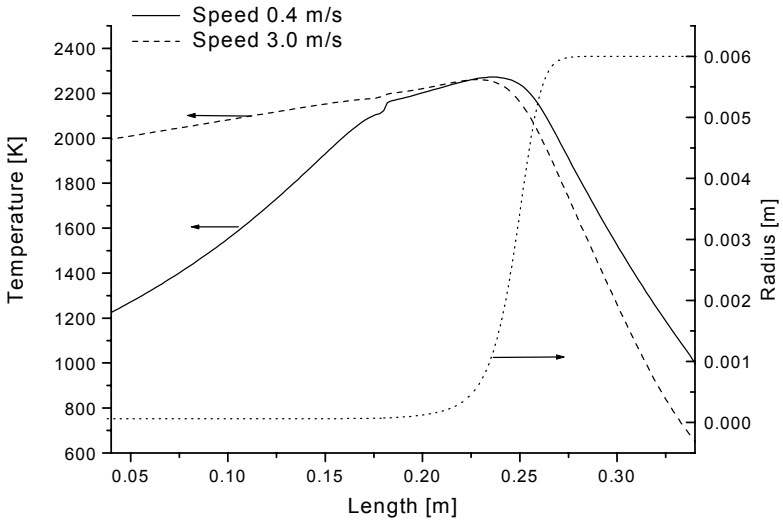

Figure 6-10. Core temperature along the length of the model at different draw speeds. The neck-down profile is for the case of 0.4m/s.

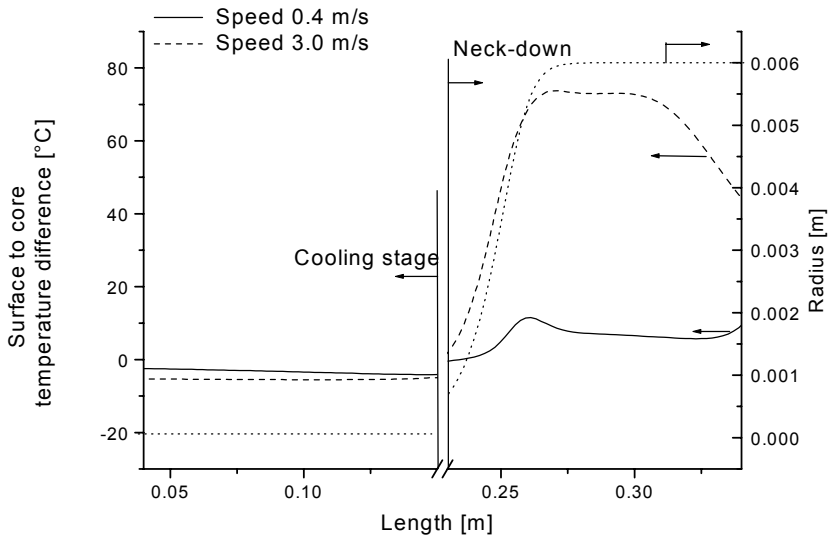

Figure 6-11. Surface to core temperature difference along the length of the preform-fibre at different draw speeds. The neck-down profile is for the case of 0.4m/s.

6.3.3 Preform diameter

The effect of preform diameter was simulated with two preform sizes, 12mm and 24mm diameter, this being a typical range of diameters used in specialty fibre fabrication. The furnace heating was adjusted (by changing the heat generation term H in Eq. (34)) to give similar neck-down glass temperatures. Figure 6-12 shows the neck-down profiles for the two preform sizes at two draw speeds. For both sizes the neck-down for faster speed occurs later. For both speeds the necking is more elongated for the smaller preform. This is because the smaller preform and neck-down stays hotter longer. This is shown in the temperature profile comparison in Figure 6-13. For the slower speeds the smaller preform is about 190°C hotter above the neck down region and 120°C colder in the cooling fibre.

Figure 6-14 shows the difference in surface temperature to core temperature along the length of the preform and the fibre. For the thicker preform the surface to core temperature difference is higher than for the thinner preform just above the neck-down. The draw speed does not have much effect on this difference. A distinctive surface to core temperature difference increase is seen for thicker preforms just above the neck down region. Being so sharp and situated in the fibre formation region this should be studied further as it can also influence the fibre diameter fluctuations. Again

this could also cause radial flow in the glass with highly doped regions or unwanted deformation in PCFs due to large temperature gradient. The fibre diameter also affects the neck-down and temperature distribution and is discussed in the Refs. [17, 209]. As most fibres are drawn to the "standard" 125μm, no further simulations were made in this study.

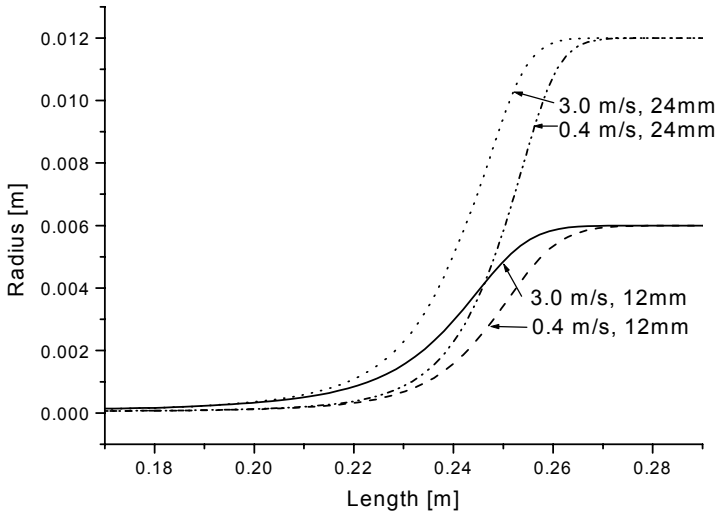

(a)

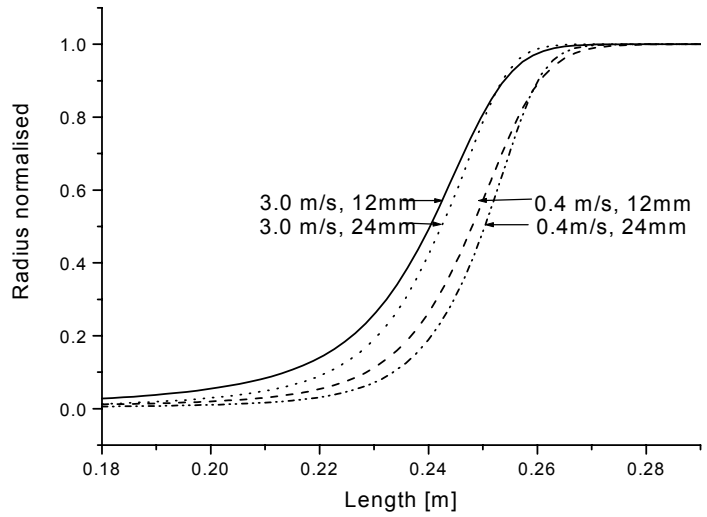

(b)

Figure 6-12. Neck-down profiles for profiles for preform diameters of 12mm and 24mm at draw speeds of 0.4 m/s and 3.0 m/s (a) absolute and (b) normalised (to preform radius).

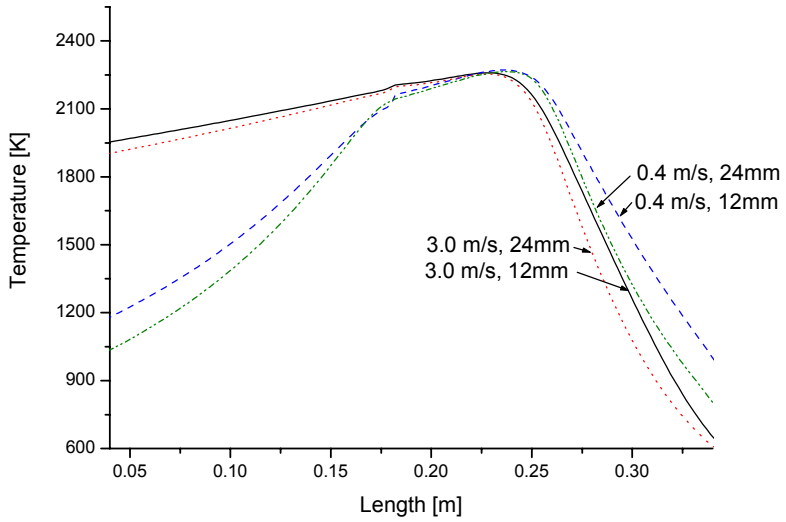

Figure 6-13. Core temperature profiles for preform diameters of 12mm and 24mm at draw speeds of 0.4 m/s and 3.0 m/s.

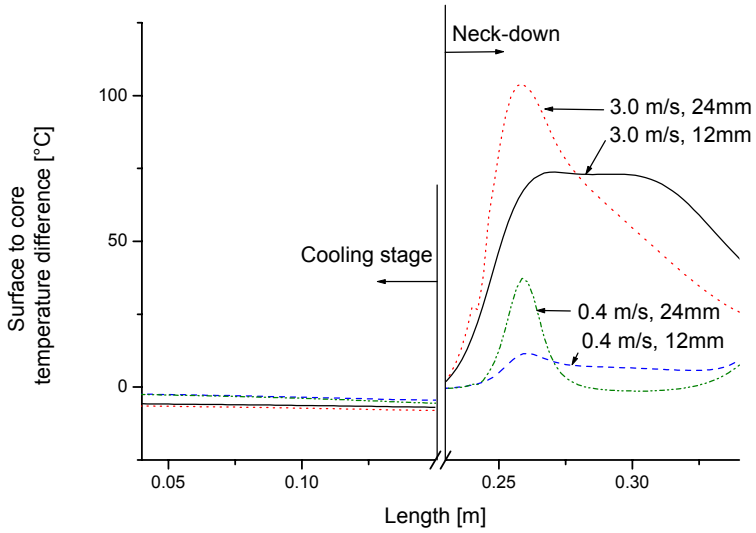

Figure 6-14. Surface to core temperature difference along the length of the preform-fibre for preform diameters of 12mm and 24mm at draw speeds of 0.4 m/s and 3.0 m/s.

6.3.4 Doped core

A simulation was performed for a preform structure with 4mm core diameter and 12mm outer diameter. The results were compared with a homogeneous preform structure with no core. The material properties for the core were estimated for a GeO_2 doped silica, where the doping level was 20 mol%. These are listed in Appendix III. The relatively large core size was chosen to emphasise the effect. An ideal step index profile was assumed. Simulations were performed for two draw speeds, 0.4m/s and 3.0 m/s.

The effect of the doped core was found to be very small. The temperature difference of the centre of the preform with no core and GeO_2 doped core was 0.5°C above the neck down and –0.2°C for the fibre part at draw speed 0.4m/s. At higher speed, 3.0 m/s, the differences were slightly larger, for just above neck-down 3°C and in fibre 0.2°C. In order to affect the heat transfer, the doped area should have considerably different material properties. Typically in MCVD the doping levels are restricted resulting in relatively modest changes in thermal properties. The viscosity changes between silica doped with different species could be significant and affect the radial flow of glass and deformation of the refractive index profile under certain conditions. In this case a 3-dimensional draw model should be applied to study such effects.

6.3.5 Furnace design

Two different furnace designs were modelled to see the effect on temperature distribution when the furnace maximum temperature was kept the same. The two furnaces designs (A and B) represented two production furnaces made by different manufacturers. The main differences in mechanical design was that Furnace B used an extension tube below the furnace and the cooling water circulation was slightly different and more efficient in the top part of Furnace B. Furnace B also had a larger inner diameter (see Table 6-2 for typical dimensions).

Simulations were performed for each design using a 12mm diameter preform and drawing speed of 0.4m/s. The neck down shape was different for the two furnaces, being slightly more elongated for Furnace A, Figure 6-15. This can be accounted for by the longer hot-zone. Figure 6-16 shows the core temperature profile along the length for Furnace A and B. The results showed that when the heating element maximum temperature was set equal for both furnaces, the preform core temperature above the neck-down was about 300°C lower for Furnace B. This was expected, as the cooling circulation is more efficient in this part compared to Furnace A.

Table 6-2. Furnace dimensions

[cm]	*Furnace A*	*Furnace B*
Diameter	3	4
Hot-zone length	5	4
Above hot-zone	10	14
Below hot-zone	3.5	14
Element length	14	18
Extension tube length	0	20

The fibre temperature below the furnace was 90°C hotter for Furnace B, which is due to the effect of the extension tube. The different temperature profile could affect the hole deformation during PCF draw, as collapse will differ at the different diameters of the neck-down. If the temperature profile along the neck-down is very different the final collapse behaviour would be altered. Due to slow draw speed the surface to core temperature differences are not large for either furnace. Furnace B has slightly higher thermal gradient being about 9°C in the preform and only 2°C in the fibre.

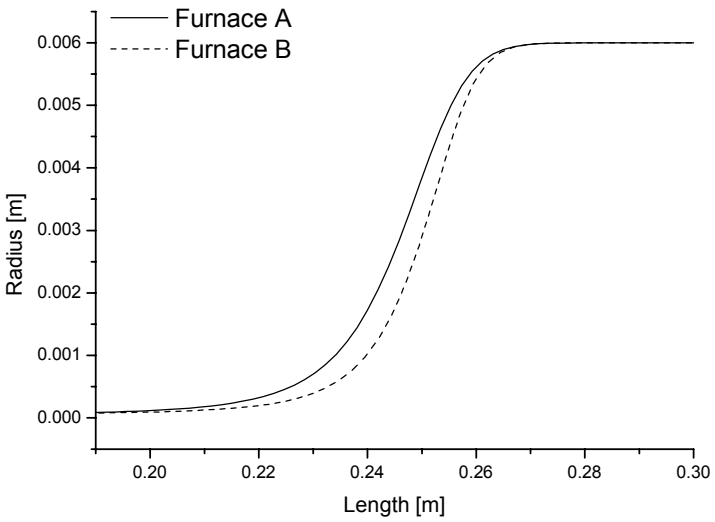

Figure 6-15. Comparison of neck-down profile for Furnaces A and B.

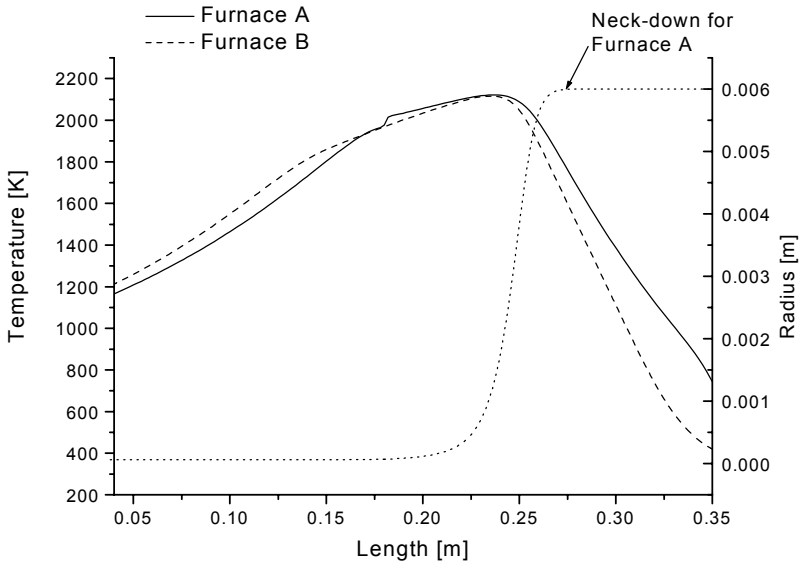

Figure 6-16. Preform and fibre core temperature along the length of Furnace A and B.

6.3.6 Air-silica structures

To study the effect of air structures, simulations were performed for two air-silica structures; an air core structure and air-silica layered structure, see Figure 6-17. A simulation was performed where a 12mm diameter preform had a 4mm diameter air core. Simulations with the air core structure showed that the effect of an air core was not very big when the results were compared to that of the solid core simulation. The draw speed was kept at 0.4 m/s. Figure 6-18 shows the temperature difference of the solid core to the air core along the length of the model. It is seen that the air core fibre cools down slower giving a temperature difference of only 2°C at the exit of furnace and about 20°C difference 14cm below the furnace. These are fairly small differences and there was no significant difference in the preform temperatures.

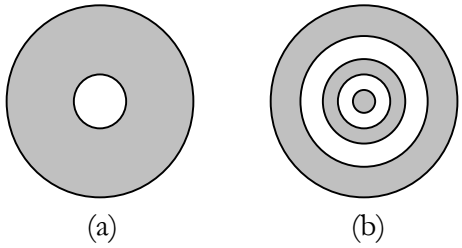

Figure 6-17. Diagram of air silica structures, (a) an air core structure and (b) air layered preform structure, shaded areas are silica.

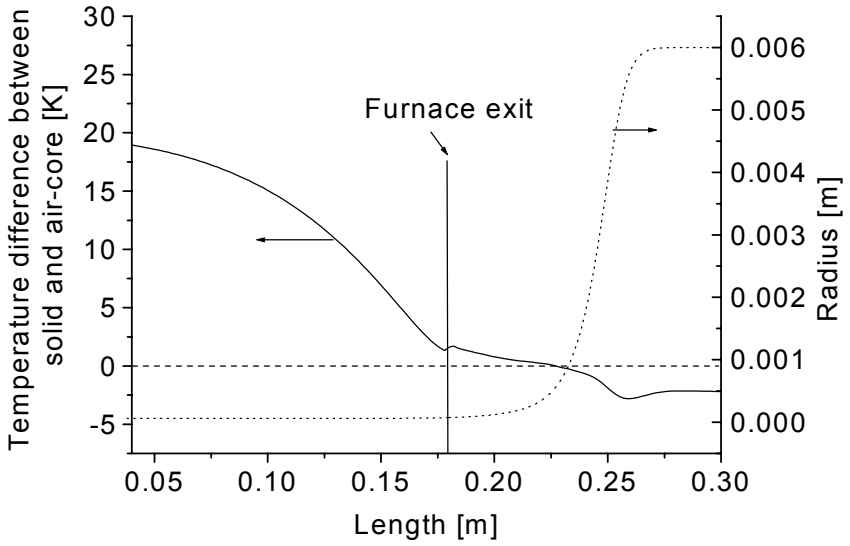

Figure 6-18. Solid core to air core temperature difference along the length of the model.

As the geometry of the model is restricted to axisymmetric structures, rings of holes were replaced by a layered air silica structure when modelling a more complicated air structure. A solid 1mm radius core was surrounded by two air layers each 1mm in thickness and separated by 1mm solid silica layer, see Figure 6-17 (b). Overall diameter was 12mm. If the holes are closely spaced a layered structure will give a fairly good estimation of the real geometry. Figure 6-19 shows the temperature contour plot of the model, where the ring structure effect can be seen as increased radial temperature gradients.

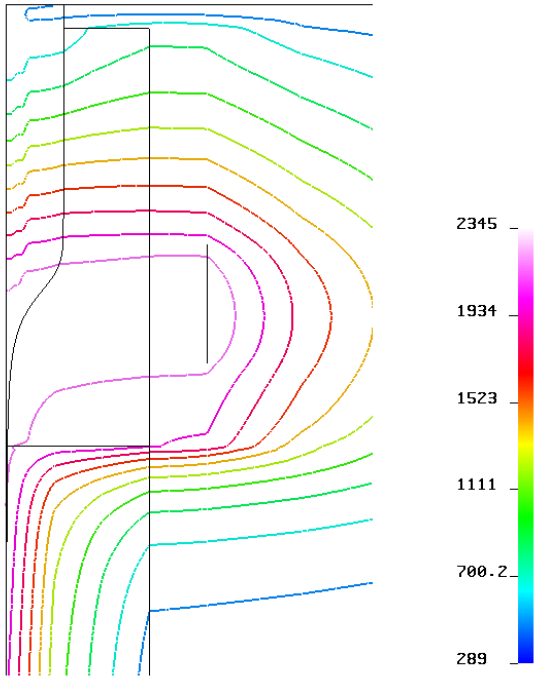

Figure 6-19. Temperature contour plot of air silica layered preform at draw speed of 3 m/s, x-axis has been scaled by 4. Temperature in K. Dimensions and axis as in Figure 6-3.

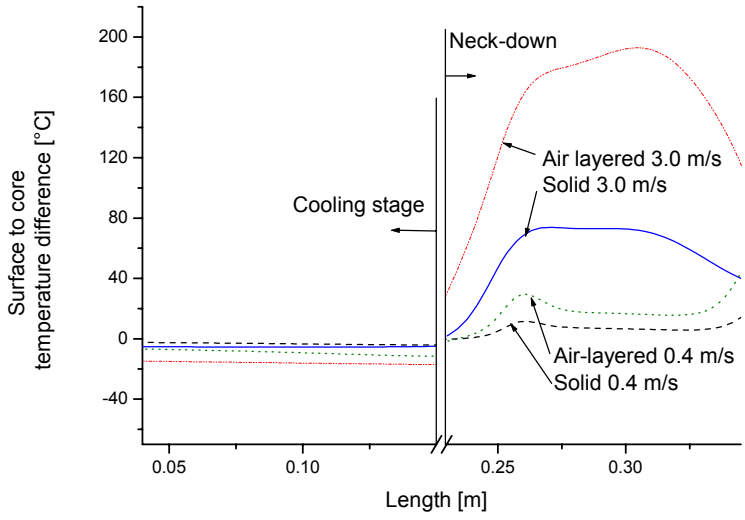

Figure 6-20. Surface to core temperature difference for solid and air layered structures.

Figure 6-20 shows the comparison between surface and core temperatures for both solid and ring structured preforms at slow, 0.4 m/s, and high, 3m/s, speeds. It is clearly seen that the air rings have an insulation effect on the core, and that at higher speeds this effect is greater. At 3 m/s the surface to core temperature difference is 190°C above the neck-down region for the ring structure and 75°C for solid structure. The fibre core is 16°C higher than the surface for the ring-structured fibre and for solid structure 5°C for draw speed of 3.0m/s. The differences are less at slower speeds.

6.3.7 Effect of air fraction on heating of microstructured polymer optical fibre preforms

During the course of the present study, heat transfer simulations for microstructured polymer optical fibre (MPOF) preforms were also conducted. Although material properties for silica, which is the focus of this work, differ greatly from those of polymer, the issues of heat transfer are similar for both. MPOFs are fabricated in a similar manner to silica PCFs in that air holes are introduced to the preform, which is then drawn down to fibre using a drawing tower. The effect of air holes on heat transfer in MPOF fabrication is as important as in silica PCF fabrication. Due to the material properties of PMMA (polymethylmethacrylate), which is typically used for MPOFs [38], the furnace temperatures are much lower (160-250°C) but draw rates can be comparable to that of specialty silica fibre. Although the findings of the study with MPOF heating might not directly apply to silica PCF heating, the underlying physics is the same and thus is of interest to the current work.

6.3.7.1 Introduction

Due to advantages such as low manufacturing cost and increased material flexibility, polymer has been recognized as a suitable material for certain PCFs [38, 233] and a number of studies have since been conducted in the area [38, 39, 234]. In order to manufacture microstructured fibres with the required optical properties, it is essential to retain the designed air-structure of the preform stage. The presence of air holes within the polymer will affect the temperature of the preform during the heating process. Heat transfer in solid polymer preforms has been studied by Reeve *et al* [235-237]. These studies provide a detailed investigation of the polymer preform heating process, however they cast no light on the effects that internal preform structures have on the heat transfer.

Preform heating is one of the most important steps in the polymer fibre fabrication process, due to the potential distortion that can be introduced when exposing the structure to high temperatures. Such heating is further complicated when internal air-structures are introduced into the preform. A two-dimensional conductive heat transfer model with surface radiation was used in simulating the transient heat transfer in MPOF preforms, with the results compared to those for a solid preform.

6.3.7.2 Model description

A 2-dimensional model was used where the preform was assumed to be infinitely long. The model allowed for an arbitrary hole pattern in the preform. The air-structure design chosen for this study was an hexagonal arrangement of holes with three rings surrounding a solid core, as shown in Figure 6-21. An infinite cylinder of polymer was assumed with an outer diameter of 50 mm and 72 air holes positioned in an hexagonal pattern. The geometries differ in that the air fraction of the air-structured section is 0.4 for Preform A, 0.7 for Preform B and 0.1 for Preform C. These differences were achieved by keeping the hole positions in the same place but varying the hole diameter from 2.0 mm (A) to 2.6 mm (B) to 1.0mm (C). Note that for comparative purposes, a 'solid case' was also simulated by assigning polymer properties to the holes, without changing either the hole geometry or the finite element meshing.

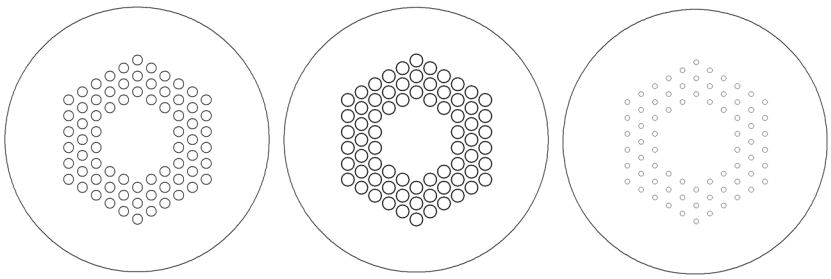

Figure 6-21. Schematics representations of the model geometry for the two-dimensional infinite cylinder with air-structured air fractions of (a) 0.4, (b) 0.7, and (c) 0.1.

Heat transfer within the preform was assumed to occur by conduction only, for which the time dependent conduction equation is expressed in Equation (45),

$$\rho c_p \frac{\partial T}{\partial t} = \nabla \cdot (k \nabla T) \tag{45}$$

The boundary condition at the surface of the preform is given by Equation (46). A constant heat transfer coefficient, h, was used while the external temperature, T_{ext}, was set to the measured furnace air temperature, 130°C. The initial temperature within the entire polymer rod was set to 24°C, that is, at the ambient value external to the furnace. Radiative heat transfer from the external surface was taken into account via a constant surface emissivity ε. Note that σ is the Stefan-Boltzmann constant. The contribution of 'internal' radiative heat transfer within the polymer rod was neglected.

$$-k \frac{\partial T}{\partial r} = h\left(T - T_{ext}\right) + \sigma\varepsilon\left(T^4 - T_{ext}^4\right) \tag{46}$$

The polymer properties were taken as those of PMMA and the gas properties as those of air. The physical properties for both are listed in Table 6-3. The thermal conductivity for PMMA was adjusted to fit the experimental results, as no measured data were available for the specific grade of PMMA material used in this study. This adjusted value is of the same order of magnitude as that reported in the literature (0.19 W/mK) for other grades of PMMA [196]. An estimated (from engineering correlations) value of 8 W/m^{2}K was used for the external heat transfer coefficient.

Table 6-3. Material properties for PMMA and air

Material	*PMMA*	*Air*
Density ρ [kg/m^3] [196]	1170	0.93
Specific heat capacity c_p [J/kgK] [196]	1380	1010
Thermal conductivity k [W/mK]	0.15	0.032
Emissivity ε [236]	0.96	-

Variable time step sizes were used - from 0.5s at the beginning where the temperature changes were the greatest, to 400s as the preform moved towards thermal equilibrium, totalling some 130 steps for a heating period of five hours. Due to the complex air hole structure, a non-uniform grid was employed. As an example, the mesh for Preform A is shown in Figure 6-22 consisting of an unstructured mesh of 6700 bilinear elements. For the axisymmetric model, a uniform structured mesh with quadrilateral elements was used consisting of 1000 elements. A typical simulation for the axisymmetric model was 55 CPU seconds on a single processor SGI Origin 2000 computer. For the 2-dimensional infinite length model case (with its larger number of elements), 300 CPU seconds were required on the same computer.

For this study, the numerical results were compared with those for an analytical solution of an infinite cylinder, with a homogeneous cross-sectional structure. The results agreed well, provided small enough time steps were used. The effects of alternative meshing were also tested by simulating a two-dimensional infinite cylinder with one air-layer using both unstructured and structured meshes. The results were found to be identical for both cases.

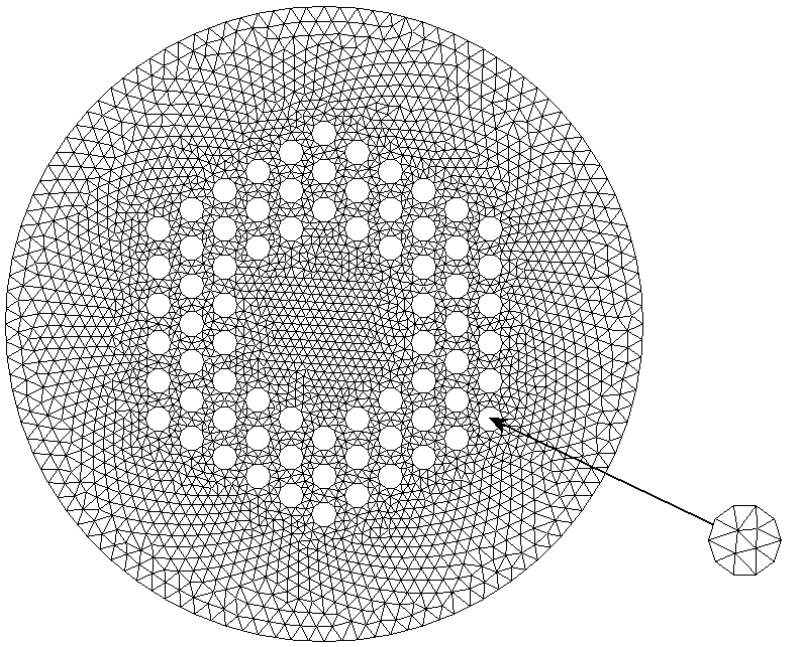

Figure 6-22. Unstructured mesh used for Preform A. The mesh used for the air holes is shown as an inset.

6.3.7.3 Results and Discussion

A temperature contour plot for Preform A after 30 minutes of heating is shown in Figure 6-23. The contours in the air-structured region show the effect of the holes on the temperature profile. The radial temperature profiles as a function of time are plotted in Figure 6-24 for both the solid cylinder case and for Preform A. Significant differences between the solid and structured cases are evident after five minutes of heating. The temperature in the outer part of the preform rises, relative to the solid case, as the air holes act as a heat barrier. Note however that the entire structured preform heats up faster than the solid case. Such behaviour was somewhat unexpected, as it was initially felt that the presence of the air holes would slow down heat transfer into the central region of the preform. The results indicate that the relatively low thermal capacity of the air (which means that the heat transfer across the holes is always essentially at pseudo steady-state) together with the fact that the structured preform contains less polymer than the solid case, resulted in a faster dynamic response in the central portion of the structured preform than expected.

Figure 6-25 shows the corresponding experimental results (Appendix IV) comparing the heating of the solid rod and the structured Preform A. The experimental data confirms the findings of the simulations in that the structured preform heats up faster than the solid preform.

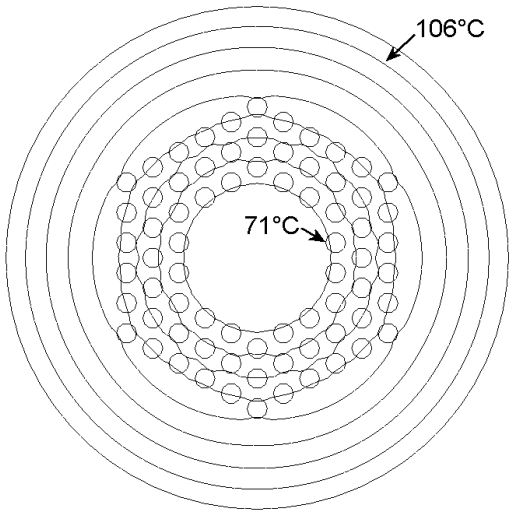

Figure 6-23. Simulated temperature contour plot for Preform A at time 30min, contour lines every 5°C.

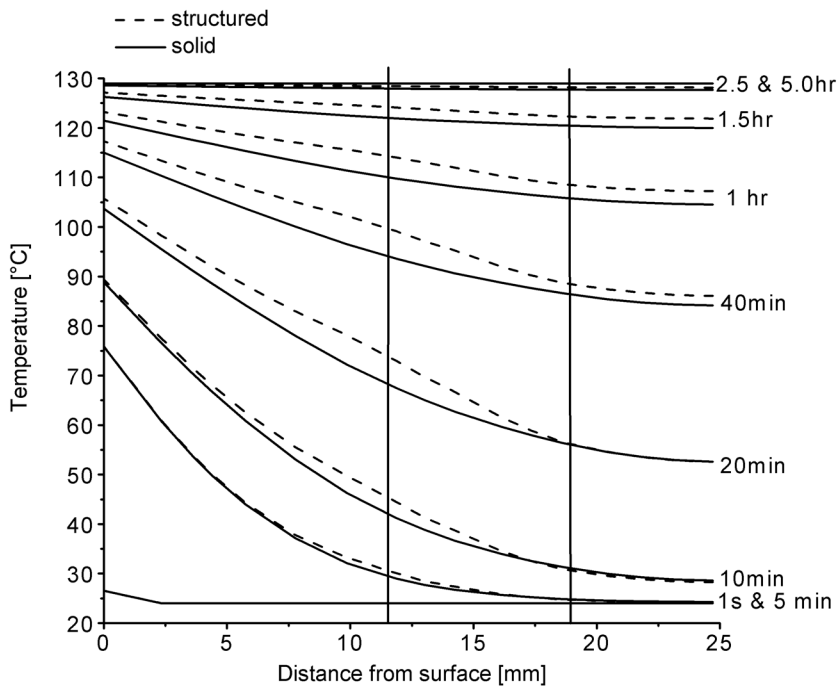

Figure 6-24. Simulated radial temperature profiles across the preform at different heating times, comparison of the solid rod and Preform A. Vertical lines show the position of the air-hole structure within the preform.

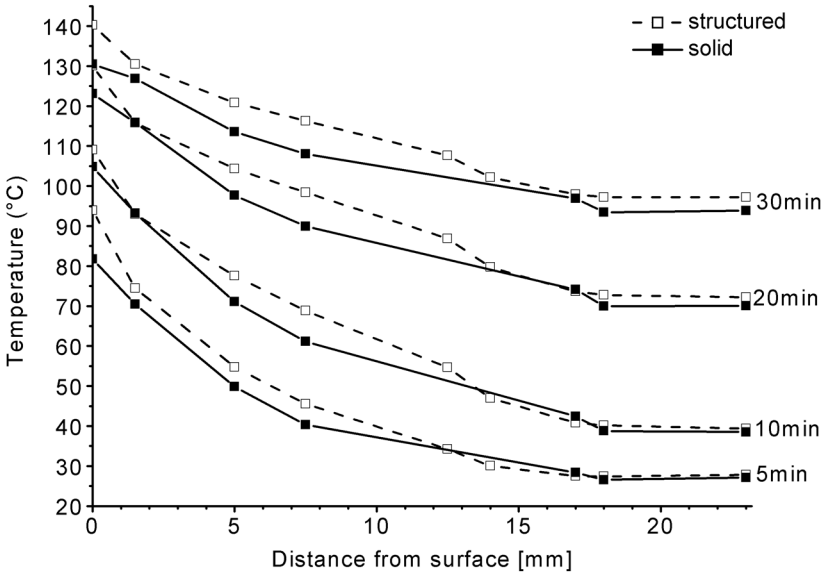

Figure 6-25. Experimental heating results. Radial temperature profiles across the preform at different heating times: comparison of the solid rod and Preform A.

Figure 6-26 shows the simulated heating-up phases for the three structured preforms and the solid case. After only five minutes, differences between the preforms start to be seen. The outer part of the preform heats up faster for all the structured preforms when compared to the solid case, such that a higher air fraction results in faster heating. The centre of the preform heats up faster than the solid case for all the structured preforms except for Preform C which had the lowest air fraction. After 20 minutes heating, the centre of Preform C is 1°C lower than the solid case. This result indicates that there exists an air fraction below which the effect of greater thermal resistance of the air structure exceeds the effect of lower thermal mass and results in slower heating of the preform centre.

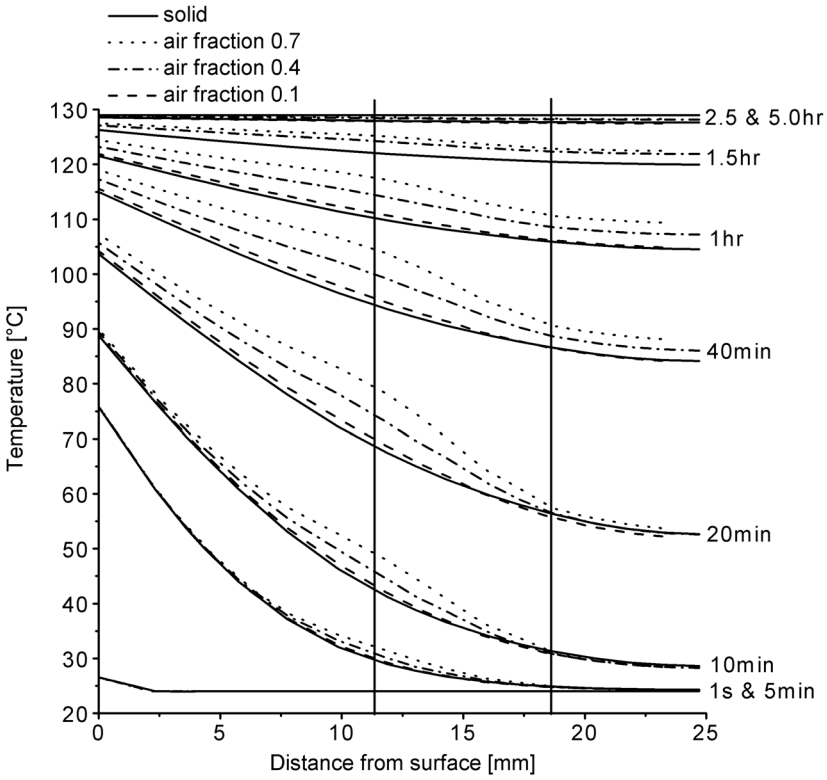

Figure 6-26. Radial temperature profiles at different heating times, comparison of the air-structured Preforms A, B, and C with air fractions 0.4, 0.7, and 0.1, respectively.

Both the solid and the structured preforms reached the furnace temperature after about 2.5hr of heating. This is a relatively long time in production terms and illustrates the basic problem with this type of heating where the outer part of the preform will reach the fibre draw temperature before the central part. This situation can result in deformation of the structure with the hotter outer part drawing at a different rate to the cooler inner part. In order to minimise such potential problems, alternative heating schemes can be employed to provide uniform, symmetric heating. Other types of heating methods such as infrared or microwave heating may be advantageous.

It can be concluded that depending on the air fraction of the structured preform its centre can heat up either faster or slower than the centre of a solid preform. At higher air fractions (here 0.4 and 0.7) the structured preform heated up faster than the solid preform due to the effect of reduced thermal mass being greater than the effect of the thermal resistance of the air holes. At a lower air fraction (here 0.1) the centre of the preform heated up more slowly than the solid preform centre.

The hexagonal hole pattern used distorted the temperature profile only slightly compared with the radially symmetric case. This distortion was greater for the higher air fraction, indicating that preforms with highly asymmetric hole structures and a high air fraction could experience radially asymmetric temperature profiles. In order to produce structured optical fibres with undistorted structures the heating process must be optimised so that any asymmetries are minimised. A heat transfer model such as that used in this study can be used both in optimising the preform heating conditions and also as a tool in designing the heating furnace.

6.3.8 Effect of air-fraction - comparison simulation with silica

To verify that the above results apply also to the heating of a silica preform, comparative simulations were performed. The air-structure chosen was that of Preform A. The model used was identical to the case presented above for polymer in both construction of the mesh, selection of equations and the type of boundary and initial conditions. The material parameters were chosen for silica and can be found in Appendix III. The furnace temperature (T_{exp}) was set at 1900°C.

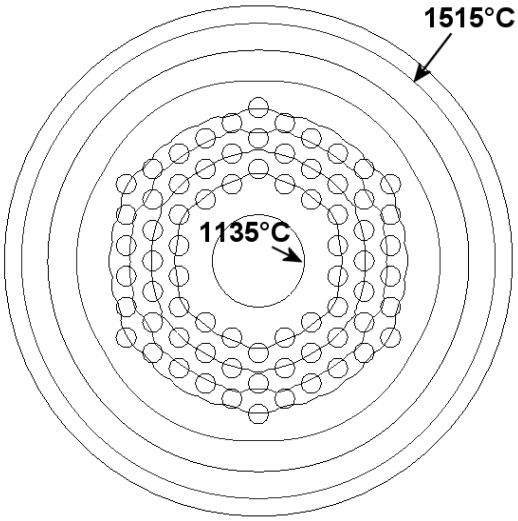

Figure 6-27. Simulated temperature contour plot for silica material with geometry of Preform A heated for 6.6min, with contour lines every 55°C. Radiation is not included. External temperature was set at 1900°C.

Figure 6-27 shows a simulated temperature contour plot when the structured preform has been heated up for 6.6min. The air holes cause a similar distortion of the temperature contours (compared to the solid case where they are axisymmetric) as was seen in the case of structured polymer preform heating in Figure 6-23. Figure 6-23 is the polymer equivalent of Figure 6-27. The simulations show that silica heats up much faster than polymer. In the above case after just 6.6min the temperature difference between the core and the preform surface is about 25% of the external temperature. As seen in Figure 6-23 a difference with similar magnitude is achieved after 30min of heating for polymer. This is more clearly seen in Figure 6-28 where it takes only 28min to reach equilibrium temperature in the case of the structured silica preform heating, whereas the structured polymer preform takes at least 2.5hr.

The effect of radiation heat transfer was studied by simulating two cases; one with ideal radiation (emissivity 0.9) and the other without radiation heat transfer. Figure 6-28 shows the surface and the core temperatures during heating up. With radiation transfer included the preform heats up much faster and reaches equilibrium temperature after approximately 15min of heating. The case including radiation is expected to be closer to reality.

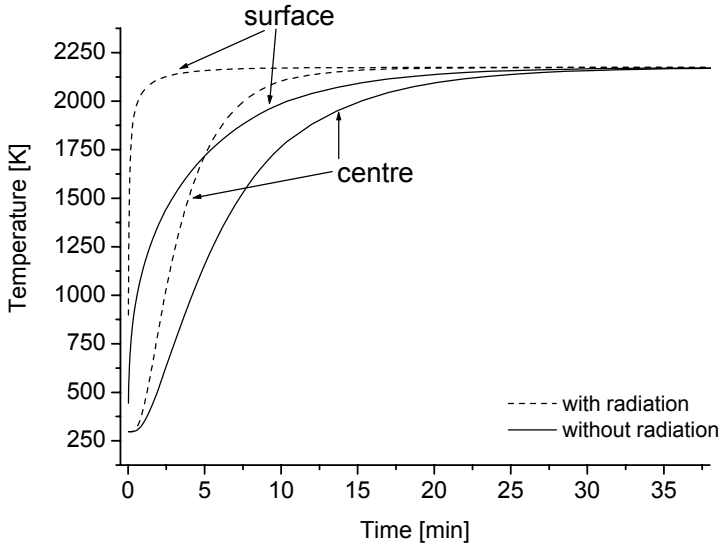

Figure 6-28. Simulated temperature during heating up of a structured silica preform comparing simulations with and without radiation heat transfer. Heating curves shown at the surface and centre of the preform.

To compare the solid preform heating to a structured preform, simulations were also done for a solid rod. The comparison is presented in Figure 6-29. Similar to the polymer case, the structured preform (Preform A) heats up faster than the solid rod. (Figure 6-24 is the polymer equivalent of Figure 6-29.) This confirms that although silica heats up much faster than polymer the effect of air holes in the structure is similar. The radial temperature profiles for the simulations with radiation effects included are presented in Figure 6-30. The results are similar, with the exception of faster heating at the preform surface. The overall heating was also faster.

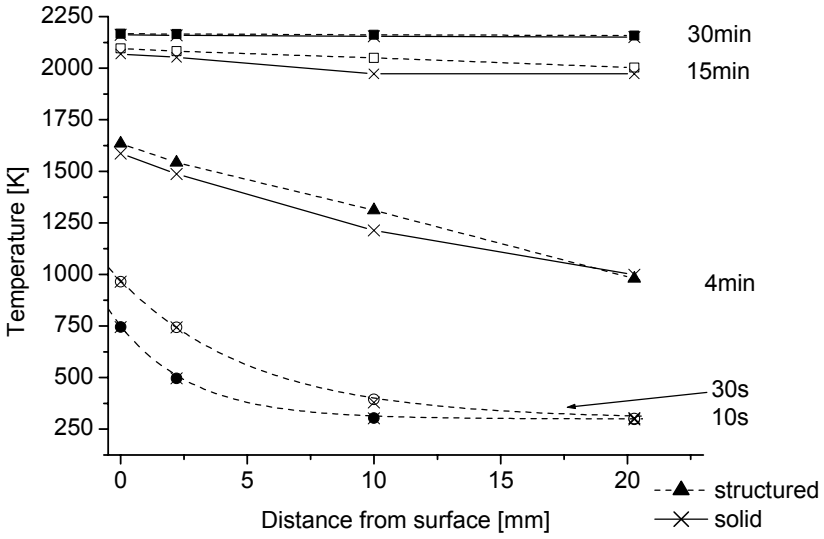

Figure 6-29. Simulated radial temperature profiles across the silica preform at different heating times. The solid rod and Preform A are compared. Radiation is not included. Structured preform is shown with dashed line and solid case with solid line. At times 30s and 10s the solid case is identical to the structure case.

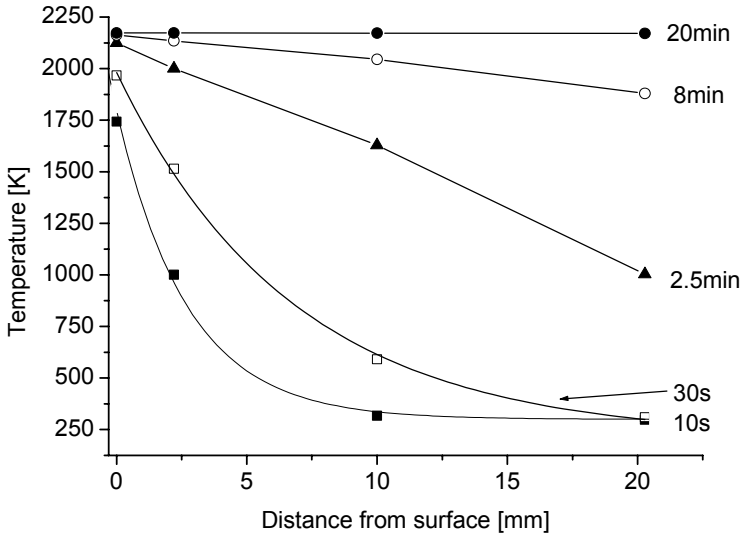

Figure 6-30. Simulated radial temperature profiles across the structured silica preform (Preform A) at different heating times. Radiation included.

6.4 Simulations of Ge diffusion in silica

6.4.1 Diffusion computations

In order to estimate dopant diffusion during drawing, a program was written to solve the diffusion equation. Diffusion was assumed to occur according to Fick's law, Equation (47) [121]. The diffusion coefficient was assumed to be independent of

concentration but dependent on temperature according to the Arrhenius equation, Equation (48). The fibre profiles studied were circularly symmetric and diffusion was assumed to happen in the radial direction only. As the diffusion coefficient is dependent on temperature, the variation in temperature along the preform, neck-down and fibre had to be taken into account.

The 1-dimension, cylindrical, diffusion equation is presented in Equation (47).

$$\frac{\partial c}{\partial t} = D\left(\frac{1}{r}\frac{\partial c}{\partial r} + \frac{\partial^2 c}{\partial r^2}\right) \tag{47}$$

where D is the diffusion coefficient [m^2/s], c is dopant concentration [mole-fraction], r is radius [m] and t is time [s].

$$D = D_O \exp\left(-\frac{E}{RT}\right) \tag{48}$$

where T is temperature [K], D_O is pre-exponential term [m^2/s], E is activation energy [J/mol] and R is the gas constant [J/(molK)].

The differential diffusion equation was converted into an approximate finite-difference equation and solved numerically (Appendix V). Depending on the case, the temperature was either assumed constant or varied according to the appropriate heat transfer situation for the current simulation. When diffusion was simulated for the entire length of the furnace, from preform to fibre, the temperature distribution was obtained from the heat and mass transfer simulations described in Section 6.3. In this case, the geometry was divided into finite lengths along the z-axis (longitudinal) for which the glass velocity and radius of the glass was taken from the heat transfer simulations and used in the calculation of the computational parameters for the diffusion program. Diffusion was then computed at each position and the calculated profile read in as the initial profile for the next z-position.

When the diffusion coefficients are known for the dopants, the expected diffusion can be simulated using thermal history data. The calculation of diffusion coefficient for

germanium in silica from the draw experiments is presented below. The derived value is then used for various draw conditions using the data from the heat transfer simulations, Section 6.3. The diffusion results are then used to demonstrate the effect on dispersion of a dispersion compensating fibre. Since only germanium diffusion has been simulated, a discussion on diffusion of other dopants based on literature values is given in the light of the present findings.

6.4.2 Calculating the diffusion coefficient for germanium from experiment

To determine the diffusion coefficient for germanium in silica, the experimental results from the 3-ring Ge-doped fibre (3R) draw were used (Section 4.3.3). As the diffusion coefficient depends on temperature, diffusion data for a number of temperatures would be required in order to determine both the pre-exponential diffusion coefficient, D_0 and the activation energy, E. As the draws were only performed at two furnace temperatures, and at the low temperature no significant diffusion occurred, only the pre-exponential diffusion coefficient was derived and an activation energy of 310 kJ/mol was taken from the literature [137]. The longitudinal temperature, velocity and radius profiles from the heat transfer simulations, Section 6.36.2, were produced using parameters from the experimental draw conditions and used in the diffusion simulations. The preform initial GeO_2 concentration profile for the simulations was taken from preform microanalysis measurements. The innermost ring in the 3-ring structure was used to determine the pre-exponential diffusion coefficient D_0.

Figure 6-27 shows the measured fibre GeO_2 molar concentration profile against the initial and simulated profile for diffused fibre. The best fit was found using coefficient D_0 of $2.4\times10^{-6}m^2/s$, which agrees with the coefficient determined by Yamada and Hanafusa [137]. The effect of different D_0 values on the diffused profile is shown in Figure 6-32. An error of about $\pm0.1\times10^{-6}m^2/s$ can be estimated for the calculations, although the error of the temperature profile and the neck-down shape simulations is very difficult to establish. Using the determined value for D_0, simulations were also performed for the fibre drawn at 1800°C and are shown in Figure 6-33. There is hardly any diffusion observed at this temperature as also shown in the simulation.

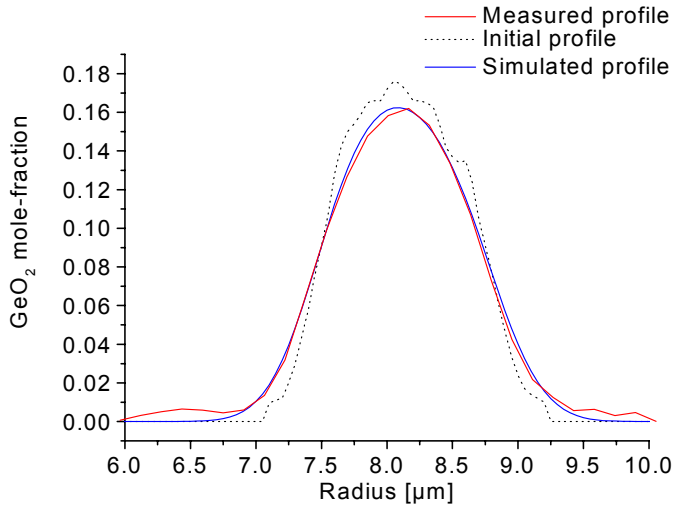

Figure 6-31. Measured, initial and simulated profile for the innermost ring of 3R fibre drawn at 2100°C and 10m/min draw speed.

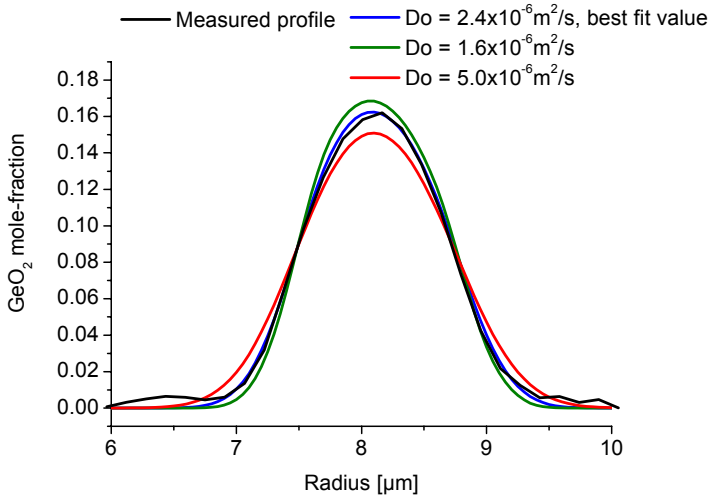

Figure 6-32. Simulated profile at different values of the pre-exponential coefficient Do.

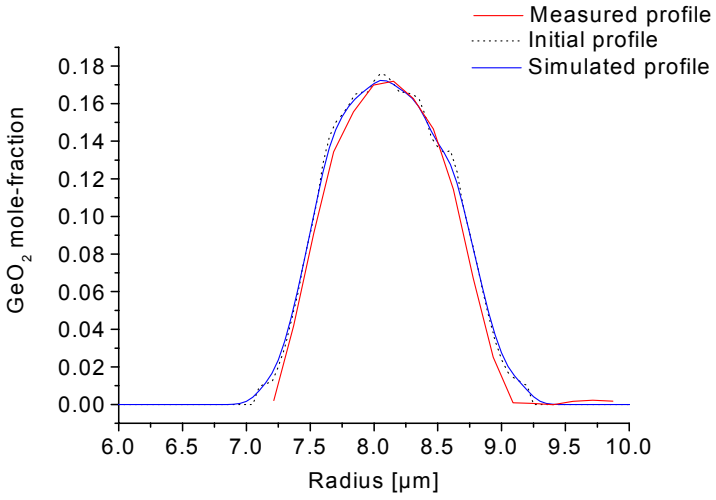

Figure 6-33. Measured, initial and simulated profile for the innermost ring of 3R fibre drawn at 1800°C and 10m/min draw speed.

Diffusion simulations were also made for the Ge-doped single ring fibre profile (1R). Figure 6-34 shows the comparison between the measured and simulated profile. There is some discrepancy on the shape of the profile. This was noticed when the measured preform profile (corresponding to initial profile here) was compared with the etched fibre profile (Section 4.3.2) and is probably due to the high etchant concentration, where the exact relation of etching depth to germania concentration could not be determined. The amount of diffusion however correlates well with the simulated result.

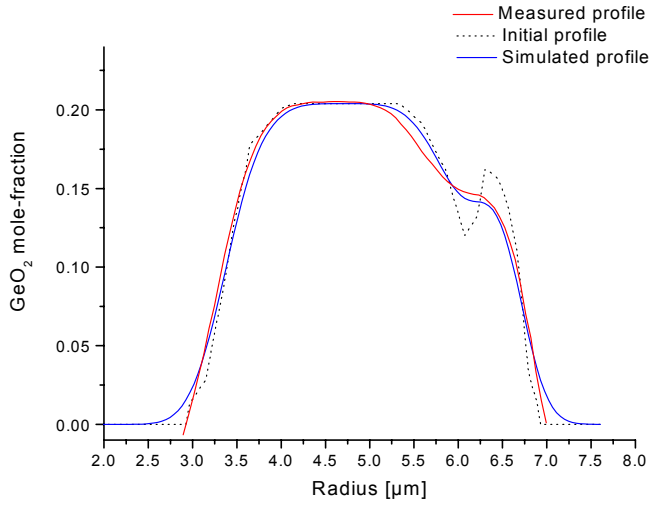

Figure 6-34. Measured, initial and simulated profile of 1R fibre drawn at 2100°C and 10m/min draw speed.

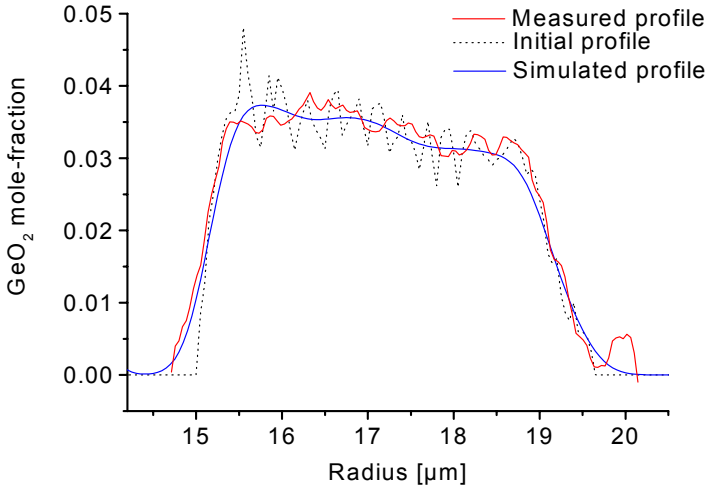

Figure 6-35. Measured, initial and simulated profile for the outermost ring of 3R fibre drawn at 2100°C and 10m/min draw speed.

When diffusion simulations were compared to the outermost ring of the 3R fibre, an interesting point was noticed. In the high temperature samples the measured profile showed features from the preform that were diffused according to the simulations, see Figure 6-35. The initial profile shows the MCVD layer structure where the number of Ge concentration peaks corresponds to the number of MCVD layers in the ring. This structure is still seen in the measured fibre profile although not as distinctive. The computed profile is smooth due to the resulting dopant diffusion. There are three possible explanations for this; (i) there is a high enough temperature gradient radially in the preform and fibre to cause different diffusion rates, (ii) an impurity from the cladding tube has diffused into the outer ring and affected Ge diffusion or (iii) the diffusion coefficient depends on GeO_2 concentration.

Since the outer layer is less diffused, this means that the temperature should be lower in the outer part of the fibre at a given axial position. This can only be possible during draw when the fibre is cooling down, since the surface cools down first. In the heating phase, the surface is always hotter than the core due to the heating technique used. During cooling the centre of the fibre would stay hotter longer than the outer surface causing more diffusion in the centre. Diffusion simulations were done to calculate the required temperature difference between the layers to cause the diffusion differences. This temperature gradient was held for the entire length of the drawn fibre giving a conservative estimate of the temperature difference required. A 150°C temperature difference was found to be necessary to cause the reduced diffusion. Since the inner and outermost layers are just 6μm apart (10% of cladding radius), the temperature gradient should be much larger across the fibre. Heat transfer simulations also show that at a 10m/min draw speed, the differences between surface and core temperature are only a few degrees. It therefore seems unlikely that different radial cooling rates could have caused the reduced diffusion.

Impurity diffusion from the cladding tube is possible as very high temperature and slow drawing speed were used. It is known that diffusion of impurities such as Na [150] is much higher than dopant diffusion. It is also possible that diffusion of such impurities would not have reached the inner-most core. Studies from Kirchhof *et al* [135, 149] show however, that all co-dopants caused higher diffusion rates for germania. This would speak against the hypothesis of the impurity diffusion effect.

It seems most likely that the reduced diffusion in the outer layer is due to the diffusion coefficient being concentration dependent. At lower germanium concentration the diffusion coefficient would be lower resulting in a less diffused profile as observed in the experiments. To verify this a number of experiments would be required, where for example fibres with different Ge concentrations are heated at various temperatures and the diffusion measured. This will be left for future studies. In the following diffusion simulations the diffusion coefficient is assumed independent of concentrations and coefficients for Arrhenius equation are those that matched the experiments at 20-30mol% GeO_2 concentrations.

6.4.3 Diffusion along the neck-down

In order to determine where most of the diffusion occurs in the neck-down region, diffusion was calculated at three positions along the neck-down. Figure 6-36 shows the resulting dopant profiles scaled to fibre dimension for neck-down diameters 17, 8 and 2mm, where 17mm is the preform diameter. For each position the initial profile was assumed to be that of a step-index core and only diffusion at that position was taken into account. Temperature was assumed to be 2000°C and fibre draw speed 10m/min. The differences in speed resulting from the neck-down process were calculated for fixed fibre draw speed. Although the preform is exposed to the high temperature longer than other parts of the neck-down the diffusion is insignificant due to the long radial distance. However, significant change to the profile can be seen in the 8 and 2mm neck-down positions.

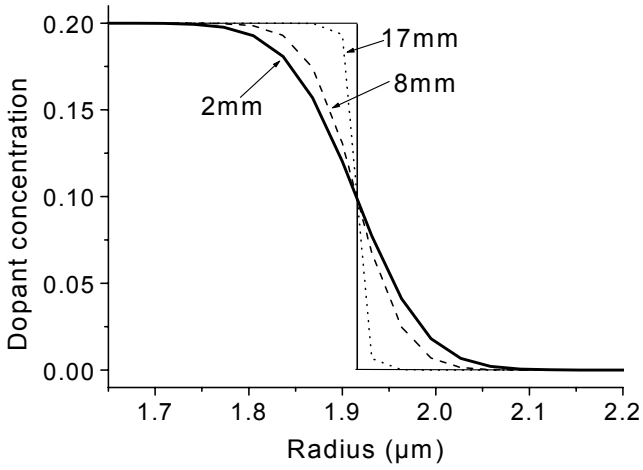

Figure 6-36. Diffusion of Ge (simulation) during the neck-down for draw speed 10m/min and draw temperature 2000°C.

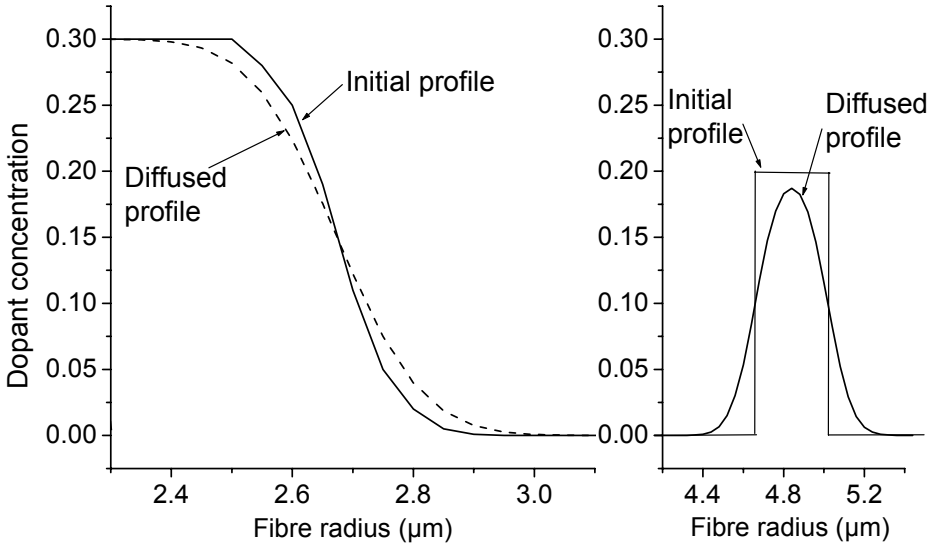

Figure 6-37. (a) Diffusion of Ge (simulation) during fibre drawing stage after neck-down for ~5.4μm diameter doped core, (b) diffusion in a 0.5μm narrow doped ring for similar conditions

Figure 6-37 shows the diffusion simulation result for a fibre with a ~3μm radius core. The diffusion was calculated for a fibre only. The initial profile was chosen to represent the already diffused profile to reflect the diffusion from the neck-down. Slight broadening of the profile is observed and it can be concluded that most of the diffusion occurs in the neck-down region of the fibre draw and cannot be omitted when estimating diffusion.

6.4.4 Effect of different draw conditions on germanium diffusion

The effect of various draw conditions on diffusion was studied for a step index profile using the thermal history data computed in Sections 6.3.1 to 6.3.5. A high NA fibre design was chosen to maximise the diffusion effect. The GeO_2 concentration of the core was taken as 35 mol% and core diameter 3μm chosen. This design is applicable in high NA Ge-doped fibres where high non-linearities are required.

The diffusion at different furnace temperature and draw speeds is shown in Figure 6-38 and Figure 6-39. The parameter range is typical for specialty fibre drawing thus the resulting diffusion would represent the maximum change expected during draw. As expected higher furnace temperature and slower speed increase the degree of diffusion. The relative effects of change in draw speed and temperature are comparable in magnitude. In order to minimise diffusion, the fibres should be drawn at lower

temperatures and higher speeds. Frequently fibres are drawn at a specific tension, which is kept constant from draw to draw. This is good practice since it gives more accurate measurement of glass temperature than the furnace element temperature. It must be noted however that diffusion is also affected by the neck-down shape and drawing speed and thus tension may not be an appropriate indication for diffusion at least on its own. To demonstrate that it may be possible to have more diffusion at higher tension two simulation results are shown in Figure 6-40. The fibre which has been drawn at higher tension diffuses more. Note that different maximum glass temperature and draw speed were used for each simulation. The increased diffusion in the higher tension draw results from the significantly smaller draw speed which increases exposure time of the preform and fibre in the hot-zone.

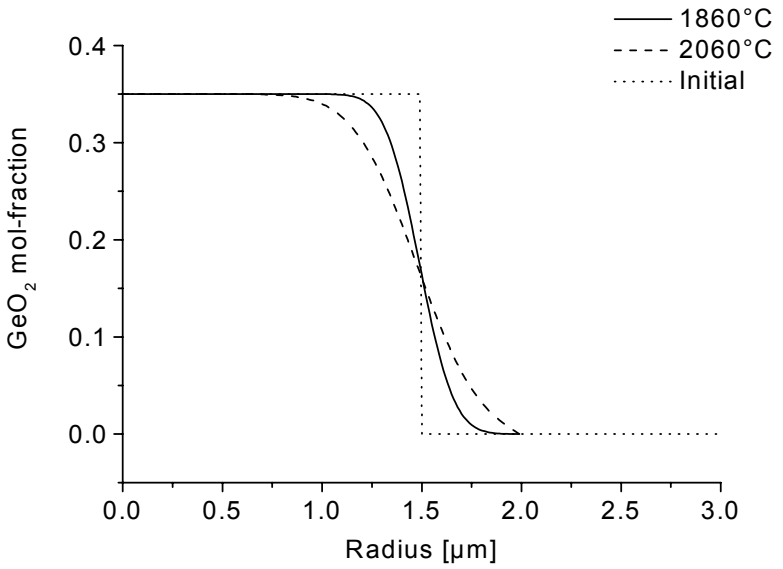

Figure 6-38. The effect of drawing temperature (simulated) on Ge-diffusion in a high NA fibre.

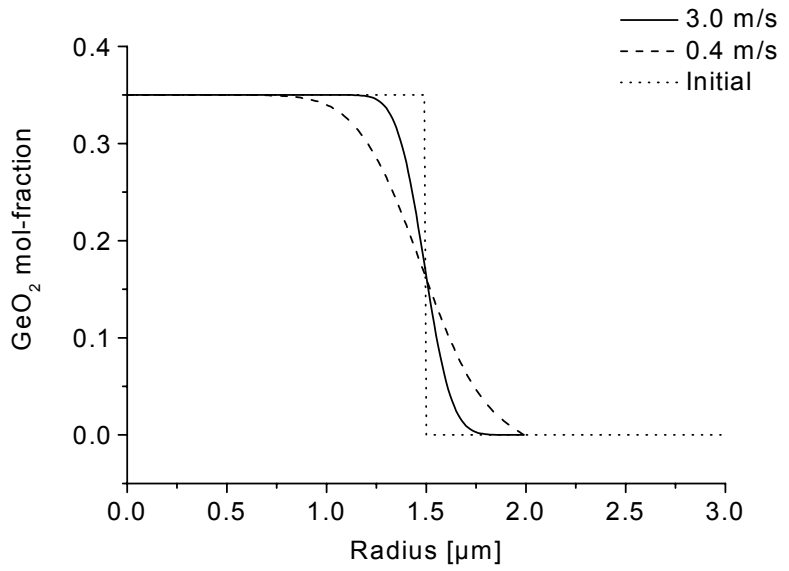

Figure 6-39. The effect of draw speed on Ge-diffusion (simulated).

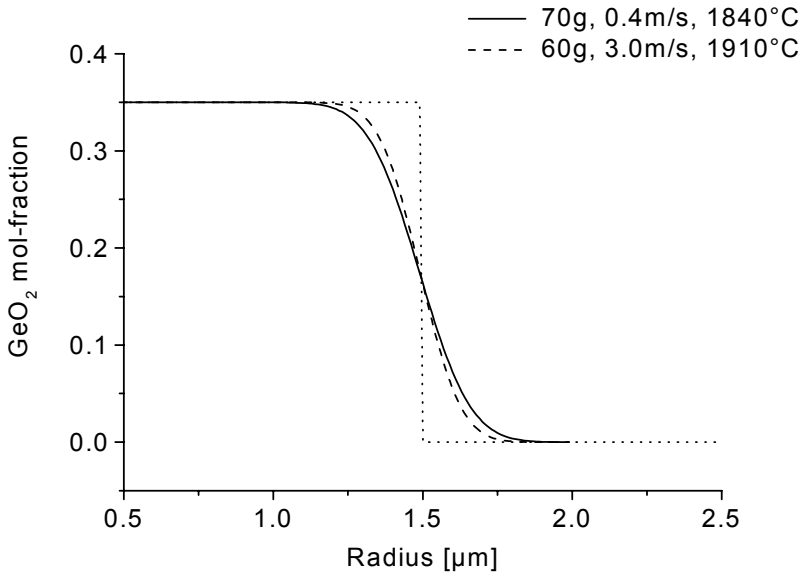

Figure 6-40. Example of a case (simulated) where higher tension resulted in increased diffusion.

The effect of preform diameter on diffusion is shown in Figure 6-41. The draw speed (0.4m/s) and the maximum glass temperature were kept constant (1980°C). Due to changed preform diameter the corresponding preform feed rate was decreased for the larger preform and the temperature profile changed accordingly, Figure 6-13. The temperature profile in the neck-down region, where most diffusion occurs, is very similar and no significant differences in diffusion are found.

It was shown in Section 6.3.5 that furnace design had a significant effect on the temperature profiles of the preform and fibre. Diffusion simulations for fibres drawn in the different furnaces are shown in Figure 6-42. Furnace temperature, draw speed and preform and fibre diameter were same for both cases. The fibre drawn in Furnace A diffused more. This is explained by the longer hot-zone of Furnace A which alters the temperature profile along the neck-down to enhance diffusion, Section 6.4.3.

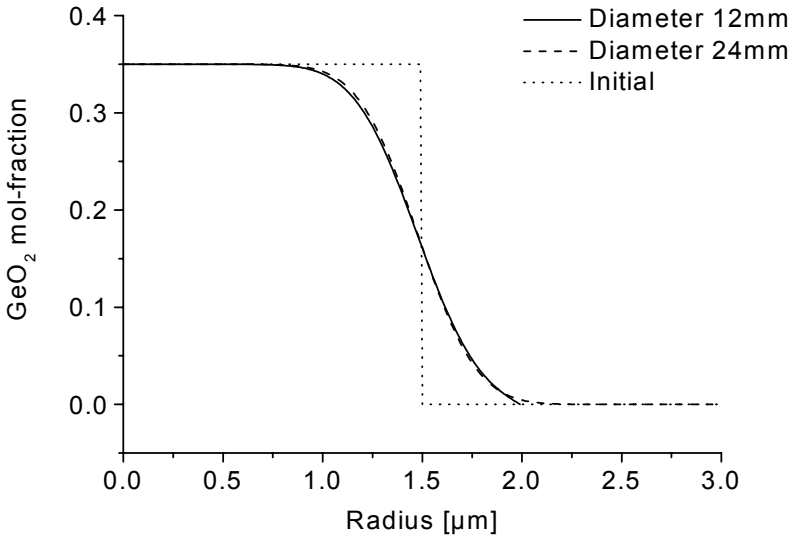

Figure 6-41. Effect of preform diameter (simulated) on Ge-diffusion in fibre drawing.

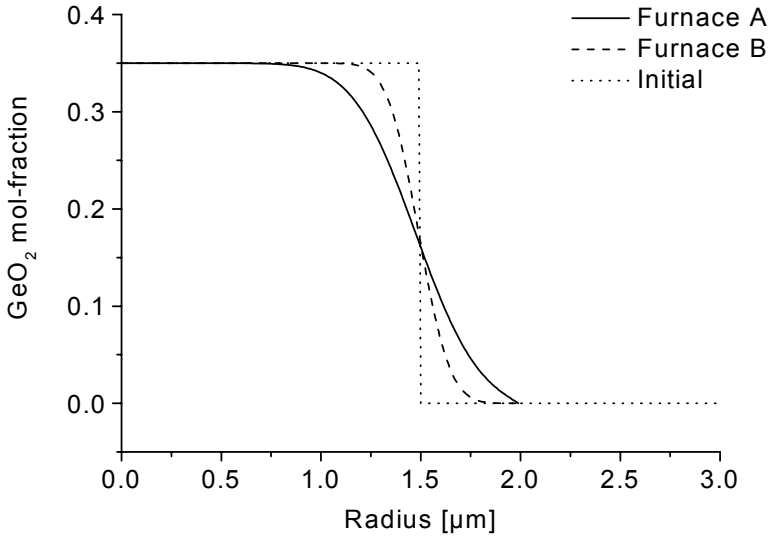

Figure 6-42. Effect of furnace geometry (simulated) on Ge-diffusion in fibre drawing

6.4.5 An example of diffusion effect on dispersion

As an example to illustrate how dopant diffusion during drawing can affect the optical properties of the fibre, dopant diffusion was simulated for a NZ-DSF resembling Corning's LEAF fibre. LEAF fibre is designed to give large effective area (~72μm^2) by introducing a ring with increased RI surrounding the core. The large effective area reduces significantly the non-linearity of the fibre. The concentration profile was simplified and assumed to be a binary mixture of SiO_2 and GeO_2. The draw conditions were chosen to enhance the degree of diffusion. Draw temperature of 2050°C, draw speed 10m/min, preform diameter 16mm and fibre diameter 125μm were used. Figure 6-43 shows the profile before (scaled to fibre dimensions) and after draw.

The dispersion was then simulated for both of the profiles, see Figure 6-44. The computational technique used is described in Ref. [238]. There is about 10% change in dispersion for the diffused fibre, and the dispersion slope is only slightly modified. The zero dispersion wavelength is shifted from 1458nm to 1451nm. The difference is insignificant for this type of fibre. However, it can be seen that dopant diffusion will reduce the peak RI of both the core and the ring. For a highly doped non-linear dispersion shifted fibre with high dopant level and small effective area the diffusion effects would be further enhanced. In addition to this for these types of fibre (w-type) both change in the RI of the RI-increased and the RI-reduced ring and their ratio will significantly affect the dispersion properties [239].

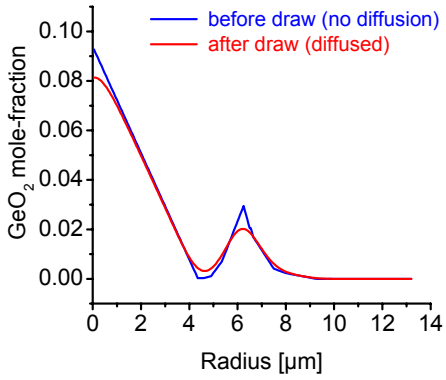

Figure 6-43. Simulated diffusion effect on the dopant concentration profile of a NZ-DSF.

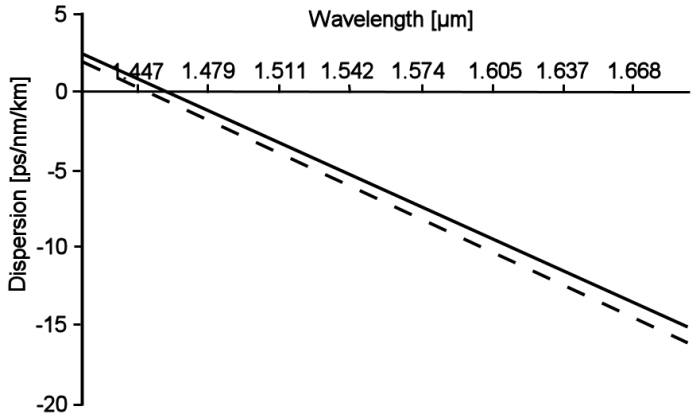

Figure 6-44. Simulated diffusion effect on the dispersion of a NZ-DSF. Solid line is before the draw and broken like after the draw.

6.4.6 Diffusion of other dopants in silica

The focus of the diffusion simulations was on germanium diffusion in silica as it could be verified experimentally. The findings however also apply to other dopants and even impurity diffusion during drawing, although the magnitude of diffusion will depend on the particular diffusion parameters for that element. To summarise the diffusion effects of other dopants compared to that of germanium, Figure 6-45 shows the Arrhenius plot for various elements in silica found in literature. These values are also given in Section 4.1.3. Within the temperature range typically used for drawing it can be said that boron diffusion would most likely show very similar behaviour for germanium. According to Ref. [127], phosphorus would not diffuse as readily and fluorine diffuses faster at drawing temperatures and this was also confirmed experimentally. If the activation energy in the Arrhenius equation is very different in the range of drawing temperatures, it is possible the relative importance of draw parameters to diffusion is changed.

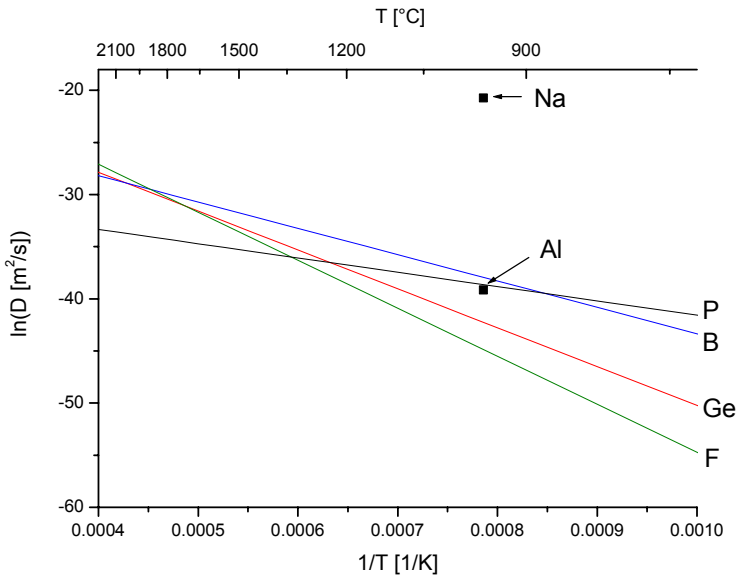

Figure 6-45. Arrhenius plot for dopant diffusion in silica reported in literature, Na, Al [150], Ge,B [137], P [127], F [146] .

6.5 Discussion

A detailed numerical study of the transport phenomena in the fibre drawing process has been conducted. The heat transfer simulations showed that drawing parameters, preform structure and external factors such as furnace design affect the heat transfer and the resulting neck-down shape and temperature distribution in the preform and fibre. It was found that the draw speed and preform diameter had significant effects on radial and longitudinal temperature distributions, while change in the hot-zone temperature did not alter the shape of the longitudinal temperature profile and affected the radial surface-to-core temperature difference only slightly.

As the furnace structure was included in the model, different structural designs could be compared. It was found that the furnace structure had major effects on both longitudinal and radial temperature distributions in the preform and fibre. The effect of a GeO_2 doped core was found not to be significant and a similar size air core had only a slight effect on the temperature distribution. An air-silica layered structure, however, produced a different temperature distribution, where the air layers acted as insulators. It was also shown that depending on the air-fraction of an air-structured MPOF preform the preform heated either slower or faster than a solid preform, indicating the importance of the air-structure in heating schemes. Comparison simulations with a preform with an air-silica structure produced similar results except that the heating up was about five times faster compared to MPOF.

The results from the heat transfer simulations have been used to compute germanium diffusion during drawing. First the pre-exponential diffusion coefficient, D_0, for germania in silica was determined from the experimental results using an activation energy of 310 kJ/mol taken from the literature [137]. It was found that this agreed with the value found by Yamada and Hanafusa [137] being 2.4×10^{-6} m^2/s. It is also possible that the diffusion coefficient for germanium depends on concentration; however further studies are required to verify this.

Diffusion was found to occur mostly in the neck-down region of the drawing process, although in the simulation some of the diffusion also occurred in the fibre. Furnace temperature and draw speed had comparable effects on diffusion, in that hotter temperatures and slower speeds resulted in greater degree of diffusion. The diameter of the preform was found not to affect diffusion significantly at slow speeds. The furnace structure was found to affect the magnitude of diffusion possibly due to a changed longitudinal temperature profile. To minimise diffusion low temperatures and high speeds should be used. This was also verified experimentally (see Chapter 4).

The above general results also apply to other dopants in silica, however if the diffusion parameters are very different the relative importance of draw parameters could be different. It is also noted that since dopants have different diffusion characteristics and co-doping often affects these [135, 149] useful alteration of index profiles during drawing can be achieved by using several dopants to create the index profile. Once the diffusion characteristics are known for each species, simulations such as those carried out in this work can be made to determine optimal drawing conditions. It was also demonstrated how diffusion during drawing can alter the optical properties of the fibre such as dispersion. Although the altered dispersion characteristics were insignificant for the application of the NZ-DSF fibre (LEAF), non-linear fibres with small core size and high dopant concentration are expected to be more sensitive to such profile change.

It is concluded that computational fluid dynamics provides a useful tool for investigating the complex heat and mass transfer processes during the specialty optical fibre fabrication process and that subsequent results give insight into the means by which optical properties can be changed during fibre drawing.

CHAPTER 7 CONCLUSIONS AND FURTHER WORK

In this thesis changes during drawing in geometry of two different types of optical fibre have been studied, namely doped silica fibres and PCFs. In the more conventional silica optical fibres changes in dopant profile were investigated in germanium and fluorine doped silica preforms. Dopant mobility was studied by drawing preforms with different drawing conditions and analysing the dopant profiles before and after draw. Geometry control during drawing of PCFs was studied experimentally by drawing PCF preforms under different drawing conditions. The change in air-silica structural geometry was measured and related to the draw parameters. Numerical heat and mass transfer computations were used to complement the experimental studies. The effects of the different drawing parameters on diffusion were simulated for the doped preforms and the effects of the air-structure on heat transfer were studied in the case of PCF fabrication.

7.1 Dopant diffusion during fibre drawing

The experimental results showed that a change in dopant profile was induced in both germanium and fluorine doped fibres during drawing. Not surprisingly, the change was more noticeable at higher temperatures and at lower drawing speeds. Germanium diffusion during drawing has been observed in the past by Hersener *et al* [6], however claims that germanium does not diffuse during drawing have been published by Pugh *et al* [9] in a more recent study. Insuffucient details of the drawing conditions were given in either of these two studies to make further comparison with the findings in this thesis.

Theoretical dopant diffusion computations were performed and agreed well with the experimental germanium and refractive index profiles of a 17mol% GeO_2-doped ring in a multi-ring structured fibre. Germanium diffusivity was calculated based on this sample and is in agreement with measurements obtained by Yamada and Hanafusa [137]. Rings with lower concentration of GeO_2 (8 and 4mol%) appeared to be less diffused than estimated by the computations. This could be due to a concentration dependent diffusion coefficient or a greater radial temperature gradient of the preform and fibre during drawing than was computed with the heat transfer calculations.

Fluorine diffusion was studied experimentally by drawing pure silica core multimode fibre with a fluorine-doped cladding. Results showed qualitatively that fluorine in the cladding appeared to migrate both into the pure silica core and outwards towards the cladding outer surface and be removed from the fibre at the surface. Quantitative results were not obtained as the reaction order for etching of fluorine doped silica was not available. The results however showed that both drawing temperature and preform feed rate had significant and comparable effects on fluorine diffusion, as predicted by the simulations for germanium dopant diffusion.

The effects of different drawing parameters on diffusion were studied using numerical heat and mass transfer simulations and the diffusion coefficient determined for germanium in silica. The diffusion was found to occur mostly in the neck-down region. It was found that the extent of diffusion was governed both by temperature and preform feed speed, where hotter temperatures and slower feed speeds resulted in more diffusion. Preform diameter did not significantly affect the diffusion whereas the furnace structure was found to affect the magnitude of diffusion due to changed temperature profiles along the length of the preform and fibre. Diffusion during drawing has not been studied in detail in the past, however several heat transfer studies of the drawing process have been conducted. The effects of draw variables such as temperature, feed rate, preform diameter and furnace structure on the temperature distribution and neck-down shape generally agreed with the findings in this thesis.

Although the findings agree with previously reported results where quantitative results are available and reasonable agreement between theory and experiments has been shown, there are some limitations to this study. Measurements of fibre dopant profiles posed a great challenge and eventually a relatively recent technique, employing etching and Atomic Force Microscopy, was chosen to profile the fibres. This technique offers spatial resolution previously inaccessible, but involves an etching step that complicates the interpretation of the results. Great care was taken to obtain reliable etching reaction data, however there is a possibility that drawing induced stresses and glass fictive temperature could increase the measurement error. The theoretical heat and mass transfer calculations are another possible source of inaccuracies in the determination of the Ge diffusion coefficient. The drawing process involves complicated and interrelated

heat transfer phenomena and some assumptions are always necessary in numerical computations. The computations were validated with experimental results when possible, but due to difficult measurement conditions the available validation data is limited.

The drawing process has been optimised in the past for standard long-haul telecommunication fibre with a view to obtaining low transmission losses, high fibre strength and high production speed. For specialty fibres with high dopant concentration and multi-doped structures, diffusion effects cannot be ignored. Specialty fibres are frequently drawn at significantly lower drawing speeds and wider range of draw tensions, which further increase the likelihood of substantial diffusion effects. Combined with more stringent requirements for accurate profile control, it is essential to consider the draw conditions in terms of diffusion and other structural changes. Diffusion can be suppressed by using low draw temperatures and higher drawing speeds. The findings in this study also imply that draw tension, often used to establish proper drawing conditions, is not appropriate in diffusion control, but that both preform feed rate and draw temperature have to be considered. When diffusion parameters for all dopants in the fibre are known, diffusion during drawing can also be used to advantage. It is possible to induce a required refractive index profile change in the fibre during drawing by carefully adjusting the draw parameters and using a suitable initial preform profile. As short lengths of fibre are commonly used in specialty fibre products, the ability to produce fibres with varying profiles from one preform can be a great benefit to the manufacturer.

In order to fully benefit from this study, detailed knowledge of the diffusion behaviour of various dopants must be known. The qualitative findings in this study can be applied to dopants other than germanium and fluorine, however once detailed diffusion parameters have been established, quantitative calculations can be made to achieve maximum advantage from diffusion control. Germanium diffusion was considered in greatest detail in this study and some evidence was obtained of a concentration dependent diffusion coefficient. Such behaviour has already been reported for dopants in silica [149]. Conclusive results were not obtained for germanium in this respect and further studies should be carried out. There are several studies of dopant diffusion in optical fibres, however these studies lack consistency in terms of heating methods and

measurement techniques employed. Often the exact fibre composition is not known, complicating the task even further. A study concentrating on dopant diffusion in silica as a physical phenomena, rather than from an application point of view, with carefully chosen heating methods and specifically manufactured preform and fibre samples, together with reliable measurement techniques would be highly desirable. To maximise success of a dopant diffusion study, processes that complicate such a study should be removed. For example by using large samples difficulties in chemical analysis could be avoided and by using an optimised furnace with proper on-line temperature measurements, the complications of application specific processes such as fusion splicing, tapering or drawing can be removed. Diffusion in preform and fibre samples could be studied separately to obtain data from draw induced structural effects. These studies would then complement the studies presented here on the drawing process.

7.2 Control of photonic crystal fibre geometry during drawing

The effects of various drawing parameters on the geometry of PCFs were studied and are reported in this thesis with a focus on controlling the structure during drawing. Drawing temperature, preform feed rate, preform internal pressure and preform structure were all found to have an effect on the hole dimensions. Draw temperature and preform feed rate had a comparable effect on the hole structure and a relatively large range of air-fractions could be fabricated by adjusting the temperature or the preform feed rate. The response of the hole diameter (whilst keeping the fibre diameter constant) to change in draw temperature was surprisingly similar to that seen in different preforms drawn at various speeds and diameters. A linear relationship was found in the fibre structures studied here when operating at a temperature range where holes were not collapsed more than 60-80%. In contrast, the response to change in preform feed rate was found to depend strongly on other draw conditions and the preform structure. Radial hole size gradient was also more pronounced with faster feed rates.

A more modest change (but still about 1.5 times the hole diameter) in the air fraction was induced by a change in preform internal pressure. Despite the smaller change in hole size internal preform pressure was found to be a superior control mechanism in terms of response speed. Change in both draw temperature and preform feed rate took several minutes, if not tens of minutes, to stabilise whereas pressure change stabilised

significantly faster, enabling on-line control. Past literature recognises the use of draw temperature as the main control parameter for air-structures of PCFs, however no details are given. A theoretical study by Fitt *et al* [11] considered pressure control in capillary drawing but focussed on the upper ('explosion') and lower (total collapse) limits of pressure, not actual fine-tuning of the structures. Their study concluded that pressure might have limited use for control; this is in slight disagreement with the current study where pressure has been shown to be a useful control parameter. It is recommended here that drawing temperature is used as the means by which the hole dimensions are preset for the draw and preform feeding rates kept constant and in a suitable range from draw to draw. Preform internal pressure can then be used as an additional control whereby the fine-tuning of the hole size is obtained during the drawing.

In addition to the experimental study the effect of the air-structure on heat transfer has been studied employing fluid dynamics computations. It was found that during drawing air-structures acted as heat barriers to radial heat transfer from surface to the core of the fibre. More detailed simulations on heating of air-structured preforms revealed that the preforms heated up either slower or faster than solid preforms depending on the air-fraction in the preform. This is an important finding and implies that when fabricating fibres with different air-structures the optimised drawing conditions must be carefully considered.

As with the diffusion study there are limitations in the study of PCF drawing. Because of the great number of samples required for conducting the study, the majority of the fibre samples were measured using a relatively simple optical microscope available on-site. This is reflected in the relatively large error bars in the figures and places constraints on interpretation of the trends. Availability of a more accurate technique such as AFM on-site would greatly help in conducting any further studies.

Whereas drawing temperature measurement and preform feeding units are standard equipment in the drawing tower and known techniques are employed, preform internal pressure control systems are not available as standard on the drawing towers. Since there are several ways pressure can be controlled and various types of pressure sensors

and locations can be used, the results presented here may not apply to all pressure control systems. This should be kept in mind when applying the findings of this thesis.

Due to the quite recent renewed interest into air-structures in optical fibres there are still plenty of areas requiring research and development in PCF fabrication. This thesis has studied the effects of the main draw parameters and focussed on hexagonally packed hole structure in fibres with reasonably low air-fractions. Some fibre designs require much higher air-fractions (e.g. PBG fibres) and further study should be carried out with regard to fabrication of these types of fibres. On-line measurement of the hole structure should also be considered and would enable a more detailed investigation of geometry control of these fibres. Internal pressure control in the preform during drawing seems promising but further study should be undertaken into its effects on matters such as high frequency fluctuations and other structural changes (e.g. surface properties).

Overall in this study, some of the key changes that can occur during drawing of specialty fibres have been identified. This is, I believe, the first comprehensive study of diffusion during fibre drawing and the first comprehensive study of effects of drawing parameters on PCFs. In conventional silica fibres dopant diffusion plays an important role and both germanium and fluorine diffusion were shown to alter the fibre profiles. Whilst diffusion can be minimised by low draw temperatures and fast drawing speeds, there is also a possibility to use dopant diffusion to advantage in creating modified profiles during drawing. In PCFs the drawing-induced changes are much greater due to the presence of a hole structure. It was shown that additional control mechanisms are required to fabricate geometries with high precision. More specifically, the preform internal pressure control was found to be suitable for fast on-line control and the drawing temperature was found to provide a constant hole size response in a relatively large draw condition space. Numerical simulations of the heat and mass transfer during drawing showed the importance of both draw temperature and preform feed rate on the transfer processes as well as the complex effect of preform air-fraction on the temperature profile. It is anticipated that the results presented in this thesis will be useful both in avoiding problems in fabrication of specialty fibres and in providing new controls for making better and novel fibres.

REFERENCES

[1] Kao, K. C. and Hockham, G. A., "Dielectric-fibre surface waveguides for optical frequencies," Proceedings of IEE, Vol. 113, pp. 1151-1158, 1966.

[2] Kapron, F. P., Keck, D. B., and Maurer, R. D., "Radiation losses in glass optical waveguides," *Applied Physics Letters*, Vol. 17, pp. 423-425, 1970.

[3] Midwinter, J. E., "The start of optical fiber communications as seen from a U.K. perspective," *IEEE Journal on Selected Topics in Quantum Electronics*, Vol. 6, No.6, pp. 1307-1311, Invited paper, 2000.

[4] Gambling, W. A., "The rise and rise of optical fibers," *IEEE Journal on Selected Topics in Quantum Electronics*, Vol. 6, No.6, pp. 1084-1093, Invited paper, 2000.

[5] Mears, R. J., Reekie, L., Jauncey, I. M., and Payne, D. N., "Low-noise erbium-doped fiber amplifier operating at 1.54 μm," *Electronic Letters*, Vol. 23, pp. 1026-1028, 1987.

[6] Hersener, J., Huber, G. P., and von Wienskowski, J., "Semiquantitative X-ray microanalysis on preforms for optical fibres," *Electronic Letters*, Vol. 20, No.5, pp. 208-209, 1984.

[7] Pugh, A., *Elemental analysis of glass optical fibres with high spatial resolution*, Ph.D. Thesis, School of Engineering, Sheffield City Polytechnic, Sheffield, 176p., 1991.

[8] Pugh, A. C., Stratton, R. P., and Lewis, D. B., "Preparation of thin films of optical fibre samples for high-resolution X-ray analysis," *Journal of Materials Science Letters*, Vol. 12, pp. 1-2, 1993.

[9] Pugh, A. C., Stratton, R. P., and Lewis, D. B., "Investigation of elemental diffusion during the drawing and heat treatment of glass optical fibres," *Journal of Materials Science*, Vol. 29, pp. 1036-1040, 1994.

[10] Fitt, A. D., Furusawa, K., Monro, T. M., and Please, C. P., "Modeling the fabrication of hollow fibers: capillary drawing," *Journal of Lightwave Technology*, Vol. 19, No.12, pp. 1924-1931, 2001.

[11] Fitt, A. D., Furusawa, K., Monro, T. M., and Please, C. P., "The mathematical modelling of capillary drawing for holey fibre manufacture," *Journal of Engineering Mathematics*, Vol. 43, No.2, pp. 201-227, 2002.

[12] Deflandre, G., "Modeling the manufacturing of complex optical fibers: the case of the holey fibers," Proceedings of 2nd International Colloquium of Modelling of Glass Forming and Tempering, Valenciennes, France, pp. 150-156, 2002.

[13] Homsy, G. M. and Walker, K., "Heat transfer in laser drawing of optical fibres," *Glass Technology*, Vol. 20, No.1, pp. 20-26, 1979.

[14] Paek, U. C. and Runk, R. B., "Physical behavior of the neck-down region during furnace drawing of silica fibers," *Journal of Applied Physics*, Vol. 49, No.8, pp. 4417-4422, 1978.

[15] Paek, U. C. and Kurkjian, C. R., "Calculation of cooling rate and induced stresses in drawing of optical fibers," *Journal of the American Ceramic Society*, Vol. 58, No.7-8, pp. 330-335, 1975.

[16] Glicksman, L. R., "The dynamics of a heated free jet of variable viscosity at low Reynolds numbers," *Journal of Basic Engineering*, Vol. 90, No.9, pp. 343-354, 1968.

[17] Choudhury, S. R. and Jaluria, Y., "A computational method for generating the free-surface neck-down profile for glass flow in optical fiber drawing," *Numerical Heat Transfer, Part A*, Vol. 35, pp. 1-24, 1999.

[18] Nicolardot, M. and Orcel, G., "Numerical simulation of optical fiber preform neck-down for draw process optimization," Proceedings of International Wire & Cable Symposium, Atlantic City, NJ, pp. 369-376, 1999.

[19] Forest, M. G. and Zhou, H., "Unsteady analyses of thermal glass fibre drawing processes," *European Journal of Applied Mathematics*, Vol. 12, pp. 479-496, 2001.

[20] Liu, J., Zhang, J., and Chen, Y. S., "Advanced simulation of optical fiber drawing process," *Numerical Heat Transfer, PartA*, Vol. A 40, pp. 473-495, 2001.

[21] Cheng, X. and Jaluria, Y., "Effect of draw furnace geometry on high-speed optical fiber manufacturing," *Numerical Heat Transfer, PartA*, Vol. 41, pp. 757-781, 2002.

[22] Neumann, E.-G., *Single-mode fibers : fundamentals*, vol. 57, Berlin, New York: Springer, 530 p., 1988.

[23] Li, T., *Optical fiber communications volume 1 Fiber fabrication*, vol. 1, Orlando: Academic Press inc, 363 p., 1985.

[24] Kashyap, R., *Fiber bragg gratings*, San Diego, London: Academic Press, 458 p., 1999.

[25] Becher, P. C., Olsson, N. A., and Simpson, J. R., "Optical Fiber Fabrication, Chapter 2," in *Erbium-Doped Fiber Amplifiers: Fundamentals and Technology*, 1999, pp. 13-43.

[26] Wadsworth, W. J., Percival, R. M., Bouwmans, G., Knight, J. C., and Russell, P. S. J., "High power air-clad photonic crystal fibre laser," *Optics Express*, Vol. 11, No.1, pp. 48-53, 2003.

[27] Kaiser, P. and Astle, H. W., "Low-loss single-material fibers made from pure fused silica," *The Bell System Technical Journal*, Vol. 53, pp. 1021-1039, 1974.

[28] Birks, T. A., Roberts, P. J., Russell, P. S. J., Atkin, D. M., and Shepherd, T. J., "Full 2-D photonic bandgaps in silica/air structures," *Electronics Letters*, Vol. 31, No.22, pp. 1941-1943, 1995.

[29] Cregan, R. F., Mangan, B. J., Knight, J. C., Birks, T. A., Russell, P. S. J., Roberts, P. J.*, et al.*, "Single-mode photonic band gap guidance of light in air," *Science*, Vol. 285, pp. 1537-1539, 1999.

[30] Knight, J. C., Birks, T. A., Russell, P. S. J., and Atkin, D. M., "All-silica single-mode optical fiber with photonic crystal cladding," *Optics Letters*, Vol. 21, No.19, pp. 1547-1549, 1996.

[31] Birks, T. A., Knight, J. C., and Russell, P. S. J., "Endlessly single-mode photonics crystal fibre," *Optics Letters*, Vol. 22, pp. 961-963, 1997.

[32] Russell, P. S. J., "Photonic crystal fibers," *Science*, Vol. 299, pp. 358-362, 2003.

[33] Monro, T. M., Richardson, D. J., Broderick, N. G., and Bennett, P. J., "Holey optical fibres: an efficient modal model," *Journal of Lightwave Technology*, Vol. 17, No.6, pp. 1093-1102, 1999.

[34] Ranka, J. K., Windeler, R. S., and Stentz, A. J., "Optical properties of high-delta air-silica microstructure optical fibers," *Optics Letters*, Vol. 25, No.11, pp. 796-798, 2000.

[35] Canning, J., van Eijkelenborg, M., Ryan, T., Kristensen, M., and Lyytikäinen, K., "Complex mode coupling with in-air silica structured optical fibres and applications," *Optics Communications*, Vol. 185, No.4-6, pp. 321-324, 2000.

[36] Canning, J., Buckley, E., and Lyytikäinen, K., "Propagation in air by field superposition of scattered light within a Fresnel fibre," *Optics Letters*, Vol. 28, No.4, pp. 230-232, 2003.

[37] Eijkelenborg, M. A. v., Argyros, A., Barton, G., Bassett, I. M., Fellew, M., Henry, G.*, et al.*, "Recent progress in microstructured polymer optical fibre fabrication and characterization," *Optical Fiber Technology*, Vol. 9, No.4, pp. 199-209, 2003.

[38] Eijkelenborg, M. A. v., Large, M. C. J., Argyros, A., Zagari, J., Manos, S., Issa, N. A.*, et al.*, "Microstructured polymer optical fibre," *Optics Express*, Vol. 9, No.7, pp. 319-327, 2001.

[39] Choi, J., Kim, D., and Paek, J., "Fabrication and properties of polymer photonic crystal fibres," Proceedings of Plastic Optical Fibres Conference, Amsterdam, The Netherlands, Sep 27-30, pp. 355-360, 2001.

[40] Monro, T. M., West, Y. D., Hewak, D. W., Broderick, N. G. R., and Richardson, D. J., "Chalcogenide holey fibres," *Electronics Letters*, Vol. 36, No.24, pp. 1998-2000, 2000.

[41] Knight, J. C., Birks, T. A., Cregan, R. F., Russell, P. S. J., and de Sandro, J.-P., "Large mode area photonic crystal fibre," *Electronics Letters*, Vol. 34, No.13, pp. 1347-1348, 1998.

[42] Knight, J. C., Arriaga, J., Birks, T. A., Ortigosa-Blanch, A., Wadsworth, W. J., and Russell, P. S. J., "Anomalous dispersion in photonic crystal fiber," *IEEE Photonics Technology Letters*, Vol. 12, No.7, pp. 807-809, 2000.

[43] Saitoh, K., Koshiba, M., Hasegawa, T., and Sasaoka, E., "Chromatic dispersion control in photonic crystal fibers: application to ultra-flattened dispersion," *Optics Express*, Vol. 11, No.8, pp. 843-852, 2003.

[44] Birks, T. A., Mogilevtsev, D., Knight, J. C., and Russell, P. S. J., "Dispersion compensation using single-material fibers," *IEEE Photonics Technology Letters*, Vol. 11, No.6, pp. 674-676, 1999.

[45] Broeng, J., "Photonic crystal fibers: A new class of optical waveguides," *Optical Fiber Technology*, Vol. 5, pp. 305-330, 1999.

[46] Ferrando, A., Silvestre, E., and Andres, P., "Designing the properties of dispersion-flattened photonic crystal fibers," *Optics Express*, Vol. 9, No.13, pp. 687-697, 2001.

[47] Wadsworth, W. J., Ortigosa-Blanch, A., Knight, J. C., Birks, T. A., Mann, T. P. M., and Russell, P. S. J., "Supercontinuum generation in photonic crystal fibers

and optical fiber tapers: a novel light source," *Journal of the Optical Society of America B*, Vol. 19, pp. 2148-2155, 2002.

[48] Ranka, J. K., Windeler, R. S., and Stentz, A. J., "Visible continuum generation in air-silica microstructure optical fibers with anomalous dispersion at 800nm," *Optics Letters*, Vol. 25, pp. 25-27, 2000.

[49] Suzuki, K., Kubota, H., Kawanishi, S., Tanaka, M., and Fujita, M., "Optical properties of a low-loss polarization-maintaining photonic crystal," *Optics Express*, Vol. 9, No.13, pp. 676-680, 2001.

[50] Ortigosa-Blanch, A., Knight, J. C., Wadsworth, W. J., Arriaga, J., Mangan, B. J., Birks, T. A.*, et al.*, "Highly birefringent photonic crystal fibers," *Optics Letters*, Vol. 25, No.18, pp. 1325-1327, 2000.

[51] Kuhlmey, B. T., McPhedran, R. C., and de Sterke, C. M., "Modal cutoff in microstructured optical fibers," *Optics Letters*, Vol. 27, No.19, pp. 1684-1686, 2002.

[52] Birks, T. A., Knight, J. C., Mangan, B. J., and Russell, P. S. J., "Photonic crystal fibres: an endless variety," *IEICE Trans. Electron. (Japan)*, Vol. E84-C, pp. 585-591, 2001.

[53] Monro, T. M., Bennett, P. J., Broderick, N. G. R., and Richardson, D. J., "Holey fibers with randomly arranged air holes," *Pacific Rim Conference on Lasers and Electro-Optics, CLEO - Technical*, No.SN: 0013-5194 CODEN: ELLEAK, pp. 607-608, 2000.

[54] Tajima, K., Zhou, J., Nakajima, K., and Sato, K., "Ultra low loss and long length photonic crystal fiber," Proceedings of Optical Fibre Communication Conference OFC2003, Atlanta, Georgia, USA, Optical Society of America, pp. PD1-1-3, 2003.

[55] Mangan, B. J., Farr, L., Langford, A., Roberts, P. J., Williams, D. P., Couny, F.*, et al.*, "Low loss (1.7 dB/km) hollow core photonic bandgap fiber," Proceedings of Optical Fibre Communication Conference, Los Angeles, US, Feb 22-27, pp. PDP24, post-deadline paper, 2004.

[56] Nagel, S. R., MacChesney, J. B., and Walker, K. L., "An overview of the Modified Chemical Vapor Deposition (MCVD) process and performance," *IEEE Journal of Quantum Electronics*, Vol. QE-18, No.4, pp. 459-475, 1982.

[57] MacChesney, J. B. and DiGiovanni, D. J., "Materials development of optical fiber," *Journal of the American Ceramic Society*, Vol. 73, No.12, pp. 3537-3556, 1990.

[58] Wood, D. L., Walker, K. L., MacChesney, J. B., Simpson, J. R., and Csencsits, R., "Germanium chemistry in the MCVD process for optical fiber fabrication," *Journal of Lightwave Technology*, Vol. LT-5, No.2, pp. 277-285, 1987.

[59] Lewis, J. A., "The collapse of a viscous tube," *Journal of Fluid Mechanics*, Vol. 81, No.Part 1, pp. 129-135, 1977.

[60] Bubnov, M. M., Semjonov, S. L., Likhachev, M. E., Dianov, E. M., Khopin, V. F., Salganskii, M. Y.*, et al.*, "Optical loss reduction in highly GeO_2-doped single-mode MCVD fibers by refining refractive index profile," Proceedings of European Conference on Optical Communication, Rimini, Italy, Vol. 2, pp. 212-213, 2003.

[61] Tumminelli, R. P., McCollum, B. C., and Snitzer, E., "Fabrication of high-concentration rare-earth doped optical fibers using chelates," *Journal of Lightwave Technology*, Vol. 8, No.11, pp. 1680-1683, 1990.

[62] Morse, T. F., Kilian, A., Reinhart, L., Risen Jr, W. and Cipolla, J. W., "Aerosol techniques for glass formation," *Journal of Non-Crystalline Solids*, Vol. 129, pp. 93-100, 1991.

[63] Tammela, S., Kiiveri, P., Särkilahti, S., Hotoleanu, M., Valkonen, H., Rajala, M., *et al.*, "Direct Nanoparticle Deposition Process for manufacturing very short high gain Er-doped silica glass fibers," Proceedings of 28th European Conference on Optical Communication, Copenhagen, Denmark, Sept 8-12, Vol. 4, pp. 9.4.2, 2002.

[64] Hibino, Y. and Hanafusa, H., "Defect structure and formation mechanism of drawing-induced absorption at 630 nm in silica optical fibers," *Journal of Applied Physics*, Vol. 60, No.5, pp. 1797-1801, 1986.

[65] Hibino, Y. and Hanafusa, H., "Formation mechanism of drawing-induced peroxy radicals in pure silica optical fibers," *Journal of Applied Physics*, Vol. 62, No.4, pp. 1433-1437, 1987.

[66] Atkins, G. R., Poole, S., Sceats, M., and Simmons, H. W., "Profiling of drawing induced defects in optical fibre preforms," *Electronics Letters*, Vol. 28, No.8, pp. 768-769, 1992.

[67] Limberger, H. G., "Photosensitivity and stress in optical fiber," Proceedings of the 3rd Summer School on Photosensitivity in Optical Waveguides and Glasses, St. Petersburg, Russia, 2002.

[68] Yablon, A. D., Yan, M. F., Wisk, P., DiMarcello, F. V., Fleming, J. W., Reed, W. A., *et al.*, "Refractive index perturbations in optical fibers resulting from frozen-in viscoelasticity," *Applied Physics Letters*, Vol. 84, No.1, pp. 19-21, 2004.

[69] Canning, J., Buckley, E., Lyytikäinen, K., and Ryan, T., "Wavelength dependent leakage in a Fresnel-based air-silica structured optical fibre," *Optics Communications*, Vol. 205, No.1-3, pp. 95-99, 2002.

[70] Knight, J., Birks, T., and Russell, P., ""Holey" silica fibers, Chapter 2," in *Optics of Nanostructured Materials*, V. A. Markel and T. F. George, Eds. New York: Wiley, 2001, pp. 39-71.

[71] Zhao, Y., Fleming, S., Lyytikäinen, K., and Poladian, L., "Nondestructive measurement for arbitrary RIP distribution of optical fiber preforms," *Journal of Lightwave Technology*, Vol. 22, No.2, pp. 478-486, 2004.

[72] Zhao, Y., Lyytikainen, K., van Eijkelenborg, M., and Fleming, S., "Nondestructive measurement of refractive index profile for holey fiber preforms," *Optics Express*, Vol. 11, No.20, pp. 2474-2479, 2003.

[73] Chu, P. L., "Nondestructive measurement of index profile of an optical fibre perform," *Electronic Letters*, Vol. 13, No.24, pp. 736-738, 1977.

[74] Chu, P. L., "Nondestructive determination of refractive-index profile and cross-sectional geometry of optical-fibre preform," *Electronic Letters*, Vol. 15, No.20, pp. 635-637, 1979.

[75] Specification for S14 Fiber Refractive Index Profiler, 90-0560-00-Rev.B, Nettest, 2001.

[76] Zhao, Y., Fleming, S., Lyytikäinen, K., and Poladian, L., "Nondestructive measurement of two dimensional refractive index profile of non-circularly symmetric optical fibre preform," Proceedings of Conference on the Optical Internet & Australian Conference on Optical Fibre Technology, Melbourne, Australia, July 13-16, pp. 323-326, 2003.

[77] Technical Note: Determination of CCDR values of Fluosil preforms, Heraeus-Tenevo, Hanau, Germany, February, 2001.

[78] Gauthier, F., Auge, J., Gallou, D., Wehr, M., and Blaison, S., "Consistent refractive index profile measurement of a step-index monomode optical fiber attained by several techniques," *IEEE Journal of Quantum Electronics*, Vol. QE-17, No.6, pp. 885-889, 1981.

[79] Specification for NR-9200HR Optical Fiber Analyser, SPNR9200/HF.4AN 01/05, EXFO, 2001.

[80] Carter, A. L. G., Sceats, M. G., Poole, S. B., and Berkahn, M. B., "A new technique for studying microheterogeneity in optical fibre cores," Proceedings of Australian Conference on Optical Fibre Technology, Melbourne, Australia, pp. 379-382, 1994.

[81] Zhong, Q. and Inniss, D., "Characterization of the lightguiding structure of optical fibers by atomic force microscopy," *Journal of Lightwave Technology*, Vol. 12, No.9, pp. 1517-1523, 1994.

[82] White, K. I., "Practical application of the refractive near-field technique for the measurement of optical fiber refractive index profiles," *Optical and Quantum Electronics*, Vol. 11, pp. 185-196, 1979.

[83] Baselt, D., *The tip-sample interaction in atomic force microscopy and its implications for biological applications*, Ph.D. Thesis, California Institute of Technology, 1993.

[84] Fogler, H. S., *Elements of chemical reaction engineering*, Third ed., New Jersey: Prentice Hall PTR, 1008 p., 1998.

[85] Spierings, G. A. C. M., "Review Wet chemical etching of silicate glasses in hydrofluoric acid based solutions," *Journal of Materials Science*, Vol. 28, pp. 6261-6273, 1993.

[86] Buhler, J., Steiner, F. P., and Baltes, H., "Silicon dioxide sacrificial layer etching in surface micromachining," *Journal of Micromechanics and Microengineering*, Vol. 7, No.1, pp. R1-R13, 1997.

[87] Knotter, D. M., "Etching mechanism of vitreous silicon dioxide in HF-based solutions," *Journal of the American Chemical Society*, Vol. 122, No.18, pp. 4345-4351, 2000.

[88] Tso, S. T. and Pask, J. A., "Reaction of glasses with hydrofluoric acid solution," *Journal of the American Ceramic Society*, Vol. 65, No.7, pp. 360-362, 1982.

[89] Judge, J. S., "A study of the dissolution of SiO_2 in acidic fluoride solutions," *Journal of the Electrochemical Society*, Vol. 118, No.11, pp. 1171-1175, 1971.

[90] Monk, D. J., Soane, D. S., and Howe, R. T., "A review of the chemical reaction mechanism and kinetics for hydrofluoric acid etching of silicon dioxide for surface micromachining applications," *Thin Solid Films*, Vol. 232, pp. 1-12, 1993.

[91] Blumberg, A. A., "Differential thermal analysis and heterogeneous kinetics: The reaction of vitreous silica with hydrofluoric acid," *Journal of Physical Chemistry*, Vol. 63, pp. 1129-1132, 1959.

[92] Osseo-Asare, K., "Etching kinetics of silicon dioxide in aqueous fluoride solutions: A surface complexation model," *Journal of Electrochemical Society*, Vol. 143, No.4, pp. 1339-1347, 1996.

[93] Spierings, G. A. C. M., "Compositional effects in the dissolution of multicomponent silicate glasses in aqueous HF solutions," *Journal of Materials Science*, Vol. 26, pp. 3329-3336, 1991.

[94] Spierings, G. A. C. M. and Van Dijk, J., "The dissolution of Na_2O-MgO-CaO-SiO_2 glass in aqueous HF solutions," *Journal of Materials Science*, Vol. 22, pp. 1869-1874, 1987.

[95] Huntington, S. T., *Advances in photonic device characterisation using scanning probe microscopy*, Ph.D. Thesis, School of Physics, University of Melbourne, Melbourne, 247p., 1998.

[96] Puygranier, B. A. F. and Dawson, P., "Chemical etching of optical fibre tips - experiment and model," *Ultramicroscopy*, Vol. 85, No.4, pp. 235-248, 2000.

[97] Gibson, B. C., Huntington, S. T., Love, J. D., Ryan, T. G., Cahill, L. W., and Elton, D. M., "Controlled modification and direct characterization of multimode-fiber refractive-index profiles," *Applied Optics*, Vol. 42, No.4, pp. 627-633, 2003.

[98] Lee, M.-T., "Reaction of high-silica optical fibers with hydrofluoric acid," *Journal of the American Ceramic Society*, Vol. 68, No.2, pp. 21-22, 1984.

[99] Tenney, A. S. and Ghezzo, M., "Etch rates of doped oxides in solutions of buffered HF," *Journal of Electrochemical Society*, Vol. 120, No.8, pp. 1091-1095, 1973.

[100] Huntington, S. T., Nugent, K. A., Roberts, A., Mulvaney, P., and Lo, K. M., "Field characterization of a D-shaped optical fiber using scanning near-field optical microscopy," *Journal of Applied Physics*, Vol. 82, No.2, pp. 510-513, 1997.

[101] Huntington, S. T., Mulvaney, P., Roberts, A., Nugent, K. A., and Bazylenko, M., "Atomic force microscopy for determination of refractive index profiles of optical fibers and waveguides: A quantitative study," *Journal of Applied Physics*, Vol. 82, No.6, pp. 2730-2734, 1997.

[102] Huntington, S. T., Ashby, S. J., Elias, M. C., and Love, J. D., "Direct measurement of core profile diffusion and ellipticity in fused-taper fibre couplers using atomic force microscopy," *Electronics Letters*, Vol. 36, No.2, pp. 121-123, 2000.

[103] Pace, P., Huntington, S. T., Lyytikainen, K., Roberts, A., and Love, J. D., "Refractive index profiles of Ge-doped optical fibers with nanometer spatial resolution using atomic force microscopy," *Optics Express*, Vol. 12, No.7, pp. 1452-1457, 2004.

[104] Grundy, P. J. and Jones, G. A., *Electron microscopy in the study of materials*, London: Edward Arnold, [12], 174 p., 1976.

[105] Operation of scanning electron microscope, course notes, 27 Nov-1 Dec, Australian Key Centre for Microscopy and Microanalysis, The University of Sydney, Sydney, 2000.

[106] Anderson, S. C., *Electron-optical approaches to quantitative compositional measurement at high spatial resolution*, Ph.D. Thesis, The University of Sydney, Sydney, 206p., 1997.

[107] Electron probe microanalysis, 7-10 May, Australian Key Centre for Microscopy and Microanalysis, The University of Sydney, Sydney, 2001.

[108] Gauvin, R., Drouin, D., Couture, A. R., Hovington, P., Horny, P., and Demeres, H., "Casino, Monte Carlo simulation of electron trajectory in solids," 2.41 ed. Quebec: http://www.gel.usherb.ca/casino/index.html, 2001.

[109] Varshneya, A. K., *Fundamentals of inorganic glasses*, Boston: Academic Press, 570 p., 1994.

[110] Zachariasen, W. H., "The atomic arrangement in glass," *Journal of American Chemical Society*, Vol. 54, pp. 3841-3851, 1932.

[111] Lebedev, A. A., "Über Polymorphismus und das Kühlen von Glas," *Arb. Staatl. Opt. Inst. Leningrad*, 1921.

[112] Wefing, S., "Modeling of continuous random networks: a case study for vitreous GeO_2. II. Topological analysis and refinement," *Journal of Non-Crystalline Solids*, Vol. 244, pp. 112-127, 1999.

[113] Swenson, J. and Björjesson, L., "Intermediate range ordering in a network glass," *Journal of Non-Crystalline Solids*, Vol. 223, pp. 223-229, 1998.

[114] Marians, C. S. and Hobbs, L. W., "Local structure of silica glasses," *Journal of Non-Crystalline Solids*, Vol. 119, pp. 269-282, 1990.

[115] Gaskell, P. H., "Medium-range order and random networks," *Journal of Non-Crystalline Solids*, Vol. 293-295, pp. 146-152, 2001.

[116] Elliot, S. R., "Extended-range order, interstitial voids and the first sharp diffraction peak of network glasses," *Journal of Non-Crystalline Solids*, Vol. 182, pp. 40-48, 1995.

[117] Margaryan, A. and Piliavin, M. A., *Germanate Glasses: Structure, Spectroscopy, and Properties*, Boston, London: Artech House, 245 p., 1993.

[118] Bansal, N. P. and Doremus, R. H., *Handbook of Glass Properties*, 1 ed., Orlando: Academic Press, Inc., 680 p., 1986.

[119] McCabe, W. L., Smith, J. C., and Harriot, P., *Unit operations of chemical engineering*, 5th ed., New York: McGraw-Hill, 1130 p., 1993.

[120] Frischat, G. H., *Ionic diffusion in oxide glasses*, Bay Village, Ohio: Trans Tech Publications, 1975.

[121] Crank, J., *The Mathematics of Diffusion*, 2 ed., Oxford: Clarendon Press, 1975.

[122] Bejan, A., *Heat transfer*, New York, Chichester: John WIley & Sons, 674 p., 1993.

[123] Cussler, E. L., *Multicomponent diffusion*, vol. 3, Amsterdam, New York: Elsevier Scientific Pub. Co., 176 p., 1976.

[124] Batchelor, G. K., *An introduction to fluid dynamics*, London: Cambridge University Press, 615 p., 1967.

[125] Hondros, E. D., "Rule for surface enrichment in solutions," *Scripta Metallurgica*, Vol. 14, pp. 345-348, 1980.

[126] Personal communication with McNamara, P., Optical Fibre Technology Centre, The University of Sydney, Australia, August 2003.

[127] Fleming, J. W. and Kurkjian, C. R., "Measurement of cation diffusion in silica light guides," *Journal of the American Ceramic Society*, Vol. 68, No.9, pp. 246-248, 1985.

[128] Krause, J. T., Reed, W. A., and Walker, K. L., "Splice loss of single-mode fiber as related to fusion time, temperature, and index profile alteration," *Journal of Lightwave Technology*, Vol. LT-4, No.7, pp. 837-840, 1986.

[129] McLandrich, M. N., "Core dopant profiles in weakly fused single-mode fibers," *Electronic Letters*, Vol. 24, No.1, pp. 8-10, 1988.

[130] Shiraishi, K., Aizawa, Y., and Kawakami, S., "Beam expanding fiber using thermal diffusion of the dopant," *Journal of Lightwave Technology*, Vol. 8, No.8, pp. 1151-1161, 1990.

[131] Horiguchi, M., Shimizu, M., Yamada, M., Yoshino, K., and Hanafusa, H., "Highly efficient Er-doped fibre amplifiers pumped in 660 nm band," *Electronics Letters*, Vol. 27, No.25, pp. 2319-2320, 1991.

[132] Hanafusa, H. and Horiguchi, M., "Thermally-diffused expanded core fibres for low-loss and inexpensive photonic components," *Electronics Letters*, Vol. 27, No.21, pp. 1695-1696, 1991.

[133] Wada, A., "High efficiency erbium-doped fiber amplifier using mode-field diameter adjusting technique," Proceedings of Topical Meeting on Optical Amplifiers and Their Applications, Snowmass, US, FD3-1, pp. 258, 1991.

[134] Himeno, K., Kumayasu, S., Aikawa, K., Wada, A., and Yamauchi, R., "Splice loss of large effective area fiber and its reduction by mode field conversion," Proceedings of 23rd European Conference on Optical Communications, Edinburg, Scotland, UK, Sept 22-25, Vol. 1, pp. 131-134, 1997.

[135] Kirchhof, J., Unger, S., and Knappe, B., "Interaction of germanium and fluorine in the preparation of optical waveguides," Proceedings of Optical Fibre Communication Conference, San Jose, CA, Vol. 4, pp. 134-135, 1994.

[136] Hanaizumi, O., Aizawa, Y., Minamade, H., and Kawakami, S., "Fabrication of an expanded core fiber having MFD of 40 μm preserving outer diameter," *IEEE Photonics Technology Letters*, Vol. 6, No.7, pp. 842-844, 1994.

[137] Yamada, H. and Hanafusa, H., "Mode shape convertor produced by the thermal diffusion of different dopants," *IEEE Photonics Technology Letters*, Vol. 6, No.4, pp. 531-533, 1994.

[138] Okude, S., Sakai, T., Sudoh, M., Wada, A., and Yamauchi, R., "A novel chirped fiber bragg grating utilizing thermal diffusion of core dopant," *IEICE Transactions on Communications*, Vol. E80-B, No.4, pp. 551-556, 1997.

[139] Stevenson, A. J., Garchev, D. D., Dragomir, N. M., Walter, B. R., Baxter, G. W., and Farrell, P. M., "Effects of differential thermal dopant diffusion on splice loss arising in mode mismatch between dissimilar fibres," Proceedings of 25th Australian Conference on Optical Fibre Technology, Canberra, Australia, pp. 71-73, 2000.

[140] Huntington, S. T., Ashby, S. J., Love, J. D., and Elias, M. C., "Direct measurement and modelling of core dopant diffusion within fused biconical fibre couplers," Proceedings of Australian Conference on Optical Fibre Technology, Sydney, Australia, 1999.

[141] Englund, M. A., Lovseth, S. W., Stepanov, D. Y., and Mägi, E. C., "Selective gain tuning in erbium doped fibres," Proceedings of Australian Conference on Optical Fibre Technology, Sydney, Australia, 2001.

[142] Hermann, W., Raith, A., and Rau, H., "Diffusion of fluorine in silica," *Berichte der Bunsen-Gesellschaft für Physikalische Chemie*, Vol. 91, pp. 56-58, 1987.

[143] Harper, J. S., Botham, C. P., and Hornung, S., "Tapers in single-mode optical fibre by controlled core diffusion," *Electronics Letters*, Vol. 24, No.4, pp. 245-247, 1988.

[144] Botham, C. P., "Theory of tapering single-mode optical fibres by controlled core diffusion," *Electronics Letters*, Vol. 24, No.4, pp. 243-245, 1988.

[145] Botham, P. and Harper, S., "Design of adiabatic tapers produced by controlled core diffusion," *Electronics Letters*, Vol. 25, No.22, pp. 1520-1522, 1989.

[146] Kirchhof, J., Unger, S., Klein, K.-F., and Knappe, B., "Diffusion behaviour of fluorine in silica glass," *Journal of Non-Crystalline Solids*, Vol. 181, pp. 266-273, 1995.

[147] Fokine, M., "Thermal stability of chemical composition gratings in fluorine-germanium-doped silica fibers," *Optics Letters*, Vol. 27, No.12, pp. 1016-1018, 2002.

[148] Hellsing, M., Fokine, M., Claesson, A., Nilsson, L.-E., and Margulis, W., "ToF-SIMS imaging of dopant diffusion in optical fibers," *Applied Surface Science*, Vol. 203-204, pp. 648-651, 2003.

[149] Kirchhof, J., Unger, S., and Knappe, B., "Diffusion processes in lightguide materials," Proceedings of Optical Fiber Communication Conference OFC2000, Baltimore, Maryland, USA, Vol. 2, Optical Society of America, pp. 212-214, 2000.

[150] Iino, A., Ogai, M., and Matsubara, K., "Impurity diffusion from jacketing material in silica optical fiber," *The Transactions of the IEICE*, Vol. E70, No.4, pp. 278-279, 1987.

[151] Tammela, S., Zhan, X., and Kiiveri, P., "Comparison of gain dependence of different Er-doped fibre structures," Proceedings of SPIE Fiber Laser Sources and Amplifiers II, San Jose, CA, US, Vol. 1373, pp. 103-110, 1990.

[152] Gibson, B. C., Huntington, S. T., Love, J. D., Sader, J. E., Cahill, L. W., and Elton, D. M., "Controlled modification and direct characterisation of multimode fibre refractive index profiles," Proceedings of 25th Australian Conference on Optical Fibre Technology, Canberra, Australia, pp. 144-147, 2000.

[153] Ghezzo, M. and Brown, D. M., "Diffusivity summary of B, Ga, P, As and Sb in SiO_2," *Journal of Electrochemical Society*, Vol. 120, No.1, pp. 146-148, 1973.

[154] Mathiot, D., Straboni, A., Andre, E., and Debenest, P., "Boron diffusion through thin gate oxides: Influence of nitridation and effect on the Si/SiO_2

interface electrical characteristics," *Journal of Applied Physics*, Vol. 73, No.12, pp. 8215-8220, 1993.

[155] Campbell, D. R., Alessandrini, E. I., Tu, K. N., and Lewis, J. E., "Phosphorus diffusion in partially crystallized films of SiO_2," *Journal of Electrochemical Society*, Vol. 121, No.8, pp. 1081-1085, 1974.

[156] Bubnov, M. M., Dianov, E. M., Egorova, O. N., Semjonov, S. L., Guryanov, A. N., Khopin, V. F.*, et al.*, "Fabrication and investigation of single-mode highly phosphorus-doped fibers for Raman lasers," Proceedings of SPIE, E. M. Dianov, Vol. 4083, pp. 12-21, 2000.

[157] Iino, A., Ogai, M., and Matsubara, K., "Behavior of impurities in starting natural silica tube during MCVD deposition process," *The Transactions of the IEICE*, Vol. E 70, No.4, pp. 280-281, 1987.

[158] McNamara, P., Lyytikäinen, K., Ryan, T., Kaplin, I. J., and Ringer, S. P., "Germanium-rich "starburst" cores in silica-based optical fibres fabricated by modified chemical vapour deposition," *Optics Communications*, Vol. 230, No.1-3, pp. 45-53, 2003.

[159] Raine, K. W., "Effects of internal stress and near cleaved ends of optical fibres," Proceedings of 6th Optical Fibre Measurement Conference, Cambridge, UK, pp. 119-122, 2001.

[160] Personal communication with Schötz, G., Heraeus-Tenevo, November 2003.

[161] Haken, U., Humbach, O., Ortner, S., and Fabian, H., "Refractive index of silica glass: influence of fictive temperature," *Journal of Non-Crystalline Solids*, Vol. 265, pp. 9-18, 2000.

[162] Personal communication with Huntington, S. T., School of Physics, The University of Melbourne, Australia, March 2004.

[163] Scherer, G. W., *Relaxation in glass and composites*, New York: Wiley, 331 p., 1986.

[164] Agarwal, A. and Tomozawa, M., "Correlation of silica glass properties with infrared spectra," *Journal of Non-Crystalline Solids*, Vol. 209, pp. 166-174, 1997.

[165] Wootton, A., Thomas, B., and Harrowell, P., "Radiation-induced densification in amorphous silica: A computer simulation study," *Journal of Chemical Physics*, Vol. 115, No.7, pp. 3336-3341, 2001.

[166] Kim, D.-L. and Tomozawa, M., "Fictive temperature of silica glass optical fibers - re-examination," *Journal of Non-Crystalline Solids*, Vol. 286, pp. 132-138, 2001.

[167] Peng, Y.-L., Agarwal, A., Tomozawa, M., and Blanchet, T. A., "Radial distribution of fictive temperatures in silica optical fibers," *Journal of Non-Crystalline Solids*, Vol. 217, pp. 272-277, 1997.

[168] Kim, D.-L., Tomozawa, M., Dubois, S., and Orcel, G., "Fictive temperature measurement of single-mode optical-fiber core and cladding," *Journal of Lightwave Technology*, Vol. 19, No.8, pp. 1155-1158, 2001.

[169] Knight, J., Broeng, J., Birks, T., and Russell, P. S. J., "Photonic band gap guidance in optical fibers," *Science*, Vol. 282, No.1476, 1998.

[170] West, J. A. and Allan, D. C., "Effect of disorder on photonics band-gap fibers," Proceedings of 28th European Conference on Optical Communications, Copenhagen, Denmark, Sep 8-12, 2002.

[171] Venkataraman, N., Gallagher, M. T., Smith, C. M., Müller, D., West, J. A., Koch, K. W., *et al.*, "Low loss (13 dB/km) air core photonic band-gap fibre," Proceedings of 28th European Conference on Optical Communication, Copenhagen, Denmark, Sep 8-12, 2002.

[172] Saitoh, K. and Koshiba, M., "Confinement losses in air-guiding photonic bandgap fibers," *IEEE Photonics Technology Letters*, Vol. 15, pp. 236-238, 2003.

[173] Mortensen, N. A. and Nielsen, M. D., "Improved large-mode-area endlessly single-mode photonic crystal fibers," *Optics Letters*, Vol. 28, No.6, pp. 393-395, 2003.

[174] Mortensen, N. A. and Folkenberg, J. R., "Low-loss criterion and effective area considerations for photonic crystal fibres," *Journal of Optics A: Pure and Applied Optics*, Vol. 5, pp. 163-167, 2003.

[175] Yarin, A. L., Gospodinov, P., and Roussinov, V. I., "Stability loss and sensitivity in hollow fiber drawing," *Physics of Fluids*, Vol. 6, No.4, pp. 1454-1463, 1994.

[176] Gospodinov, P. and Yarin, A. L., "Draw resonance of optical microcapillaries in non-isothermal drawing," *International Journal of Multiphase Flow*, Vol. 23, No.5, pp. 967-976, 1997.

[177] Bennett, P. J., Monro, T. M., and Richardson, D. J., "A robust, large air fill fraction holey fibre," Proceedings of Conference on Lasers and Electro Optics, Baltimore, MD, US, pp. 293, 1999.

[178] Personal communication with Xue, S., School of Aerospace, Mechanical and Mechatronic Engineering, The University of Sydney, Australia, March 2004.

[179] Choudhury, S. R. and Jaluria, Y., "Forced convective cooling of an optical fiber during thermal processing," Proceedings of American Society of Mechanical Engineers, Heat Transfer Division, pp. 57-71, 1993.

[180] Dianov, E. M., Kashin, V. V., Perminov, S. M., Perminova, V. N., Rusanov, S. Y., and Sysoev, V. K., "The effect of different conditions on the drawing of fibres from preforms," *Glass Technology*, Vol. 29, No.6, pp. 258-262, 1988.

[181] Dianov, E. M., Kashin, V. V., Perminov, S. M., Perminova, V. N., Rusanov, S. Y., and Sysoev, V. K., "Dynamics of the drawing zone of a lightguide blank for different drawing regimes with furnace and laser heating," *Journal of Engineering Physics*, Vol. 55, No.1989, pp. 1059-1065, 1989.

[182] Geyling, F. T. and Homsy, G. M., "Extensional instabilities of the glass fibre drawing," *Glass Technology*, Vol. 21, No.2, pp. 95-102, 1980.

[183] Gupta, G. K., Schultz, W. W., Arruda, E. M., and Lu, X., "Nonisothermal model of glass drawing stability," *Rheologica Acta*, Vol. 35, No.6, pp. 584-596, 1996.

[184] Myers, M. R., "A model for unsteady analysis of preform drawing," *AIChE Journal*, Vol. 35, No.4, pp. 592-602, 1989.

[185] Ramos, J. I., "Drawing of annular liquid jets at low Reynolds numbers," *Computational and Theoretical Polymer Science*, Vol. 11, No.6, pp. 429-443, 2001.

[186] Vasiljev, V. N. and Naumchic, V. D., "Analysis of the hydrodynamic stability of the glass fibre drawing process," *Glass Technology*, Vol. 31, No.6, pp. 240-244, 1990.

[187] Gospodinov, P. and Roussinov, V., "Nonlinear instability during the isothermal draw of optical fibers," *International Journal of Multiphase Flow*, Vol. 19, No.6, pp. 1153-1158, 1993.

[188] Transparent and Opaque Fused Silica, product information data sheet, Q-A 1/112.2, Heraeus Quartzschmelze, Hanau, Germany.

[189] Griscom, D. L., "Defect structures of glasses," *Journal of Non-Crystalline Solids*, Vol. 73, pp. 51-77, 1985.

[190] Atkins, G. R., Poole, S., and Sceats, M., "Defects in optical fibres in regions of high stress gradients," *Electronics Letters*, Vol. 27, No.16, pp. 1432-1433, 1991.

[191] Kim, D.-L., Tomozawa, M., Dubois, S., and Orcel, G., "Fictive temperature measurement of single-mode optical-fiber core and cladding," *Journal of Lightwave Technology*, Vol. 19, No.8, pp. 1155-1159, 2001.

[192] Peng, Y.-L., Agarwal, A., Tomozawa, M., and Blanchet, T. A., "Radial distribution of fictive temperatures in silica optical fibers," *Journal of Non-Crystalline Solids*, Vol. 217, No.1997, pp. 272-277, 1997.

[193] Siegel, R. and Howell, J. R., *Thermal radiation heat transfer*, New York,: McGraw-Hill, xiv, 814 p., 1971.

[194] Papamichael, H. and Miaoulis, I. N., "Heat transfer in the heating region of the optical fiber drawing process," Proceedings of SPIE Properties and Characteristics of Optical Glass III, San Diego, CA, USA, Vol. 2287, SPIE, pp. 11-21, 1994.

[195] Lee, S. H.-K. and Jaluria, Y., "Simulation of the transport processes in the neck-down region of a furnace drawn optical fiber," *International Journal of Heat and Mass Transfer*, Vol. 40, No.4, pp. 843-856, 1997.

[196] Krevelen, D. W. v., *Properties of polymers, their estimation and correlation with chemical structure*, 2nd ed., Amsterdam, New York: Elsevier Scientific Pub. Co., 1976.

[197] Smithgall, D. H., "Application of optimization theory to the control of the optical fiber drawing process," *The Bell System Technical Journal*, Vol. 58, No.6, pp. 1425-1435, 1979.

[198] Denn, M. M., "Continuous drawing of liquids to form fibers," *Annual Review of Fluid Mechanics*, Vol. 12, pp. 365-387, 1980.

[199] Huynh, B. P. and Tanner, R. I., "Study of the non-isothermal glass fibre drawing process," *Rheologica Acta*, Vol. 22, No.1983, pp. 482-499, 1983.

[200] Sayles, R. and Caswell, B., "A finite element analysis of the upper jet region of a fiber drawing flow field of a temperature-sensitive material," *International Journal of Heat and Mass Transfer*, Vol. 27, No.1, pp. 57-67, 1984.

[201] Yarin, A. L., "Effect of heat removal on nonsteady regimes of fiber formation," *International Journal of Theoretical Physics*, Vol. 25, pp. 569-575, 1986.

[202] Paek, U. C., Schroeder, C. M., and Kurkjian, C. R., "Determination of the viscosity of high silica glasses during fibre drawing," *Glass Technology*, Vol. 29, No.6, pp. 263-266, 1988.

[203] Imoto, K., Sumi, M., Toda, G., and Suganeva, T., "Optical fiber drawing method with gas flow controlling system," *Journal of Lightwave Technology*, Vol. 7, No.1, pp. 115-121, 1989.

[204] Vasiljev, V. N., Dulnev, G. N., and Naumchic, V. D., "The flow of a highly viscous liquid with a free surface," *Glass Technology*, Vol. 30, No.2, pp. 83-90, 1989.

[205] Rosenberg, S. E., Papamichael, H., and Miaoulis, I. N., "A two-dimensional analysis of the viscous problem of a glass preform during the optical fibre drawing process," *Glass Technology*, Vol. 35, No.6, pp. 260-264, 1994.

[206] Lee, S. H.-K. and Jaluria, Y., "Effects of variable properties and viscous dissipation during optical fibre drawing," *Journal of Heat Transfer*, Vol. 118, pp. 350-358, 1996.

[207] Choudhury, S. R., Jaluria, Y., and Lee, S. H.-K., "Generation of neck-down profile for furnace drawing of optical fiber," Proceedings of 1995 National Heat Transfer Conference, Portland, OR, US, Vol. 4, pp. 23-32, 1995.

[208] Choudhury, S. R. and Jaluria, Y., "Practical aspects in the drawing of an optical fiber," *Journal of Material Research*, Vol. 13, No.2, pp. 483-493, 1998.

[209] Råback, P., *Valokuidun vetoprosessin numeerinen simulointi ja optimointi (Numerical modelling of optical fiber drawing process)*, M.Sc. Thesis, Department of Engineering Physics and Mathematics, The Helsinki University of Technology, Espoo, 86p., 1994.

[210] Choudhury, S. R. and Jaluria, Y., "Thermal transport due to material and gas flow in a furnace for drawing an optical fiber," *Journal of Material Research*, Vol. 13, No.2, pp. 494-503, 1998.

[211] Gardon, R., "A review of radiant heat transfer in glass," *Journal of the American Ceramic Society*, Vol. 44, No.7, pp. 305-312, 1961.

[212] Liu, J., Zhang, J., and Chen, Y. S., "Modeling of radiative transfer in optical fiber drawing processes with Fresnel interfaces," *Numerical Heat Transfer, Part B*, Vol. 39, pp. 345-370, 2001.

[213] Lee, S. H.-K. and Jaluria, Y., "The effect of geometry and temperature variations on the radiative transport during optical fiber drawing," *Journal of Materials Processing & Manufacturing Science*, Vol. 3, pp. 317-331, 1995.

[214] Yin, Z. and Jaluria, Y., "Zonal method to model radiative transport in an optical fiber drawing furnace," *Journal of Heat Transfer*, Vol. 119, pp. 597-603, 1997.

[215] Yin, Z. and Jaluria, Y., "Thermal transport and flow in high-speed optical fiber drawing," *Journal of Heat Transfer*, Vol. 120, pp. 916-930, 1998.

[216] Choudhury, S. R. and Jaluria, Y., "Convective transport in furnace for drawing an optical fiber," Proceedings of 4th ASME/JSME Thermal Engineering Joint Conference, Maui, Hawaii, US, Vol. 4, pp. 69-76, 1995.

[217] Papamichael, H. and Miaoulis, I. N., "Mixed convection effect during the drawing of optical fibers," Proceedings of SPIE Submolecular Glass Chemistry and Physics, Boston, MA, US, Vol. 1590, SPIE, pp. 122-130, 1991.

[218] Pellon, C., Papamichael, H., and Miaoulis, I. N., "Numerical simulation of the air flow patterns in an optical fiber drawing furnace," Proceedings of SPIE Properties and Characteristics of Optical Glass III, San Diego, CA, US, Vol. 2287, SPIE, pp. 22-32, 1994.

[219] Vascopulos, T., Polymeropoulos, C., and Zebib, A., "Cooling of optical fiber in aiding and opposing forced gas flow," *International Journal of Heat and Mass Transfer*, Vol. 38, No.11, pp. 1933-1944, 1995.

[220] Papamichael, H., Pellon, C., and Miaoulis, I. N., "Air flow patterns in the optical fibre drawing furnace," *Glass Technology*, Vol. 38, No.1, pp. 22-29, 1997.

[221] Papamichael, H. and Miaoulis, I. N., "Thermal modeling of the optical fiber drawing process," Proceedings of Materials Research Society Symposium, Vol. 172, Materials Research Society, pp. 43-48, 1990.

[222] Papamichael, H. and Miaoulis, I. N., "Thermal behavior of optical fibers during the cooling stage of the drawing process," *Journal of Material Research*, Vol. 6, No.1, pp. 159-167, 1991.

[223] Papamichael, H. and Miaoulis, I. N., "The cooling of optical fibres during the drawing process," *Glass Technology*, Vol. 33, No.4, pp. 136-140, 1992.

[224] Vasiljev, V. N., Dulnev, G. N., and Naumchic, V. D., "Investigation of nonstationary conditions of optical fiber formation, III. Drawing process reaction under thermal actions and perturbations of the blank radius," *Journal of Engineering Physics*, Vol. 58, No.3, pp. 370-375, 1990.

[225] Gospodinov, P. and Roussinov, V., "Drawing of optical fibers under nonsteady heat exchange," *Mechanics Research Communications*, Vol. 20, No.2, pp. 129-135, 1993.

[226] Shankarananda, B. and Rao, B. V., "Modelling and identification of optical fibre drawing process," *Modelling, Simulation & Control, A, AMSE Press*, Vol. 40, No.1, pp. 1-12, 1991.

[227] Mulpur, A. and Thompson, C., "Modal diameter control of linear isothermal optical fibers," Proceedings of Second IEEE Conference on Control Applications, Vancouver, B.C., Canada, IEEE, pp. 433-438, 1993.

[228] Bogatyrjov, V. A., Bubnov, M. M., Semenov, S. L., and Sysoliatin, A. A., "Length-varying computer-controlled fibre drawing," *Measurement Science and Technology*, Vol. 5, pp. 1370-1374, 1994.

[229] Mulpur, A. and Thompson, C., "Nonlinear control of optical fiber diameter variations," *IEEE Transactions on Control Systems Technology*, Vol. 4, No.2, pp. 152-162, 1996.

[230] Tchikanda, S. and Lee, K.-M., "State space modeling for optical fiber drawing process," Proceedings of the American Control Conference, Anchorage, Alaska, USA, Vol. 6, pp. 4954-4959, 2002.

[231] ELMER, Computational resource in research and development, CSC - Scientific Computing Ltd, http://www.csc.fi/elmer/, 21/1, 2003.

[232] Franca, L. P., Frey, S. L., and Hughes, T. J. R., "Stabilized finite element methods," *I. Comp. Meths. Appl. Mech. Engrg*, Vol. 95, pp. 253-276, 1992.

[233] Han, H., Park, H., Cho, M., and Kim, J., "Terahertz pulse propagation in plastic photonic crystal fibres," Proceedings of the 4th Pacific Rim Conference on Lasers and Electro-Optics, Chiba, Japan, July 15-19, post-deadline paper, 2001.

[234] Large, M. C. J., Eijkelenborg, M. A. v., Argyros, A., Zagari, J., Manos, S., Issa, N. A., *et al.*, "Microstructured polymer optical fibres: a new approach to POFs,"

Proceedings of Plastic Optical Fibres Conference, Amsterdam, The Netherlands, Sep 27-30, post-deadline paper, 2001.

[235] Reeve, H. M. and Mescher, A. M., "A study on transient heating of polymer fiber preforms," *Journal of Materials Processing & Manufacturing Science*, Vol. 1999, No.8, pp. 94-105, 1999.

[236] Reeve, H. M., Mescher, A. M., and Emery, A. F., "Experimental and numerical investigation of polymer preform heating," *Journal of Materials Processing & Manufacturing Science*, Vol. 9, No.April, pp. 285-301, 2001.

[237] Reeve, H. M., Mescher, A. M., and Emery, A. F., "The effect of natural convection heating instabilities on the diameter of polymer optical fiber," Proceedings of 11th International Plastic Optical Fibres Conference 2002, Tokyo, Japan, Vol. Post-deadline papers, pp. 5-8, 2002.

[238] Issa, N. A. and Poladian, L., "Vector wave expansion method for leaky modes of microstructured optical fibers," *Journal of Lightwave Technology*, Vol. 21, No.4, pp. 1005-1012, 2003.

[239] Hiroishi, J., Kumano, N., Mukasa, K., Sugizaki, R., Miyabe, R., Matsushita, S.*, et al.*, "Dispersion slope controlled HNL-DSF with high γ of $25W^{-1}km^{-1}$ and band conversion experiment using this fiber," Proceedings of 28th European Conference on Optical Communication, Copenhagen, Denmark, Sep 8-12, pp. PD1.5, 2002.

[240] Brugger, K., "Effect of thermal stress on refractive index in clad fibers," *Applied Optics*, Vol. 10, No.2, pp. 437-438, 1971.

[241] Park, Y. and Paek, U. C., "Residual stresses in a doubly clad fiber with depressed inner cladding (DIC)," *Journal of Lightwave Technology*, Vol. 17, No.10, pp. 1823-1834, 1995.

[242] Bachmann, P. K., Hermann, W., Wehr, H., and Wiechert, D. U., "Stress in optical waveguides. 2: Fibers," *Applied Optics*, Vol. 26, No.7, pp. 1175-1182, 1987.

[243] Scherer, G. W., "Thermal stresses in a cylinder: application to optical waveguide blanks," *Journal of Non-Crystalline Solids*, Vol. 34, pp. 223-238, 1979.

[244] Scherer, G. W., "Stress-optical effects in optical waveguides," *Journal of Non-Crystalline Solids*, Vol. 38-39, pp. 201-204, 1980.

[245] Scherer, G. W., "Stress-induced index profile distortion in optical waveguides," *Applied Optics*, Vol. 19, No.12, pp. 2000-2006, 1980.

[246] Scherer, G. W. and Cooper, A. R., "Thermal stresses in clad-glass fibers," *Journal of the American Ceramic Society*, Vol. 63, No.5-6, pp. 346-347, 1980.

[247] Chu, P. L. and Whitbread, T., "Measurement of stresses in optical fiber and preform," *Applied Optics*, Vol. 21, No.23, pp. 4241-4245, 1982.

[248] Bachmann, P. K., Hermann, W., Wehr, H., and Wiechert, D. U., "Stress in optical waveguides. 1: Preforms," *Applied Optics*, Vol. 25, No.7, pp. 1093-1098, 1986.

[249] Rongved, L., Kurkjian, C. R., and Geyling, F. T., "Mechanical tempering of optical fibres," *Journal of Non-Crystalline Solids*, Vol. 42, pp. 579-584, 1980.

[250] Hibino, Y., Hanawa, F., Abe, T., and Shibata, S., "Residual stress effects on refractive indices in undoped silica-core single-mode fibres," *Applied Physics Letters*, Vol. 50, No.22, pp. 1565-1567, 1987.

[251] Hibino, Y., Hanawa, F., and Horiguchi, M., "Drawing induced residual stress effects on optical characteristics in pure-silica-core single-mode fibers," *Journal of Applied Physics*, Vol. 65, No.1, pp. 30-35, 1989.

[252] Hibino, Y., Edahiro, T., Horiguchi, T., Azuma, Y., and Shibata, N., "Evaluation of residual stress and viscosity in SiO_2-core/F-SiO_2 clad single-mode optical fibers from Brillouin gain spectra," *Journal of Applied Physics*, Vol. 66, No.9, pp. 4049-4053, 1989.

[253] Tajima, K., Tateda, M., and Ohashi, M., "Viscosity of GeO_2 doped silica glasses," *Journal of Lightwave Technology*, Vol. 12, No.3, pp. 411-415, 1994.

[254] Hermann, W., Hutjens, M., and Wiechert, D. U., "Stress in optical waveguides. 3: Stress induced index change," *Applied Optics*, Vol. 28, No.11, pp. 1980-1983, 1989.

[255] Okamoto, K., Hosaka, T., and Edahiro, T., "Stress analysis of optical fibers by a finite element method," *IEEE Journal of Quantum Electronics*, Vol. QE-17, No.10, pp. 2123-2129, 1981.

[256] Hayata, K., Koshiba, M., and Suzuki, M., "Stress-applied optical fiber having inhomogeneous core," *Electronics and Communications in Japan*, Vol. 70, No.9, pp. 74-81, 1987.

[257] Hayata, K. and Koshiba, M., "Characteristics of graded-core stress-applied polarization-maintaining single-mode fibres," *Journal of the Optical Society of America A*, Vol. 5, No.4, pp. 535-541, 1988.

[258] Wong, D., "Thermal stability of intrinsic stress birefringence in optical fibers," *Journal of Lightwave Technology*, Vol. 8, No.11, pp. 1757-1761, 1990.

[259] Hadjipocopiou, M. and Reed, G. T., "Optimisation of coating properties for fibre optic smart structures using finite element analysis," Proceedings of Smart Structures and Materials 1995: Mathematics and Control in Smart Structures, SPIE Proceedings, San Diego, CA, US, Vol. 2442, pp. 109-120, 1995.

[260] Digas, J., Pierrejean, I., Farenc, J., and Peichot, J. P., "Birefringence and internal stress in polystyrene optical fibers," *Applied Optics*, Vol. 33, No.16, pp. 3454-3548, 1994.

[261] Nakai, T., Norimatsu, N., Noda, Y., Shinbori, O., and Mimura, Y., "Changes in refractive index of fluoride glass fibers during fiber fabrication processes," *Applied Physics Letters*, Vol. 56, No.3, pp. 203-205, 1990.

[262] Gianino, P. D. and Bendow, B., "Calculation of stress-induced changes in the traverse refractive-index profile of optical fibres," *Applied Optics*, Vol. 20, No.3, pp. 430-434, 1981.

[263] Simpson, A. M., Sikorski, A., Ringer, S. P., and Keast, V. J., "Recent advances in specimen preparation for the materials sciences," in *Science, Technology and Education of Microscopy: an Overview*, vol. 1, *FORMATEX Microscopy Book Series*, A. Méndez-Vilas, Ed. Madrid, Spain, 2003, pp. 34-42.

[264] Vargaftik, N. B., *Handbook of physical properties of liquids and gases : pure substances and mixtures*, 2nd ed., Washington: Hemisphere Pub. Corp., xii, 758 p., 1983.

[265] Barin, I. and Knacke, O., *Thermochemical properties of inorganic substances*, Berlin, New York,: Springer-Verlag, 921 p., 1973.

[266] Lyytikäinen, K., Zagari, J., Barton, G., and Canning, J., "Heat transfer within a microstructured polymer optical fibre," *Modelling and Simulation in Materials Science and Engineering*, Vol. 12, pp. S255-S256, 2004.

[267] Zagari, J., *The fabrication of microstructured polymer optical fibres*, M.Sc. Thesis, Department of Chemical Engineering, Faculty of Engineering, the University of Sydney, Sydney, 180p., 2003.

[268] Landau, R. H. and Páez Mejía, M. J., *Computational physics: Problem solving with computers*: Wiley, 1997.

APPENDIX I: STRESS-INDUCED INDEX PROFILE CHANGE

This appendix presents a literature review of the stress-induced index profile change.

1. INTRODUCTION

As a result of the manufacturing of optical preforms and fibres thermal and mechanical stresses develop in the structure. For example when an optical preform with a core and a cladding is cooled down from the processing temperature, thermal stresses develop due to differences in thermal expansion coefficients of the core and the cladding, when one is doped more heavily than the other. Also differences in viscosity of the core and the cladding will create additional stresses as well as differences in Young's modulus and Poisson's ratio. Under these stresses the core and cladding can become optically anisotropic. This is known as stress birefringence or photo-elastic effect and is well understood and documented in the literature.

Basically, under tensile stress the refractive index of the material will decrease and under compressive stress increase. Stresses resulting from manufacturing steps such as preform fabrication, fibre drawing and other thermal processing can be readily calculated based on structural mechanics [121, 240]. At first most of the studies were concentrating on the thermal stresses in optical preforms and fibres, but later it was realized that the drawing process introduced additional mechanical stresses which had a major effect on certain fibre structures and a number of studies resulted about mechanically induced residual stresses for different fibres.

The three major stress-inducing mechanisms are 1) thermal stresses, 2) hydrostatic pressure, 3) mechanically induced stresses. Thermal stresses arise due to mismatch of expansion coefficients of different regions in the preforms and fibres. Thermal stresses arising from preform manufacture and fibre drawing are very similar and the same methods can be used to estimate them. For accurate estimations the different setting temperatures have to be taken into account [241]. Stresses due to hydrostatic pressure are generated in regions where certain material components behave elastically but

others are still fluid. If the core is still fluid when the cladding is solidified, the fluid core with no free surfaces exerts a hydrostatic tension on the cladding on cooling. Mechanically induced stresses are due to the drawing process, namely the drawing tension. Mechanically induced stress is related to cross-sectional areas, elastic moduli and viscosities of different regions in the fibre. When the pulling force is released a frozen-in stress remains. The final residual stresses in the fibre are the superposition of the stresses due to the above mechanisms. More details are given in [242] and [15].

2. THERMAL STRESSES

Based on thermal stress calculations in a simple fibre structure with core and cladding, Brugger [240] concluded that if the thermal expansivity of the core is much larger than that of the cladding the cut-off wavelength will be changed due to the stress effect on refractive index difference. By assuming constant material properties but differences in thermal expansion coefficients he obtained an equation to estimate the effect and concluded that unless the expansivities of the two media differ by a much larger amount than the refractive indices, the thermal stress effect can be neglected. This is true based on the assumption of the same material properties, other than expansion coefficient, of the two media. However if the setting temperatures, i.e. viscosities, are different for the two media then the solidification at different temperatures has to be taken into account.

This was recognized by Scherer [243] who took into account in his thermal stress calculations the fact that the setting point, T_s, below which glass behaves elastically, is different for the core and the cladding. In a case where the core has a lower setting temperature it still remains fluid when the cladding sets. As the thermal expansion coefficient for fluid is about three times greater than for solid, additional stress develops in the core. Scherer [244, 245] and Scherer and Cooper [246] calculated thermal stresses taking into account the viscoelastic behaviour of the problem, where they also noted that for the fibre drawing process, due to cooling rates, fibres behave elastically at temperatures well above the annealing range. Scherers analysis [244] for graded index fibres showed that as a result of the core setting later than the cladding the axial stresses increase less than for the fully elastic case, but that radial and circumferential stresses are greater. For step index fibres he concluded` that as the stresses start to develop as

early as 600°C before the annealing point, the real stresses would be 20-50% larger than those calculated in his analysis.

The effect of different dopants was also studied by Scherer [245] based on differences in thermal expansion coefficient. In his analysis he concluded that thermal stresses are higher in P_2O_5 doped fibres compared to GeO_2 doped glass due to two factors a) the thermal expansion coefficient is larger for P_2O_5-doped fibres when the refractive index is matched to be the same as in GeO_2 doped fibres and b) doping with P_2O_5 reduces the setting temperature rapidly while GeO_2 has little effect. Both of the above mentioned causes, Scherer reports, also apply for B_2O_3 doped regions, thus concluding that thermal stresses in a GeO_2 doped core are minimized by having a B_2O_3 –doped ring surrounding the core.

A measurement technique for measuring stresses in optical preforms and fibres was presented by Chu and Whitbread [247]. They measured the retardation of the components of the polarized light ray emerging from the preform or fibre in an index matching fluid. For the measurements of thermal stresses they used two preforms, one having a P_2O_5 doped core and the other a GeO_2 doped core surrounded by a B_2O_3 doped ring, both manufactured by the MCVD process. For both cases the thermal stresses were compressive for the cladding, while the cores and the ring had tensile stresses. Stress measurements were also conducted by Bachmann *et al* [248] who used the same measurement technique as describe by Chu and Whitbread [247]. In their study they found that thermal stresses due to GeO_2 doping increased linearly as the doping level increased, however for fluorine they reported a non-linear behaviour which they believed to be due to a complex relationship between thermal expansion coefficient of fluorine doped silica, temperature and concentration.

3. Mechanical stresses

The first studies of drawing-induced residual stresses in optical fibres were done for fibres manufactured with rod in tube method. Paek and Kurkjian [15] and then later Rongved, Kurkjian and Geyling [249] studied the fibre drawing effect on stresses for clad fibres with harder core and softer outer cladding. Paek and Kurkjian [15] showed that by drawing (18m/min) fibres at different pulling tensions, 4-80g, the residual stresses in the cladding changed from compressive to tensile or the opposite if cladding-

core materials were switched. Their experiment showed that the mechanically induced stresses are significant and cannot be neglected.

Based on a similar analysis, compressive cladding stresses were studied by Rongved, Kurkjian and Geyling [249]. The motivation for their study was to enhance the compressive cladding residual stresses in the fibre in order to improve its mechanical properties. They concluded that in order to maximise mechanically induced stresses the pulling force must be large or the viscosity difference between the core and the cladding be large. In addition to structural analysis they measured axial stresses in fibres using a polariscope to determine the relative retardation for a ray normal to the fibre axis and tangential to the core. Their fibre design had a silica core of 110μm with a 4μm borosilicate cladding and the pulling tension used was very high, 680g. In their analysis the different setting temperatures of the core and cladding were not taken into account but the annealing temperature of the softer glass was used as was the case in reference [15].

Residual stresses in a single mode silica core fibre were studied by Hibino *et al* [250-252]. Their fibre had a pure silica core with a fluorine doped cladding. The fibre was drawn with low tension of 5g and high tension of 85g at draw speed of 30m/min. The residual stresses in fibres were measured by photoelastic CT (computer tomography) method and refractive index measurements were also conducted. Their stress analysis assumed that the thermal stresses can be neglected due to the small cross-sectional area of the core. They also assumed that the radial refractive index change is mainly due to the axial stress. This is true when radial and hoop stresses are much smaller than the axial stress. Their refractive index profile comparison of the fibres showed a 50% decrease in the refractive index difference of the core and the cladding for the fibre pulled at 85g tension compared to the one pulled at 5g tension. The calculated and measured residual stresses show a much higher tensile stress in the core, which causes the decreased refractive index of the core. To check this, the fibres were annealed and it was reported that the additional tensile stress in the core was released after 10min at 1000°C. The cut-off wavelength was also measured for the two fibres and showed a decrease from 1400nm to 900nm when the pulling tension was increased from 16g to 80g [251]. This behaviour was reported to be similar to fibres with different fluorine concentrations, the cut-off decrease rate being similar with increased tension. They also

measured a GeO_2 doped fibre and found no cut-off shift in a range of 16 to 80g. In another publication by Hibino *et al* [252] they propose a new evaluation of residual stresses and viscosity from Brillouin gain spectra.

Fibres with doped cores were studied by other groups. Chu and Whitbread [247] measured stresses in fibres. Their fibre design had a GeO_2 doped core surrounded by a B_2O_3 doped ring made by the MCVD process. The preforms were drawn with 32g tension and Chu and Whitbread found that the cladding stress had changed from compressive to tensile due to pulling-induced stresses. The average stress in the core was changed from tensile to compressive. Due to the more viscous cladding, it absorbs most of the stresses from pulling and when these are relieved the core stresses become compressive to comply with the equilibrium condition in the fibre.

Bachmann *et al* [242] studied two different fibre designs, one with a GeO_2 doped core where the doping level was changed gradually but in a few steps, and another with a fluorine doped core. In both cases the viscosity was lower in the core as opposed to the previously mentioned studies. Thermal stresses in the preforms were earlier published in Ref. [248]. Their structural analysis assumed constant setting temperature and Young's modulus and Poisson's ratio were kept constant. However their analysis was more complicated as they took into account not two but N number of layers in a fibre. In their experiments they drew fibres with different dopant concentrations at 5-60m/min and 1900-2100°C temperatures and changed the drawing tension between 5-100g. They concluded from measurements and analysis that the stress levels in different layers were constant thus representing the refractive index profile plot, i.e. if concentration was constant with radius, then stress level was constant for that region. The stress was found to change linearly with draw tension, such that in the cladding the stress increased when pulling tension was increased, causing the compressive cladding stress to change to tensile for high pulling tensions. For the core this was the opposite. This behaviour was the same for all concentrations. They also found that the stress was only dependent on draw tension and not temperature. GeO_2 doped core fibres were also studied by Tajima *et al* [253], who measured the viscosities of Ge-doped fibres in order to produce viscosity matched fibres to avoid residual stresses from the drawing process.

For F-doped fibres, Bachmann *et al* [242] found that the drawing process always enhanced the stress difference between F-doped material and the quartz substrate tube. The behaviour of stress with F concentrations was not however linear and Bachmann *et al* [242] suggested a concentration dependent hysteresis of the thermal expansion coefficient of fluorine doped glass. The results might however be also due to the fact that Young's modulus of fluorine doped silica shows a non-linear decrease as a function of fluorine concentration as measured by Hibino *et al* [251].

A more complex fibre structure was studied by Hermann *et al* [254]. They studied a dispersion flattened single mode fibre drawn at different tensions. The fibre had a GeO_2 doped core surrounded by alternating fluorine and GeO_2 doped rings. Refractive index profile measurements were done for both preforms (York P102) and fibres (RNF technique) to observe the stress induced refractive index change. The measurement set-up for fibre refractive index profiling caused limitations on resolution and thus only effects on cladding vs. substrate tube were studied. The fibres were drawn at tensions of 50g, 120g and 240g. They concluded that the cladding to substrate tube refractive index difference increased, changing from negative to positive for higher tensions. The stress measurements showed that the tensile stress in the substrate tube increased with the draw force while the core and the cladding became more compressive. This was due to the substrate tube taking most of the draw force as the core and the cladding were still fluid.

The effects of depressed inner cladding on residual stresses in the core were studied by Park *et al* [241]. The fibre had a GeO_2 doped core with fluorine doped inner cladding. In their structural analysis they took into account the different setting temperatures of each layer when evaluating the thermal stresses. They concluded that the depressed inner cladding did not have a substantial effect on the stresses in the core. Unfortunately they could not measure the drawing induced mechanical stresses due to resolution limitations on their measurement equipment.

All the above-mentioned studies used fibre design with cylindrically symmetric profiles. Stress-induced birefringent single-mode fibres are made by introducing asymmetry in the fibre. Especially fibres with two refractive index pits in either side of the core and elliptical core designs have been of special interest in structural stress calculations. The

first such calculation was published by Okamoto *et al* [255]. As the fibre structures were not cylindrically symmetric, analytical methods could not be used, thus the finite element method was used in their calculations. In their analysis they calculated modal birefringence in elliptical core fibres as a function of ellipticity. For elliptical core fibres they concluded that for small refractive index differences (0.2-0.4%) the stress induced birefringence was greater than the geometrical anisotropy, however, for index differences higher than 1.5% the geometrical anisotropy becomes greater than the stress induced. They also analysed the so called side-pit fibre which had P-doped core with B-doped side pits and concluded that the numerical results agreed well with measured results.

Later on Hayata *et al* [256, 257] used a similar finite element method to analyse a bow-tie fibre. In addition to thermal residual stress calculations they also did a modal analysis of the fibre. Elliptical core and bow-tie fibres were also studied by Wong [258] who considered the effects of different fictive temperatures of the different regions in the fibres. Stress analysis is widely used in other industries and a multitude of commercial calculation packages can nowadays be bought to analyse e.g. thermal or load induced stresses.

There are some other publications not so relevant but closely relating to drawing and optical fibres. For example stress analysis has been used in optimisation of coating properties of optical fibres [259] and drawing of polymer optical fibres [260]. Stresses induced in fluoride glasses during drawing have been studied [261] and stress induced changes from diametral stress in optical fibres have been reported in Ref. [262].

APPENDIX II: TRANSMISSION ELECTRON MICROSCOPY SPECIMEN PREPARATION

The following describes a detailed preparation of TEM specimens from optical fibres developed by Mr Adam Sikorksi of the Electron Microscopy Unit (EMU), the University of Sydney and is modified from the Ref. [263].

1. BACKGROUND

Conventional cross-sectional methods of preparation are not suitable due to the geometry of the specimens and the small size of the core. Another option would be to use a Focused Ion Beam (FIB) system, which has been very successful in a number of difficult specimen preparation situations. However, preparing specimens < 100 nm in thickness and suitable for high resolution compositional analysis is very difficult with FIB, primarily because of the surface damage layers produced by the implantation of the Ga ions. In this work we apply tripod polishing, a method mainly used for site-specific specimen preparation in the semiconductor industry, to prepare thin cross sectional specimens of optical fibres.

2. METHOD

One approach to preparing a cross-section specimen would be to prepare a specimen from a single fibre. However, due to the small size of the fibres, handling of one piece is quite difficult. In this work we built a block with several pieces of fibre sandwiched between supporting pieces of Si wafer. This block was then tripod polished, ensuring the cross-section passed through the central 3μm core. Final ion milling to electron transparency was done with a Gatan precision ion polishing system[16] (PIPS). The flow chart in Figure 1 shows the major steps in going from the as-given optical fibre to a final longitude cross-section specimen ready for TEM and suitable for high-resolution microanalysis. Each step is described in detail below.

[16] Ar ions are used in PIPS.

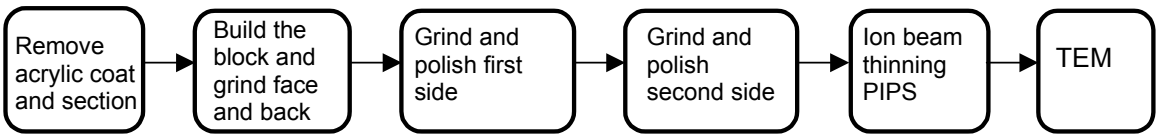

Figure 1. Flow chart of specimen preparation.

1. **Remove acrylic coat.** The acrylic coating was removed by simply soaking in acetone for 10 minutes and then removing by hand. Sectioning of small pieces was done with a razor blade.
2. **Build the block**. Next, a block was built containing several fibres sandwiched between 2mm x 2mm x 0.5mm Si pieces, cleaved from an Si wafer (see Figure 2). The block was bonded together using G1 epoxy, cured at 800°C for 20 min. After the block was completed the front and back of the block were ground and polished. A smooth face is important in the later steps as it helps to monitor the progress of further grinding. At this stage diamond papers of 30, 9, 3, 1μm were used progressively and the specimen was fixed on the tripod polisher stage with crystal bond glue (melting point 1200°C) on a hot plate.

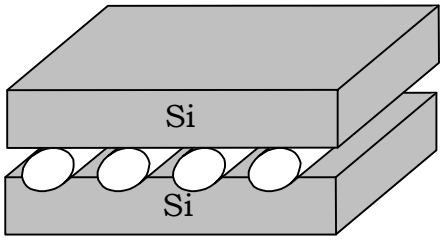

Figure 2. Optical fibres sandwiched between silicon wafers and bonded in G1 glue.

3. **Grind and polish first side**. The specimen was then removed from the tripod polisher stage and reattached with Si wafer down. The tripod polisher legs are adjusted so that the specimen surface is in the same plane as the legs. This is done by placing the tripod polisher, specimen down, on a glass plate and adjusting the legs until there are no gaps between the surface of the specimen and the glass plate. The tripod legs are then turned by 15 microns in

opposite directions. This means that when the specimen is ground it will be ground at an angle to produce a wedge, see Figures 3. The specimen is then ground and polished with diamond papers as before, monitoring progress with an optical microscope, until the core is reached.

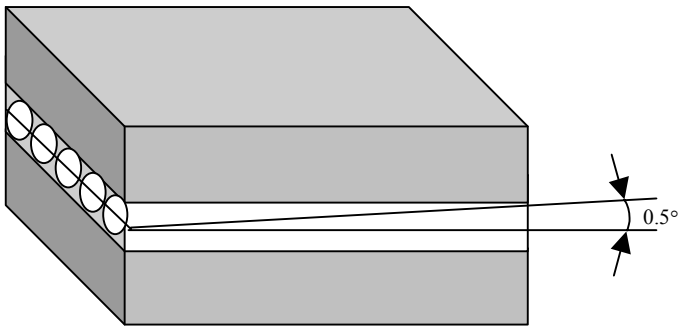

Figure 3. Wedge angle on specimen after legs on tripod are adjusted for angled grinding.

4. **Grind and polish second side**. The specimen was removed from the tripod stage using a hot plate and carefully cleaned in acetone before proceeding. During polishing of the second side, the specimen becomes very thin and prone to fracture. It has been found that gluing the specimen on a piece of Si, rather than directly on the Pyrex tripod stage, makes polishing of the second side easier. The Si base is actually ground as part of the wedge and, as it is much easier to grind Si than Pyrex, it seems to protect the thin specimen, causing less fracture. A piece of Si wafer, 5 mm x5 mm x 0.5 mm, was attached to the tripod stage with superglue. After 10 min the superglue had set sufficiently to hold the Si. The tripod stage, with the Si on the top, was then fixed in the tripod polisher. Alignment was done on the glass plate to give one plane between the Si top surface and the back tripod legs, as was done with the first side. The Si was ground with 30μm diamond paper until the entire surface of the Si had been ground. A thin layer of superglue was applied to the Si and the specimen fixed, with the previously polished side down (Figure 4), and left overnight to ensure the superglue is completely set. The tripod polisher legs are turned 30μm in opposite directions to produce a wedge shape on the specimen during grinding, see Figure 4. Grinding and polishing of the second side is done, using on 30, 9, 3, 1μm diamond papers, until the 3μm core was reached. The final thickness of the sample was around 5-10μm.

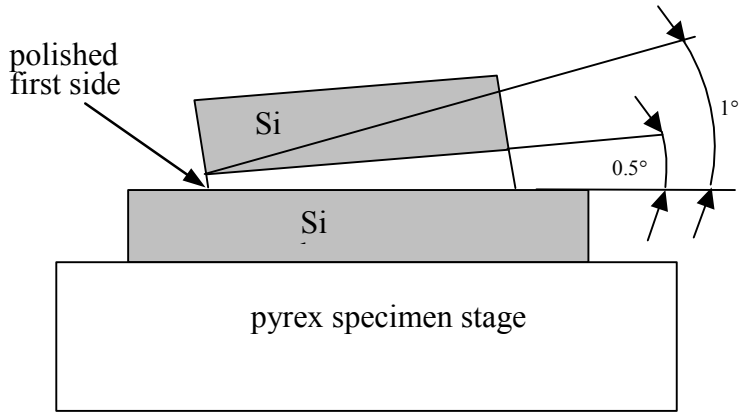

Figure 4. Wedge angle on specimen for angled grinding of second side after adjustment of tripod polisher legs.

5. **Removing specimen from tripod stage**. After the second side is completed the specimen is very thin and breaks easily when removed from the stage. To protect the specimen from damage and to ease handling, a Cu "notched" slot grid was fixed to the specimen before removal. Notched Cu grids are a Cu-Be alloy, are twice the thickness of regular grids and can be easily cut. Before attaching the grid, the specimen is thoroughly cleaned in ethanol and a thin layer of superglue applied around the specimen to fill in any gaps and left for 15min to dry. The grid was cut to open it up on one side to face the ion guns during ion milling. A small amount of M-bond 610 epoxy was applied to the specimen, the grid fixed to the top, and then cured at 100°C for 20min. After curing, the specimen was placed in an acetone bath, for several hours or overnight, to separate the specimen with the attached grid from the Si and Pyrex stage.

6. **Ion beam thinning**. The PIPS was then used for final thinning to electron transparency. The milling was done using single sided modulation with the guns set with one at +8° and the other at -8°. Milling was done at 4 kV and with a stage rotation of 3 rpm. Final milling took around 4 hours.

APPENDIX III: MATERIAL PARAMETERS FOR SILICA AND VIEW FACTOR CALCULATIONS

1. MATERIAL PARAMETERS

See Table 6-1 on page 184 for nomenclature.

Table 1. Material properties

Properties	*Glass*	*Gas [264]*	*Graphite*	*Insulation*
Density ρ [kg/m^3]	2200	0.4	2250	2200
Conductivity k [W/mK]	Eq.(51)	Eq. (55)	20.0	1.0
Heat capacity c_P [[J/kgK]	Eq.(50)	520	2000	1000
Emissivity ε	Eq. (53)	N/A	0.9	0.9

Viscosity of silica [188]:

$$\mu = 10^{\left(-7.24+26900/T\right)} \tag{49}$$

Specific heat capacity of silica [188]:

$$c_p = 1350.0\left(1-e^{0.11945-0.003T}\right) \tag{50}$$

Heat conductivity of silica:

$$\begin{aligned} k_c &= a_1\left(bT-c\right)^3 + a_2\left(bT-c\right)^2 + a_3\left(bT-c\right) + a_4 \\ k_r &= d\,T^3 \end{aligned} \tag{51}$$

where a_n, b, and c are fitted constants [195]. The following values were used:

$$a_1 = -1.68\times10^{-11},\ a_2 = 4.74\times10^{-9},\ a_3 = -4.31\times10^{-4}$$

$$a_4 = 1.34,\ b = 9/5 \text{ and } c = 459.4$$

d is calculated from Equation (52) as presented in Equation (32), [14].

$$k_r = \frac{-16n^2\sigma T^3}{3\alpha} \tag{52}$$

The average absorption coefficient, α, 4cm^{-1} was used [184]. Emissivity for glass depends on the preform/fibre radius [184].

$$\varepsilon = 0.885 \times \left(1 - e^{(-1.2 \times 2.0 \times 400.0 \times r)}\right) \tag{53}$$

For the 20 mol% GeO_2 doped core specific heat capacity is [265]:

$$\begin{aligned} c_p &= 0.8 \times 1350.0\left(1 - e^{0.11945 - 0.003T}\right) \\ &+ 0.2 \times 770.0\left(1 - e^{-0.454 - 0.002T}\right) \end{aligned} \tag{54}$$

and density, ρ = 2150 kg/m^3 [118]. Heat conductivity was taken as that of silica, as no material data was found for GeO_2 doped silica.

Heat conductivity for gas [264]:

$$k = -8.0 \times 10^{-9} T^2 + 4.7 \times 10^{-5} T + 4.8 \times 10^{-3} \tag{55}$$

2. GEBHARDT AND VIEW FACTORS

Gebhardt factors shown in Equation (41) can be computed from Equation (56)

$$G = F(I - (I - E)F)^{-1} E \tag{56}$$

where F is the view factor matrix and E a diagonal matrix of surface emissivities. A view factor between two surface patches of a geometrical model is defined as

$$F_{ij} = \frac{1}{A_i} \int_{A_i} \int_{A_j} \frac{\cos\theta_i \cos\theta_j}{\pi s^2} H_{ij} dA_j dA_i \tag{57}$$

where A is area of the patch i or j and θ_i and θ_j the angles between the normals of the surfaces at given points and s the distance between the points. H_{ij} is the visibility function and shading is taken into account.

APPENDIX IV: HEAT TRANSFER EXPERIMENT WITH MPOF PREFORM

The following text is an extract from Ref. [266] by Lyytikäinen *et al.* The experimental work was carried out by J. Zagari at OFTC, and was part of his M.Sc. [267] for the University of Sydney.

In order to validate the heat transfer modelling work in Section 6.3.7, experiments were conducted with MPOF preforms. These preforms were prepared from a 5cm diameter piece of extruded PMMA with a length of 140mm. Both a solid and an air-structured preform were used. The air-structure was the same as that for Preform A shown in Figure 6-21 with 2mm diameter holes extending throughout the entire length. A convection type furnace was used in these experiments, with the preform suspended in a metal cylinder hung within the furnace chamber and hot air blown in via a ring of holes situated near the centre of the metal cylinder, Figure 1(a). T-type thermocouples were embedded in the preform to measure the temperature at various positions during the heating-up process, see Figure 1(b). The thermocouple holes extended down some 70mm to the position of the 'hot-zone' created by the hot air inlets. The airflow through the holes was restricted by blocking them at both ends of the preform. The heating was very efficient in that the furnace air temperature reached its set value in two minutes, from room temperature. A temperature lower than the usual PMMA draw temperature was used so that the preform did not deform while being heated. The oven temperature was set at 130°C while the preform was heated up over a period of two hours.

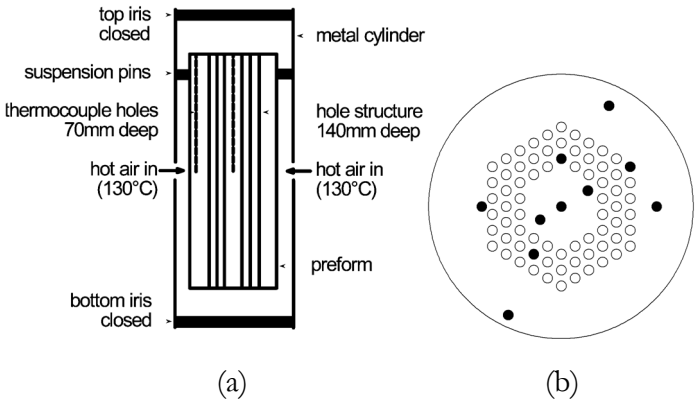

Figure 1. (a) Heating experiment set-up, preform inside the furnace. (b) Cross-section of the preform showing thermocouple positions (filled circles).

Figure 2 shows a comparison between simulated and measured data for air-structured Preform A at a position 2mm from the preform surface and in the centre of the rod. In the initial modelling work radiative heat transfer from the surface was ignored, however it soon became apparent that this mode of heat transfer could not be omitted. After inclusion of the thermal radiation term, the simulated temperatures showed good agreement with the measured values. Again it must be noted that the thermal conductivity of the polymer was adjusted such that the simulated data (after radiative heat transfer was included) matched the experimental data as closely as possible. No other parameters were adjusted. The measured temperatures steadied out to a lower temperature than the oven air temperature, as can be seen from Figure 2. This was felt to be due to the finite length of the preform, which was not taken into account in the simulations that assumed an infinitely long cylinder.

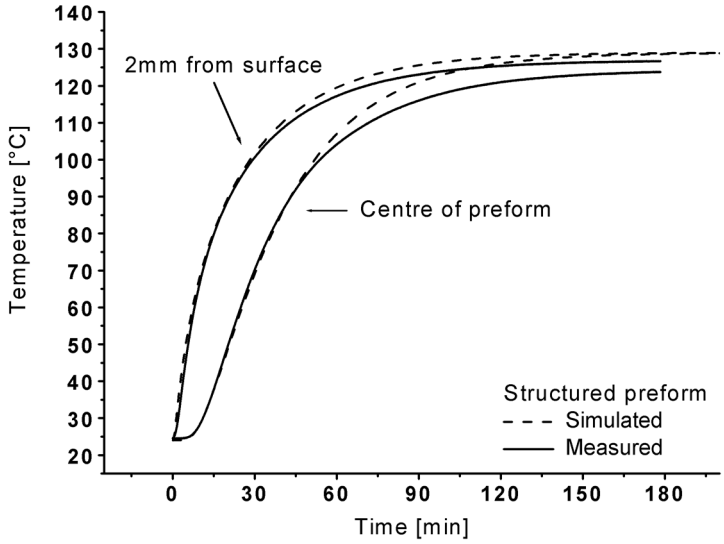

Figure 2. Measured vs. simulated data for MPOF preform.

Figure 3 shows temperature contour plots at 2, 3 and 4hr from an axisymmetric model, where the finite length of the preform was taken into account [266]. As can be seen from Figure 3 there is hardly any change between 3 and 4hr of heating while the top half of the preform has steadied out to a lower temperature than the furnace temperature of 130°C. These simulation results showed that the measured lower steady-state temperature was almost certainly due to heat loss from the preform top end which was exposed to a lower air temperature. The initial heating-up phase (that

is, well before the temperatures began to approach their equilibrium values), however, agreed well with the two-dimensional infinite cylinder model, which could thus be used to study the effect of air structures on heat transfer in MPOF's.

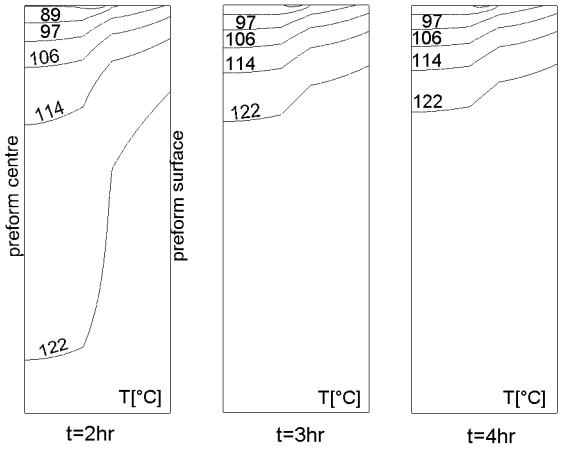

Figure 3. Temperature contour plot of the axisymmetric model after 2, 3 and 4 hr of heating.

APPENDIX V: DIFFUSION COMPUTATIONS

The diffusion problem involved solving the partial differential equation (47) numerically. The equation is coupled to the temperature via the temperature dependence of the diffusion coefficient, Equation (48). Diffusion was assumed to occur only in the radial direction and so a 1-dimensional cylindrical equation can be used. The differential diffusion equation was converted into an approximate finite-difference equation. The algorithm is derived by expanding $c(r, t+\Delta t)$ and $c(r+\Delta r, t)$ in a Taylor series. The program was written in FORTRAN77 using an example code eqheat.f from Landau [268], as a starting point. An analytical solution to a steady-state cylindrical 1D diffusion equation with constant diffusion coefficient, constant "dopant source" in the middle and zero concentration on the surface [121] was used to verify the code.

The list below describes the calculation sequence of the program.

1. Define material parameters for Arrhenius equation
2. Define computational parameters e.g. Δr, Δt
4. Define initial concentration profile and boundary conditions
5. Loop over z (longitudinal sections)
    - Read fibre temperature, draw speed and radius for z_i – position
    - Calculate diffusion coefficient and maximum number of time iterations from glass velocity, Δz and Δt
    6. Loop over time
        7. Loop over space
        - Calculate new concentration profile
    8. Recycle values, new becomes old
    9. Stop after max number of iterations done
10. Calculate scaling factor for profile (as preform necks-down)
11. Stop after all z done.